This electronic thesis or dissertation has been downloaded from Explore Bristol Research, http://research-information.bristol.ac.uk

Author:
Butler, Peter A

Title:
Neutron- and Photon-Induced Charge Dynamics in Group III-Nitride Semiconductor Devices

General rights
Access to the thesis is subject to the Creative Commons Attribution - NonCommercial-No Derivatives 4.0 International Public License. A copy of this may be found at https://creativecommons.org/licenses/by-nc-nd/4.0/legalcode This license sets out your rights and the restrictions that apply to your access to the thesis so it is important you read this before proceeding.

Take down policy
Some pages of this thesis may have been removed for copyright restrictions prior to having it been deposited in Explore Bristol Research. However, if you have discovered material within the thesis that you consider to be unlawful e.g. breaches of copyright (either yours or that of a third party) or any other law, including but not limited to those relating to patent, trademark, confidentiality, data protection, obscenity, defamation, libel, then please contact collections-metadata@bristol.ac.uk and include the following information in your message:

- Your contact details
- Bibliographic details for the item, including a URL
- An outline nature of the complaint

Your claim will be investigated and, where appropriate, the item in question will be removed from public view as soon as possible.

Neutron- and Photon-Induced Charge Dynamics in Group III-Nitride Semiconductor Devices

By

PETER ANTHONY BUTLER BSC (HONS) MINSTP

H.H. Wills Physics Laboratory
UNIVERSITY OF BRISTOL

A dissertation submitted to the University of Bristol in accordance with the requirements of the degree of DOCTOR OF PHILOSOPHY in the Faculty of Science.

MAY 2019
SCHOOL OF PHYSICS

Word count: ≈ 62000

Abstract

Semiconductor devices formed from the group III-nitride materials, aluminium gallium nitride (AlGaN) and gallium nitride (GaN), have the potential to increase the efficiency and performance of electrical systems for safety-critical applications and harsh radiation environments. In this thesis, the electrical characteristics and irradiation response of AlGaN and GaN heterostructures, and High Electron Mobility Transistors (HEMTs), were studied using electron conduction, trapping, and generation. An admittance-based method was developed to measure mobility in a two-dimensional electron gas (2DEG) without using Ohmic contacts. Using the technique, the 2DEG density dependence of mobility in AlGaN/AlGaN heterostructures was measured from 80 K to 400 K, providing insights into mobility-limiting scattering mechanisms and the sources of carriers in the 2DEG. A current transient spectroscopy technique was developed to study charge trapping effects in HEMTs exposed to neutron irradiation. Two mechanisms contributing to irradiation-induced performance degradation were identified: increases in trap density, and changes to inter-trap coupling behaviour. *In situ* measurements were made of Schottky-gate and Metal-insulator-semiconductor-gate (MIS) HEMT response to the highly challenging Omega laser Inertial Confinement Fusion (ICF) pulsed neutron environment. Schottky-gate HEMTs proved more irradiation-sensitive than MIS HEMTs, but recovered in as little as $10\,\mu$s after irradiation, with no catastrophic failures observed for drain biases of up to 150 V. These differences will inform the design of circuits for use in neutron radiation environments, and merit further investigation.

A pulsed femto-second laser system was developed to simulate irradiation-induced Single Event Effects (SEE), and to probe HEMT internal electric field profiles, by using localised two photon absorption (TPA). The system induced ion irradiation-like enhanced charge collection effects in HEMTs, with distinct prompt and delayed conduction processes. Peak currents and charge collected at HEMT contacts displayed power law dependences on pulse energy. Locations of electric field peaks within HEMTs, associated with reliability-limiting degradation processes and susceptibility to SEE, were located, found to depend on buffer doping, and shown to move when electrical biasing was altered. These findings are important for testing the safe operating area of HEMTs. The magnitude and duration of the SEE-like electrical transients varied with irradiation pulse repetition frequency (PRF): peak current increased as a sub-unity power of PRF, suggesting a dependence upon excess carrier lifetime and defect density. SEE susceptibility testing using repetitive irradiation sources should account for the PRF effect. Finally, a fast-acting mechanism was found to limit the combined effect of two discrete irradiation pulses that arrive in quick succession. For inter-pulse delays of the order ≈ 100 ps, peak drain current and total charge collected decrease by up to a third, as compared to $\approx$ ns delays, where the effects of two pulses combine constructively. This limiting mechanism fundamentally connects the prompt and delayed current components of irradiation response, and may help to explain the lack of catastrophic breakdown events observed in HEMTs irradiated at pulsed neutron sources.

Acknowledgements

This work would not have been possible without the support of AWE Plc. I am particularly indebted to the Technical Outreach programme and to the Radiation Science Group for their ongoing commitment to this project. Special thanks are due to Mr David Osborne, who supported my change from part-time to full-time study. There is no doubt that this change was instrumental in enabling progress to be made with this project. I would like to thank my supervisor, Professor Martin Kuball, for allowing me to join the group to pursue my research, and for continuing to encourage me to develop my scientific writing. Thanks are also due to Professor Michael Uren for suggesting the possibility of converting a successful collaboration into a PhD studentship, and for being a diligent co-author. I have also greatly benefited from progress monitoring reviews with Professor David Cherns and Dr Andrei Sarua, for which I am grateful.

Dr James Pomeroy has been a source of insightful advice and clear thinking when circumstances permitted, particularly on experimental matters. It was fun building a lab from scratch with James' help, and coming all the way to France with me to learn something about laser radiation effects testing was very much appreciated. When Dr William Waller was a still a lowly PhD student we collaborated easily, achieving success in the form of my first publication in an academic journal. Tea and 'skivey coffee' breaks undoubtedly contributed to realising the good teamwork. I would like to thank Dr Roland Baranyai Simon, a fellow victim of the need to conduct sensitive optics experiments after everyone else has gone home, for popping into M20 to provide late night moral support and enthusiastic criticism on many occasions. I thank Dr Hareesh Chandrasekar for his friendly and enthusiastic help, particularly at sub-zero temperatures.

I would like to thank my US colleagues, in particular Dr William (Billy) Martin of Sandia National Laboratories. Without Billy's enthusiastic support, the study of 14 MeV neutron effects on mobility, and the pulsed neutron testing at the University of Rochester's Omega laser, would not have been possible. Dr Mark Gadja at Nexperia is thanked for helpful discussions and for GaN-on-Si devices. Dr Benoit Lambert at UMS is thanked for packaged GaN-on-SiC devices. Drs Andrew Armstrong, Andrew Allerman and Robert Kaplar, for ultra-wide band gap material, and for being excellent co-authors. Thanks are also due to Dr Trevor Martin (IQE). I am grateful to Mr Adam Frydland for supporting this research project, particularly earlier in my studies and in preparing for and attending the Omega laser experiments.

I have been fortunate to meet and get to know many lovely people during my time in Bristol: Drs Máire Power, Richard Webster, Richard Brooke, Gary Sitbon, Miguel Montes Bajo, 'the kids', and of course Dr Julian Anaya, to name but a few. Thanks Drs Stefano Dalcanale and Filip Gucmann for sharing your enthusiasm for running with me. I can't possibly name everyone, but to everyone who I have enjoyed games of badminton with, or even better, drinks together at Friday pub, you guys are great! My friends and family have been a tremendous support throughout. But finally, I would like to thank Hannah Carroll for supporting me through the crazy working hours, and especially for ensuring that we escaped to the great outdoors occasionally.

Author's declaration

I declare that the work in this dissertation was carried out in accordance with the requirements of the University's Regulations and Code of Practice for Research Degree Programmes and that it has not been submitted for any other academic award. Except where indicated by specific reference in the text, the work is the candidate's own work. Work done in collaboration with, or with the assistance of, others, is indicated as such. Any views expressed in the dissertation are those of the author.

SIGNED: .... DATE: ....

Table of Contents

Abstract **i**

Acknowledgements **iii**

Author's declaration **v**

List of Tables **ix**

List of Figures **xi**

Page

1 Introduction **1**

1.1 World dependence on electricity, and the role of electronics 1
1.2 The need for radiation-hard electronics 2
1.3 The potential of wide band-gap semiconductors 6
1.4 Circuit applications for HEMTs 8
1.5 The objectives of this thesis 8
1.6 Thesis structure 9

2 Theoretical background **11**

2.1 Growth and epitaxy 11
2.2 (Al)GaN electrical properties and crystal structure 12
2.3 High electron mobility transistors (HEMTs) 18
2.4 Mobility - bulk and two-dimensional 20
2.5 Neutron irradiation interactions 27
2.6 Ionisation localised along tracks 36
2.7 Optical ionisation 38
2.8 Summary 41

3 Experimental techniques **43**

3.1 Sample preparation for measurement and irradiation 44
3.2 Electrical instruments and methods 45

3.3 Temperature control 48
3.4 Femto-second pulsed laser irradiation 50
3.5 Summary 53

4 Mobility in two-dimensional electron gases 55
4.1 Sample details 57
4.2 Ohmic contact-free mobility measurement 58
4.3 Mobility in a graded Al-composition structure 69
4.4 The effect of varying epitaxial layer thickness 70
4.5 The temperature dependence and impact of neutron irradiation on mobility from 80 to 400 Kelvin 73
4.6 Conclusions 87

5 Neutron-induced charge trapping effects 89
5.1 Details of UMS devices studied with CTS 91
5.2 Experimental details 91
5.3 Method of determining trapped charge density 93
5.4 Producing current transient spectra 96
5.5 The 'range' of active trap density as a damage measure 97
5.6 Results 97
5.7 Damage modelling 101
5.8 Discussion of the neutron testing results 104
5.9 Conclusions 107

6 Pulsed Inertial Confinement Fusion (ICF) neutron effects 109
6.1 Experimental Details 111
6.2 Results 116
6.3 Discussion 121
6.4 Conclusions 125
6.5 Acknowledgements 126

7 Pulsed ionisation effects using femto-second lasers 127
7.1 Experimental details 130
7.2 Charge deposition due to a representative knock-on ion 134
7.3 Charge generation by sub-band-gap laser illumination 138
7.4 Measurements of charge collection and enhancement 147
7.5 A pulse repetition frequency (PRF) effect 160
7.6 Simulating a double ion strike 167
7.7 Irradiation location sensitivity and electric-field profile 178
7.8 Summary 186

8 Summary and conclusions **189**

Publications and conference contributions **193**

Publications . . . 193

Conference contributions . . . 193

Bibliography **195**

Glossary of Terms **216**

List of Tables

Table **Page**

1.1 Indicative material properties for some important semiconductors. . . . 6

2.1 Primary knock-on atom energies and average displacement energies in GaN. . . . 31

4.1 Epitaxy details of mobility test samples. . . . 58

4.2 Table of model parameters for the source of the 2DEG. . . . 80

4.3 Peak and open channel mobility at 80, 300, and 400 K, before and after irradiation. . 81

4.4 Model parameters for the temperature dependence of mobility. . . . 84

7.1 Epitaxy details of wafers used for femto-second laser studies . . . 131

List of Figures

Figure		Page
1.1	Cosmic ray-generated secondary particle flux at sea level.	3
1.2	Geographic map of energetic electron and proton activity at around 840 km.	4
1.3	Generic neutron energy spectra for several environments.	5
1.4	Radar plot comparing semiconductor properties.	7
2.1	AlGaN/AlGaN epitaxial structure.	13
2.2	Wurtzite GaN crystal structure.	14
2.3	Polarisation in AlGaN/GaN epitaxial layers.	15
2.4	2DEG dependence on barrier thickness.	16
2.5	High Electron Mobility Transistor (HEMT) designs.	19
2.6	Electron drift velocity in wurtzite GaN.	27
2.7	Mean free path for neutrons in Ga-69.	29
2.8	Neutron scattering cross-sections for Al, Ga, and N.	30
2.9	An illustration of the GaN hexagonal lattice.	34
2.10	A two-dimensional illustration of crystallographic point defects.	35
2.11	Plot of linear energy transfer (LET) against depth for 3.5 MeV nitrogen ions in GaN.	38
2.12	Wurtzite GaN band diagram.	41
3.1	Sample packaging and wire bonding.	45
3.2	Keithley parameter analyser and test enclosure.	46
3.3	Schematic illustrating a device under test (DUT) to SMU connection.	47
3.4	Cryostat experimental setup.	49
3.5	AlGaN/AlGaN test structures contacted by probes in the cryostat.	49
3.6	Pulsed femto-second laser setup constructed for this work.	51
4.1	Micrograph of a Schottky disc contact and surrounding annulus contact deposited on the AlGaN/AlGaN.	58
4.2	Equivalent circuit model of the AlGaN/AlGaN Schottky contact disc-annulus structures.	61
4.3	Sample 1 G_p/ω vs. frequency plot for a subset of the disc voltages tested.	65
4.4	Mobility as a function of channel carrier density, n_{2DEG}, at 25 °C.	66

4.5 Mobility plotted against n_{2DEG} as a function of temperature. 68
4.6 Capacitance-voltage profiles obtained from testing the graded composition Sample 3. 70
4.7 C-V profiles for Samples 1 and 2, with n_{2DEG} also plotted as a function of voltage. . . 71
4.8 G_p/ω vs. frequency plot for Sample 2. 72
4.9 Mobility as a function of n_{2DEG} measured for Sample 2 at 300 K. 73
4.10 n_{2DEG} plotted against temperature for Sample 1 and 2, before and after irradiation. . 79
4.11 Arrhenius plot of n_{2DEG}, before and after irradiation. 80
4.12 Mobility-channel carrier density plots measured at 80, 300, and 400 K. 82
4.13 Mobility plotted against temperature prior to and following irradiation. 83
4.14 Sheet resistance plotted against temperature. 85

5.1 UMS GH-25 HEMT packaged, and installed into temperature controlled test fixture. 92
5.2 Illustration of HEMT charge trapping locations and a current transient spectrum. . . 95
5.3 Drain current transients prior to and following irradiation. 99
5.4 Measured current transient spectra as function of t_{fill} and neutron irradiation fluence. 100
5.5 Effective density of depletion region trapped charge emitted during a measurement. . 101
5.6 Source-gate and source-drain currents plotted against gate-source voltage before and after irradation. 102
5.7 Total stable defect density plotted against neutron fluence. 103
5.8 Band diagrams showing charge (de)trapping currents under the HEMT gate. 106

6.1 The relative timings of X-ray and neutron outputs during an Omega laser ICF burn. 111
6.2 Characteristic curves for large L-Type and M-Type HEMTs fielded at Omega. 112
6.3 Final Omega Laser test PCB design. 114
6.4 Omega facility noise and cable pickup measurement using an off-state resistor pack. 116
6.5 On-state current transients due to exposure to an Omega laser ICF neutron pulse. . . 117
6.6 Drain current transients measured during exposure to an Omega laser ICF burn. . . 118
6.7 On-state HEMT drain current transients measured during exposure to Omega laser ICF burn shots. 119
6.8 On-state long duration transient measurements. 120
6.9 Peak 1 drain current magnitude shown as a function of gate bias, V_{GS}. 120
6.10 Peak 2 drain current magnitude shown as a function of $V_{DS} - V_{GS}$. 121
6.11 Drain current settling times after exposure to an Omega ICF neutron pulse. 122
6.12 HEMT DC parameters measured during the Omega laser 2017 ICF neutron tests. . . 123

7.1 Top side images of HEMTs used for laser testing. 131
7.2 Intensity profile of laser spot reflected from back surface of wafer. 132
7.3 Measured transmittance against change in semiconductor-objective lens separation. . 134
7.4 Transmitted laser power variation with incident power. 135
7.5 1-D projection of a TRIM calculation of ionisation due to 1 MeV Ga ion into GaN. . . . 136

7.6 TRIM calculation of ionisation due to 1 MeV Ga ion into GaN. 137
7.7 Asymmetric charge generation as a function of depth due to refraction. 141
7.8 Calculated density of charge generated by TPA in the focal region. 146
7.9 Delay between Photodiode signal and HEMT gate transient. 148
7.10 Gate and drain photocurrent transients at $V_{DS} = 0\,V$ as a function of gate voltage. . . 149
7.11 Gate current against time as a function of gate-source voltage. 149
7.12 Peak current and charge collection with zero drain bias. 150
7.13 Peak current and total charge collected as a function of gate voltage for Wafer B. . . . 151
7.14 Peak current and charge collected as a function of V_{DS} for two laser pulse energies. . 152
7.15 Wafer A: peak current and charge collected as a function of incident laser pulse energy.153
7.16 Wafer B: peak current and charge collected as a function of incident laser pulse energy.153
7.17 Electric field maps and band diagrams from TCAD simulations. 155
7.18 TCAD calculation of the electron concentration within a HEMT due to a laser pulse. . 157
7.19 HEMT drain transients exhibiting a pulse repetition frequency effect 161
7.20 Peak drain current and collected charge plotted against PRF. 161
7.21 Pulse repetition frequency effect on Wafers A and B. 163
7.22 Drain transients measured on Wafers A and B at 3 kHz. 164
7.23 Combined direct and delayed beam profiles. 169
7.24 Drain current transient measured using a HEMT irradiated with a double laser pulse.171
7.25 Speed of light calculated using double pulse rise time to calibrate distance scale. . . . 172
7.26 Charge collected at a HEMT drain contact plotted against the second pulse delay time.173
7.27 Plot showing $\Delta Q = Q_{\mathrm{double}} - (Q_1 + Q_2)$ against delay time. 174
7.28 Peak gate and drain currents plotted against second pulse delay time on Wafer A. . . 175
7.29 Composite image of a HEMT source-drain gap and the laser spot. 180
7.30 Peak current and collected charge as a function of irradiation position. 182
7.31 Surface topography of a HEMT as measured with an atomic force microscope (AFM). 183

Chapter 1

Introduction

1.1 World dependence on electricity, and the role of electronics

World energy use is rising, and its supply by fossil fuels continues to cause greenhouse gas emissions. Demand for energy in the form of electricity is rising faster than total energy demand, meaning global energy use is increasingly becoming electrical in nature [1]. In 2017 global energy usage in the form of electricity had reached 25570 TWh [1]. The United Nations Intergovernmental Panel on Climate Change (IPCC) has concluded that human activities have caused approximately 1.0°C of global warming above pre-industrial levels [2]. The IPCC found that global temperature rise is expected to reach 1.5°C between 2030 and 2052, if there is no change in its rate of increase. Therefore, increasing the efficiency of electricity production, transmission, and end usage, can help to limit anthropogenic climate change. Increased efficiency will also enable cost reductions. With the urgent need to reduce greenhouse gas emissions, particularly CO_2, due to the disastrous consequences of climate change [2], reducing losses of electrical energy is becoming an increasingly critical global objective. Power distribution improvements, using solid-state switching and conversion can improve efficiency and so reduce greenhouse gas emissions for a given power level. The use of electricity to provide lighting accounts for around 15% of electrical power usage, and changing from incandescent bulbs to light-emitting diodes (LEDs) can cut that electrical power use by up to 90% [3]. This change is being enabled in part by blue LEDs constructed from gallium nitride (GaN) which can be used to produce efficient bright light, for which the inventors, Akasaki, Amano, and Nakamura, received the 2014 Nobel Prize in Physics.

Systems that depend on electronics are now ubiquitous and have become integral to society and the global economy. As suggested by the improvements in lighting efficiency already underway,

there remains significant potential for improvements in efficiency in, for example, electrical power distribution, and usage for heating and transport. Where electronics are used for infrastructure, or to control or monitor safety- or performance-critical systems, very high standards of reliability must be assured. Understanding of reliability must therefore be developed along with the new technologies and existing ones. Ageing and random failures need to be considered, but another factor that can affect reliability and even cause sudden catastrophic failure is radiation. If the benefits of the energy savings possible with new electronic technologies are to be realised, by their insertion into key infrastructure and systems, then their performance and reliability must be assured in the naturally occurring and artificial radiation environments that are found where such systems are used.

1.2 The need for radiation-hard electronics

The vulnerability of electronic systems to failure caused by radiation effects was dramatically demonstrated following the STARFISH PRIME high-altitude exo-atmospheric nuclear test on the 9th of July 1962 [4]. That nuclear explosion, detonated at around 400 km over Johnston Atoll in the Pacific Ocean, had an explosive yield equivalent to around 1.4 million tonnes of trinitrotoluene (TNT). The approximately 10^{29} fission electrons released by that explosion became trapped by the Earth's magnetic field, increasing the charge concentration in the inner zone radiation belt by several orders of magnitude [5]. The TELSTAR communications satellite, launched the day after the nuclear test, was the first satellite to fail due to total ionising dose, and within six months ten satellites had failed due to the elevated radiation levels. The failures were attributed to be primarily due to solar cell damage [4]. Since then destructive 'hard errors' have been observed due to energetic single particles that include burn-out, gate rupture, and latch-up, an overview of which has been given by Sexton [6]. Following the hard failures observed in the satellites, soft failures became apparent. Binder *et al.* looked at anomalies in communication satellite operation [7], and found that whilst it was known that the majority of the digital errors were caused by the high temperature plasma of the radiation belts, cosmic rays also contributed. At Intel, the 'alpha particle problem' was recognised in 1978 at sea level, as reported by May and Woods [8]. This phenomenon is where the ionisation caused by alpha particles emitted from trace amounts of uranium or thorium, present in semiconductor devices or their packaging, is sufficient to cause random single bit errors - 'bit flips'. The problem was initially recognised in charge coupled devices (CCDs) and dynamic random access memories (DRAMs), where the concept of critical charge (Q_{crit}) was defined as the number of electrons which differentiates between a '0' and a '1'. As recognised by Ziegler (IBM) and Lanford [9], the reduction in the size of circuit features, which has continued to this day, enabled the charge deposited by a single alpha particle to be sufficient to cause bit flips. This raised the question of effects due to cosmic rays at sea level.

Cosmic rays were discovered by V.H. Hess who received a half share of the Nobel Prize for

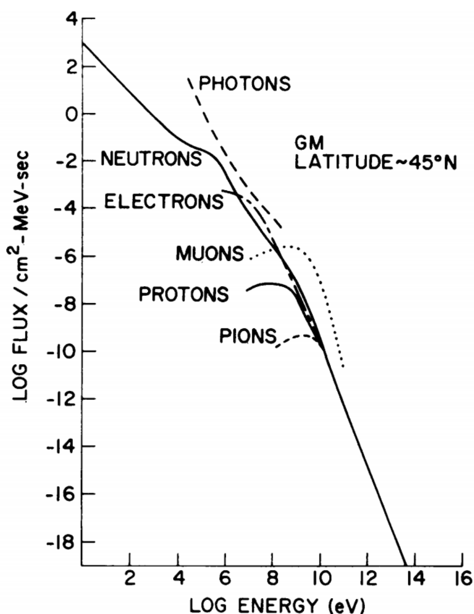

Figure 1.1: Cosmic ray-generated secondary particle flux at sea level, averaged over time and angle of incidence, at 45 degrees geomagnetic (GM) latitude, plotted against particle energy. Reproduced with permission from [9].

physics in 1936 for his discovery of cosmic radiation. The other half was received by C.D. Anderson for his discovery of the positron. By performing electroscope measurements in a hot air balloon, in 1912 Hess found that the flux of cosmic rays changes with altitude - first decreasing with increasing altitude, but then increasing. He established their origin was not solar by performing experiments at night and during solar eclipses. Experimental evidence that they originate from super nova remnants has recently been found by observing gamma rays with energies characteristic of pion decay following high energy proton-proton or nuclear-nuclear collisions [10]. Incidentally, pi-mesons (pions) were discovered by Cecil Powell when he was at Bristol, for which he received the Nobel Prize in Physics 1950. Primary cosmic rays are predominantly protons but there is also a proportion that is due to heavier ions. Primary cosmic rays interact with the air to produce secondary cosmic rays, and most primaries do not reach below around 20 km [9]. Secondaries consist of various species of particles, of these neutrons are the most numerous, as shown in Figure 1.1. Cosmic ray flux is affected by solar activity, and is a maximum when solar activity is at its 11-year minimum. Sunspot activity has also been found to affect galactic cosmic ray flux by up to a factor of two [11]. Secondary cosmic ray flux varies with respect to altitude, position with respect to the Earth's magnetic field, and radiation belts. Many models of radiation environments are available, and the reader is referred to [4] and references therein for a further information on space, atmospheric, and terrestrial radiation environments.

The South Atlantic Anomaly (SAA) is a rather dramatic example of the positional variation of the radiation environment near Earth. The effects of the SAA can be seen on the energetic

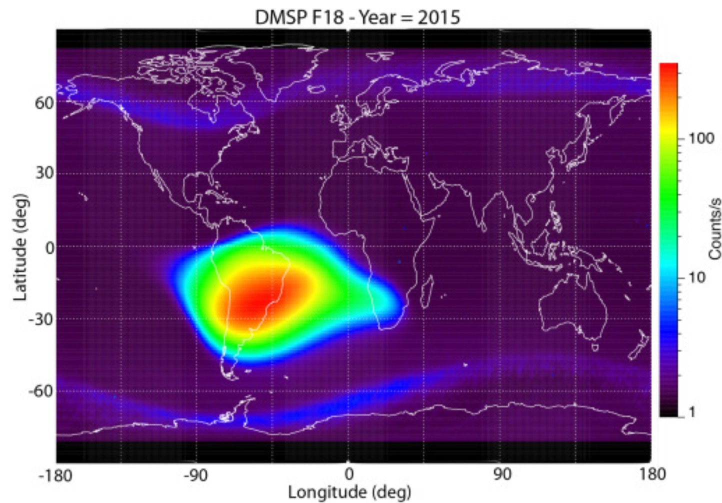

Figure 1.2: Geographic map of counts per second due to energetic electrons (>2.4 MeV) and protons (>29 MeV) inferred from signal contamination at around 840 km by an instrument designed to measure 30 eV to 30 keV electrons and ions. The instrument was flown in an US Air Force meteorological satellite during 2015. The South Atlantic Anomaly is shown as the highest activity region. The Northern and Southern regions where radiation belts pass through that altitude are clear. Reproduced with permission from [14].

electron flux and proton flux recorded by an US Air Force meteorological satellite in a polar orbit at around 840 km during the year 2015, as shown in Figure 1.2. In 2015 Stassinopoulos *et al.* reviewed the available literature which showed that the SAA had been drifting over a 40 year period [5]. Solar flares and storms can quickly alter the Earth's radiation environment due to changes in the solar wind. In 1989 a coronal mass ejection intercepted the Earth, causing a geomagnetic storm that overloaded the electricity grid in much of North East America due to the large induced currents, and caused a complete black out across the province of Quebec, Canada [12]. Solar superstorms, known as Carrington Events, the last of which occurred in 1859, are inevitable and estimated to intercept the Earth around every 250 years. Along with other technologically developed countries, the United Kingdom is vulnerable to a solar superstorm, including from the effects due to the ionising radiation that would accompany it. However, mitigation is in place in a number of industries [13]. It can be seen that the near-Earth radiation environment is complex, and it can change on timescales of years to seconds.

As shown in Figure 1.1, neutrons can be the dominant radiation environment at sea level. For typical aircraft flying altitudes, the radiation environment can also be dominated by neutrons, which are expected to be the principal cause of single event upsets (SEUs) [15]. The same is true near nuclear fission reactors, within shielded spacecraft, and for electronic control systems near radioisotope thermoelectric generators (RTGs). Military equipment in hostile environments may also be sensitive to radiation effects due to neutrons. As shown in Figure 1.3 (a), the effects from nuclear weapon outputs include those due to the neutron environment, which covers

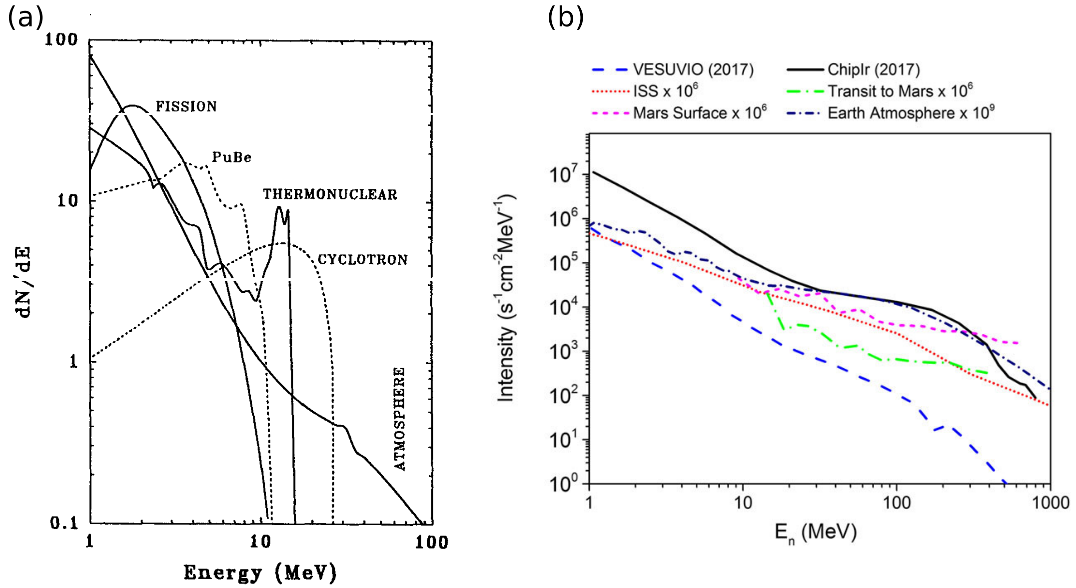

Figure 1.3: (a) Normalised generic neutron energy spectra for several environments, reproduced with permission from [15] ©1991 IEEE. (b) neutron flux as a function of energy for example terrestrial and space environments compared to the Rutherford Appleton Laboratory's ISIS Vesuvio and ChipIR spallation neutron beam lines.

energies up to and including 14 MeV neutrons. The above applications demand the electronic systems tolerate irradiation by neutrons with energies from thermal (25 meV), to hundreds of GeV in the case of neutrons generated by high energy primary cosmic rays [16]. Prototype electronic systems for future fusion power facilities, such as the International Thermonuclear Experimental Reactor (ITER [17]), will be exposed to 2.45 MeV and 14 MeV neutrons at fluences of up to 10^{14} n/cm^2 per year [18]. Reliable radiation-hardened electronics will be required for such future large-scale fusion devices [19]. In addition to SEUs and hard failures caused by neutrons, displacement damage and Non-Ionising Energy Loss (NIEL) effects, discussed further in Chapter 2, are an important consideration. Space missions featuring proton-rich orbits also need to consider displacement damage effects, for example the European Space Agency's JUICE mission to Europa will be exposed to 10^6 p^+ cm^{-2} sr^{-1} s^{-1} MeV^{-1} [20]. Measurements performed by the Pioneer 10 probe, and confirmed by Pioneer 11, showed that the inner radiation belt of Jupiter had an intensity comparable to that found in the upper atmosphere of Earth following the explosion of a nuclear device [4].

The above discussion shows that electronic systems used for defence, infrastructure, commercial, and private applications are all vulnerable to radiation effects due to natural and man-made sources. By developing a scientific and engineering understanding of the effects of radiation on electronic devices and systems, it is possible to assess the reliability and vulnerability of those systems. That understanding can also be used to design electronic systems that can survive

exposure to and even operate during exposure to radiation sources.

1.3 The potential of wide band-gap semiconductors

Wide band-gap semiconductors are strong candidates for use in challenging radiation environments, because they display good radiation environment-relevant material properties. Devices made from wide band-gap semiconductors, like GaN, aluminium nitride (AlN) and their alloys aluminium gallium nitride (AlGaN) can operate at higher temperatures than narrow band-gap semiconductors because of the higher thermal temperatures required to excite carriers across their forbidden bands. GaN is a direct band-gap semiconductor, which means that the maximum of the valence band exists at the same point in momentum space as the minimum of the conduction band. The result of this property is efficient radiative transitions, because momentum exchange with the lattice via phonons is not required for carriers to move between the valence and conduction bands, hence its use in the LEDs discussed earlier. The electron-hole pair creation energy, an important factor in photocurrent generation, and the minimum displacement energy, an important factor determining damage in a neutron environments, are higher in GaN and AlN and their alloys, than in gallium arsenide (GaAs) or silicon (Si), for example, as visible in Figure 1.4. These properties, and those for some other important semiconductors, are listed in Table 1.1. The nitride semiconductor materials discussed here are therefore well suited for use in radiation environments: photocurrents due to ionisation, and displacement damage due to nuclear interactions, would be lesser in materials like GaN and AlN than in GaAs or Si. This makes them inherently more suitable for use in radiation environments, and particularly suitable for use in demanding applications. The material properties shown in the figure, and given in Table 1.1 and [21], for example, show that group III-nitride materials have the potential to build electronics that can withstand higher temperatures, electric fields, and harsher radiation environments than more established technologies. By building smaller devices, enabled by the high breakdown fields and thermal conductivities, potential for gains in power transmission efficiency are available.

	AlN	Diamond	GaN	4H-SiC	GaAs	Si	Ge
Band gap (eV)	6.2	5.5	3.39	3.23	1.424	1.12	0.661
e-h pair creation energy (eV)	15.3	12	8.9	7.8	4.2	3.62	2.96
Electron mobility (cm^2/Vs)	300	2000	1000	900	8500	1450	3900
Breakdown field (10^6 V/cm)	1.2	1	5	3	0.4	0.3	0.1
E_D (eV)	43	35	(Ga:18, N:22)*	20	10	13	25

Table 1.1: Indicative material properties for some important semiconductors. Band gap, electron-hole (e-h) pair creation energy, electron mobility, breakdown field, and threshold displacement energy (E_D) are given for AlN, diamond, GaN, SiC, Si, and germanium (Ge). Data taken from [21]. *Average displacement energies are much higher than the threshold energies in GaN, with values of (45 ± 1)eV and (109 ± 2)eV for Ga and N, respectively [22].

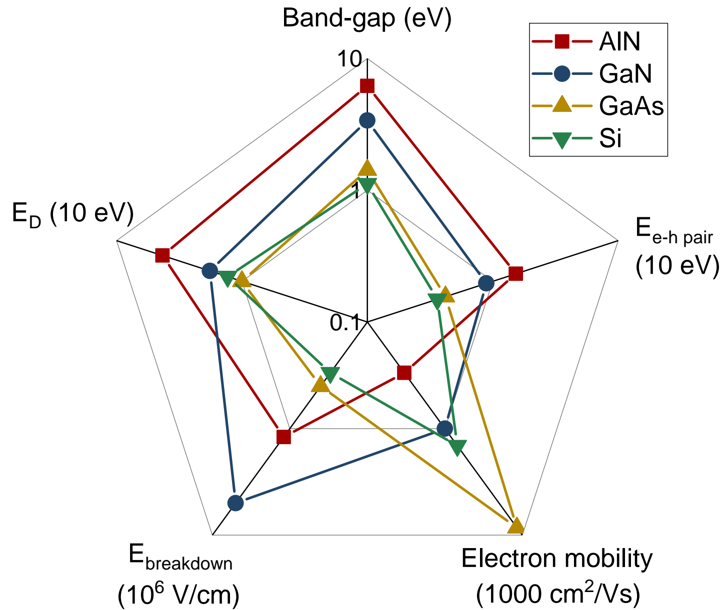

Figure 1.4: Radar plot comparing radiation environment-relevant properties of some semiconductors. Data taken from [21]. E_D is the minimum energy required to displace one of the atomic species in the semiconductor. $E_{e-h\ pair}$ is the average energy required to create an electron-hole pair. Note the log-scale and units given for each axis.

Wide band-gap, and ultra-wide band-gap materials have lots of potential to contribute to the requirements for increased efficiency in electrical power. The heterojunction between two such materials, AlGaN and GaN, is the fundamental building block of an AlGaN/GaN High Electron Mobility Transistor (HEMT). HEMTs are a class of field effect transistor (FET) which enables simultaneous high frequency operation with low noise, they are sometimes referred to as a heterojunction field effect transistor (HFET)s. GaN HEMTs are already being used in mobile phone basestations, and they are expected to be deployed in hybrid and electric vehicles, power supplies and inverters to produce AC electricity from the DC produced by photovoltaic solar panels. These and other outstanding research challenges are discussed in the detailed review by Tsao *et al.* [23]. Further information on why GaN HEMTs are good for power switching, and the potential for vertical structures is given by Baliga in [24]. Recent advancements in GaN technology, including enhancement-mode devices and vertical devices for high power applications are discussed in [25], along with future circuit applications. In summary, the limits of GaN device performance due to material properties have not yet been reached. Further progress is expected, including the development of devices produced from other wide- and ultra-wide band-gap materials.

1.4 Circuit applications for HEMTs

Utilising HEMT-based technology is one way to exploit the beneficial properties of wide band-gap materials to achieve increases in electrical system efficiency and performance, particularly in radiation environments. The high mobility of the Two-dimensional Electron Gas (2DEG) at the heterointerface within a HEMT enables fast switching speeds. In a 2DEG, electrons are confined to a thin film, an inversion layer in the case of a HEMT, where the thickness of the film is comparable to the de Broglie wavelength of the electrons, $\lambda = \frac{h}{p}$ where h is Planck's constant and p is electron momentum. The properties of a 2DEG, including electron transport, can be quite different and often far superior to those of the bulk material in which it is located. The inversion layer sits in the un-doped GaN layer, and so carriers experience no scattering from intentionally added dopant sites. HEMTs enable high-frequency, low-noise amplification. As discussed by Millan *et al.* [26], the properties of wide band-gap semiconductors, some of which are discussed above, enable the construction of more efficient power converters than can be produced using silicon.

GaN HEMTs are now approaching 10 kV operation, and can be used to make switched-mode power supplies that operate in the mega-Hertz (MHz) range. They can also be used for high-frequency radio frequency (RF) (microwave) applications, including monolithic microwave integrated circuits (MMICs) that operate at up to 100 GHz. GaN MMICs are anticipated to be a key technology for 5G communications network infrastructure. RF power amplifiers and high linearity 'robust' low noise amplifiers (LNAs) have been produced in GaN. It should be noted that for the highest RF performance, SiC remains the substrate of choice for GaN devices.

The ESA Proba-V Earth vegetation monitoring satellite has an x-band transmitter which uses a GaN power amplifier. In 2014 the GaN amplifier was reported to have been in orbit for around 10 months. Throughout that time it had reported nominal operation operating at around 8 GHz [27]. Thus GaN technology has been demonstrated to be effective in the space environment. Since that time the data shown earlier for the SAA in Figure 1.2 has been confirmed by the Proba-V satellite [14].

1.5 The objectives of this thesis

The objectives of this thesis are to develop techniques that can be used to study the effects of irradiation on semiconductor devices; to determine how wide band-gap semiconductor devices are affected by neutron irradiation; and to develop a means of simulating the effects of neutron irradiation on semiconductor devices, and exploring in detail the charge dynamics in operating devices, without recourse to the use of large pulsed power experimental facilities. By doing this, the aim is to determine whether electrical devices made from Wide Band-Gap (WBG) materials like GaN and AlGaN are in fact insensitive to damage and Single Event Effect (SEE) from 14 MeV neutrons; to understand the effect on switching performance of neutron irradiation, an important

factor in many applications, including the switched-mode power supplies discussed above; to increase understanding of the impact neutron irradiation has on the fundamental electrical material properties of WBG and especially Ultra-Wide Band-Gap (UWBG) materials like AlGaN, where very little is known; and to explore how irradiation response depends on electrical biasing during irradiation, the quantity of charge deposited, and on the frequency of localised ionisation events resulting from, for example, neutron scattering-induced displacement damage. The work contained in this thesis should therefore support the integration of WBG/UWBG material-based devices into safety- and performance-critical systems, to enable increases in efficiency and performance, particularly in challenging radiation environments.

It is usual to use one kind of radiation to simulate the effects of another, as discussed by Melhorn [28] in the context of simulating high fluxes of gamma radiation using flash X-ray machines. It was shown earlier that neutrons are often the dominant radiation environment in applications where electronic systems are used. The effects of the complex neutron spectra found in, for example, aerospace environments and shown in Figure 1.3, can be simulated, at least in part, by using fast neutron irradiation. In this manner 14 MeV neutron testing is representative of atmospheric SEE environments in integrated and bipolar technologies [29], provided that the LET threshold of the technology under test is below 8 to 9 MeV $cm^2\,mg^{-1}$ [30, 31]. For technologies with higher LET thresholds, the 14 MeV neutrons will be unable to generate sufficiently energetic collisions within the semiconductor to initiate damaging SEE. It has been suggested that GaN may be insensitive to single event gate rupture (SEGR) at these LET values [32], and this suggestion will be tested. Understanding AlGaN/GaN HEMT susceptibility to high fluence 14 MeV neutron irradiation is therefore a key step towards their insertion into nuclear fusion systems, and aids in understanding their performance in aerospace and other nuclear applications. By studying the effects, and trying to understand degradation and failure mechanisms, different device designs that would be more radiation hard can be suggested.

1.6 Thesis structure

In this thesis the electron mobility, trapping, and charge generation due to illumination, of the group III-V semiconductors, AlGaN and GaN are investigated. The effect of neutron irradiation on these properties is explored, as is the connection between optical charge generation, and that due to Coulomb interactions with energetic ions passing through the semiconductor, as would be generated following scattering by neutrons. The work contained in this thesis should be of wide interest because the techniques developed herein can be used to study and characterise many other materials and device types, they are not limited to the study of AlGaN and GaN systems.

This thesis is structured to move from device physics, and *ex-situ* radiation effects, into *in-situ* radiation effects, and finally onto the simulation of neutron radiation effects using femto-second (fs) pulsed lasers. Chapter 2 provides background information and theory necessary to understand

the remaining chapters. In Chapter 3, the experimental techniques and apparatus that were used to produce the results discussed later in the thesis are presented.

Chapter 4 covers 2DEG mobility - the ability of electrons confined in a two-dimensional well to move in response to an applied electric field. 2DEGs are common to many kinds of field effect transistor, and so this work should be of broad utility. The sensitivity of electron mobility to epitaxy design, temperature, and irradiation are explored. Transistor switching speed and efficiency are very important, as discussed above, and they are inherently linked to mobility.

In GaN-based devices switching effectiveness is affected by off-state duration, due to the action of electrically active defects which trap charge. Ultra-wide band-gap (UWB) heterojunctions enable higher breakdown voltage capability than the more common AlGaN/GaN field effect transistor devices [33], however, mobility may be a performance limiting factor due to alloy scattering in a ternary channel. Displacement damage due to neutron irradiation can create crystallographic defects, so in Chapter 5 changes to off-state duration-dependent switching effectiveness, resulting from neutron irradiation, are presented.

Having established elements of switching and conduction behaviour in the previous two chapters, in Chapter 6 the *in-situ* response of HEMTs to a transient nuclear fusion neutron environment is presented. In that chapter an attempt is made to determine whether ions knocked on by 14 MeV neutrons are able to deposit sufficient charge in the high-field region of an operating GaN HEMT to cause gate rupture or other deleterious effects.

Testing in transient radiation environments is costly, and poses experimental difficulties in the form of electrical interference and noise, and radioactivity. Therefore, in Chapter 7 a femtosecond laser is used to clarify the electrical bias sensitivity, position sensitivity, and irradiation event frequency-dependence of HEMT transient irradiation response. The system is used to simulate some aspects of real radiation environments, but it is shown it can also be used to elucidate some of the device physics of transistor irradiation response, and to probe electric field distributions within operating devices. Finally, in Chapter 8 a summary of the findings reported in this thesis is presented, and recommendations are made for future work.

CHAPTER 2

Theoretical background

In this chapter the theory and background information necessary for understanding the later chapters of the thesis are presented. It is not intended to be exhaustive, and where appropriate, material relevant only to individual chapters has been omitted here in order that it be more helpfully presented within the chapter it supports. The structure of this chapter is as follows. Material growth is summarised initially, and followed by a description of the structure and relevant properties of GaN. The electrical properties of junctions between semiconductors and other materials are then described, along with the formation of a 2DEG. A more macroscopic view is then taken to describe the functional aspects of HEMTs and their use in application circuits. Charge transport and conduction are addressed next, along with the effect of temperature on those properties. Having established some material properties under normal conditions, the interaction of neutron irradiation with semiconductors is summarised. Localised ionisation effects due to knock-on ions and secondary products of irradiation are then considered, as are some effects of bulk ionisation. Finally, ionisation by optical irradiation is described, with a focus on pulsed laser irradiation.

2.1 Growth and epitaxy

Heterojunctions between two semiconductors of differing composition form the basis for all of the test structures and devices studied in this thesis. The growth of heterojunctions between III-V materials differs from the growth of bulk elemental semiconductors. In that case a seed crystal is used to grow a large single crystal of the elemental semiconductor from a melt. Growing GaN in this manner has proven difficult, and the largest examples are a few inches in diameter. Growing the alloys with the correct elemental ratio necessary for desired III-V heterojunction formation by solidifying a molten mixture can lead to non-stoichiometric alloy composition [34].

For this reason, materials like AlGaN and GaN are typically grown layer by layer on non-native substrate materials like SiC, sapphire, Si, and more recently, diamond. To grow these epilayers, Molecular beam epitaxy (MBE) can be used to produce high quality epilayers, and is often used in academic settings. MBE systems can achieve growth rates on the order of 1 μm/hr. However, it is Metal organic chemical vapour deposition (MOCVD) which is typically used at industrial scale for device manufacture because of its suitability for growing epitaxial layers over large substrate areas [34]. In this case the gas used within the growth chamber can be varied quickly to produce heterojunctions with sharp changes in composition.

An example of an UWBG AlGaN/AlGaN HEMT structure grown using MOCVD is shown in Figure 2.1. The epitaxy is similar to that used for the work discussed in Chapter 4. In part (a) of the figure the different epitaxial layers are illustrated. The substrate material, sapphire in this case, is typically several hundred microns thick. The choice of substrate is determined by lattice parameter similarity, thermal conductivity, cost, and ease of growth. Si has advantages due to the availability of large area substrates, whereas SiC has better thermal conductivity and is the current optimal substrate for the highest performance devices, at higher cost. Diamond has the best thermal conductivity, and research and development work is currently underway on GaN-on-Diamond devices. The basic epitaxial layer structure for a heterojunction device is, from bottom to top, substrate, stain relief layer, buffer layer, barrier layer, and cap layer.

2.2 (Al)GaN electrical properties and crystal structure

The work in this thesis used devices based on AlGaN and GaN, or combinations thereof. Both materials can be found in Zincblende and Wurtzite crystal structures. However, Wurtzite is the most common structure found in semiconductor devices. The crystal structure of GaN in its Wurtzite form is shown in Figure 2.2. As shown in the figure, in GaN each atom is bonded to its four nearest neighbours to form a tetrahedron. Bonding is covalent, with each bond consisting of two electrons with opposite spins. The structure lacks inversion symmetry, it is non-centrosymmetric, a necessary condition for piezoelectricity, which it displays. It also exhibits spontaneous polarisation. The crystal structure is hexagonal, and so has four crystallographic axes. The length of the hexagonal prism base sides is denoted a. Three of the axes are in the same plane, of equal length, and separated by 120°. The fourth axis is perpendicular to the other three, and describes the height of the hexagonal prism, c. It describes movement from one plane containing hexagonal symmetry to the next, with each alternating plane being composed of one element of the binary structure. The [0001] direction in GaN is conventionally defined as the Ga-N bond direction [36], from the Ga-terminated plane to N-terminated. Growth of III-Nitride expitaxial layers is typically performed along this polar axis, and HFETs, or more specifically in this case HEMTs, are typically grown on Ga-face material [37], as illustrated in Figure 2.2 (a). In part (b) of the figure N-face material is illustrated, in which the spontaneous

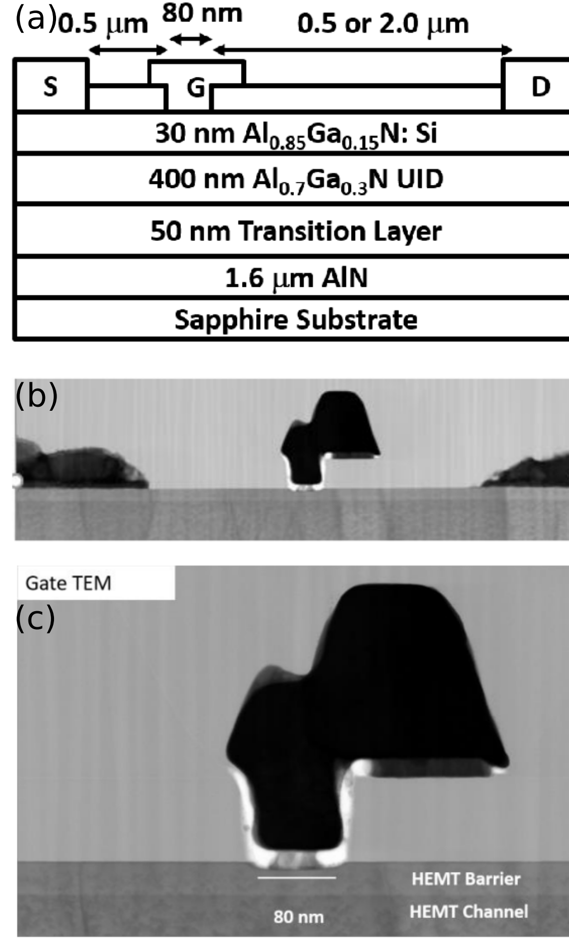

Figure 2.1: (a) Ultra-wide band-gap AlGaN/AlGaN HEMT epitaxial structure, (b,c) transmission electron microscope (TEM) image of a HEMT, centred on the gate. Gate-connected field plate 'wing' is shown. ©2018 IEEE. Reprinted, with permission, from [35].

and piezoelectric polarisation directions are reversed as compared to Ga-face material. This causes 2DEG formation, discussed below, to occur at different interfaces than found in the more technologically-relevant Ga-face material. The anion-cation bond length along the (0001) axis, u, is described in terms of c.

Unlike electric field vectors, $\vec{E}$, which originate at positive charges, polarisation vectors, $\vec{P}$, are conventionally directed from negative towards positive charges, thus indicating the direction a negative test charge would move. The electric dipole moment produced by charges $+q$ and $-q$, separated by displacement vector d, is given by

$$\vec{p} = q\vec{d}, \tag{2.1}$$

and has units C · m. The polarisation can then be defined as the electric dipole moment per unit volume, and is the polarisation charge per unit area perpendicular to the direction of polarisation

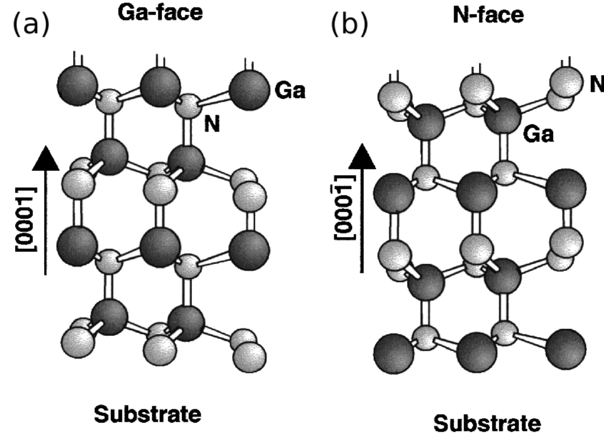

Figure 2.2: Wurtzite GaN structure when grown with (a) gallium face, and (b) nitrogen face. The non-centrosymmetric structure is apparent, a necessary condition for piezoelectricity. Reprinted from [38], with the permission of AIP Publishing.

[39], with units $\mathrm{C \cdot m^{-2}}$. The electric flux density, or displacement field, $\vec{D}$, within a dielectric is given by

$$\vec{D} = \epsilon_0 \vec{E} + \vec{P}. \tag{2.2}$$

Although Wurtzite structures are anisotropic, it is useful to consider isotropic materials as a simplifying case. Then, provided that applied $\vec{E}$ fields are not too large, the polarisation within the material is given by

$$\vec{P} = \epsilon_0 \chi \vec{E}, \tag{2.3}$$

where χ is the dielectric susceptibility, and ϵ_0 is the permittivity of free space. When no external $\vec{E}$ fields are applied to the semiconductors, the macroscopic polarisation is given by the sum of the spontaneous polarisation, $\vec{P}_{sp}$, and the piezoelectric polarisation due to strain caused by residual strain in the crystal lattice after growth, $\delta\vec{P}$. Residual strain can be either compressive or tensile, depending on growth and annealing conditions, and on the extent of lattice parameter mismatch between the substrate and semiconductor layers grown upon it. In bulk materials screening charges are usually present which prevent polarisation charges due to spontaneous polarisation from being observed. At heterojunctions between semiconductors with different compositions, however, interfaces charges can manifest due to the differing polarisation of the two layers. This fact is central to the construction of HEMTs.

2.2.1 The source of 2DEG carriers

The distinctive feature of a HEMT is the existence of a high mobility 2DEG adjacent to an interface within the device between two regions of differing composition, known as a hetero-interface. The high mobility 2DEG is used to conduct electrical current from a source contact to a drain contact, and that conduction is controlled by an electrical signal applied to a gate contact

situated adjacent to the 2DEG between the two other contacts. Here the formation of the 2DEG will be discussed.

The polarisation present with no strain or external applied field, the spontaneous polarisation, is very large in nitrides compared to other semiconductors [40]. Considering the transition from GaN to AlN via increasing the proportion x in $Al_xGa_{1-x}N$, the non-ideality of the crystal structure increases, meaning that u increases, whereas the ratio c/a decreases. The result is an increased spontaneous polarisation. For GaN and AlGaN grown Ga(Al)-face, the spontaneous polarisation has been found to be negative. Piezoelectric polarisation is proportional to strain, assuming strain is small enough to maintain linearity. The piezoelectric polarisation along the c-axis in terms of strain in plane with the a axes can be calculated once the piezoelectric coefficients are known from measurement, or they can be calculated using a Berry Phase approach [40]. It has been found that the piezoelectric polarisation in AlGaN is negative under tensile strain, with the inverse being true for compressive strain. The illustration in Figure 2.3(b), shows the resulting parallel alignment of piezoelectric and spontaneous polarisations for an AlGaN barrier with a residual tensile strain on a strain-free GaN buffer layer. Because of the difference in resultant polarisation across the AlGaN-GaN interface a fixed positive polarisation charge will be present there. To maintain charge neutrality, a compensating negative charge will be drawn to the interface. When the band offset at the interface is sufficient, discussed below, a 2DEG of charge density qn_{2DEG} will form at the interface.

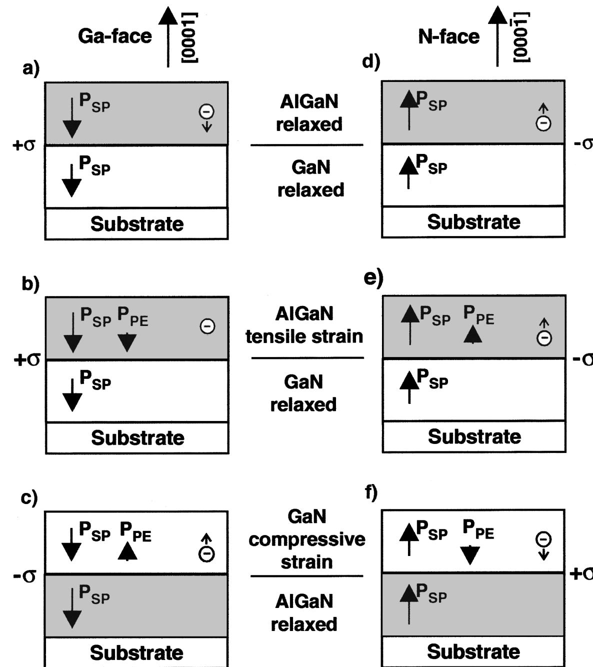

Figure 2.3: Illustration of the dependence growth direction and strain of the spontaneous and piezoelectric polarisation vectors. Reprinted from [38], with the permission of AIP Publishing.

Ibettson *et al.* argued that because the polarisation is due to dipoles, for it to be maintained the source of negative charge at the AlGaN/GaN interface can not be 'piezoelectric doping'. The negative charge carriers can not be provided by thermally ionising buffer states, because that would leave a net positive charge in the buffer, which would cause a band bending that would prevent confinement of a 2DEG at the heterointerface. Ionised donors present in the AlGaN, when integrated over the barrier volume could provide a sheet charge σ_{AlGaN}. Ionised surface states could provide $\sigma_{\mathrm{surface}}$, leaving a positive surface charge behind. To maintain overall charge neutrality, the sum of the charge donor sources, and the 2DEG charge must cancel:

$$\sigma_{\mathrm{AlGaN}} + \sigma_{\mathrm{surface}} - qn_{\mathrm{2DEG}} = 0. \tag{2.4}$$

According to Equation (2.4), the source of electrons for the 2DEG, in the absence of barrier doping, must be donor-like surface states. The occupancy of the surface states is determined by their position with respect to the Fermi level in the bulk material, E_F. Figure 2.4(a) depicts the case of no 2DEG due to the surface state level being below E_F. In that case the dipole charges would be uncompensated, generating a constant E-field in the AlGaN barrier, as shown in the figure. Increasing the thickness of the barrier would therefore raise the position of the surface donor levels with respect to E_F. Once a sufficient thickness is reached, known as the critical thickness, the donor- and Fermi-levels would be coincident, and the 2DEG would form, as shown in part (b) of the figure. The density of the 2DEG would continue to increase with increasing barrier thickness until all surface states were depleted, shown in Figure 2.4(c).

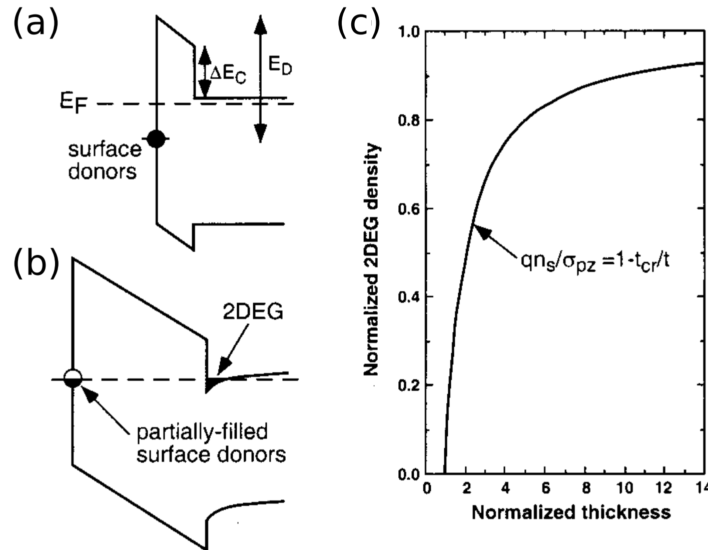

Figure 2.4: Schematic band diagram for barriers with insufficient (a), and sufficient (b), barrier thickness to produce a 2DEG. (c) calculated 2DEG density as a function of barrier thickness. Reprinted from [41], with the permission of AIP Publishing.

2.2.2 Barrier composition and band gap

The confinement of the 2DEG at the heterointerface relies on a band gap offset at the interface. This is achieved by growing a barrier layer with a wider band gap than the buffer layer. Alloying materials allows the tailoring of the band gap, enabling the growth of technologically useful heterojunctions like AlGaN/GaN. Using Vegard's law an estimate can be made for the band gap of an alloy as an interpolation of the band gaps of the two constituent binary compounds as follows:

$$E_g(x) = xE_g(\mathrm{AlN}) + (1-x)E_g(\mathrm{GaN}) - x(1-x) \tag{2.5}$$

$$= (6.13x + 3.42(1-x) - x(1-x))\,\mathrm{eV}, \tag{2.6}$$

where $E_g(x)$ is the band gap of the alloy formed from a number fraction of x parts AlN with $(1-x)$ of GaN, where x has a value between 0 and 1. A larger band gap reduces the thermal generation of carriers, decreasing electronic noise and enabling device operation at higher temperatures. A larger band gap also enables the construction of semiconductor devices with smaller dimensions for operation at a given voltage. The reason for this is that the critical electric field which can be applied to a semiconductor before avalanche breakdown occurs, E_{crit}, has been show empirically to vary as $E_g^{2.5}$ in direct band gap semiconductors, and as E_g^2 for indirect band gap semiconductors. A complete understanding of these empirical relationships in the context of impact ionisation remains to be formed [42]. Figures of merit (FOM) derived from design considerations have been presented in the literature, for example the Baliga FOM [43], some of which are discussed in Chapter 4. However, a very simple scaling argument can be made as follows. Conduction in the 2DEG is through the cross sectional area, A, presented by the product of a small height and a non-negligible device width, W, and a channel length spanning the source to drain distance, L. Resistance is proportional to volume as $R = \rho L/A$. Or in terms of sheet resistance, $R = R_s L/W$. Maintaining a constant applied electric field as E_{crit} increases, gives a linear reduction in L, and if we choose to maintain a constant volume of the device, thus increasing performance within a fixed volume, then W will increase linearly with E_{crit}. This gives

$$R \propto 1/E_{\mathrm{crit}}^2 \propto 1/E_g^5. \tag{2.7}$$

The potential reductions in semiconductor device on-resistance, and subsequent decrease in resistive energy losses, suggested by the simple scaling relationship of Equation (2.7) are a clear incentive for developing power switching devices from UWBG materials.

2.2.3 Practical estimates of 2DEG density

The sheet resistivity of the 2DEG at the AlGaN/GaN interface can be found from

$$\rho_{\mathrm{2DEG}}(x) = \frac{1}{e n_{\mathrm{2DEG}} \mu_{\mathrm{2DEG}}}, \tag{2.8}$$

where μ_{2DEG} in the above expression is not a constant, but is a function of n_{2DEG}, as will be discussed below. After Ambacher *et al.* [38] the relative static dielectric constant of AlGaN is taken to be

$$\epsilon_{AlGaN}(x) = -0.5x + 9.5, \tag{2.9}$$

where x is the aluminium nitride alloy fraction, as usual. The Schottky barrier height is [38]

$$e\phi_{barrier} = (1.3x + 0.84)\,\text{eV}. \tag{2.10}$$

The final interpolated value is the conduction band offset, ΔE_c:

$$\Delta E_c = 0.7(E_g(x) - E_g(0)). \tag{2.11}$$

Then, once the Fermi level with respect to the GaN conduction band edge is determined, for a barrier width, d, the 2DEG density can be estimated from [38]

$$n_{2DEG}(x) = \frac{\sigma(x)}{e} - \left(\frac{\epsilon_0 \epsilon_{AlGaN}(x)}{de^2}\right)\left[e\phi_{barrier} + E_F(x) - \Delta E_c\right]. \tag{2.12}$$

However, for $d > 15\,\text{nm}$ 2DEG concentration as a function of aluminium fraction can be determined from an empirical relationship [44] which has been shown to reproduce measured channel densities well:

$$n_{2DEG}(x) = \left(-0.169 + 2.61x + 4.5x^2\right)10^{13}\text{cm}^{-2}. \tag{2.13}$$

For $x = 0.3$, a representative value used in HEMTs, using Equation (2.13) gives an expected 2DEG density of $n_{2DEG}(0.3) = 1.019 \times 10^{13}\,\text{cm}^{-2}$.

2.3 High electron mobility transistors (HEMTs)

The maximum available 2DEG density, discussed above, is modulated in HEMT devices by the application of an electric field normal to the heterojunction surface. The change in gate potential generates a change in charge density under the gate to screen it. By applying a negative potential to a gate contact, with respect to the channel potential, the negative charge density under the gate must decrease, equivalent to an increase in positive charge density. This is the mechanism used to switch the channel current in 'normally-on' devices. The modulating potential is applied via a gate contact, which is typically a rectifying Schottky contact, although metal-insulator-semiconductor (MIS) contacts can also be used. MIS contacts demonstrate reduced leakage currents across the gate, but slower switching speeds than Schottky contacts because of their increased capacitance. Most HEMTs are normally-on devices, but normally-off devices are available. These can be native normally-off devices, based on recessed or doped gates, or cascode configuration devices which incorporate a normally-off silicon FET to control the operation of a normally-on GaN HEMT.

HEMTs consist of a gate contact, discussed above, and source and drain contacts which are used to make electrical contact between the 2DEG channel and the external circuit. In normal operation the source contact is connected to the lower potential part of a circuit or the ground, and the drain is connected to the power supply. Because the potential required to switch the gate is typically much smaller than the power supply line voltage being switched, device designs optimised for high voltage operation feature gate contacts located closer to the source contact than the drain, in order to maximise the breakdown voltage of the device. In contrast, HEMTs optimised for high frequency operation typically feature gates situated centrally between the source and drain to reduce parasitic capacitances. Gate widths may also be smaller to reduce carrier transit times, and so enable higher switching speeds.

It is possible to construct lateral devices such as HEMTs, as shown in Figure 2.5 (a,c,d), the focus of the work presented herein, and also vertical devices, shown in Figure 2.5 (b). Vertical devices are able to operate at higher electrical bias levels because of the increased breakdown field achievable for geometric reasons. However, they are unable to operate at the high switching speeds achieved by HEMTs, which are lateral devices. Because they do not benefit from the screening of bulk defects by a high electron density channel, they are likely to be more sensitive to a decrease in conductivity resulting from neutron-induced displacement damage.

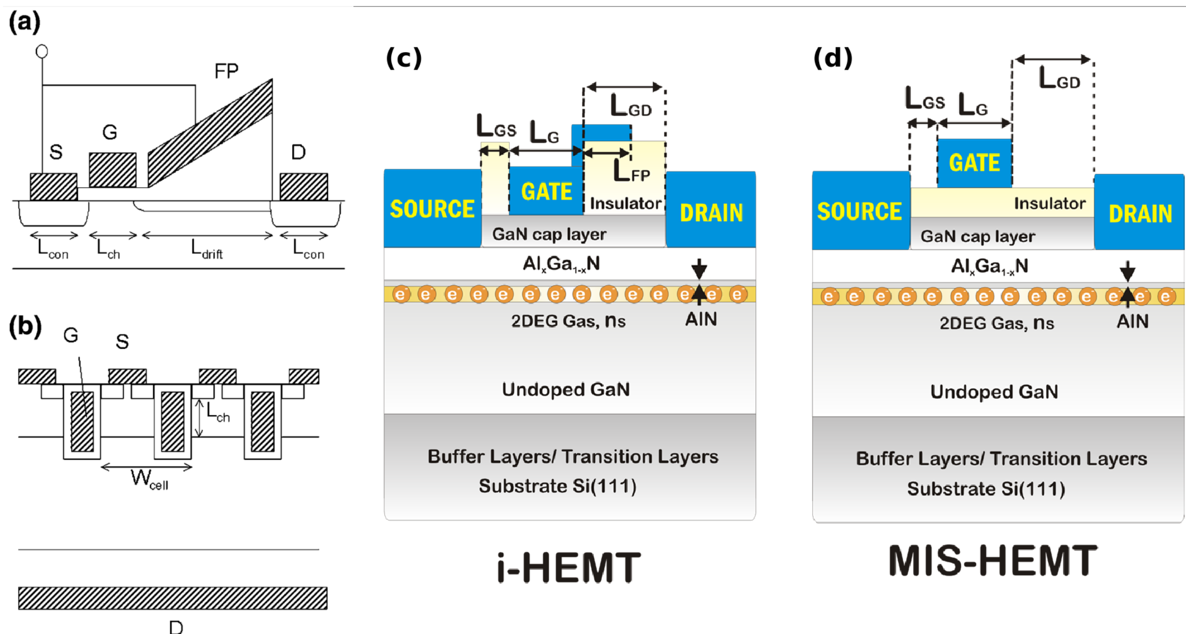

Figure 2.5: (a) Lateral High Electron Mobility Transistor (HEMT) layout including a source-connected field plate (FP), and source (S), gate (G), and drain (D) contacts. (b) Vertical metal oxide semiconductor FET (MOSFET) layout. (c, d) GaN-on-Si HEMT showing position of two-dimensional electron gas (2DEG), and including a cap layer, with a Schottky gate and metal-insulator-semiconductor gate, respectively. (a, b) Reproduced, with permission, from [45]. (c, d) ©2012 IEEE. Reprinted, with permission, from [46].

Electric field shaping conducting plates can be included in designs to, for example, reduce the magnitude of the high electric field region which is present that the gate edge on the drain side, as illustrated in Figure 2.5 (b). Field plates can be gate- or source-connected. For sufficiently high drain bias, the vertical band profile means that the electric field distribution due to the field plate is effectively applying a negative bias to the top surface, and so the 2DEG becomes depleted, to an extent, in the access region between the gate and drain. This reduces the potential drop at the gate edge, which in turn reduces Joule heating there, and so can increase device reliability and lifetime.

2.3.1 Circuit applications

The circuit applications for devices based on group III-Nitride semiconductors, AlGaN and GaN in particular, range from RF amplifiers and switches through to power switching. For details of the circuit applications of GaN-based technology for power switching, the reader is referred to the review by Chen *et al.* [47]. The review by Millan *et al.* [26] compares GaN and SiC-based technologies, including GaN HEMTs approaching 10 kV class operation, and switching power supplies operating at up to MHz switching frequencies. A fairly recent overview of some technical achievements of GaN HEMTs for applications in RF MMICs in the 1 GHz to 100 GHz range can be found in [48].

2.4 Mobility - bulk and two-dimensional

2.4.1 Classical models

In the absence of an applied electric field, the motion of electrons within a semiconductor will be random. There will be some average time between collisions, τ, and a mean free path between collisions, λ, quantities which are of particular relevance when considering semiconductor operation in radiation environments. Electrons experience the Lorentz force

$$\vec{F} = q\left(\vec{E} + \vec{v} \times \vec{B}\right), \tag{2.14}$$

where the charge on an electron, $q = -e$. In the presence of an electric field only, an electron will experience an acceleration determined by a force, $F = -e\vec{E} = m_e^* \vec{a}$, where m_e^* is the effective mass of the electron in the semiconductor, discussed below, and $\vec{a}$ is the resultant acceleration. The acceleration, when averaged over the entire electron ensemble, will result in a net drift of electrons in the opposite direction to the electric field. Averaged over the entire ensemble, the net velocity of the electrons immediately after scattering is zero, $<\vec{v_0}>= 0$. Therefore, the only component of the electron ensemble velocity is due to the acceleration arising from the Lorentz force. That velocity achieved in the time between collisions is then

$$\vec{v} = \frac{-e\tau\vec{E}}{m_e^*}. \tag{2.15}$$

The constant of proportionality in Equation (2.15) is the electron mobility

$$\mu = \frac{-e\tau}{m_e^*}. \tag{2.16}$$

The net current density can then be found from

$$j = -en\vec{v} = n\frac{e^2\tau}{m_e^*}\vec{E}, \tag{2.17}$$

where n is the free electron density per unit volume, and the constant of proportionality on the right hand side of the equation is defined as the conductivity

$$\sigma = n\frac{e^2\tau}{m_e^*}. \tag{2.18}$$

This simplistic model is essentially the Drude model for conduction in metals, which is given here as a convenient way to introduce the concept of mobility. The Drude model is consistent with Ohm's law. Electron mobility is a property of a semiconductor system that characterises how quickly electrons can drift in response to an applied electric field. It determines the asymptotic electron drift velocity achieved in a material per unit applied electric field. In terms of material dependent properties, a mobility, μ, can be defined for each species of charge carrier in a semiconductor by combining Equations (2.18) and (2.16) such that

$$\sigma = q(n\mu_e + p\mu_h), \tag{2.19}$$

where it is understood that the scattering times, τ, and effective masses, m_e^*, in the above are usually different for electrons and holes. The conventionally used units of mobility are $\mathrm{cm^2V^{-1}s^{-1}}$. In the simple model above, the effective masses of charge carriers play an important role. Effective mass is determined by the electronic band structure of the semiconductor, and can also depend on temperature. The mean free paths found by considering the individual scattering processes which occur due to, for example, carrier-phonon scattering or charged defect scattering, can be added in reciprocal to determine the effective mean free path. This enables the combination of terms with different dependencies on material properties such as carrier density or temperature, as follows

$$\frac{1}{\lambda_{\text{effective}}} = \frac{1}{\lambda_1} + \frac{1}{\lambda_2}. \tag{2.20}$$

This empirical relation is known as Matthiessen's rule. From the above discussion, μ is linearly dependent on λ, and so Matthiessen's rule can be used to determine the net effect on mobility of several different scattering mechanisms as a function of carrier density and temperature.

2.4.2 Quantum statistics

To properly account for the wave-like behaviour of electrons in solids it is necessary to restrict the values of their momenta, because of the boundary conditions imposed by the finite number

of available electron states in a given energy range within a finite material sample. Here the approach adopted in [49] will be taken. Electron momentum can be described by a vector, $\vec{p}$, directed from an origin to a point in $\vec{p}$-space. The kinetic energy of the electron can be given in terms of momentum as

$$E = \frac{p^2}{2m_0}. \tag{2.21}$$

A sphere with its centre at the origin of $\vec{p}$-space will describe a surface of constant kinetic energy. Electrons behave as waves with a de Broglie wavelength given by

$$\lambda = \frac{h}{p}, \tag{2.22}$$

where h is Planck's constant. A wave-vector can then be defined as

$$\vec{k} = \frac{p}{\hbar}, \tag{2.23}$$

which allows a k-space to be constructed analogous to momentum space. In k-space electron kinetic energy in terms of momentum is given by

$$E = \frac{\hbar^2}{2m_0}\left(k_x^2 + k_y^2 + k_z^2\right) = \frac{\hbar^2 k^2}{2m_0}. \tag{2.24}$$

The probability of an electron with a wave function, ψ, occupying a region, dr, is given by $|\psi|^2$. The wave function itself must be a solution of Schrödinger's equation as given by

$$-\frac{\hbar^2}{2m_0}\nabla^2\psi = \vec{E}\psi \tag{2.25}$$

If electron wave functions have a period in x, y, and z, given by L, and wave vectors given by integer multiples of $k_x = \frac{2\pi n_x}{L}$, where n is any integer and the same applies to y and z axes, then solutions of Equation (2.25) are plane waves given by

$$\psi = C\exp\left(i\vec{k}\cdot\vec{r}\right) \tag{2.26}$$

The possible wave functions for electrons which satisfy the above correspond to a limited set of $\vec{k}$ values, which restricts the possible momenta, and hence the possible energies, of the electrons.

The one electron wave function described above must include the effect of the periodic potential of the atoms in a semiconductor crystal, and a contribution to the potential due to all other electrons in the solid. This potential, which has the periodicity of the lattice, can be described by $V(\vec{r})$. The Schrödinger equation can then be written as

$$\frac{\hbar^2}{2m_0}\nabla^2\psi + \left[\vec{E} - V(\vec{r})\right]\psi = 0. \tag{2.27}$$

Solutions to this equation can take the form of Bloch waves described by

$$\psi = U_k(\vec{r})\cdot\exp(i\vec{k}\cdot\vec{r}), \tag{2.28}$$

where U_k has the periodicity of the crystal lattice. Only energies which correspond to real values of $\vec{k}$ correspond to electron wave functions. These energies form the energy bands of interest in semiconductor science.

Due to the Heisenberg uncertainty principle, uncertainty in momentum in each coordinate is $\Delta p = h/L$, giving a wave-vector uncertainty of $\Delta k = \frac{2\pi}{L}$, describing a volume, $\left(\frac{2\pi}{L}\right)^3$. The number of these volumes present in a range of k-space given bounded by k and $k + \mathrm{d}k$, with volume $4\pi k^2 \mathrm{d}k$, is then given by $\left(\frac{k^2 L^3}{2\pi^2}\right)\mathrm{d}k$, or by $\left(\frac{k^2}{2\pi^2}\right)\mathrm{d}k$, per unit volume. Because electrons of two different spins can occupy the same position in k space, the number of electron states available per unit volume is given by

$$g(E)\cdot \mathrm{d}E = g(k)\cdot \mathrm{d}k = \left(\frac{k}{\pi}\right)^2 \mathrm{d}k. \tag{2.29}$$

To find $\frac{\mathrm{d}k}{\mathrm{d}E}$ we differentiate Equation (2.24) with respect to k, and take the reciprocal yielding

$$\frac{\mathrm{d}k}{\mathrm{d}E} = \frac{4\pi^2 m_0}{h^2 k}, \tag{2.30}$$

which on combining with Equation (2.29), and substitution of k found by re-arranging Equation (2.24), yields the density of states

$$g(E) = 4\pi\left(\frac{2m_0}{h^2}\right)^{3/2} E^{1/2}, \tag{2.31}$$

where $g(E)$ described the density of electron states at an energy, E. The distribution of electrons as a function of energy can be found from the Fermi-Dirac distribution function

$$f(E) = \frac{1}{1+\exp\left(\frac{E-E_\mathrm{F}}{kT}\right)} \tag{2.32}$$

where E_F is the Fermi level in the material. As is apparent from Equation (2.32), the probability of an electron having $E = E_\mathrm{F}$ is 0.5. The product of the density of states, Equation (2.31), and the Fermi-Dirac distribution function, Equation (2.32), gives the volume density of occupied states as a function of energy. It is connected to the density of electrons in a material by

$$n = \int_{-\infty}^{\infty} n(E)\cdot \mathrm{d}E = \int_{-\infty}^{\infty} f(E)\cdot g(E)\cdot \mathrm{d}E. \tag{2.33}$$

In a HEMT 2DEG, the electrons are confined within a thin potential well in the $z-$direction, defined to be perpendicular to the heterointerface between the barrier and buffer layers, but are free to move in the $x-y$ plane, parallel to the heterointerface. Schrödinger's equation can then be solved as above, but with the boundary conditions $\Psi = 0$ at $z = 0$ and at $z = d$, where d is the well thickness. Using the periodic boundary conditions, $\Psi(x+L, y+L, z) = \Psi(x, y, z)$, results in a travelling wave for $x-y$ movement, but a standing wave in z, as follows [50]

$$\Psi(x,y,z) = \mathrm{e}^{(ik_x x)}\mathrm{e}^{(ik_y y)}\sin(k_z z) \tag{2.34}$$

which means we must have $k_x = \frac{2\pi p}{L}$, $k_y = \frac{2\pi q}{L}$, and $k_z = n\pi$, with p, q, and n as integers. This gives an electron kinetic energy of

$$E = \frac{\hbar^2}{2m_0}\left(k_x^2 + k_y^2 + k_z^2\right) = \frac{\hbar^2}{2m_0 L^2}\left(p^2 + q^2\right) + \frac{n^2 h^2}{8 m_e d^2}, \tag{2.35}$$

where the potential well energy levels are given by

$$E_n = \frac{n^2 h^2}{8 m_e d^2} \tag{2.36}$$

The exclusively two-dimensional nature of the electron motion can now be seen by considering the energy associated with different wave vector values in z, by using Equation (2.36). Taking the quantum well thickness to be $d = 1 \times 10^{-9}$ m, to move from the $n = 1$ level to the lowest energy $n = 2$ level, where $p = q = 0$, requires an increase in energy of at least 1.13 eV at 300 K. However, at 300 K the thermal energy $kT = 0.026$ eV, meaning essentially all of electrons in the potential well will remain in the $n = 1$ ground state. They will, therefore, have zero motion in the $z-$direction, but will be free to move in the $x - y$ plane, forming a 2DEG.

Following the same procedure as above, but in this case for a two-dimensional k-space with an area per state of $(2\pi/L)^2$, we find for a given n , e.g. $n = 1$, the density of states in the 2DEG is

$$g(E) = 2g(k)\frac{\mathrm{d}k}{\mathrm{d}E} = \frac{m_0}{\pi\hbar^2}. \tag{2.37}$$

The density of states in the 2DEG is therefore independent of energy, and hence temperature. From Equation (2.33), any changes in 2DEG electron density as a function of temperature will be due to a change in the distribution function, $f(E)$, and not the density of states, $g(E)$.

The Bloch waves described by Equation (2.28) are unchanged across all unit cells in a perfect crystal, leading to an infinite mean free path. In reality, however, defects and thermal vibrations in crystals restrict the periodicity of the crystal lattice, and lead to a finite mean free path, and hence a finite conductivity. In contrast to the non-localised band states, defects cause permitted states which are localised to their position. When localised defect states are found in the band gap of a semiconductor, they can form recombination centres or traps. Electrons can be captured by these defects states, reducing the free electron density available for conduction, and altering the band bending within the material. Such a defect state which is most likely to release the electron by subsequently capturing a hole is known as a recombination centre, whereas one which is most likely to release the electron back to the conduction band is known as an electron trap. A complementary argument exists for hole traps. In this work, the term trap is used to describe deep traps, which are those where a defect's position within the band gap is at an energy several kT from a band edge. Traps and their impact on HEMTs is discussed further in Section 2.5.4.

In real semiconductors, the crystal structure and lattice parameters determine the band structure. The nearly-free electron theory, builds on the above arguments by using perturbation theory to account for the negative peaks in potential present at each lattice site. This modifies the

$E(k)$ dispersion relation curves, previously described by Equation (2.24). The result is that there are regions in E on the $E(k)$ curves where no electron states exist. These regions form forbidden bands, and their width in energy is known as a band gap. The surfaces formed by the allowed states in k-space are polyhedra. The region in between two successive polyhedra is known as a Brillouin zone. All Brillouin zones of a given crystal occupy an identical volume in k-space, and can contain two electron states for each atom in the semiconductor crystal. The k values corresponding to the breaks in the $E(k)$ curves, described above, mark the boundaries of Brillouin zones.

When the Fermi level is located within a permitted band, electrons near the Fermi surface are able move into adjacent states in k-space with infinitesimal energy input, permitting electrical conduction. However, if the Fermi energy is located within a forbidden band, and the permitted band below E_{F} is full, conduction requires a finite energy input to promote electrons into an available state within a higher permitted band. The result is insulating behaviour. In semiconductors, conductivity can increase with increasing temperature due to electron excitation from the valence band, the highest filled band, to the lowest empty band, the conduction band. However, increasing temperature also increases scattering from quantized thermal vibrations, phonons, which can cause a net decrease in the conductivity of a semiconductor system. This latter effect is apparent in the experimental results presented in Chapter 4.

2.4.3 Electron transport calculations

In bulk semiconductors, the electrons can be considered as an ensemble with a continuum of energies. In that case, distribution functions in terms of position, wave vector, and time, can specify the properties of the ensemble. The Boltzmann Transport Equation (BTE) can then be used to determine how a distribution function, f, evolves with time due to the application of an external electric field [51]. The BTE can be written as

$$\frac{\partial f\left(\vec{r},\vec{k},t\right)}{\partial t} = -\vec{v}\cdot\Delta_r f\left(\vec{r},\vec{k},t\right) - \dot{\vec{k}}\cdot\Delta_k f\left(\vec{r},\vec{k},t\right) + \frac{\partial f\left(\vec{r},\vec{k},t\right)}{\partial t}\Big|_{\text{scattering}} \tag{2.38}$$

where the first term on the right of the equals sign represents diffusion, the second represents the effect on the distribution function due to applied external fields, and the third term accounts for scattering processes. The effect of an applied field on electrons within an allowed band causes a change in electron momentum via the Lorentz force, thus altering k, as given by Equation (2.23), and causing a non-zero $\dot{\vec{k}}$ term in Equation (2.38), above. Asymptotic solutions of Equation (2.38) have been found for the low-field case, and approximate solutions have also been found for high-field cases, see references within [51] for details. The BTE was solved for the case of isotropic elastic scattering by Sommerfeld to show that, in a degenerate system, electrical conduction due to an external electric field was due only to electrons in states near E_f [49]. Conduction electrons

are those in states for which $\frac{\partial f}{\partial E} \neq 0$. The reason is that only electrons in those states are able to change their occupancy in a distinguishable manner, and thus create a measurable current.

Electron transport in semiconductors has both steady-state and transient components, and BTE solutions which are suitable to describe both must be found. Monte Carlo techniques can be used to find numerical solutions to the BTE by calculating the motion of many individual electrons, or by following a single electron for a long time. To simplify calculations, the lowest three valleys of the conduction band can be simulated, rather than the entire band structure. Further simplification can be applied by neglecting the delocalised nature of the electrons. This is known as a semi-classical treatment. In this case the electrons in the ensemble are treated as point particles, which respond to an applied electric field as

$$\hbar \frac{d\vec{k}}{dt} = -q\vec{E}, \tag{2.39}$$

which is remarkably similar to the starting point for the classical conduction model discussed earlier. Scattering due to defects and other mechanisms is introduced into the simulations through scattering rates. The results of calculations using the approach described above are shown in Figure 2.6. In the low-field region of the figure, drift velocity can be seen to depend approximately linearly on electric field. From the discussion above it is clear that the gradient in that region indicates the electron mobility. The slope can be seen to decrease slightly as temperature is increased from 100 K to 300 K. However the decrease in low-field slope is greater when changing from 300 K to 500 K. Measurements of low field mobility in AlGaN spanning the 80 K to 400 K are shown to behave similarly in Chapter 4. Another characteristic of interest in the figure is the negative differential mobility, apparent from the decrease in drift velocity as electric field is increased beyond around 150 kV/cm. The reason for the decrease is that as the applied field is increased, an increasing proportion of the electron ensemble becomes scattered into higher energy sub-bands.

In HEMTs, the confinement of the 2DEG at the heterointerface, determined by the steepness of the potential well, is dependent on the density of the 2DEG there. This is because of the band bending caused by the potential gradient generated by the charges, as described by the solution of Poisson's equation in the direction perpendicular to the heterointerface [53]. Results of calculations for AlGaN/GaN heterojunctions at 300 K found that as the carrier density was varied the mobility passed through a maximum for an n_{2DEG} value of around $2 \times 10^{12}\,\mathrm{cm}^{-2}$. The reason for this behaviour is that at very low carrier densities, corresponding to the sub-threshold region of HEMT operation, quantum-mechanical confinement at the interface is poor, and mobility is predominantly determined by bulk conduction. As channel density is increased, by decreasing the magnitude of the negative bias applied to the gate in the case of a depletion mode HEMT, 2DEG confinement near the interface is improved. Conduction is then quasi-2D. The quasi-2D behaviour has been modelled by assuming that electrons in all but the lowest sub-band scatter in a bulk manner. It has been found that two-dimensional (2D) mobility can be much higher than

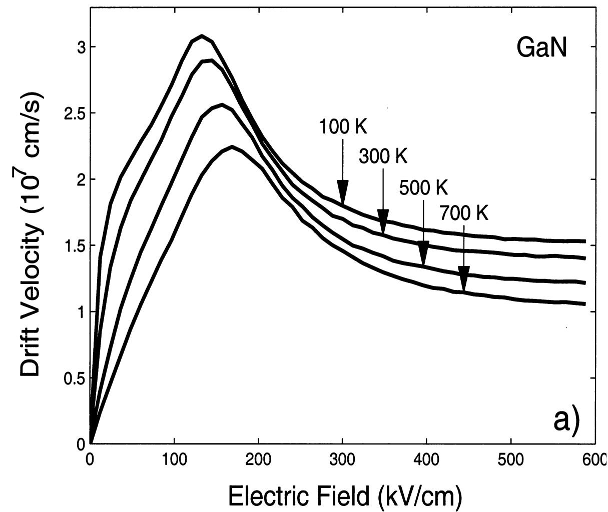

Figure 2.6: Electron drift velocity in wurtzite GaN as a function of temperature and applied electric field. Values were determined from Monte Carlo electron transport simulations. Reproduced with permission from [52].

bulk mobility [54]. The higher mobility in the 2D case can be partly understood by considering confining potential scattering the electrons back into the plane of drift conduction.

2.5 Neutron irradiation interactions

Neutrons are uncharged particles, and so do not directly ionise matter they interact with. However, when neutrons do interact with matter, via scattering and capture events, they can generate secondary particles which are charged and go on to ionise the material they pass through. When an atomic nucleus is scattered by an incident neutron it is known as a Primary Knock-on Atom (PKA). When just one scattering event is generated which causes a noticeable change in the permanent or transient electrical behaviour of a semiconductor device it is known as a SEE. The scattering processes themselves are also of interest here, because they can lead to the creation of vacancies in a crystal lattice, interstitial atoms, and surface defects. The creation of such crystallograpic defects in this context is known as displacement damage. When initial scattering events are sufficiently energetic, the generated secondary particles can go on to create generate further scattering events. As these damage cascades evolve, the kinetic energy available in each collision decreases, and so then does the range of the knocked-on nuclei. Such a series of events can cause clustering of damage in a confined region of the irradiated material. The energy lost to the creation of vacancy-interstitial pairs, known as Frenkel defects, and the creation of lattice vacancies without an associated interstitial, known as Schottky defects, is known as non-ionising energy loss (NIEL).

2.5.1 Neutron interaction cross-sections

To understand neutron irradiation effects, interaction cross-sections must first be considered. Each nucleus in the material being irradiated presents an effective cross-sectional area to the incident neutron beam, known as the microscopic cross section, σ. Here, σ is the total cross-section, which includes scattering and capture events. The target material has a number density of atoms per unit volume, ρ, and a thickness $\mathrm{d}x$. If the incident neutron beam has a flux density of I neutrons per unit area per unit time, then the number of interactions, N, per unit area per unit time is given by

$$N = I\sigma\rho\mathrm{d}x. \tag{2.40}$$

The probability of a neutron interaction occurring within a layer of cross-sectional area, A, is then given by $\sigma\rho\mathrm{d}x/A$. A macroscopic cross-section, Σ, can be defined as the product of the microscopic cross-section and the number density of the material,

$$\Sigma = \rho\sigma, \tag{2.41}$$

which has units of m^{-1}. The mean free path of neutrons in the target material is given by $\lambda = 1/\Sigma$. Figure 2.7 is a range plot showing the mean free path as a function of energy, for neutrons in gallium-69. From the figure, for neutron energies around 14 MeV, λ is on the order of 10 cm. Active regions within HEMTs have a thickness on the order of 100 nm. For such a region composed of Ga-69, the expected number of neutron interactions would be 10^{-8} per unit neutron fluence.

Scattering and capture events are themselves composed of inelastic- and elastic-scattering, and absorption and fission, respectively. Spallation, where a target nucleus captures a neutron and splits into multiple parts, can occur for neutron energies of hundreds of MeV. Units of Barns are conventionally used for cross-sections, which, in SI units is $10^{-28}\,\mathrm{m}^2$. The cross section for each of these events depends not only on the target nuclei species, but also on the incident neutron energy.

Neutron cross-sections used in calculations are typically taken from libraries derived from measured values, see for example the Evaluated Nuclear Data File, available at `https://www-nds.iaea.org/exfor/endf.htm`. In general for thermal neutrons, where energies are a few tens of meV, neutron capture cross sections decrease with increasing incident neutron velocity as $1/v$. This relationship is intuitive, because of the reduced time an incident neutron will spend in the vicinity of a target nucleus as its velocity is increased. Generally, cross-sections change slowly with neutron energy, however resonances are found in cross-sections where neutron energies correspond to excited states of the target nuclei plus incident neutron system. In the case of inelastic scattering events, the incident neutron is absorbed by the target nucleus, then re-emitted, leaving the target nucleus in an excited state. The subsequent relaxation of the target nucleus can be associated with emission of a gamma ray, which can cause ionisation in the irradiated material. Non-elastic scattering is also possible, where after the initial neutron capture, a different secondary particle is emitted. In semiconductor devices the most relevant

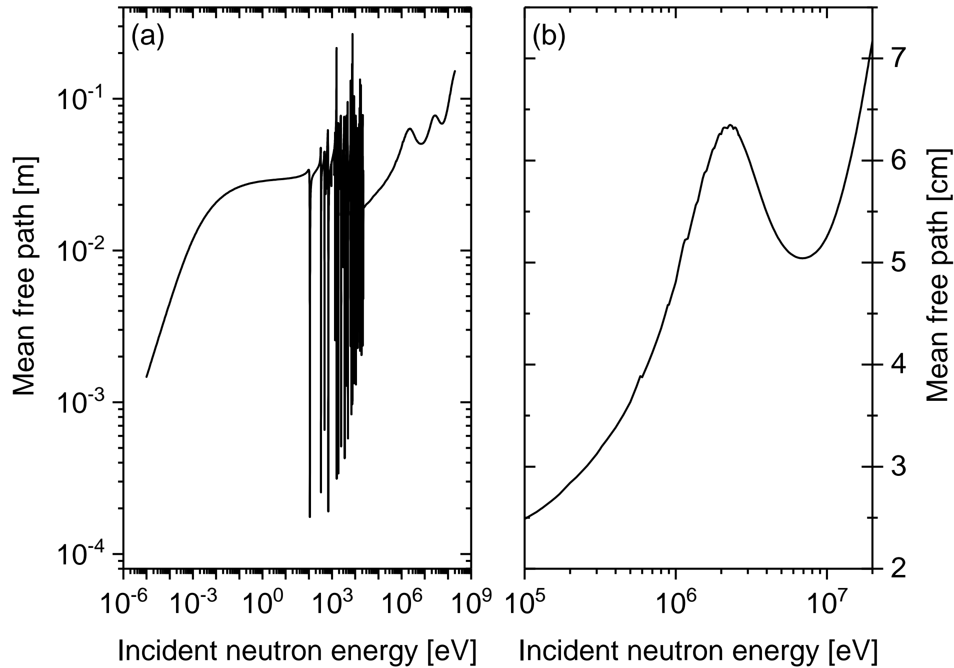

Figure 2.7: Mean free path, $\lambda = 1/\Sigma$, for neutrons in Ga-69, as a function of incident neutron energy. Macroscopic cross-section, Σ, was calculated using the total interaction microscopic cross-section as input. The effect of cross-section resonances is apparent in (a). (b) is an expanded view showing λ values around the incident primary neutron energies used in this thesis.

reactions of this sort are the (n,p) and (n,α) reactions. In these cases the emitted proton or α particle can have an energy in the MeV range, and cause significant localised ionisation within the semiconductor along their paths. Other reactions may also occur, for example $(n,2n)$ reactions, which can lead to the creation of displacement damage, and further subsequent (n,p) and (n,α) reactions. At thermal neutron energies, (n,γ) reactions can produce displacement damage when the emitted γ photon is sufficiently energetic to cause the emitting nucleus to recoil with an energy greater than the minimum displacement damage energy, E_D [55].

Figure 2.8 shows the total, elastic and non-elastic scattering cross sections for the most abundant isotopes of the elements forming the compound semiconductors studied in this work. In the figure it can be seen that the elastic scattering cross-section is much larger than the non-elastic cross-sections for nitrogen-14 across almost the entire energy spectrum. For aluminium-27 and gallium-69 the cross-sections are similar near the 14 MeV point, but quickly diverge for lower energies. This means that the interactions of the scattered neutrons within the semiconductors will be predominantly elastic in nature. For these reasons, the emphasis in this work will be on elastic scattering collision events.

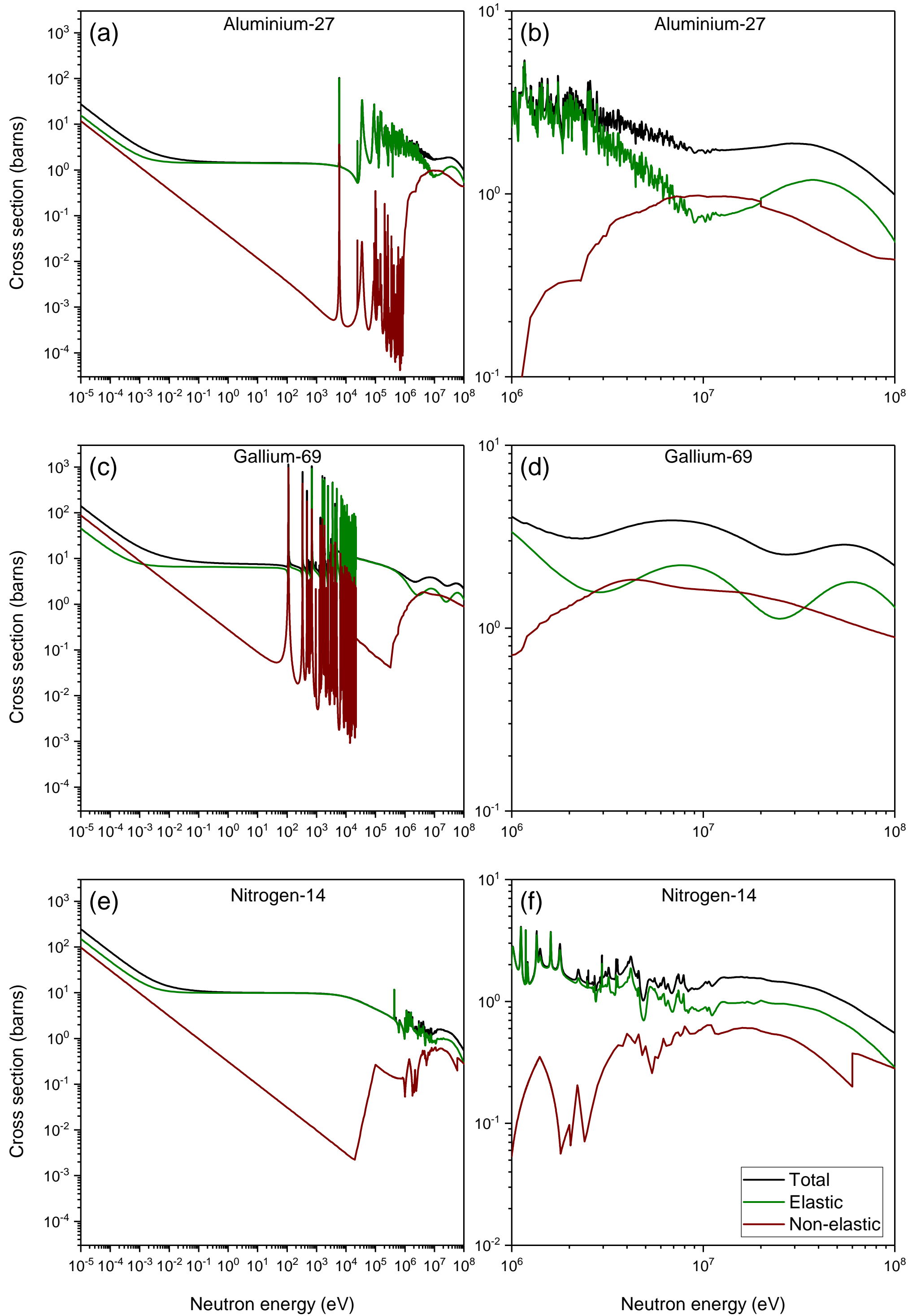

Figure 2.8: Total, elastic, and non-elastic neutron scattering cross-sections for the most abundant isotopes of aluminium ((a,b), gallium (c,d), and nitrogen (e,f), respectively. (b), (d), and (f) are detailed views of the cross sections near to the 14 MeV incident neutron energy used in this work.

2.5.2 Elastic collisions

In an elastic collision the kinetic energy imparted to the target nuclei depends on the relative masses of neutron and the nuclei, and the kinetic energy of the incident neutron. It is useful to find the maximum possible target nuclei velocity for a given incident neutron energy. In this case a head-on collision at non-relativistic velocities is considered, which is appropriate for the neutron energies found in this work. Then by conservation of momentum, for the neutron, n, and target nuclei, t, in initial, i, and final, f, states, we have

$$m_n v_{n,i} + m_t v_{t,i} = m_n v_{n,f} + m_t v_{t,f}, \tag{2.42}$$

where m and v are the respective masses and velocities. Kinetic energy is also conserved,

$$\frac{1}{2} m_n v_{n,i}^2 + \frac{1}{2} m_t v_{t,i}^2 = \frac{1}{2} m_n v_{n,f}^2 + \frac{1}{2} m_t v_{t,f}^2. \tag{2.43}$$

By combining Equations (2.42) and (2.43), a pair of equations for the neutron and target velocities after collision are found:

$$v_{t,f} = v_{n,i} \frac{2m_n}{m_n + m_t} + v_{t,i} \frac{m_t - m_n}{m_n + m_t} \tag{2.44}$$

$$v_{n,f} = v_{t,i} \frac{2m_t}{m_n + m_t} + v_{n,i} \frac{m_n - m_t}{m_n + m_t} \tag{2.45}$$

Target nuclei with thermal velocities low compared to the incident neutron velocities can be considered as stationary. In that case the second term of Equation (2.44), and the first term of Equation (2.45) are zero. Under such conditions the maximum kinetic energy imparted to the target nuclei by a 14 MeV neutron for the three isotopes considered here, and the final neutron energy are given in Table 2.1, as calculated using Equations (2.44) and (2.45). The displacement damage energy, E_D, that is the energy required to displace a nuclei from its lattice site, averaged over all crystallographic directions for Ga-69 and N-14 is also provided in the table, as calculated in [22]. By considering the data presented in Table 2.1 it is clear that 14 MeV neutron irradiation will cause displacement damage in GaN, and that the scattered nuclei, the PKAs, will have sufficient energy to go on to create many further secondary displacement damage events.

Isotope	$E_{t,f}$ (MeV)	$E_{n,f}$ (MeV)	Average displacement energy (eV)
aluminium-27	1.9	12.1	
gallium-69	0.8	13.2	45 ± 1 in GaN [22]
nitrogen-14	3.5	10.5	109 ± 2 in GaN [22]

Table 2.1: Primary knock-on atom energies and average displacement energies in GaN.

2.5.3 Defect density estimation

To estimate the ionisation and displacement damage caused by all the scattering reactions which would occur, the angular dependence of the scattering vectors must be calculated in terms of the differential cross-section. Additionally it is clear from consideration of the PKA energies involved that the ionisation and displacement damage of secondaries must be included in the calculation. The cascade of collisions which must be included continues until all incident and secondary particles have been captured or left the material volume of interest. In practice, because of the large number of possible nuclear reactions, the energy-dependent cross-sections, and the large number of particles involved in the cascade created by even a high-energy neutron scattering event, a statistical approach is required. Monte-Carlo methods are therefore used to calculated neutron interactions with matter. GEANT4 and Monte Carlo N-particle (MCNP) are two examples in widespread use. Using a radiation transport code such as MCNP, it is possible to calculate a number spectrum of PKA energies for a given incident neutron energy spectrum, and target material. The results of such an approach are discussed in Chapter 5. As discussed in that chapter, the calculated PKA spectrum can be used to estimate the displacement damage and ionisation caused by the reactions resulting from the neutron irradiation.

To estimate the number of crystallographic defects created by the neutron scattering-induced PKAs and the subsequent secondary scattering events, the model developed by Kinchin and Pease [56] is adopted, as modified by Torrens and Robinson [57]. The model can also be applied to ion irradiation by considering the incident ion spectrum to be the PKA spectrum. In the model, scattered atoms with energies above E_e lose energy only by Coulomb interactions with electrons. Conversely, atoms with energies below E_e are taken to interact only by hard-sphere inter-atomic scattering. When an atom receives a knock-on energy greater than E_D it is considered to be displaced permanently, whereas for lower knock-on energies it is considered to return to a lattice site. The result of the model is an expression for the number of Frenkel defects, N_d given by

$$N_d = \frac{\kappa \hat{E}}{2E_D} \tag{2.46}$$

where κ is the efficiency of damage production and is predominantly a temperature- and material-independent constant with a value taken to be 0.8. $\hat{E}$ is the energy available to cause displacement damage via elastic collisions. $\hat{E}$ is estimated by taking the PKA energy and reducing it by a factor to account for inelastic energy losses. That correction is neglected here, and instead the average energy in each division, or 'bin', of the calculated PKA spectrum is used to estimate the number of Frenkel pairs due to that part of the knock-on spectrum. This approach is justified because of the large uncertainty surrounding creation of damage clusters and replacement collisions in compounds with large mass differences between the constituent atoms. Applying Equation (2.46) to the calculated energies listed in Table 2.1 shows that each PKA is capable of producing several thousand defects after scattering by 14 MeV neutrons.

More sophisticated modelling of damage production is typically done in one of two ways. In the first, a molecular dynamics calculation is performed with an appropriate choice of inter-atomic potential. In this case, the classical equations of motion are solved for many atoms simultaneously. The second approach is to use a model based on the binary collision approximation (BCA). In this latter case, each collision is considered as a two body event in isolation. Simulations based on the BCA approach can either use amorphous models of the target material, as is done by Monte Carlo codes like Transport of Ions in Matter (TRIM), or they can use a crystalline target in the calculation where atoms are sited at appropriate positions rather than homogeneously, as is done by the MARLOWE code. Phenomena including ion channelling were predicted by BCA codes which accounted for the crystal structure of targets. Such methods are appropriate when increased precision of defect density and species is required, or when the trajectories of the scattered PKAs and secondaries is important. For the work described in this thesis, the model described above is sufficiently accurate to calculate defect densities for comparison to measured quantities.

2.5.4 Impact of defects on semiconductor electrical properties

The creation rate of crystallographic point defects due to neutron irradiation was discussed above. Sources of crystallographic point defects include vacancies, interstitials, anti-sites, foreign atomic species, and defect complexes formed from those. In Figure 2.9 the GaN hexagonal lattice is shown complete, and with Ga and N vacancies. In Figure 2.10 a 2D representation of a lattice is shown, with a vacancy, native and foreign species interstitials, and substitutional impurities. When discussing electronic energy band structure the idea of crystallographic defects leading to localised allowed energy states was introduced. These states can form generation and recombination centres for free charges, or if their energy lies far from a band edge in terms of kT, then they can form charge traps with time-constants large compared to device switching times. When discussing classical models of electron transport the idea of a mean free path was introduced, the concept is also present in modern methods of calculation based on Monte Carlo techniques to solve the BTE in the form of scattering cross-sections. Clearly then, knowledge of the density and nature of point defects is important to understand device operation, particularly in a radiation environment where displacement damage can modify the density and species of the defects within a material.

The density of stable point defects estimated by using Equation (2.46) is less than the number of displacements initially produced, due to displaced atoms relaxing into their former lattice sites if they are not displaced be a great enough distance. Replacement collisions are also included in that model. However, it is important to note that even in the absence of displacement damage, and under ideal growth conditions, and allowing for thermal annealing, there is no such thing as a defect-free crystal. The reason for this is that vacancies and interstitial atoms increase the entropy of the crystal. The increase in entropy decreases the free energy, and so is thermodynamically

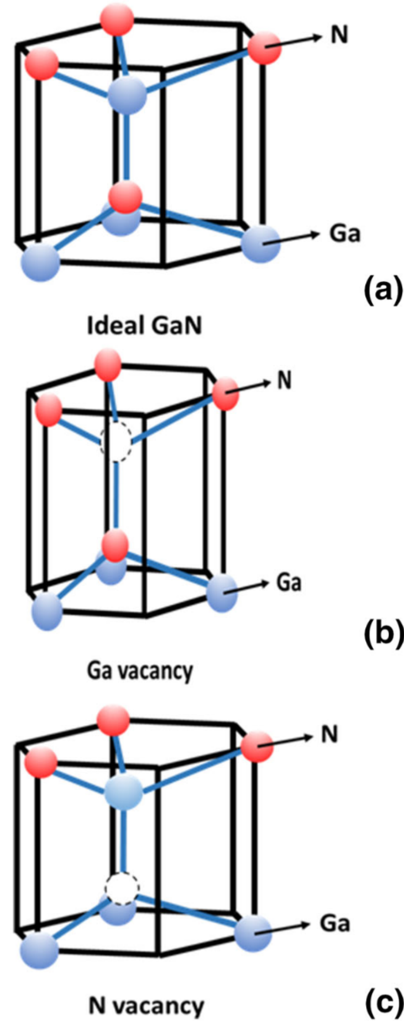

Figure 2.9: An illustration of the GaN hexagonal lattice (a), and as modified by a nitrogen vacancy (b), or by a gallium vacancy (c). Reproduced with permission from [58].

favourable. It can be shown that the number, n, of defects of a particular species can be estimated as follows. For a crystal with N atoms, and a defect creation energy, E, from Boltzmann's entropy formula we have $S = k\ln(W)$, where S is the entropy and W is the number of microstates given by $\frac{N!}{(N-n)!n!}$. The change in free energy due to the presence of the defects is $\Delta F = nE - T\Delta S$, and taking the most probable value for n to correspond to where $\frac{\partial \Delta F}{\partial n} = 0$, we have

$$\frac{n}{N-n} = \exp\left(-\frac{E}{kT}\right). \tag{2.47}$$

Therefore when studying the creation of defects due to displacement damage the temperature of the sample during and following irradiation must be controlled if different irradiation levels and samples are to be meaningfully compared. Due to the larger defect creation energies found in AlGaN and GaN as compared to other semiconductors, irradiation-induced defects should

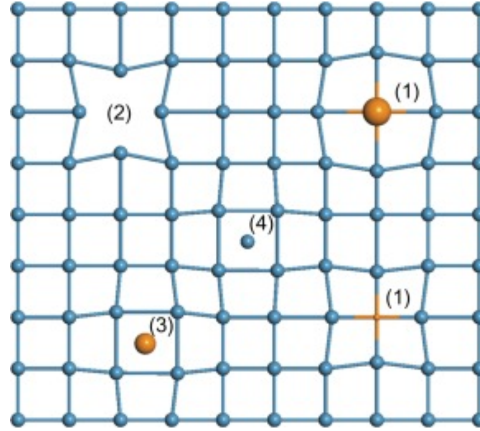

Figure 2.10: A two-dimensional illustration of crystallographic point defects. (1) large and small atom substitutional impurity defects, (2) a vacancy, (3) a foreign interstitial, (4) a native atom interstitial. Reproduced with permission from [59].

thermally anneal more quickly. This may be a factor in their observed increased irradiation tolerance when compared to other technologies.

The impact on semiconductor device electronic properties that may be expected from a change in defect density depends on the nature of the device. Devices such as bipolar junction transistors, where gain is determined by the minority carrier lifetime in the base region, are particularly sensitive to the impact of displacement damage. The states created by the defects act as recombination centres for minority carriers. Minority carrier lifetime was first related to irradiation fluence [60], and then to bipolar transistor gain [61, 62], resulting in the Messenger-Spratt equation

$$\frac{1}{G_\infty} - \frac{1}{G_0} = k\Phi, \tag{2.48}$$

where Φ is the irradiation fluence, G_∞ is the asymptotic gain, G_0 is the gain immediately after irradiation, and k is a damage constant specific to the device and neutron energy spectrum. This effect is important here because the gain degradation in silicon BJTs is commonly used as measure of the damage effect of a radiation effects environment. The value of k is used to compare effects of different neutron environments to a reference spectrum in some engineering test standards [63], and can be used to define the '1 MeV equivalent' neutron fluence of a neutron source spectrum. For completeness we note that a test standard for characterising accelerator-based neutron sources is available [64], but will not concern us here.

HEMTs are not susceptible to degradation by a decrease in minority carrier lifetime. This is because, firstly, as was shown earlier, the source of the electrons in the 2DEG is surface states, which are insensitive to minority carrier lifetime. And secondly, because the high density of the 2DEG is due to the resultant polarisation in the structure, which is also insensitive to minority carrier lifetime. Because of the confinement to a 2D channel, the electrons responsible for the conduction current in a HEMT are less sensitive to increases in defect density than bulk

conduction devices. The high density of carriers in the channel also screens the effect of ionised defects, reducing scattering by that mechanism. For these reasons HEMTs are likely to only be sensitive to mobility degradation at very high neutron irradiation fluence levels. However, when operating near threshold, when the 2DEG is largely depleted, the capacity of the 2DEG electrons to screen out scattering due to ionised impurities is reduced, and it may be possible to observe changes in mobility in that regime. The creation of electronic traps within HEMTs may, however, affect the density of carriers in the channel. Any charge trapped in a HEMT buffer layer must be compensated by a change in the 2DEG density. So the creation of displacement damage resulting in buffer traps may limit the performance of AlGaN/GaN HEMTs in neutron irradiation environments.

2.6 Ionisation localised along tracks

The creation of displacement damage due to neutron irradiation, in the form of stable crystallographic defects, was discussed above. It was stated that such defects can generate spatially localised energy levels, which can trap electrons in semiconductors. Bulk structural properties can also be changed, due to strain for example. Such effects are of particular concern to workers in the material science community developing materials for future fusion reactors, and will not be considered further here. During the creation of the displacement damage, the PKAs and secondary particles also cause ionisation via the Coulomb interaction as they move through the material. The most important measure of this ionisation is known as the stopping power, or conventionally in the field of radiation effects on electronics, the LET. The LET describes the rate of energy loss of a particle as it moves through a material, $\mathrm{d}E/\mathrm{d}x$. The conventional units for LET are $\mathrm{MeVcm^2mg^{-1}}$, which can be seen to be the rate of energy loss along the track normalised by the target material mass density, in units conventional for the semiconductor industry.

The physics of the energy loss of ions passing through matter, the stopping power, is a highly complex problem. Ziegler reviewed progress in the field, with an emphasis on the stopping of light ions with energies above 1MeV/u [65]. Because we are interested here in the passage of ions through compound semiconductors it is appropriate to restate Bragg's rule [66] that the stopping power in a compound is a linear combinations of the stopping powers of the constitutive parts. The dependence of stopping power, S, on the basic properties of the incident and target nuclei can be found by considering the simplified version of the Bethe-Bloch formula for stopping power

$$S = \frac{\kappa Z_2}{\beta^2} Z_1^2 L(\beta) \tag{2.49}$$

where $\kappa = 4\pi r_0^2 m_e c^2$, $\beta = v/c$, Z_1 and Z_2 are the atomic numbers of the incident and target nuclei. $L(\beta)$ is the stopping number, a factor containing corrective terms to account for approximations in the model. Bethe formulated the model by considering momentum transfer from the incident particle to the electrons in the target material. In the model the nuclear reactions are ignored

and energy transfer is considered to the target electrons, not the target nuclei. A kinematic justification for this approximation can be seen by considering Equation (2.44) for the case of a target mass much less than the incident particle mass, m_n in the equation above. In the simplified Bethe-Bloch equation the stopping power depends only on the atomic number of the incident nucleus, its velocity, and the electron density in the target material. It is clear from Equation (2.49) that as the velocity of the incident nucleus is reduced, due to the work done in ionising the target material along its path, the stopping power, or LET increases. As the velocity nears zero the LET dramatically increases, before dropping to zero as it comes to rest. This phenomena is the cause of the Bragg peak in a depth-dose profile, where a large proportion of ionising dose is deposited in a well defined region near the end of a particle track. A practical use of the Bragg peak is the treatment of tumours by depositing a large ionising radiation dose to the tumour without causing excessive damage to surrounding tissue.

An uncorrected form of the simplified Bethe-Bloch formula [67], is modified here to account for the permittivity of GaN, giving

$$S = -\frac{\mathrm{d}E}{\mathrm{d}x} = \frac{4\pi n Z_1^2}{m_e c^2 \beta^2} \left(\frac{e^2}{4\pi\epsilon_0\epsilon_r}\right)^2 \left(\ln\left(\frac{2m_e c^2\beta^2}{I\left(1-\beta^2\right)}\right) - \beta^2\right), \tag{2.50}$$

where n is the electron density in the target material, GaN in this case, and I is the mean ionisation potential. Equation (2.50) was used to iteratively calculate the LET values as a function of depth for an incident 3.5 MeV nitrogen ion, as displayed in Figure 2.11. The data in the figure are for indication only, due to the relatively low specific ion energy of 0.25 MeV/u used in the calculation.

The stopping of ionising particles in matter is inherently statistical in nature. Stopping power calculated as above is an average quantity, and so range straggling will occur. In practice, to calculate stopping, ranges, and straggling, Monte Carlo codes are typically used, such as Stopping and Range of Ions in Matter (SRIM). Recently, a massively parallel 3D Monte Carlo code, IM3D [68], which incorporates SRIM models has been made available. IM3D may prove useful for further studies of damage creation in semiconductor devices once initial PKA spectra have been calculated with, for example MCNP or GEANT4.

Once the ionisation has been generated along the particle track, as discussed above, several processes occur. In the absence of a regenerative mechanism, diffusion will cause the highly localised radial charge distribution to widen and decrease in density. In the case of extremely high density of charge generation, the heating caused by the thermalisation of the generated free carriers can be sufficient to cause material phase changes, including melting or vaporisation. If the semiconductor device is electrically biased, so the material experiences an applied electric field, the generated charge track can form a conduction pathway between regions at different potentials. If a large bias was applied, and other resistances are low, then the Joule heating caused by the resulting conduction current along the track can cause catastrophic damage.

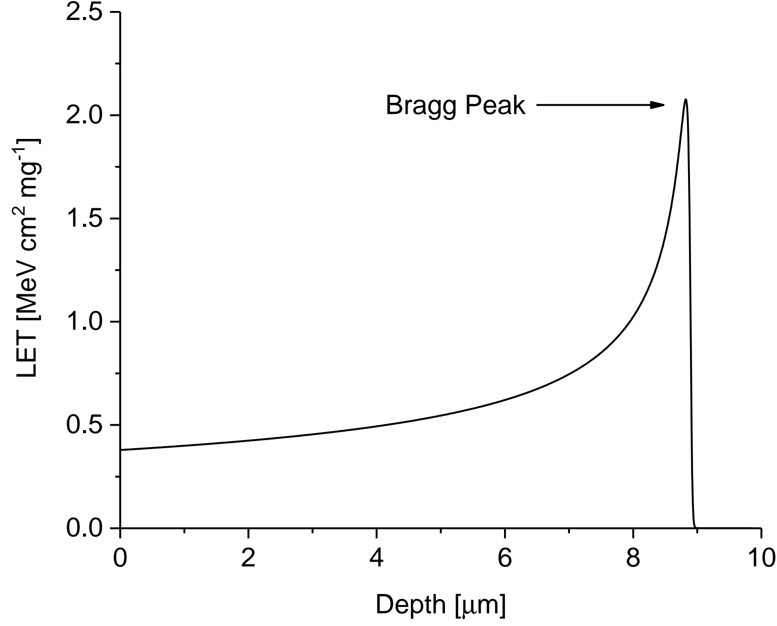

Figure 2.11: Plot of LET against depth for 3.5 MeV nitrogen ions in GaN, as calculated using Equation 2.50.

2.7 Optical ionisation

Here the basic mechanisms behind the ionisation of a semiconductor by incident laser light are presented. The problem is considered in two parts. Firstly the propagation of the electromagnetic wave as a solution of Maxwell's equations. Then the effect of the susceptibility on the polarisation induced by the wave will be stated. Firstly, Maxwell's equations are given by

$$\nabla \times \vec{E} = -\mu_0 \frac{\partial \vec{H}}{\partial t}, \tag{2.51}$$

$$\nabla \times \vec{H} = \epsilon_0 \frac{\partial \vec{E}}{\partial t} + \frac{\partial \vec{P}}{\partial t} + \vec{J}, \tag{2.52}$$

$$\nabla \cdot \vec{E} = -\frac{1}{\epsilon_0} \cdot \vec{P}, \tag{2.53}$$

$$\nabla \cdot \vec{H} = 0, \tag{2.54}$$

where the magnetic field is given by

$$\vec{H} = \frac{1}{\mu_0} \vec{B} - \vec{M}, \tag{2.55}$$

where $\vec{M}$ is the magnetisation, and $\vec{B}$ is the magnetic induction. The electric displacement, $\vec{D}$ is determined by the electric field, $\vec{E}$, and polarisation, $\vec{P}$, as

$$\vec{D} = \epsilon_0 \vec{E} + \vec{P} \tag{2.56}$$

The wave equation for the electric field can then be found by taking the curl of Equation (2.51), and combining with the derivative with respect to time of Equation (2.52) in order to remove $\vec{H}$ to give

$$\nabla \times \left(\nabla \times \vec{E}\right) + \frac{1}{c^2}\frac{\partial^2 \vec{E}}{\partial t^2} = -\mu_0 \frac{\partial^2 \vec{P}}{\partial t^2} - \mu_0 \frac{\partial \vec{J}}{\partial t}, \tag{2.57}$$

where $\frac{1}{c^2} = \epsilon_0 \mu_0$. It can be seen that in the absence of any polarisation or current terms, Equation (2.57) reduces to the usual solution for an EM wave in a vacuum. A similar approach could be adopted to find the wave equation for the magnetic component of the wave. The purpose of Equation (2.57) here is to demonstrate that the propagation of the wave in matter depends on the polarisation in the material. Microscopic polarisation, in turn, depends on the arrangement of the electrical charges throughout the material, as described by the dipole moments given by Equation (2.1). All crystals except those with a cubic crystal structure are anisotropic, and so display birefringence, where the EM wave propagation speed depends on the direction within the crystal. In this case we have

$$\vec{D} = \underline{\underline{\epsilon}}\vec{E} = \epsilon_0 \underline{\underline{1}} \cdot \vec{E} + \epsilon_0 \underline{\underline{\chi}} \cdot \vec{E}, \tag{2.58}$$

where $\underline{\underline{\epsilon}}$ is the dielectric tensor, and $\underline{\underline{\chi}}$ is the susceptibility tensor which determines the component of polarisation in each crystallographic direction due to the components of the electric field all directions. In general the electric susceptibility is a function of frequency, but the magnetic permeability is not, so the wave speed in a material is given by

$$v = \frac{c}{\Re\sqrt{\epsilon(\omega)})} = \frac{c}{n(\omega)}, \tag{2.59}$$

where $n(\omega)$ is the frequency-dependent refractive index. When electric fields are not too large, non-linear optical effects can be considered using the vectoral Taylor expansion of the polarisation. For simplicity the form of the expansion suitable for isotropic crystals, where polarisation and electric field are along the same axis, is given here

$$P = \epsilon_0 \left(\chi E + \chi^{(2)} E^2 + \chi^{(3)} E^3 + ...\right), \tag{2.60}$$

where χ is the linear susceptibility. The remaining terms represent the non-linear polarisation, and their coefficients are generally much smaller than the linear term. This is the reason why the production of non-linear effects requires intense laser sources. Second harmonic generation is due to the χ^2 term, and Two Photon Absorption (TPA) is due to the χ^3 term. In this latter case the higher order dependence on E causes charge generation by TPA to be confined to high intensity regions of a laser focus.

The above macroscopic model can be used to understand the effects of classical microscopic bound valence electrons on the propagation of light in a semiconductor. If they are assumed to be localised at ion cores with a displacement-dependent restoring force, they can be considered to act as harmonic oscillators. This leads to energy dissipation as an EM wave progresses through a material, equivalent to the absorption of light. Absorption can be shown to be maximum when

the driving frequency equals the resonant frequency of the harmonic oscillator valence electrons. The resonant frequency corresponds to a peak in the imaginary part of the dielectric constant [69]. When considering free electrons in the semiconductor in the same manner, it is clear that the binding force of the oscillator model is zero. The real part of the free electron contribution to the dielectric constant can then be written as

$$\epsilon(\omega) = 1 - \frac{\omega_p^2}{\omega^2}, \tag{2.61}$$

where ω_p is the plasma frequency of the free carrier oscillations. It can be seen that incident light with a frequency less than the plasma frequency will experience a negative dielectric constant, which by comparison with equation (2.59) will lead to an imaginary refractive index. This will result in near perfect reflectivity of the incident light. On the other hand, for incident light at a frequency greater than the plasma frequency the EM wave can propagate through the material. When using pulsed lasers to generate charge in a sample it is clearly important that charge generated by the leading edge of the pulse in time does not prevent the remainder of a pulse from propagating into the material. To estimate the charge density at which plasma frequency-induced opacity might occur we consider the displacement of a region of a free electron gas by a distance, dx. If the free electron density is n, then from Gauss's law we have

$$E_x = \frac{ne\Delta x}{\epsilon_0}. \tag{2.62}$$

Multiplying by the charge on an electron leads to a force

$$eE_x = \frac{ne^2\Delta x}{\epsilon_0} = m_e\frac{\partial \Delta x}{\partial t^2}. \tag{2.63}$$

Re-arranging and integrating twice with respect to time we find an estimate for the plasma frequency, ω_p, can be made

$$\omega_p = \sqrt{\frac{ne^2}{m_e\epsilon_0}}. \tag{2.64}$$

Equation (2.64) can be used to determine whether laser pulse propagation in a semiconductor might be self-limited due to free-carrier generation in the focal region. It can also be used to determine whether valence electrons or free electrons generated by thermal excitation will dominate the optical characteristics of a semiconductor.

The absorption of light by valence electrons increases their energy, allowing them to be promoted to become free carriers in the conduction band, thus leaving a hole behind in the valence band. Conservation of energy requires that the combined energy of the two charge carriers must equal the incident photon energy. In indirect band gap semiconductors, to account for the change in momentum that occurs when a valence electron is promoted to the conduction band, the capture or emission of phonons is also required. Under high excitation conditions the density of states in the lowest band can be insufficient to contain all of the photo-excited carriers.

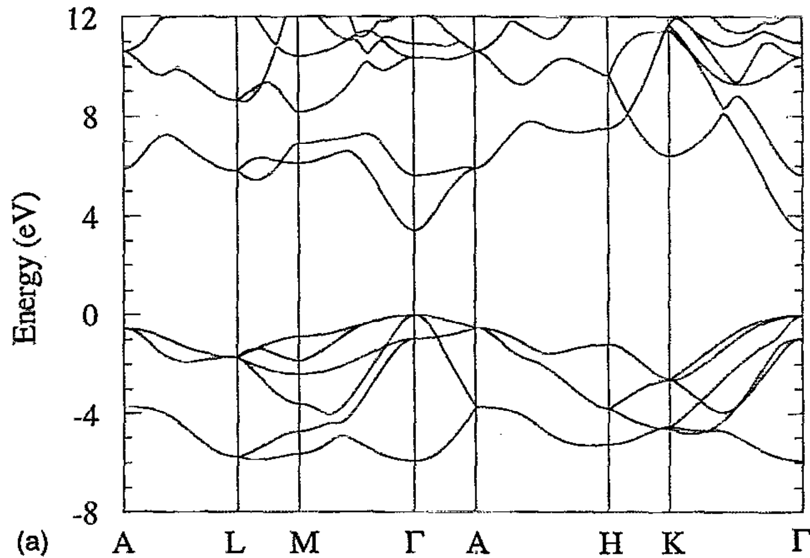

Figure 2.12: Wurtzite GaN band diagram. The main points and lines of symmetry of the first Brillouin zone are labelled. The direct fundamental band gap is visible at the Γ point. The nearest satellite valley to the central gamma valley can be seen between the *L* and *M* points. Reproduced with permission from [70].

In that case carrier-carrier scattering and carrier-phonon scattering can cause electrons to scatter into side valleys. Thus enabling further carriers to be scattered into the central gamma (Γ) valley, visible in Figure 2.12. The effective mass of the electrons in the side valleys may be different, resulting in a different effective mobility for those electrons. In the case of light absorption by free electrons in the conduction band, they are excited higher up within the band by photon absorption, increasing their energy, and also enabling further carriers to be promoted from the valence band to the newly empty state low in the conduction band. Impact ionisation is also possible under photo-excitation, where the free carrier has enough excess energy to promote a valance electron to the conduction band, increasing free electron density. Excited free carriers with excess energy above the band edge can scatter with phonons, dissipating their excess energy and heating the semiconductor lattice. Radiative recombination is more energetically favourable in direct band gap semiconductors, like GaN. In this case the rate of radiative recombination is proportional to the product of the free electron and hole concentrations and occurs on nano-second time-scales [69] for free carrier densities on the order of $10^{18}\,\mathrm{cm}^{-3}$.

2.8 Summary

In this chapter we have seen how the non-centrosymmetric crystal structure of GaN, along with built-in strain, leads to high density fixed polarisation charges at the heterointerface between AlGaN and GaN. Once compensated by electrons provided by surfaces states, a high density

2DEG is created. The band bending at the heterointerface results in strong quantum-mechanical confinement of the 2DEG to a thin sheet, with only motion parallel to the interface possible. This configuration results in high mobilities, and robustness against scattering out of the 2DEG plane. It also forms the basic building block for HEMTs, a form of FET. The material properties of AlGaN/GaN enable HEMTs constructed from them to be able to operate well at high voltage, frequency, and temperature, with the potential for good radiation-hardness.

The effects of a neutron irradiation environment on GaN-based devices were seen to include displacement damage and ionisation due to scattered lattice ions. Track lengths for scattered ions, dictated by their rate of energy loss through the semiconductor, LET, were seen to depend on species and energy. PKA track lengths on the order of μm were shown to be credible after 14 MeV neutron irradiation. The mean free path of fast neutrons in GaN was seen to be on the order of cm. However, because of the high energy of any created PKAs, thousands of crystallographic point defects can result from a single neutron interaction. The relatively high defect creation energies in AlGaN and GaN were seen to suggest a lower equilibrium defect concentration, as compared to other semiconductors. Finally, the process of the ionisation of a material by an incident optical-frequency electromagnetic wave was described, along with the effects of optically-driven high carrier generation rates.

CHAPTER 3

EXPERIMENTAL TECHNIQUES

> "The aim of the poet is to inform or delight, or to combine together, in what he says, both pleasure and applicability to life. In instructing, be brief in what you say in order that your readers may grasp it quickly and retain it faithfully. Superfluous words simply spill out when the mind is already full."
> — Horace, Epistolas Ad Pisones De Ars Poetica

The experimental work described in this thesis required the use of multiple types of scientific instrument, the construction of bespoke hardware, and the development of new measurement techniques. In this chapter a summary is provided of these scientific instruments, apparatus, and techniques.

In this work we shall frequently be concerned with the dependence of electrical quantities on independent parameters, which we control. The electrical quantities of interest include Direct Current (DC) parameters, and transient currents flowing through device contacts. In the latter case the characteristic timescales of the required measurements span 14 orders of magnitude of time, from $10^{-10} - 10^{4}$ s. The wide range of timescales necessitates differing experimental configurations for their proper measurement, from high bandwidth connections and digital storage oscilloscope-based data capture for the fastest signals, to Source Measure Units (SMUs) for precise measurements of static or slowly varying signals. By performing measurements across this range of timescales, we are able to study the intrinsic charge dynamics in semiconductor devices, and to measure their static and dynamic response to neutron and photon irradiation.

3.1 Sample preparation for measurement and irradiation

Measurements were performed both on semiconductor wafer samples, and on packaged devices. Probe stations enable convenient electrical connection to, and optical surface inspection of wafer samples, reducing the amount of sample preparation required before measurements can begin. When working with packaged devices, they must either be mounted into a purchased or custom made jig (see Chapter 5), enabling connection to a test circuit, or they must be soldered onto the test circuit Printed Circuit Board (PCB). Preparing samples for irradiation necessitates additional measures, some of which are dictated by the nature of the irradiation facility or source to be used. Some irradiation environments necessitate special packaging requirements to prevent contamination of the samples, which would otherwise limit or prevent subsequent testing. Preparing samples for irradiation when not connected to a test circuit can simply require packaging to protect the samples and to enable ease of handling at irradiation facilities (Chapters 4 and 5). To limit the build-up within samples of potentially damaging static charge caused by the irradiation, they can be mounted within a conductive medium, or a suitable sample holder, to provide an electrical connection between device contacts. When preparing samples for irradiation when connected to a test circuit, and potentially monitoring signals during a transient irradiation event, additional work must be performed to mitigate the effects of, for example, undesired electromagnetic interference, ionisation in air and in dielectrics, and often working with a long (tens of metres) cable run between the DUT and the power and diagnostic apparatus.

In the case of the Omega laser Inertial Confinement Fusion (ICF) neutron tests described in Chapter 6, it was necessary to produce packaged devices starting from the complete wafers supplied by the semiconductor manufacturer, Nexperia. After initial on-wafer testing to establish which wafer fields were most suitable for irradiation studies, wafer sawing was performed in the University of Bristol (UoB) Physics clean room. The sawed out devices were then mounted in dual in-line (DIL) packages, as shown in Figure 3.1. Initially Silver DAG, a compound commonly used for mounting samples for microscopy studies, was used to fix the devices into the packages. However, adhesion between sawed out individual transistors and the packages was insufficient to resist movement during wire bonding. Silver loaded epoxy was used next, and this was found to provide good adhesion without requiring an excessive high temperature during curing. When wire bonding, an appropriate number of bond wires must be placed for the intended current level, and stabilisation capacitors may also be required to prevent device oscillation and self-biasing.

The femto-second laser irradiation technique developed herein, as described in Chapter 7, requires a good optical surface on the backside of the wafer sample. This technique enables irradiation of any region within the semiconductor device, by bringing light to a focus at the device region of interest through the backside of the wafer, creating a high-intensity region where charge generation by TPA will occur. The samples used here for the femto-second laser irradiation work were supplied by the semiconductor manufacturer, IQE, with backside metallisation present. The metal layer forms an RF ground plane, for optimum high frequency operation, and as a side

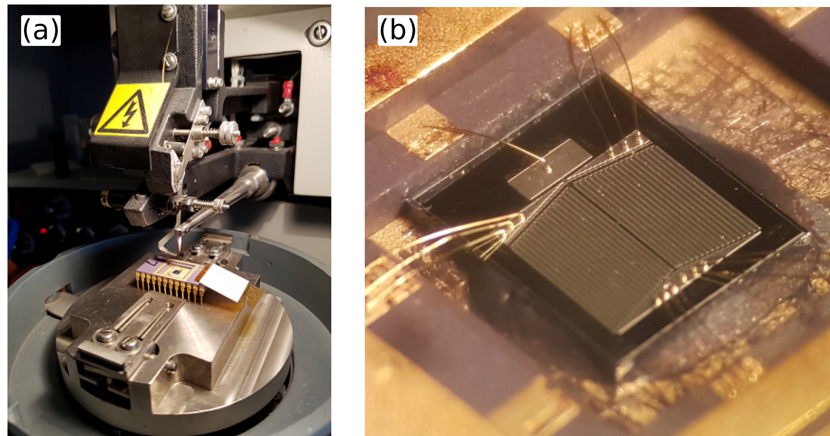

Figure 3.1: Sample packaging and wire bonding. a) Wire bonding connections to an array of HEMTs which have been mounted into a 24 pin DIL package. b) A single GaN-on-Si power HEMT (3 mm side) mounted in an eight pin DIL package showing multiple bond wires placed to the source and drain contacts, and a single bond wire to the gate contact.

effect, it provides some mechanical protection. Backside wafer polishing had been performed to a sufficient degree prior to metallisation of the wafers, so in this case, it was only necessary to remove the metal layer without damaging the optical surface.

Energy-dispersive X-ray spectroscopy (EDX) can be used to determine the composition of metallisation layers, and so to optimise the removal process. In this case, however, the UoB cleanroom EDX system was temporarily unavailable. It is possible to attempt the layer removal by trialling etchants for common metallisation materials until the correct one is found, as was done here. In this case the layer was resistant to etchants for many common metals, and was found to be mechanically very tough as demonstrated by resisting scratching by a stainless steel scalpel. This combination of factors, in the context of a metallisation layer, suggests that it may be formed from tantalum (Ta) or tungsten (W). Having exhausted all milder removal options, a hydrofluoric acid-based solution was used consisting of one part Hydrofluoric acid (HF), one part Nitric acid (HNO_3), and two parts water (H_2O) which worked quickly and left a sufficiently high-quality optical surface for the laser irradiation work to proceed. EDX analysis at a later date of an un-etched region, confirmed the metal layer was tungsten. Thanks are due to Mr Nathan Missault for suggesting the use of the above etching solution, and to UoB Physics Clean Room manager, Dr Andy Murray, for performing the etching.

3.2 Electrical instruments and methods

3.2.1 Parameter analyser Source-Measure Units (SMUs)

The majority of DC electrical testing reported in this work was performed using SMUs within a Keithley Instruments Model 4200 Semiconductor Characterisation System (SCS), also known

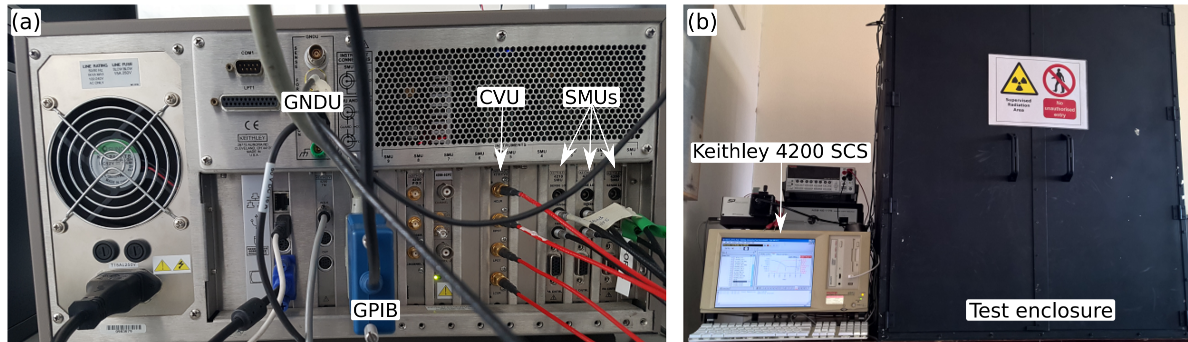

Figure 3.2: Keithley 4200 SCS parameter analyser and test enclosure. (a) Rear connection panel shown with ground unit (GNDU), capacitance-voltage unit (CVU), and source-measure units (SMUs) highlighted. The general purpose interface bus (GPIB) connection was used to enable LabVIEW control of the instrument. (b) front aspect showing a measurement in progress, with a DUT in a light-tight enclosure.

as a parameter analyser (Figure 3.2). SMUs are instruments capable of sourcing a either a current or a voltage, and simultaneously measuring the other. They are capable of high-precision measurements, and are programmable. Measurements were performed by directly programming parameter analysers containing multiple SMUs, and by using instrument control PCs running bespoke LabVIEW programmes.

SMUs are compatible with triaxial cables, enabling guarded measurements to be performed. Guarded measurements apply a voltage to the extra shield in the triaxial cable to match the voltage applied to the centre conductor. This has the effect of reducing the charge stored along the distributed capacitance of the cable. The reduced capacitance reduces the RC time constant of the measurement system, enabling faster measurement settling times. Guarding also reduces leakage currents along the cable centre conductor, which otherwise are present in parallel to the DUT current. Using guarding makes possible the measurement of extremely low currents, approaching femto-ampere level resolution under optimum conditions.

At the other measurement extreme, for the testing of low resistance samples, SMUs also support four-wire Kelvin measurements. This is done through the provision of 'Force' and 'Sense' connections. The Force and Sense connections should ideally both be made directly to the device under test contacts. When an electrical current is being sourced by SMUs, it flows in series through the two Force cable resistances as well as the device under test resistance. Kelvin measurements add a second pair of cables, known as the Sense connections, which are connected to a high resistance volt meter in SMUs. These are connected in parallel to the Force connections at the device under test, as indicated in Figure 3.3. In this manner, the sourced current is known, and the voltage drop across the device under test is known, which enables accurate device resistance measurements in the presence of finite cable resistance. It was necessary to use the Kelvin measurement mode to characterise the Nexperia high current HEMTs used in the Omega

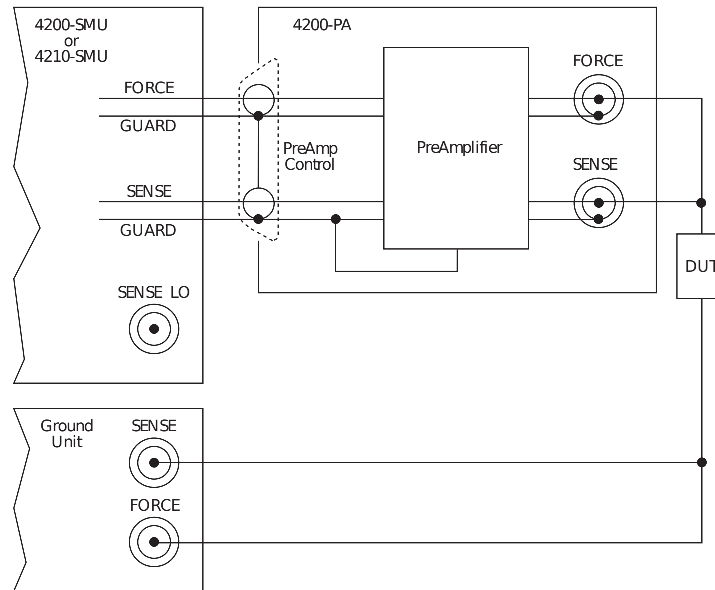

Figure 3.3: Schematic illustrating a DUT to SMU connection in four-wire Kelvin configuration. The arrangement of the guard lines is also shown. An optional pre-amplifier stage is shown, as is necessary for the highest resolution measurements. Reproduced from [71].

laser experiments.

Measurements based on SMUs were used throughout this thesis to characterise DUTs before irradiation, and to measure their properties after irradiation. These measurements typically included threshold voltage, transconductance, various leakage currents, and on-state currents. These were important measurements for understanding material samples and DUTs, and for obtaining parameters used to underpin the more advanced switching and *in situ* transient measurements described in this thesis.

The study of the effects of neutron irradiation on the off-state to on-state switching recovery of HEMTs, described in Chapter 5, was performed using the Keithley SMUs described above. The technique developed in that chapter is based on Current Transient Spectroscopy (CTS). In conventional CTS, HEMT transient current at time t, $I_D(t)$, is used directly to produce a detrapping spectrum to measure relative trap densities and activation energies by employing an underlying assumption that the transients depend on multiple independent trapping processes as described in [72, 73, 74], for example. A further assumption is often made that changes in drain current are directly proportional to the change in trapped charge density in the HEMT. This assumption is incorrect, which can be appreciated by considering that the drain current measured is flowing through not only the channel resistance, but also the contact resistances, and, if Kelvin measurements are not used, then the cable resistances will also be measured in series with these. The result of the extra series resistances is calculated in Chapter 5. In that chapter to further improve the accuracy of the charge trapping measurements a further correction is

applied for the extent of the channel that is probed by the application of an off-state bias. The measurement stability achievable by using the Keithley 4200 SCS SMUs during long current transient measurements across the ms to ks time scales of interest was essential for the study.

3.2.2 High precision LCR meter

An inductance-capacitance-resistance (LCR) meter was used to perform the admittance-based electron mobility studies described in Chapter 4. For those measurements, an Agilient (later Keysight) E4980 Precision LCR Meter was used, as visible at the top left of Figure 3.4. The four connections required for a Kelvin measurement are visible in the figure and are shown connected on the front of the instrument.

The measurements performed using the LCR meter were Alternating Current (AC), spanning a frequency range from tens of Hz up to MHz. The LCR meter was controlled directly for point measurements. However, the electron mobility measurements required testing to be performed across hundreds of different frequencies and bias levels, and so a LabVIEW programme was used to automate the control of the meter for those tests. The principle of operation of the meter is to measure two components of the DUT complex impedance, from which secondary quantities of interest can be calculated. This is achieved by measuring the voltage and current, including phase, in the test circuit. In this work, the parallel capacitance and conductance were measured, and used to determine electron mobility in the 2DEG as described in Chapter 4. The meter was used to apply a simultaneous DC bias to the DUT to enable control for the channel 2DEG density.

3.3 Temperature control

Many semiconductor parameters are temperature-dependent, as described in Chapter 2, and elsewhere in this thesis. Because of this, it is often important to control the temperature of a DUT or material sample during measurement. An environmental test chamber can be used for this purpose. Here, however, temperature control was achieved through the use of either a hot chuck or a cryostat.

3.3.1 Hot chuck

A hot chuck enables the control of DUT temperature, including the application of high temperatures, whilst allowing connecting cables and surrounding instrumentation or connected circuitry to remain at ambient temperature. The temperature dependent measurement work performed early on in this project used a hot chuck. A hot chuck was also used to apply a stable temperature to samples during DC parameter testing, and CTS testing. The hot chuck produced for this work featured a four inch wafer plate, coated with gold to reduce emissivity. The temperature was monitored using a thermocouple built into the chuck. Heating was achieved using cartridge

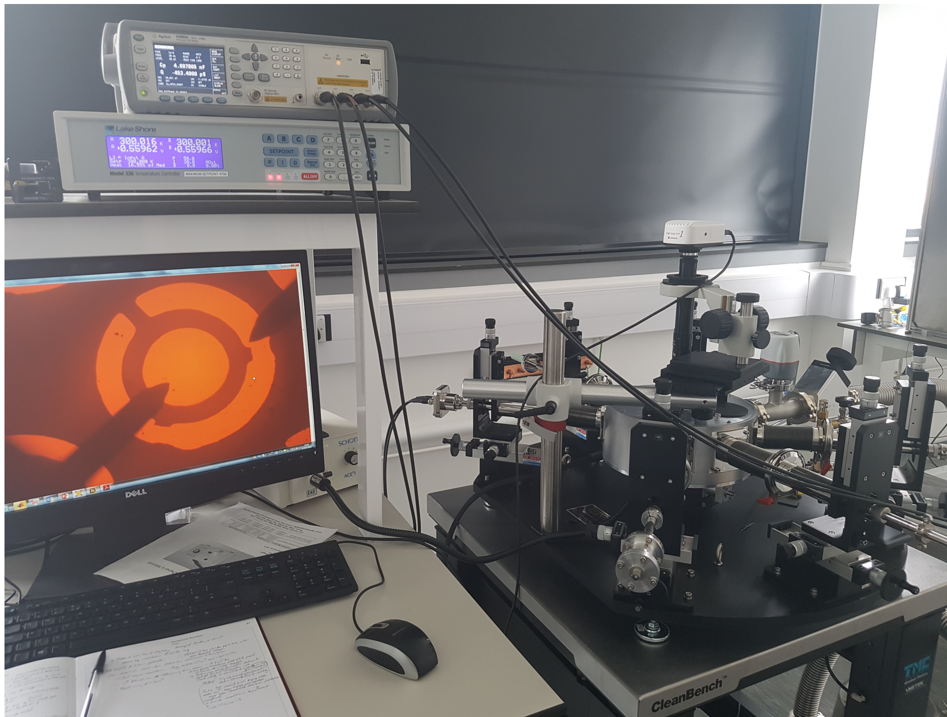

Figure 3.4: The cryostat experimental setup. The LCR meter, temperature controller, imaging system displaying AlGaN/AlGaN disc annulus structure under test, control PC, and cryostat are shown.

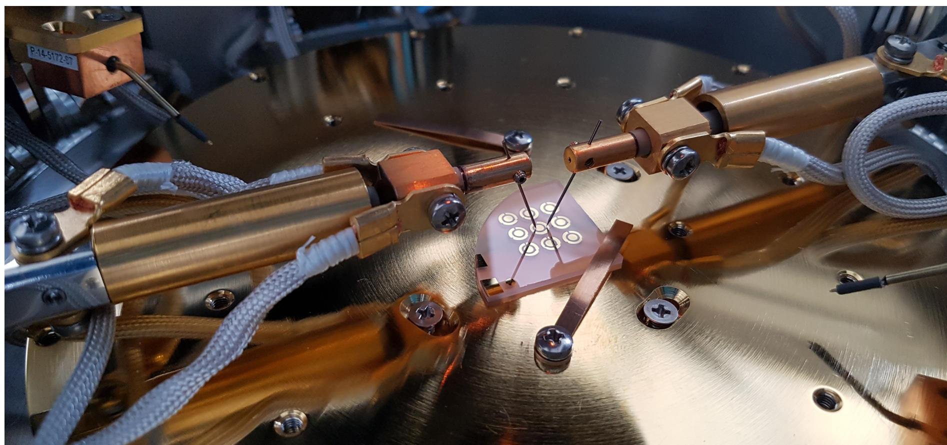

Figure 3.5: Probing arrangement within the cryostat. The Kelvin connection stops at the start of the needle probes. The contacted disc-annulus structure is one of the AlGaN/AlGaN samples used for the mobility study described in Chapter 4.

heaters powered by a Proportional Integral Differential (PID) controller, which was programmed from a PC. This system provided temperature control from ambient up to around 360 Kelvin.

3.3.2 Cryostat

The 80 K to 400 K measurements given in Chapter 4 were all performed in the Janis ST-500 cryostat shown to the right in Figure 3.4. The cryostat was a continuous flow type. It worked by evaporating liquid nitrogen from a Dewar flask, and allowing the cold nitrogen gas to pass through a cold finger in the centre of the cryostat. Heaters were built into the cryostat cold finger, and also into the surrounding enclosure. A PID controller was used to control the heating power dissipated inside the cryostat, and in that manner to control the temperature of the sample.

After samples were loaded into the cryostat and secured in place, the desired probe arms were positioned approximately adjacent to the test samples. The cryostat test chamber was then pumped down to be used at vacuum. The amount of time the chamber was allowed to be at atmospheric pressure was limited to around ten to fifteen minutes. It was found that longer durations caused excessive build up of material from the air onto the internal surfaces of the chamber, which would significantly increase the time taken to pump down to the required vacuum level. Four wire 'Kelvin' probing was desired for the mobility studies to reduce the parasitic effects of the cabling and measurement fixture on the measurements. The probing used is shown in Figure 3.5. It can be seen that the Kelvin connection in the cryostat only goes as far as the end of the probe arm. Beyond that each connection is made with a single needle probe. Measurements were performed using true Kelvin probes at a standard probe station, and compared to the cryostat probing setup. No significant differences were observed between the two.

3.4 Femto-second pulsed laser irradiation

3.4.1 Sample mounting and electrical contacts

The femto-second pulsed laser test setup constructed for the work described in Chapter 7 is shown in Figure 3.6. The sample mounting arrangement is visible in parts (b,c,d) of the figure. In order to be able to simultaneously probe the top side of the wafers under test, whilst irradiating from the rear of the devices through the substrate, the samples were mounted on a 90° mount, as shown in part (c) of the figure. The sample shown in that figure has had part of the back side metallisation removed in order to provide optical access. To bring the microscope focus to the backside of the wafer a 90° mirror cube was mounted onto the microscope column, onto which the objective lens was mounted.

High bandwidth GSG probes were used to contact the HEMTs on the wafers. The probes were mounted onto probe arms also held at 90° to the plane of the microscope stage. The arms were fitted to three-axis mounts which enabled the fine positioning of the probes onto the device contacts. The mounts themselves were fitted with magnetic bases, enabling re-positioning to

Figure 3.6: Pulsed femto-second laser setup constructed for this work. (a) In order of propagation: beam enters at bottom right through half wave plate and Brewster plate assembly for attenuation control. Pulse picker for pulse repetition frequency (PRF) control. Beam sampler diverts small fraction of beam towards photodiode for monitoring. A half wave plate controls the beam polarisation prior entering the first polarising beam splitter. Part of the beam continues into the delay line, and is then recombined with the undelayed part of the beam at the second polarising beam splitter. (b) microscope objective lens mounted on 90° mirror cube. GSG probes mounted on three-axis mounts. Camera for wafer top side imaging is visible at the bottom of the image. (c) wafer in 90° mount positioned for testing. Bias tees and semi-rigid coaxial connections to probes on custom made magnetic microscope stage plate. (d) Enclosure with adjacent instrumentation rack. (e) Setup in use.

the required positions on the custom made microscope stage, which had a thin steel layer to facilitate magnetic mounting. As shown in 3.6 (c,d) the GSG probes were connected via semi-rigid coaxial cables to high bandwidth bias tees. The bias tees were used to pass the DC bias from the programmable Power Supply Unit (PSU) to the HEMT under test, whilst maintaining a high bandwidth 50 Ω characteristic impedance path from the HEMT through to the oscilloscope used to capture the transient signals.

The transient signals from the HEMTs were connected to 50 Ω terminations on the digital storage oscilloscope. This arrangement allowed the transient current to be determined from the measured voltages by simply applying Ohm's law and dividing by 50. Electronic fuses were used in the DC arm of the bias and measurement circuit. In the event of a catastrophic device failure creating a short circuit, the electronic fuses would quickly break the PSU connection to the test circuit, and so would limit the damage caused to probe tips and bias tees.

The motorised stage visible in the figure is a Prior Scientific Proscan III. The stage enabled lateral movement in x and y with a precision of up to 100 nm when using the position encoders. To overcome drift during extended duration measurements, servo control was enabled to maintain the stage at the desired position, with a window set to '1' - smaller values would cause a continuous stage movement due to over-frequent adjustments. Translation in z was achieved by connecting a stepper motor control to the manual focus of the microscope. The enclosure door was fitted with RF gasket seals and painted black to reduce stray reflections. Control of the microscope stage and oscilloscope was achieved with a labVIEW programme produced for this project. The code used a state machine design to enable reliable switching between externally triggered single shot scope capture and continuous monitoring for setup, stage translation, and auto-focus.

3.4.2 Optics

The overall optical system is described in the caption of Figure 3.6. The laser oscillator was a Kerr-lens mode locked model, utilising Yb:KGW (Ytterbium-doped potassium gadolinium tungstate) as the gain medium, pumped by high brightness laser diodes. The laser had a native output Pulse Repetition Frequency (PRF) of around 74 MHz, at a wavelength of 1035 nm, with a nominal Full Width at Half Maximum (FWHM) of 75 fs. A pair of turning mirrors were used to direct the output of the laser into a second harmonic generator, to produce 507 nm light with a pulse energy of the order of nJ. A half wave plate and Brewster plate combination assembly was then used to control the pulse energy propagated down the optical path, and to dump the unwanted energy into a beam dump. The next element of interest in the beam path is the pulse picker. This consisted of a Pockels cell with Glan-laser prism polarisers immediately before and after the cell. The polariser axes were aligned at right angles to one another so that light could not pass through the system. The Pockels cell could then be pulsed to rotate the light reaching through the first polariser it so that it could pass through the second polariser. In this manner the 75 MHz native PRF could be blocked, and a PRF from single shot up to 3 kHz could be passed through

the cell. The dispersion in the optical elements of the pulse picker assembly is expected to have broadened the pulse to around 118 fs. Some further broadening would have been caused from the optical elements which were not specifically low group delay dispersion (GDD) components.

Next, the beam was sampled, for pulse energy measurement purposes, and passed through a beam expander consisting of a pair of lenses of differing focal length. After splitting the beam using a polarising beam splitter, the delayed part of the beam entered the delay stage which consisted of four inwards legs, followed by four outward legs. The relative intensity of the split beams could be controlled using the half wave plate immediately before the beam splitter. The delay stage leg length could be varied up to a maximum of 600 mm. Therefore the maximum delay length available was 8x600 mm, around 16 ns. Next, the beam components were recombined, and the two parts of the beam were directed into the test enclosure. Great care was needed to correctly align the beam expander, delay stage, and recombination aspects of the system. They were then directed into the microscope using a periscope. Laser light could then be focussed on the samples as desired, and monitored using a camera mounted at the top of the microscope.

3.4.3 The influence of vibrations on TPA

The experiment was built onto a bespoke optical table assembly to isolate the system from ambient vibrations such as those due to nearby road traffic. Isolation from vibrations was achieved by floating the table on a cushion of air. Instruments and apparatus on the table needed wired connections to the building to provide electrical power, and for signal and control cables to connect to the laboratory. These cables provide a means for vibrations to couple into the measurement system and affect the stability of the optical arrangement. Also, it was found that the large two part optical table could noticeably oscillate after being touched. Because of the extreme focus sensitivity of TPA, and the irradiation location sensitivity of the DUT response, it is essential to take great care to reduce vibrations as far as practical when performing such measurements.

3.5 Summary

In this chapter a brief summary has been given of the instruments and techniques most frequently used to conduct the work described in this thesis. Sample preparation for test and irradiation was discussed first. This was followed by an overview of the use of SMUs for DC parameter measurement and investigations of charge trapping and switching characteristic using CTS. Admittance measurements using LCR meters were then discussed in the context of the electron mobility measurement technique described later in this thesis. The methods of temperature stabilisation and control used in this work were then introduced. Finally, an overview was given of the optical and electrical aspects of the femto-second pulsed laser irradiation system developed in this thesis to simulate SEEs, to investigate photocurrent response, and to probe device electric field distributions.

CHAPTER 4

MOBILITY IN TWO-DIMENSIONAL ELECTRON GASES

The ultimate performance limits of a semiconductor device, irrespective of its design, can be estimated using figures of merit derived from fundamental properties of the semiconductor material itself. One such property, mobility, μ, is equal to the low-field drift velocity of charge carriers per unit applied electric field. Conventionally the units of μ are $cm^2V^{-1}s^{-1}$. Mobility contributes to the bulk conductivity of a semiconductor ($1/\rho$), as

$$\sigma = q(n\mu_e + p\mu_h) \quad [\Omega/\text{m}] \tag{4.1}$$

where n and p are the free electron and hole densities, μ_e and μ_h are the electron and hole mobilities, and q is the electronic charge. Resistive power losses due to Joule heating are described by $P = I^2R$, and so decrease in proportion to the semiconductor's mobility. When switching electrical currents quickly for radio frequency (RF) applications, the Johnson Figure of Merit (JFoM) can be used to estimate the high frequency electrical power handling capability of the semiconductor (higher number indicates shorter switching delay); it is defined as [75]:

$$\text{JFoM} = \frac{V_{\text{sat}}E_{\text{BD}}}{2\pi} \tag{4.2}$$

where V_{sat} is the saturation velocity of carriers in the material, a property related to mobility, and E_{BD} is the breakdown electric field of the material, a function of the band gap energy (E_G). There is an immediate need for measurements of AlGaN V_{sat} and its dependence on temperature to aid determination of whether AlGaN can perform well in future RF electronic systems [42]. However, due to the current lack of good Ohmic contacts to AlGaN, measurements of V_{sat} remain elusive. The Baliga FoM [43], is used to assess the potential of a material for use as a power switch, particularly for vertical channel high-voltage transistors. The higher the BFoM, the lower the expected power switching losses. It is defined as

$$\text{BFoM} = \epsilon \cdot \mu \cdot E_G^3 \tag{4.3}$$

where ϵ is the permittivity of the semiconductor. A higher semiconductor mobility therefore minimises conduction losses in power FETs.

When considering the best material for lateral HEMT structures, the change in device geometry and the change from bulk conduction to 2DEG conduction, necessitates a different figure of merit. The Baliga figure of merit for HEMTs [24], BFoM(HEMT), is suitable for this purpose. In an ideally optimised HEMT structure, electric field is uniform along the channel between the gate and drain edges. Electrical breakdown will occur when the electric field in the channel equals the critical breakdown field for the material in question. Equating the two fields and re-arranging for channel length gives

$$L_{\mathrm{GD}}(\mathrm{HEMT}) = \frac{V_{\mathrm{break}}}{E_{\mathrm{crit.}}} \tag{4.4}$$

where L_{GD} is the distance from gate edge to drain edge for the breakdown configuration, V_{break} is the potential difference at breakdown between the drain edge and gate edge, and $E_{\mathrm{crit.}}$ is the critical electric field strength that causes breakdown in the material. The contact sizes for the source, gate, and drain are not considered in BFoM(HEMT); drift region resistance only is minimised. In this manner HEMT on-resistance can be written in terms of L_{GD} as

$$R_{\mathrm{on}}(\mathrm{HEMT}) = \frac{L_{\mathrm{GD}}}{q\mu n_{\mathrm{2DEG}} W} \tag{4.5}$$

where W is the HEMT width perpendicular to the gate-drain axis, and n_{2DEG} is the carrier density in the 2DEG channel. Multiplying R_{on}(HEMT) by the surface area of the HEMT produces the specific on-resistance for a material used as a HEMT

$$\begin{aligned} R_{\mathrm{on,sp}}(\mathrm{HEMT}) &= R_{\mathrm{on}}(\mathrm{HEMT}) \times L_{\mathrm{GD}} W \\ R_{\mathrm{on,sp}}(\mathrm{HEMT}) &= \frac{L_{\mathrm{GD}}^2}{q\mu n_{\mathrm{2DEG}}} \\ &= \frac{V_{\mathrm{break}}^2}{q\mu n_{\mathrm{2DEG}} E_{\mathrm{crit.}}^2} \end{aligned} \tag{4.6}$$

The denominator in Equation 4.6 is defined as the BFoM(HEMT):

$$\mathrm{BFoM}(\mathrm{HEMT}) = q \cdot \mu \cdot n_{\mathrm{2DEG}} \cdot E_{\mathrm{crit.}}^2 \tag{4.7}$$

The greater the BFoM(HEMT) value for a material, the better its potential to produce low on-resistance HEMTs. The dependence of BFoM(HEMT) on μ demonstrates the importance of a good understanding of the electron mobility of a material when deciding whether to pursue development of devices based on it.

Given the fundamental role played by electron mobility in the effectiveness of semiconductor devices, it important to understand how it varies in response to the environmental conditions such devices are exposed to. As discussed in Chapter 2, electron drift mobility is limited by scattering

due to ionised impurity scattering, and particularly for AlGaN and GaN, polar optical phonon scattering, both of which vary with temperature. Understanding how mobility in a material varies with temperature, and changes following irradiation, can be used to help predict how devices made from it could perform in real applications.

In this chapter, we see how a technique was developed to measure mobility in an ultra-wide band-gap semiconductor system without using Ohmic contacts. The material system used was the heterojunction formed at the interface of two AlGaN alloys (AlGaN-AlGaN), with differing aluminium content. This enables the mobility of a given epitaxy to be measured without having to first develop optimised Ohmic contacts to that particular material. In doing so we are able to see how mobility varies with carrier density in the channel, shedding light on the mechanisms that limit it. This also provides insight into the near threshold regime, where channel carrier density is low, and mobility can limit switching speeds and transconductance. Building on that work it will be shown that the mechanisms limiting mobility can vary when epitaxial design is altered. We will then see how mobility is affected by temperature, an important consideration from device power density and operating environment perspectives. Finally, we see how 14 MeV neutron irradiation to a fluence less than that at which mobility changes would be expected, can alter the shape of the mobility-channel density curve, depending on the details of the semiconductor epitaxy. This is a potentially useful indicator of the performance of future AlGaN-based devices in radiation environments. The effect of neutron irradiation on mobility in compound semiconductor systems is not yet fully understood. As summarised in [76], because damage constants for carrier removal or lifetime degradation are typically higher than damage constants for mobility reduction, typically changes in mobility due to displacement damage are not observed until after changes in carrier density occur.

This chapter contains significant amounts of material reproduced and expanded from my published work [77]. Additional results are also provided, including the temperature and neutron effects studies, which have not yet been published elsewhere.

4.1 Sample details

The device structures studied in this chapter were produced and kindly supplied by Sandia National Laboratories (SNL), Albuquerque, USA. They consisted of Schottky contacts (gold on platinum), deposited by electron-beam evaporation on to ultra-wide band-gap aluminium gallium nitride / aluminium gallium nitride (AlGaN/AlGaN) heterostructures. The Schottky contacts were deposited in the form of a disc and surrounding annulus, designed in conjunction with collaborators at SNL. The AlGaN/AlGaN heterostructures consisted of a barrier layer grown on top of a buffer layer with a narrower band gap, regrown on an AlN/sapphire template. Three samples were produced by SNL; the details of their epitaxies are given in Table 4.1. Sample 1 was received first from SNL and was used to develop the Ohmic contact-free mobility measurement

Sample No. SNL ref.	1 VNA5073	2 VNA5495	3 VNA5677
contacts	100nm Au, 10nm Pt	100nm Au, 10nm Pt	100nm Au, 10nm Pt
barrier thickness	40 nm	50 nm	100 nm
barrier composition	$Al_{0.85}Ga_{0.15}N : Si \approx 10^{18}\,cm^{-3}$		$Al_{0.9}Ga_{0.1}N \rightarrow AlN$
buffer thickness	550 nm	330 nm	400 nm
buffer composition	UID $Al_{0.7}Ga_{0.3}N$		UID $Al_{0.9}Ga_{0.1}N$
substrate	AlN on sapphire		
disc radius	$840\,\mu m$		
annulus inner	$1240\,\mu m$		
annulus outer	$1760\,\mu m$		

Table 4.1: Table containing details of the epitaxy of each mobility test sample. Note: UID = unintentionally doped.

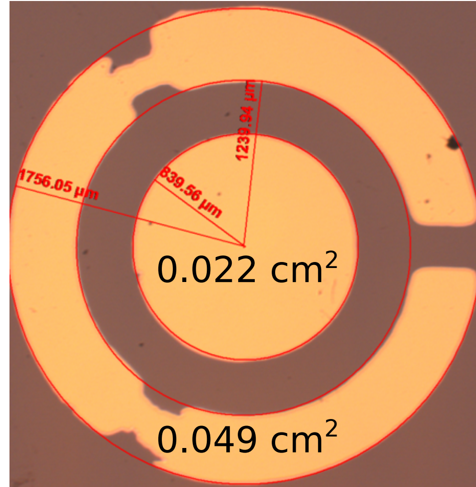

Figure 4.1: Micrograph of a Schottky disc contact and the surrounding annulus contact deposited on the AlGaN/AlGaN material, which was re-grown on an AlN/Sapphire template. Radii and areas are as indicated.

technique described in [77]. The key differences between the samples, detailed in the table, are that Sample 2 had a thicker barrier and thinner buffer than Sample 1, and Sample 3 had a barrier with a composition that varied linearly with depth from $Al_{0.9}Ga_{0.1}N$ at the surface, changing to AlN at the heterointerface. A micrograph of a test structure is shown in Figure 4.1, a schematic representation of the Sample 1 epitaxy can be seen in Figure 4.2, and a photograph of one of the disc-annulus structures being electrically contacted is visible in Figure 3.5.

4.2 Ohmic contact-free mobility measurement

In this section we see how an AC admittance-based technique was developed to enable the measurement of mobility in heterostructures without the need to first form Ohmic-contacts. This

was needed because Ohmic contact formation in ultra-wide band-gap semiconductors remains difficult, making FET based mobility measurements challenging. The developed technique was used to determine the channel sheet charge density dependence of electron mobility in the two-dimensional electron gas (2DEG) formed at the interface of two ultra-wide band-gap aluminium gallium nitride (AlGaN) alloys of differing molar aluminium composition. Sample 1, detailed in Table 4.1 was used to develop this technique.

The established methods conventionally used to determine the channel sheet charge density dependence of mobility in devices are typically DC in nature, and include field effect mobility and Hall mobility [78]. Such techniques are often limited to measuring mobility in the unbiased case, i.e. at one carrier density, or over a narrow range of carrier density. Gated Hall techniques have been used to measure mobility in AlGaN/GaN structures over almost a decade span of carrier density. For example, Manfra *et al.* [79] used an insulated gate AlGaN/GaN heterostructure to measure mobility from $2\times10^{11} - 2\times10^{12}$ cm^{-2}. They found that $\mu \propto n_{2DEG}$, due to scattering from charged dislocations limiting mobility [80]. The gated Hall measurement used by Manfra *et al.* required insulated gate Hall bars to be fabricated, and a magnetic field applied. In contrast, gate admittance techniques [81] provide mobility data over a much wider carrier density range, using simpler test structures and equipment. The technique that was developed for this work is suitable for use in characterising mobility in semiconductor materials, and requires only Schottky metal deposition.

Developing this Ohmic-contact-free mobility measurement technique enabled the extraction of the 2DEG mobility in an UWBG device (Sample 1), from the weak inversion regime through to the strong inversion unbiased case for the first time. In this context, strong inversion refers to the state where a 2DEG is present within a nominally p-type buffer, effectively creating an n-type region at its position. Weak inversion refers to the sub-threshold regime, where the 2DEG density is very low. Testing was performed over a temperature range spanning 25 °C to 75 °C. The results of those tests, when considered along with the 2DEG density dependence measurements, indicated that alloy scattering was the dominant mobility limiting mechanism at high channel carrier densities.

4.2.1 Experimental details

An Agilent E4980A Precision LCR Meter was used to measure the parallel capacitance and conductance of the disc-annulus test structure, with the annulus as the ground reference side and the oscillating bias applied to the disc contact. To mitigate against the effects of electrical parasitic elements, including stray capacitances, a four point Kelvin measurement was used whereby the disc and annulus Schottky contacts were simultaneously contacted with two probes each. Open and short calibrations of the measurement system were performed including the four point probes in place. This approach removed the effect of cabling and probes from the data, enabling accurate $C_P - G$ measurement over the wide frequency range used. Admittance-

frequency curves were measured from 20 Hz up to 2 MHz at each disc voltage (V_{disc}), with an oscillation magnitude of 20 mV. V_{disc} was varied from 0 V to -8 V. The measured threshold voltage for the disc-annulus structure was approximately -7 V. It was assumed that the true threshold voltage for the heterostructure is within a few hundred mV of that value, once the small voltage drop across the forward biased annulus Schottky diode is subtracted. The full admittance-frequency-voltage ($Y-f-V$) measurement was repeated at wafer chuck temperatures increasing from 25 °C, in 10 °C increments, to 75 °C.

4.2.2 Determining 2DEG mobility using an equivalent circuit model

To enable the extraction of 2DEG mobility from the $Y-f-V$ measurements described above, an equivalent circuit model of the disc-annulus test structure as deposited on the AlGaN/AlGaN heterostructure was developed, shown in Figure 4.2. The model presented here expands and further develops the equivalent circuit model for a fatFET previously developed by Waller *et al.* to study mobility in HEMTs [81]. The admittance-based method uses the lateral resistance and charge density of the 2DEG to extract mobility and is especially sensitive to the device threshold and sub-threshold regions. In [81] Ohmic contacts were used for the source and drain of the fatFET. In contrast, the electrical biasing used to test the disc-annulus Schottky contact structures in the present work means that the disc and annulus components of the structures will act as two back-to-back diodes. In this representation the disc contact would always be reverse biased, whereas the annulus contact would be forward biased. This ensures that the annulus contact diode would have a constant voltage drop across it, providing a fixed capacitance, $C_{Annulus}$, enabling the use of the model shown in Figure 4.2. Following on from this, the method presented here differs from that reported in [81] by the addition of the series capacitance term to represent the annulus Schottky contact, $C_{Annulus}$, a resistance to represent the un-gated channel R_{Access}, and modification to the admittance of each element to account for the circular geometry of the test structure. By showing that the slow traps present close to the AlGaN/GaN channel were unaffected by the channel electron density, whereas interface trap characteristic times are inversely proportional to channel density, Silvestri *et al.* [82], and Waller *et al.* [81] demonstrated that there was an insignificant AlGaN/GaN heterojunction interface state density. Because of those demonstrations it is assumed here that there are no interface states at the AlGaN/AlGaN heterojunction. There are likely to be bulk traps in the AlGaN barrier, which may add a background contribution to the admittance under reverse bias, however their distorting effect on G/ω-f peak positions, discussed below, is expected to be minimal.

To find the mobility in the 2DEG of a sample by using the model shown in Figure 4.2 and described above, it is necessary to determine the relationships between the elements of the model and the measured quantities. $C_{annulus}$ was calculated from the unbiased 20 Hz disc-annulus capacitance measurement by considering the series combination of the two components. Because the permittivity, ϵ, and separation between conductors, d, is the same for both the disc and

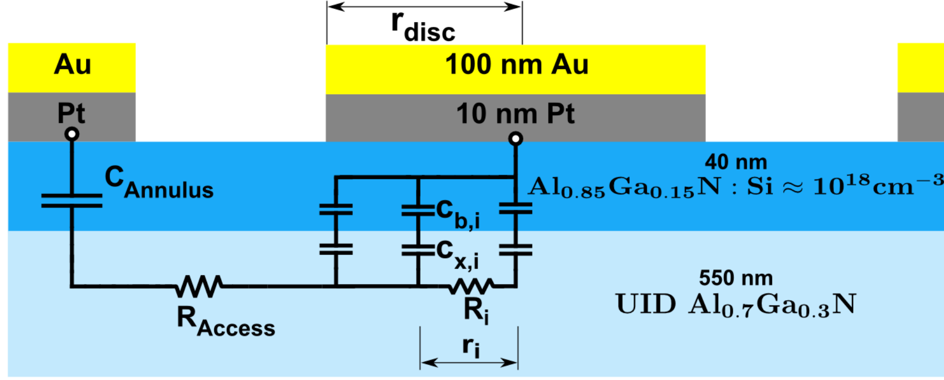

Figure 4.2: Schematic of the equivalent circuit used to model the AlGaN/AlGaN Schottky contact disc-annulus structures. The disc is modelled as a distributed lateral complex impedance constructed from finite elements, each consisting of a resistance, R_i, connected in parallel with a series combination of capacitances due to: the barrier (C_b), and the interface-2DEG distance and the density of states (C_x). Annulus area was 2.2x larger than disc area. Reproduced from [77].

annulus capacitors, an effective area for the series combination can be found using the areas of the two contacts:

$$\begin{aligned}\frac{1}{C_{measured}} &= \frac{1}{C_{disc}} + \frac{1}{C_{annulus}} \\ \frac{d}{\epsilon A_{effective}} &= \frac{d}{\epsilon A_{disc}} + \frac{d}{\epsilon A_{annulus}} \\ \frac{1}{A_{effective}} &= \frac{1}{A_{disc}} + \frac{1}{A_{annulus}}\end{aligned} \tag{4.8}$$

$C_{annulus}$ can then be found from the capacitance per unit area as follows.

$$\begin{aligned}\frac{C_{annulus}}{A_{annulus}} &= \frac{C_{measured}}{A_{effective}} \\ C_{annulus} &= C_{measured} \times A_{annulus} \times \left(\frac{1}{A_{disc}} + \frac{1}{A_{annulus}}\right)\end{aligned} \tag{4.9}$$

The equivalent circuit model can now be considered as the series combination of three impedances, with the total impedance given by

$$Z_{total} = Z_{annulus} + Z_{access} + Z_{disc} \tag{4.10}$$

where $Z_{annulus}$, due to $C_{annulus}$, is purely capacitive and assumed to be constant over the measurement voltage and frequency range (i.e. a high density 2DEG is always present under the annulus). Z_{access}, due to R_{access}, is purely resistive, with a resistance determined by the device geometry and the mobility in the channel, discussed further below. Z_{disc} is due to the distributed lateral resistance and capacitance elements illustrated in Figure 4.2.

To construct the impedance of the Schottky contact disc, Z_{disc}, the capacitance of each element of that region is taken to be comprised of three capacitances in series as outlined in [83]: (i) the fixed capacitance due to the barrier itself, $C_{barrier}$; (ii) an additional fixed capacitance due to the separation (set at 1 nm) of the 2DEG from the AlGaN/AlGaN interface, $C_{separation}$; (iii) the capacitance from the 2DEG density which is limited by the finite electronic density of states, C_{DOS}, calculated using

$$C_{DOS} = A_i \times q \times n_{2DEG} / \frac{2kT}{q} \tag{4.11}$$

where A_i is the area of the ith element, and n_{2DEG} is the 2DEG density. This final capacitance is due to the change in charge in the 2DEG as the applied voltage shifts the Fermi level [84]. When first fitting experimental data, described below, careful inspection of the $G_p/\omega - f$ curves confirmed that it was necessary to apply the factor of 2 in Equation 4.11 for the strong inversion region, changing to 1 in weak inversion where the 2DEG density is insufficient to screen the electric field [85]. The capacitance per unit area due to (ii) can be found from

$$C_{separation} = \frac{\epsilon_0 \epsilon_r}{d_{2DEG}} \tag{4.12}$$

where d_{2DEG} is the separation of the 2DEG from the interface. Here the electrical permittivity of $Al_{0.85}Ga_{0.15}N$ was determined following the linear interpolation given as Equation 54 in [44], $\epsilon_{AlGaN}(x) = 0.03x + 10.28$. When the disc-annulus structure is unbiased the capacitance due to the barrier itself, $C_{barrier}$ (i), will be much smaller than C_{DOS} and $C_{separation}$, because of the large n_{2DEG} and small d_{2DEG} in that case. $C_{barrier}$ will dominate the series combination of the three components, and so can be found from the unbiased 20 Hz capacitance measurement as

$$C_{barrier} = C_{measured} \times A_{disc} \times \left(\frac{1}{A_{disc}} + \frac{1}{A_{annulus}} \right) \tag{4.13}$$

To calculate R_i we note that the resistance of a cuboid, $R = \frac{\rho l}{w \cdot h}$, where ρ is the resistivity, l is the length of the cuboid in the direction of current flow, and w and h are the width and height of the face of the cuboid normal to the direction of current flow. In the case of conduction in a 2DEG channel it is reasonable to assume that h will be fixed for a given epitaxy, and so to define a sheet resistance as $R_{sheet} = \frac{\rho}{h}$. In the circular geometry under consideration each finite element will have an annular profile, with inner and outer radii, r_1 and r_2. In the limit $r_2 - r_1 = dr \to 0$, the width of the annuli is given by $2\pi r_1$, and the length by dr. The resistance of each infinitesimal annular ring element is then given by $R_{ring} = \frac{R_{sheet}}{2\pi r} dr$. The resistance of each annulus element can then be found by integrating with respect to r.

$$\begin{aligned} R_i &= \frac{R_{sheet}}{2\pi} \int_{r_1}^{r_2} \frac{1}{r} \cdot dr \\ &= \frac{R_{sheet}}{2\pi} [\ln(r)]_{r_1}^{r_2} \\ &= \frac{R_{sheet}}{2\pi} \ln\left(\frac{r_2}{r_1}\right) \end{aligned} \tag{4.14}$$

R_{access} was found similarly by substituting the annulus inner radius and disc radius for r_2 and r_1, respectively.

Finally, R_{sheet} was taken to be $\frac{1}{\mu Q}$, where Q is the areal carrier density (n_{2DEG}), and μ is the channel mobility. Q was determined for each V_{disc} value in the $Y-f-V$ measurement by integrating the $C_{disc}-V$ curve formed from the 20 Hz capacitance measurement from below threshold to the bias point in question, after subtracting the capacitance of the annulus. The only free parameter in the equivalent circuit model described above is therefore 2DEG mobility, μ.

Conductance, when plotted as $\frac{G}{\omega}$ against f displays a characteristic peak for each V_{disc} tested, as shown in Figure 4.3. To fit the equivalent circuit model to the measurement data obtained from the real device structure, an optimisation target is required. The position of the peak in the measured $G_p/\omega-f$ curve was chosen as the optimisation target because it represents the characteristic time constant of the equivalent RC circuit. The peak position was found by fitting a centre of mass weighting function, a Gaussian in $\ln(\omega)$, to the data, rather than simply taking the ω value associated with the maximum G_p/ω data point. The advantage of this approach is that reduces the quantization of the fitted ω value, and the subsequently determined μ value, due to the finite spacing of measurement points in the $G_p/\omega-f$ curves. A Gaussian function was chosen for computational efficiency in fitting the peak region of the model and data; it does not form part of the physical impedance model. Each tested $V_{disc-annulus}$ value corresponds to a different channel carrier density, n_{2DEG}, and produces a different $G_p/\omega-f$ curve which must be fitted to determine mobility at that bias point.

Having determined the optimisation targets, the next task is to fit the model to each $G_p/\omega-f$ curve. This requires the $G_p/\omega-f$ curves for the model to be constructed to correspond to each measured $V_{disc-annulus}$ value. The conductance of the equivalent circuit model, G_p, can be found by taking the real part of the admittance of the model; where the admittance is given by $Y=\frac{1}{Z_{total}}$. As described above, Z_{total} is found from its constitutive impedances using the per unit area values for $C_{barrier}$, $C_{separation}$, and C_{DOS}, along with Z_{access} and R_{sheet}. Z_{access} and R_{sheet} depend on μ. μ is expected to be constant in the access region for a given temperature, but will vary under the disc contact depending on n_{2DEG}. A Matlab computer programme was used to automate the fitting procedure. In addition to the parameters discussed above, a starting guess for μ was required as input to the programme. Numerical tests showed that the initial guess was not a critical parameter determining the final fitted mobility values.

Using the equivalent circuit model shown in Figure 4.2, Z_{total} was calculated for each frequency tested. Z_{disc} was constructed iteratively from parallel capacitance elements ($C_{b,i}$ and $C_{x,i}$ in series) and series resistances (R_i), corresponding to the described physical models, and using the starting guess for μ to calculate the initial estimate of Z_{total}. The first element of Z_{disc} is found using the impedance of a capacitance to represent a small contact area at the centre of the disc. Its radius was small compared to r_{disc}, and set equal to that added by each successive surrounding annular element. The impedance for the disc as a whole was iteratively constructed with every

new surrounding annular capacitance combined in parallel with the series combination of the previous impedance and the new annular R_i element. The iterative formula used is described by

$$Z_{\mathrm{disc},i+1} = \left[\frac{1}{Z_{\mathrm{disc},i} + R_{i+1}} + i\omega C_{\mathrm{disc}}\pi\left(r_{\mathrm{i+1}}^2 - r_{\mathrm{i}}^2\right)\right]^{-1} \tag{4.15}$$

where the denominator in the quotient to the left of the addition sign represents the series combination of the inner impedance and the new element of sheet resistance, $R_{i+1} = \frac{R_{\mathrm{sheet}}}{2\pi}\ln\left(\frac{r_{i+1}}{r_i}\right)$. The expression to the right of the addition sign represents the reciprocal of the impedance presented by the new parallel capacitance element. C_{disc} is the capacitance formed by the series combination of per unit area expressions for C_{barrier}, $C_{\mathrm{separation}}$, and C_{DOS}. Iteration continues until the required number of elements has been added to represent the disc contact using the chosen element size. The element size was set to $1\,\mu$m because numerical testing showed that reducing the element size further did not improve the fit of the model to the data, or significantly alter the calculated μ values.

By using the iteratively constructed Z_{disc} value for each frequency, an initial value for Z_{total} was determined, allowing a $G_{\mathrm{p}}/\omega - f$ curve for the equivalent circuit model to be constructed, as described above. The peak in the model $G_{\mathrm{p}}/\omega - f$ curve was determined as described. The Matlab fitting algorithm then used the logarithm of the ratio of the peak positions for the measured and model curves as the optimisation target to be minimised. After each iteration of the fit, the μ value used to calculate Z_{disc} was adjusted to reduce the difference between the peak positions of the two curves. A model $G_{\mathrm{p}}/\omega - f$ curve peak at a higher frequency than measured experimentally would prompt a reduction in the μ value guess, and vice versa. A new Z_{total} was then calculated, and the test repeated. This process was continued until the required tolerance was achieved, set as $\log(f_{\mathrm{measurement}}/f_{\mathrm{model}}) \leq 0.001$, or until the maximum number of iterations, set at 100, had been reached. In Figure 4.3, optimised model curves can be seen to fit the data well for much of the measured $\frac{\mathrm{G}}{\omega}$ against f curves, and particularly near the peaks, of greatest importance for determining mobility. The entire procedure was repeated to find μ at each V_{disc} value, and at each temperature.

4.2.3 Channel density-dependent mobility of Sample 1

By taking the data in Figure 4.3 and fitting the equivalent circuit model using the algorithm described above, a peak mobility value of $(154.6 \pm 0.1)\,\mathrm{cm^2/Vs}$ at 25°C, at $n_{\mathrm{2DEG}} = 5.1 \times 10^{12}\,\mathrm{cm^{-2}}$ corresponding to a voltage drop of -2.95 V across the barrier was determined for Sample 1. The complete set of mobility values determined by the fitting procedure for the 25 °C measurement is shown in Figure 4.4 as a function of channel carrier density, n_{2DEG}. Hall mobility measurements conducted by SNL using large area indium contacts, corresponding to the unbiased case on the same wafer, determined values of $135\,\mathrm{cm^2/Vs}$ at $9.9 \times 10^{12}\,\mathrm{cm^{-2}}$. Contactless sheet resistance measurements, also performed by SNL, using a Lehighton instrument and Hg-probe C-V measurements, again for the unbiased case, found $180\,\mathrm{cm^2/Vs}$ at $9.8 \times 10^{12}\,\mathrm{cm^{-2}}$. For comparison, the

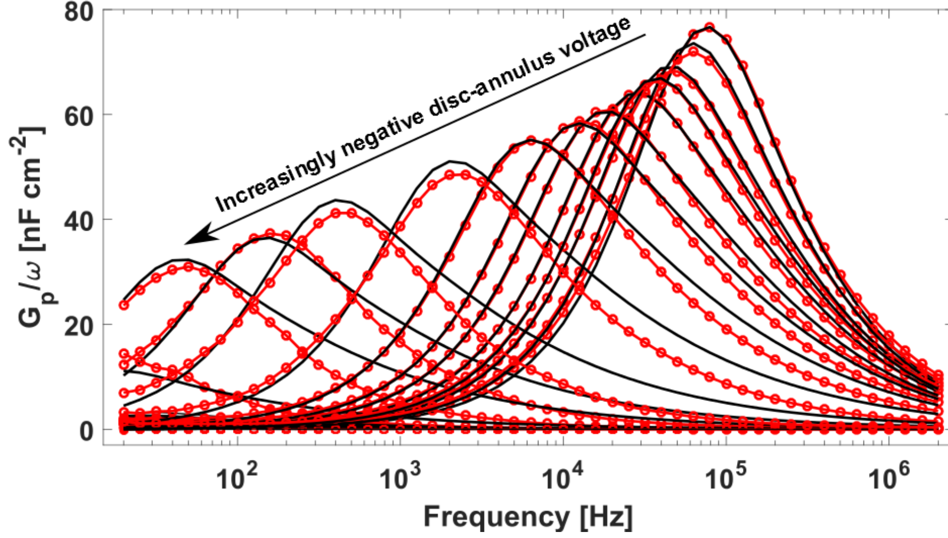

Figure 4.3: Sample 1 G_p/ω vs. frequency for a subset of the disc voltages tested. The disc voltage was decreased from 0 V to -8 V in 50 mV steps. Model conductance curves (black lines) are constructed using the mobility found by fitting the experimental data (red circles). Reproduced from [77].

Ohmic contact-free measurement method described here measured a mobility of $(122 \pm 3)\,\mathrm{cm^2/Vs}$ at $9.51 \times 10^{12}\,\mathrm{cm^{-2}}$ for the unbiased case. The discrepancy of around 10% between the conductivity mobility found using the admittance-based Ohmic contact-free measurement method, and the mobility found using the Hall method, can be plausibly attributed to the Hall factors [86], r_H, for GaN and AlN, where $\mu_{\text{Hall}} = r_H \mu_{\text{conductivity}}$. The mobility determined using the Lehighton instrument and Hg-probe C-V, however, differs by around 50% from the admittance-based method described here. Given that small differences may have arisen due to barrier thickness variations between the different wafer locations that each sample was taken from, and the impact of any voltage drop across the annulus, the values may be considered to be broadly in agreement.

As shown in Figure 4.4, for densities below $10^{10}\,\mathrm{cm^{-2}}$ the mobility becomes density independent at $(4 \pm 3)\,\mathrm{cm^2/Vs}$ due to the inability of the electrons in weak inversion to screen the scattering centres. The transition from strong- to weak-inversion occurred for carrier densities around $3 \times 10^{10}\,\mathrm{cm^{-2}}$. This point was estimated by finding the n_{2DEG} value corresponding to when the generated model $G/\omega - f$ curves using the weak-inversion expressions for C_{DOS} produced a better fit to the measured data than the model using the strong-inversion expression. The mobility then increases with increasing carrier density, following $\mu \propto n_{\text{2DEG}}^{0.88\pm0.02}$ from $10^{11}\,\mathrm{cm^{-2}}$ up to around $10^{12}\,\mathrm{cm^{-2}}$. This is consistent with scattering by ionised defects being dominant in weak inversion, and then increasingly screened by the carrier concentration in the channel as it is increased towards strong inversion. This power law has been found by empirical observations [79, 80] and by a theoretical treatment based on the solution of the Boltzmann equation [87], which found $\mu_{\text{ion}} \propto {n_{\text{2DEG}}}^b$ with b between 0.5 and 1.5. The $b = 0.5$ dependence is expected where

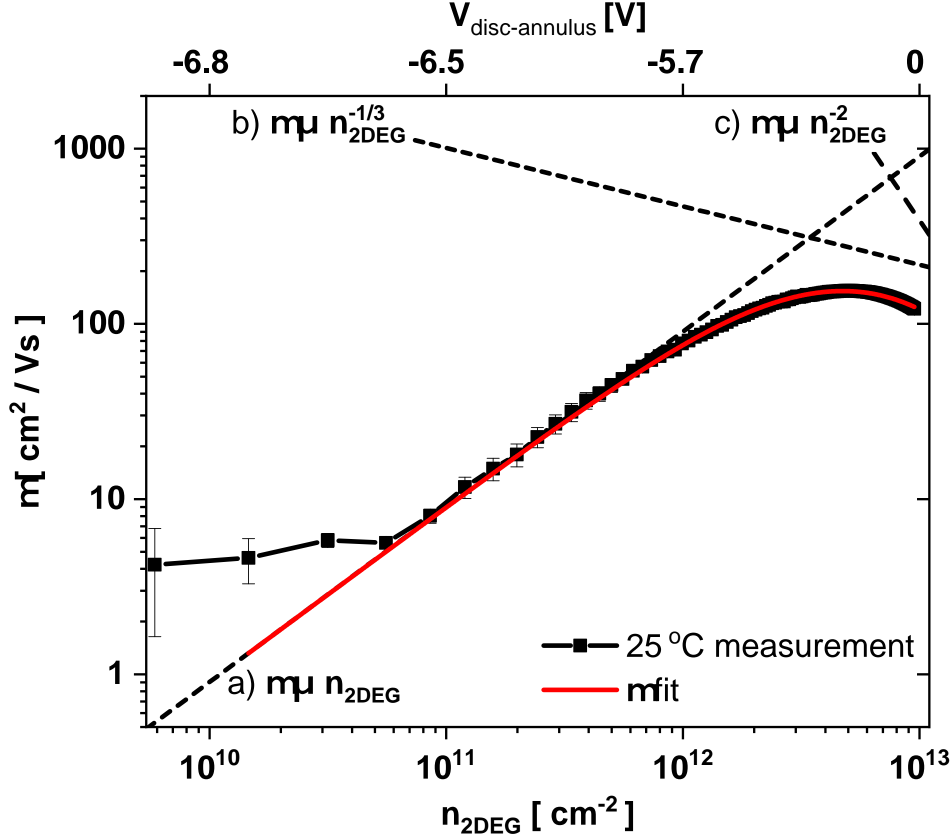

Figure 4.4: Mobility as a function of n_{2DEG} measured for Sample 1 at 25 °C. The kink near 5×10^{10} cm^{-2} is due to the change in expression for semiconductor capacitance used in weak and strong inversion regimes. Dashed lines represent mobility due to a) ionised defect scattering, b) alloy scattering, c) interface roughness scattering. The red line is a fit to the data of a function of a), b), and c) combined using Matthiessen's rule. The upper x-axis shows the values of $\text{V}_{\text{disc-annulus}}$ which correspond to each decade of n_{2DEG}. Adapted from [77].

scattering centre areal concentration equals n_{2DEG}, whereas the $b = 1.5$ dependence is expected when n_{2DEG} is independent of scattering centre concentration.

The mobility reaches a maximum at $\approx 5 \times 10^{12}$ cm^{-2} before falling. The mobility in this regime is expected to become limited by alloy scattering which varies as $n_{\text{2DEG}}^{-1/3}$ [87], since barrier and buffer materials are ternary alloys. Increasing n_{2DEG} also moves the charge distribution closer to the interface, increasing its limiting effect on mobility which is expected to scale as $\mu \propto n_{\text{2DEG}}{}^{-2}$ [88]. Summing ionised defect scattering, alloy scattering, and interface roughness via Matthiessen's rule produced an excellent phenomenological fit to the data, as shown in Figure

4.4. The function used to fit the mobility data is given by

$$\begin{aligned}\frac{1}{\mu} &= \frac{1}{\mu_{\text{ion}}} + \frac{1}{\mu_{\text{alloy}}} + \frac{1}{\mu_{\text{interface}}} \\ &= \frac{1}{a_1 n_{2\text{DEG}}} + \frac{1}{a_2 n_{2\text{DEG}}{}^{-1/3}} + \frac{1}{a_3 n_{2\text{DEG}}{}^{-2}}\end{aligned} \tag{4.16}$$

where $a_1 = 9.03 \times 10^{-11}$ [$\text{cm}^2\text{V}^{-1}\text{s}^{-1} \cdot \text{cm}^2$], $a_2 = 4.69 \times 10^6$ [$\text{cm}^2\text{V}^{-1}\text{s}^{-1} \cdot \left(\text{cm}^{-2}\right)^{1/3}$], and $a_3 = 3.90 \times 10^{28}$ [$\text{cm}^2\text{V}^{-1}\text{s}^{-1} \cdot \text{cm}^{-4}$]. The mobility values due to each scattering mechanism are shown by the dashed lines in Figure 4.4. Using equation 2.16 with $m_e^* = 0.36 m_e$, the average time between scattering events at $n_{2\text{DEG}} = 5 \times 10^{12}\,\text{cm}^{-2}$ is found to be $\tau \approx 3 \times 10^{-10}\,\text{s}$.

The fit suggests that between 1×10^{12} and $7 \times 10^{12}\,\text{cm}^{-2}$ alloy scattering reduces the rate of increase of mobility with $n_{2\text{DEG}}$, but at higher concentrations interface roughness rapidly limits mobility. Removing the fitted interface roughness term suggests that a peak mobility of 177 cm^2/Vs at 7.8×10^{12} cm^{-2} could be obtained with increased interface smoothness.

The temperature dependence of the mobility is shown in Figure 4.5. The inset shows that peak mobility decreases as $\mu \propto \text{T}^{-0.86\pm0.01}$ over the temperature range tested. Electron scattering in semiconductors has a stronger temperature dependence of $\mu \propto \text{T}^{-1.5}$ [89] when dominated by acoustic phonons. On the other hand, in semiconductor heterostructures formed from Wurtzite GaN/AlGaN where conduction occurs in a GaN channel, polar-optical phonon scattering can be the dominant factor limiting mobility near room temperature [90, 91]. However, in the $\text{Al}_{0.85}\text{Ga}_{0.15}\text{N}$ / $\text{Al}_{0.7}\text{Ga}_{0.3}\text{N}$ heterostructures considered here, the conducting channel is located near the heterointerface within a ternary alloy, $\text{Al}_{0.7}\text{Ga}_{0.3}\text{N}$.

In a group III-V ternary alloy, the periodicity of the native binary lattice is disrupted by the substitution of the second species of group III atoms at random sites within the material. Harrison and Hauser considered alloy scattering in ternary group III-V compounds by using a pseudo-binary alloy model, where the structural properties of the material are determined by the relative concentrations of the two different species of group III atoms within the ternary alloy [92]. In the model, Warren-Cowley order parameters are used to describe the amount of disorder present due to the two different species of group III atoms. The scattering potential is then determined by using Mott's 'inner-potential' model [93], where an electron moving within a semiconductor experiences a change in potential only if it passes within the Wigner-Seitz cell of an atom from the second species of group III atoms. The resulting model calculation showed a $\tau \propto \text{T}^{-0.5}$ dependence for ternary III-V compounds, giving $\mu_{\text{Alloy}} \propto \text{T}^{-0.5}$ after Equation 2.16. The model also shows that alloy scattering due to the altered periodicity of the lattice depends on alloy composition, $\text{Al}_\text{x}\text{Ga}_{1-\text{x}}\text{N}$, as

$$\mu_{\text{Alloy}} \propto \frac{1}{x(1-x)} \tag{4.17}$$

which has a maximum mobility-limiting effect at $x = 0.5$, and would therefore be expected to be present for the $x = 0.7$ channel composition used here. It is noteworthy that a $\mu_{\text{Alloy}} \propto \text{T}^{-0.7}$ to

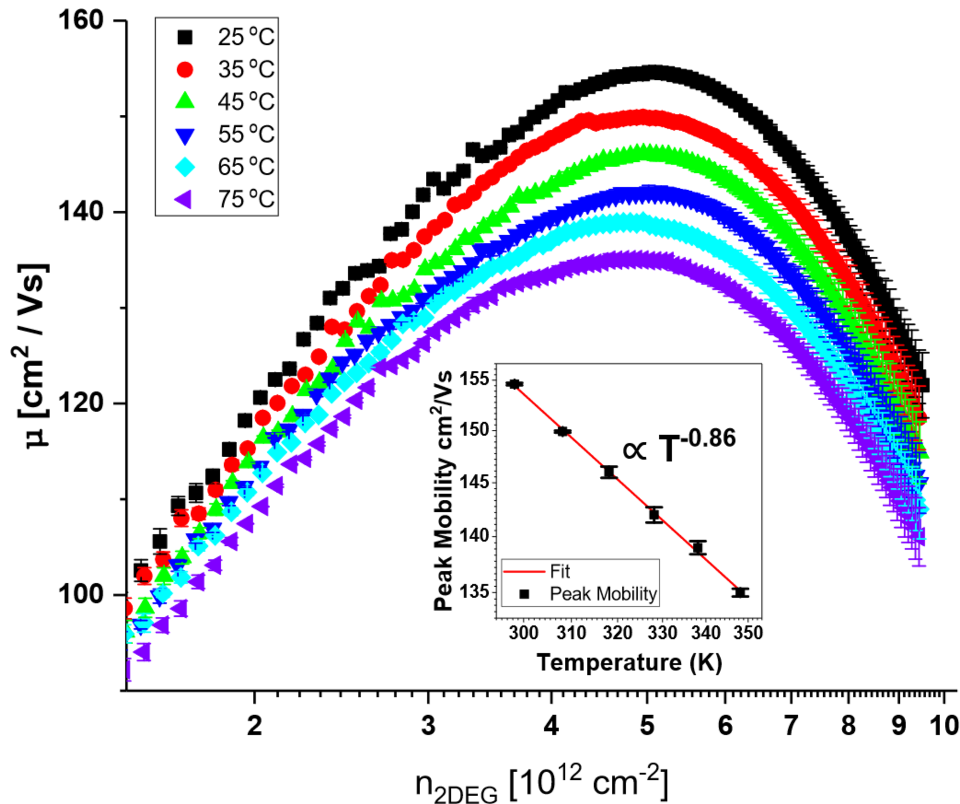

Figure 4.5: Mobility - n_{2DEG} plots showing region of peak mobility, as a function of temperature. Inset: Peak mobility plotted against temperature. Adapted from [77].

$\mu_{Alloy} \propto T^{-0.85}$ dependence due to alloy disorder scattering was found earlier by Glicksman in germanium-silicon alloys, after removal of ionised defect and phonon mobility limits [94]. The peak mobility temperature dependence observed here, $T^{-0.86\pm0.01}$, is close to the $T^{-0.5}$ expected from theory for alloy scattering in ternary III-V compounds, and is consistent with reported findings for alloy scattering in Ge-Si alloys. The measured peak mobility temperature dependence is therefore further evidence in favour of alloy scattering being a mobility limiting factor in these $Al_{0.85}Ga_{0.15}N$ / $Al_{0.7}Ga_{0.3}N$ devices.

Over the 25 °C to 75 °C temperature range tested Schottky contact leakage did not adversely affect the measurements. Leakage current would increase as chuck temperature is increased, however as demonstrated in [95], its influence is easily distinguished as an increase in $\frac{G}{\omega}$ as measurement frequency is decreased. This was not observed in the measurements. As reported in [77], my co-authors and I expected that this admittance-based Ohmic contact-free mobility measurement technique would be suitable for use at higher operating temperatures, a regime where UWB heterojunction devices are of particular interest. That expectation was tested, as described later in this chapter.

4.2.4 Conclusions from technique development using Sample 1

In developing and testing this admittance-based Ohmic contact-free mobility measurement technique as a function of disc-annulus voltage and frequency ($Y-f-V$), it was shown that 2DEG mobility can be measured from weak inversion through to the unbiased case, in ultra-wide band-gap semiconductor AlGaN heterostructures, using only Schottky contacts. This technique may therefore be especially valuable for early feedback on new material developments, as discussed earlier. The maximum mobility values extracted using this technique are in good agreement with those measured by Hall measurement, given above. Concentration-dependent mobility and temperature-dependent mobility at around 5×10^{12} cm^{-2} suggest that alloy scattering is presently limiting peak mobility in this material. This suggests a route towards higher mobility structures by increasing the Al composition of the AlGaN buffer layer where the 2DEG is formed, along with an increase in barrier Al content to maintain the required band-gap difference across the heterostructure. It is also possible that by maintaining the same alloy compositions, but reducing interface roughness, mobility could be increased closer to to 177 cm^2/Vs.

4.3 Mobility in a graded Al-composition structure

By examining the figures of merit discussed in the opening section of this chapter it can be seen that for some device applications, using the material with the highest breakdown field available will enable the production of more efficient devices. Simply increasing the Al composition of AlGaN increases its band-gap closer to that of AlN, as shown by Vegard's equation, which in its simplest form can be applied to band-gaps as $E_{G,\mathrm{Alloy}} = x\cdot E_{G,\mathrm{AlN}} + (1-x)E_{G,\mathrm{GaN}}$, where x is the molar fraction of the binary compound. Low resistance Ohmic contacts are necessary for efficient devices, however, these are difficult to form for high Al composition materials because the electron affinity of AlN is so different from the metals used for Ohmic-contacts. An ingenious potential solution is grading the molar composition of the barrier layer. In this case the Al molar fraction of the barrier is maximised at the heterointerface with the lower AlGaN buffer layer, preserving conditions necessary for 2DEG formation, and enabling higher breakdown fields. The Al composition is then gradually reduced towards the surface of the barrier layer. This enables easier formation of low resistance contacts to the structure by enabling flatter bands, hence better conduction from contact to semiconductor. A secondary benefit to such a graded structure, is that a higher Al-molar fraction buffer can be used, as was done for Sample 3, detailed in Table 4.1. This makes the buffer more binary-like and less ternary-like, reducing alloy scattering, and so potentially increasing mobility. Finally, such structures benefit from polarisation doping, eliminating the need for the Si doping used in e.g. Sample 1 and 2, and therefore reducing impurity scattering.

It was intended to study the graded-composition structure, Sample 3, using the Ohmic contact-free mobility measurement technique developed using Sample 1. Results from the first attempts

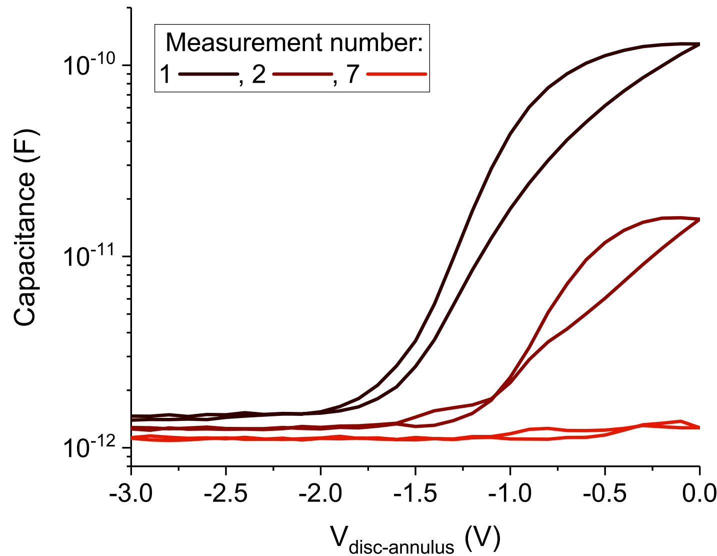

Figure 4.6: Capacitance-voltage profiles obtained from testing the graded composition Sample 3.

at performing a double sweep capacitance-voltage measurement on test structures deposited on Sample 3 are shown in Figure 4.6. It can be seen in the figure that as repeat measurements were attempted, the signal from the sample degraded. This same effect was repeated across several identical structures deposited on Sample 3. Hysteresis is present in the curves, suggesting a charge trapping process. By integrating the first measured CV curve, a channel carrier density of $2 \times 10^{10}\text{cm}^{-2}$ is obtained, significantly lower than that obtained for Samples 1 and 2, and below the $\approx 2.5 \times 10^{12}\text{cm}^{-2}$ inferred from a polarisation doping depth profile of Sample 3 performed by SNL. This suggests that the sample was degraded either by ageing effects, or by electrical stress during testing. It was not possible to measure the mobility in Sample 3 because of the degradation, so it is currently not known whether any improvements in mobility compensate for the apparent lower channel carrier density observed.

Measuring the channel mobility in such a graded composition structure would be very useful to epitaxy growers. In principle the Ohmic contact-free $Y-f-V$ method should be applicable to graded composition structures, with minor changes to the capacitance terms in the equivalent circuit model. If sample degradation can be limited, perhaps by using a different surface passivation method, or by changes to the electrical measurements, this technique should be tried again because it has the potential to provide helpful insight into the characteristics of graded-composition ultra-wide band-gap devices.

4.4 The effect of varying epitaxial layer thickness

Technology computer-aided design (TCAD) simulations of the Sample 1 and 2 epitaxies using Silvaco Atlas that included the 10^{18}cm^{-3} silicon doping in the barrier, and built-in polarisation

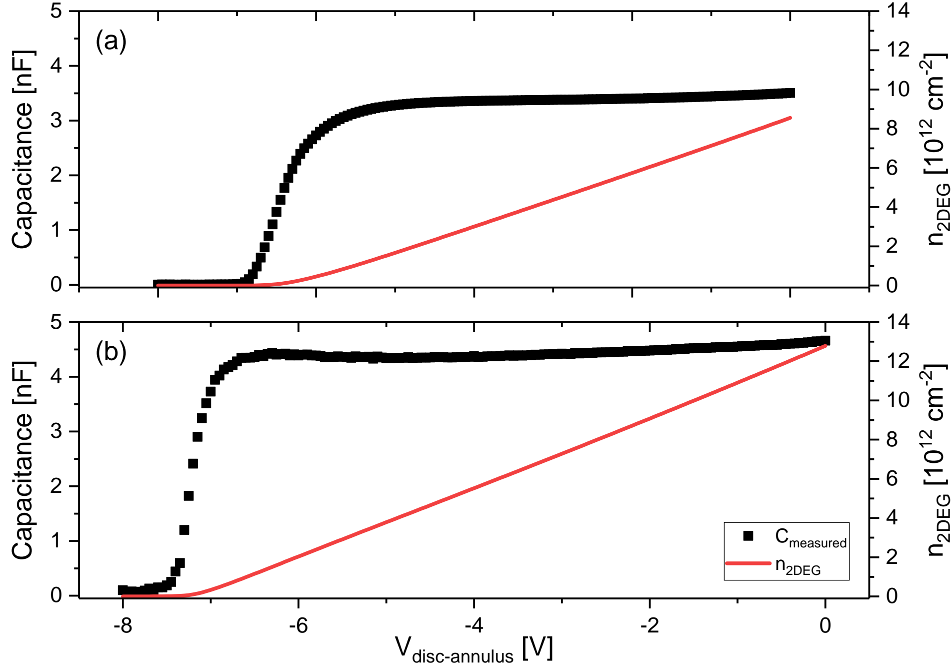

Figure 4.7: Measured capacitance-voltage profiles for test structures on Sample 1 (a), and Sample 2 (b), with n_{2DEG} also plotted as a function of voltage. $C_{measured}$ is shown, however, the plotted channel density was calculated using $n_{2DEG} = \frac{1}{qA_{disc}} \int_{-8V}^{V_{disc-annulus}} C_{disc}(V) \cdot dV$, where C_{disc} was found for each bias point by substituting $C_{measured}$ into Equation 4.8, along with the value of $C_{annulus}$, which is taken to be independent of $V_{disc-annulus}$. $C_{annulus}$ was found by substituting $C_{measured}(V_{disc-annulus} = 0\,V)$ into Equation 4.9. Measurements were performed at 300 K using the cryostat probe station shown in Figure 3.4.

and strain effects, suggest that the channel densities in the two samples should be around $2.4 \times 10^{12}cm^{-2}$ and $3.0 \times 10^{12}cm^{-2}$, respectively. Due to the increased electron concentration provided by the thicker doped barrier layer of Sample 2, and its greater polarisation doping, it would be expected that Sample 2 has a higher channel carrier density than Sample 1. CV profiling of both samples, shown in Figure 4.7, revealed that they had threshold voltages of around -6.8 and -7.4 V, respectively. Sample 2 was found to have a higher low-frequency open channel disc-annulus capacitance of around 4.7 nF, increased from around 3.5 nF for Sample 1. Channel carrier densities found by integrating the $C_{disc-channel} - V$ curves extracted from the raw CV data showed carrier density in Sample 2 was around $1.3 \times 10^{13}cm^{-2}$, increased from around $9 \times 10^{12}cm^{-2}$ found for Sample 1 at 300 K. The TCAD simulations predict the relative 2DEG densities of the two samples approximately correctly, but they underestimate the absolute magnitudes. This indicates that an additional source of carriers not included in the simulations was present in the samples, which from Equation 2.4 is expected to be surface charges.

The larger capacitance of Sample 2 than Sample 1 suggests a slower characteristic switching speed would expected from HEMTs made using that epitaxy due its larger RC time constant.

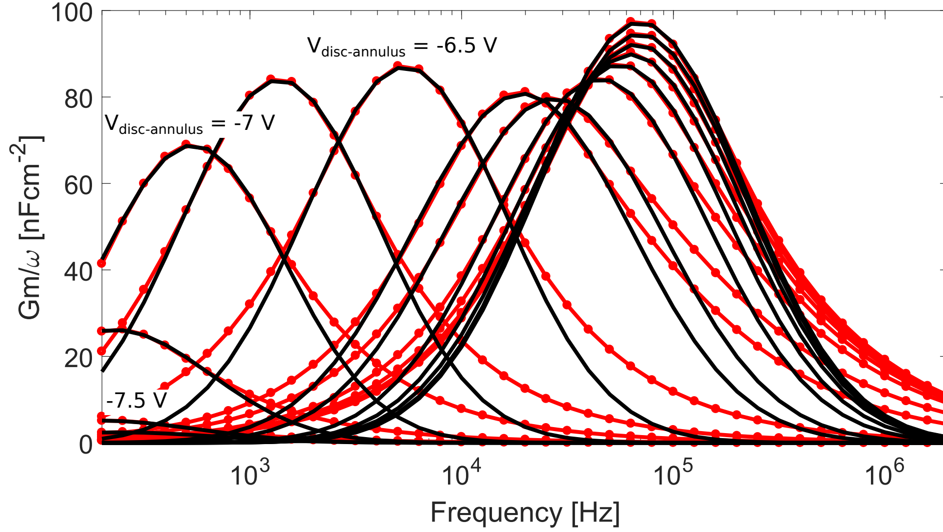

Figure 4.8: G_p/ω vs. frequency for Sample 2, measured at 300 K. For clarity, a subset of the measurement data are shown here. The red circles are measurements, and the black lines are model conductance data. The decrease in peak heights visible below around 1 kHz, corresponds with the transition to weak inversion. Note: excludes measurements below 200 Hz, as discussed in Section 4.5.2.

The 300 K un-irradiated (fresh) $G_m/\omega - f$ measurements for Sample 2 are plotted in Figure 4.8. The figure shows that the decrease of G_m/ω for Sample 1, as frequency was reduced from around 20 kHz to 400 Hz, shown in Figure 4.3, is not present for Sample 2.

The mobility at 300 K as a function of channel carrier density, extracted by fitting the equivalent circuit model described earlier to the data shown in Figure 4.8, can be seen in Figure 4.9. In that figure the region of high mobility extends over a wider range of n_{2DEG} than is the case for Sample 1. The region of mobility increasing approximately in proportion with n_{2DEG}, identified for Sample 1, is not clear for Sample 2 at 300 K. From around 6×10^{11} to $1.5 \times 10^{12}\text{cm}^{-2}$ the increase of Sample 2 mobility is closer to a n^2_{2DEG} dependence than n^1_{2DEG}. This suggests that mobility may not only be limited by ionised impurity scattering in that region, expected to have up to a $n^{1.5}_{\text{2DEG}}$ dependence [87], but also another scattering mechanism. Mobility due to dislocation scattering has been shown to have an $n^{3/2}_{\text{2DEG}}/N_{\text{dis}}$ dependence [96], where N_{dis} is the density of dislocations, which when combined with the increasing screening of ionised impurities as channel concentration increases could explain the observed mobility-n_{2DEG} dependence. The flatter top of the $n_{\text{2DEG}} - \mu$ curves seen for Sample 2 could be due to an increase in interface roughness scattering when compared to Sample 1, or it could be due ionised defect scattering being effectively screened more rapidly with increasing n_{2DEG} in Sample 2. At the highest n_{2DEG} we again see μ decrease sharply due to interface roughness scattering, as seen for Sample 1.

As discussed earlier, when 2DEG density is increased its position moves closer to the hetero-interface [88]. In fitting the experimental $Y - f - V$ data to the equivalent circuit model at

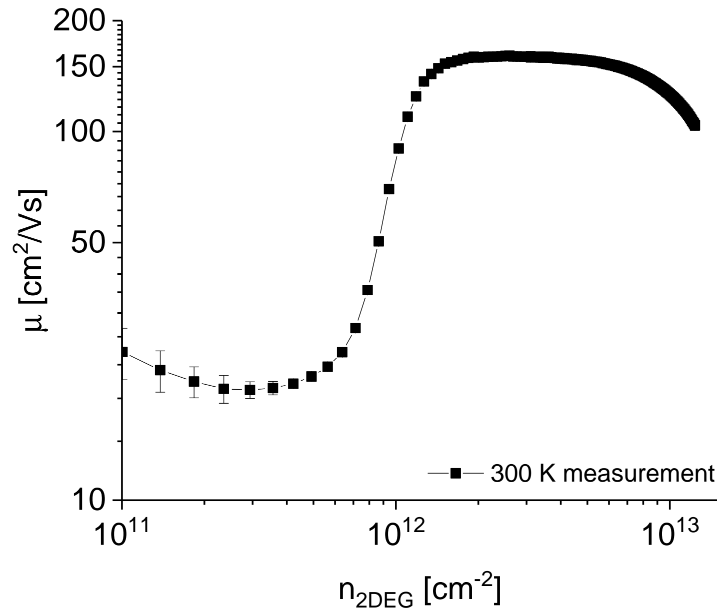

Figure 4.9: Mobility as a function of n_{2DEG} measured for Sample 2 at 300 K. Note: excludes measurements below 200 Hz, as discussed in Section 4.5.2.

n_{2DEG}-interface distance of 1.2 nm had been assumed. The fitting was re-run for a n_{2DEG}-interface distance of 0.9 nm to test the effect of that capacitance element on the extracted mobility. It was found that the extracted mobility values were not sensitive the changes in n_{2DEG}-interface distance, and so the changes in extracted mobility are due to scattering processes and not capacitance changes affecting the fit.

The implications of the 300 K $\mu - n_{2DEG}$ measurements for Sample 2 are that the change in epitaxy to thinner buffer and thicker barrier layers, as detailed in Table 4.1, whilst increasing the carrier density in the 2DEG, may however have increased the density of dislocations in the material because of changes in strain from the thinner buffer layer making dislocation formation increasingly energetically favourable.

4.5 The temperature dependence and impact of neutron irradiation on mobility from 80 to 400 Kelvin

The way a semiconductor's properties change with increasing temperature determines to a large extent the electrical power density that can be achieved from devices made from it. The temperature dependence of mobility in a material will determine its resistance (R) for a given channel density and device geometry, which in turn determines the Joule heating (P) due to current flow in the device (I), $P = I^2R$. Failure mechanisms in devices can be accelerated by

temperature, with a failure rate, A, often following an Arrhenius type relation,

$$A = C \exp\left(\frac{-E_{\mathrm{a}}}{kT}\right) \tag{4.18}$$

where E_a is the characteristic activation energy, and the pre-exponential constant C is determined by the particular process. The mean time to failure of a semiconductor device can be reduced by operation at increased temperatures. Optimising the heat flow from operating devices, in order to reduce peak operating temperatures, is currently an active field of research, as discussed for the case of wide and ultra-wide band gap device in e.g. [97]. In this section we look at the problem from the perspective of a fundamental material property that determines Joule heating, mobility.

Monte Carlo calculations performed by O'Leary *et al.* have shown that the low-field electron drift mobility of GaN should decrease rapidly with increasing temperature, and that the decrease would be particularly severe for temperatures near room temperature [98]. They suggest that property would be important for high-power device performance, presumably because of the Joule heating power dissipation concerns discussed above. In their review paper, Kaplar *et al.* describe how a better knowledge of the saturation velocity, and its temperature dependence is required to assess the benefits of AlGaN for high frequency devices [42]. Saturation velocity is caused by higher energy electrons scattering into higher bands where they have a larger effective mass (m_e^*), and hence lower velocity. Below around 100 kV/cm scattering losses are dominated by polar optical phonon scattering [98], beyond this applied electric field level other scattering mechanisms become more significant. As more electrons are added, the proportion of electrons in the higher bands increases, decreasing the overall mobility. The resulting effect is a (high-field) negative differential mobility in GaN, AlN, and other III-V compound semiconductors [98]. In the Ohmic-contact-free method developed in this chapter, we are able to study low-field mobility, because near zero lateral electric field is applied. Low-field mobility, $\partial v_{\mathrm{drift}}/\partial\mathrm{Field}$, determines the electron velocity reached before saturation occurs.

At the beginning of this chapter we discussed how the effects of neutron irradiation on the electrical properties of (ultra) wide band-gap materials are not fully understood. Johnston [76] discusses how typically changes in carrier density manifest before changes in mobility. Displacement damage caused by neutron irradiation creates additional point defects in the semiconductor lattice, which may increase disorder scattering. Some of the defects will be electrically active, and when ionised would provide additional scattering centres to limit low n_{2DEG} mobility. By gathering temperature- and n_{2DEG}-dependent mobility data we are able to explore whether these defects would affect the operation of devices produced from the material being studied if they were used in radiation environments that generate displacement damage.

In order to optimise the growth process for a material it is desirable to understand the physical mechanisms limiting mobility in it. Once limiting factors are determined, epitaxy design or growth can be altered to improve performance. It is possible to gain insight into those scattering mechanisms by studying the temperature dependence of mobility. Earlier in this

chapter, as reported in [77], we saw how alloy scattering appears to limit mobility in the Sample 1 AlGaN/AlGaN heterostructures over a temperature range of 25-75 °C (approx. 298-248 K). In this section we will see how mobility changes over a much wider temperature range (80-400 K), and will draw some helpful conclusions that may aid future material/device development.

4.5.1 Experimental details

Temperature dependent testing was performed using the cryostat described in Chapter 3. Prior to irradiation, measurements were performed from 80 K to 400 K in 20 K steps. Samples were probed using Kelvin connections as close to the probe tips as possible in the cryostat. After setting each measurement temperature before electrical measurements were begun the stage temperature was allowed to stabilise to within 0.01 K of the set temperature, in order to allow the mounted sample to reach thermal equilibrium with the stage.

Temperature dependent $Y-f-V$ measurements were conducted on Samples 1 and 2 prior to and following irradiation (discussed below). Electrical test conditions were initially the same as used during the technique development work: 20 mV oscillation, $V_{\mathrm{disc-annulus}}$ varied from 0 V to -8 V in 50 mV steps, 20 Hz to 2 MHz oscillation frequency. However, during the course of the cryostat work, low frequency measurement data (20 - 200 Hz), became noisier for $V_{\mathrm{disc-annulus}}$ values more negative than -2 V, with the effect most pronounced towards -8 V where an apparent increased capacitance was observed in the 20 Hz data. Initially the problem was intermittent, but it became consistent during the course of fault finding. The effect appeared to be due to a parallel leakage current, either in the sample, or in the test setup. The increased noise and apparent increased capacitance at large reverse bias were more apparent in the higher temperature measurements. This in turn caused an erroneously high calculation of channel carrier density given by $n_{2\mathrm{DEG}} = \int_{V_{\mathrm{disc}}=-8V}^{V_{\mathrm{disc}}=0V} dC \cdot dV$. The effect in the measurements was consistent with a parallel leakage current, which limits the effectiveness of extracting low channel density mobility data from the measurements.

Many factors were tested and ruled out as the cause including the probes, cables, and test fixtures. The remaining possibilities were the LCR instrument, and the test samples themselves. A loan instrument was obtained from Keysight (and ours was re-calibrated), but we were unable to achieve the low noise levels achieved in earlier work, even on test structures that had not been previously probed. The remaining possible explanations are that either our LCR meter worked unusually well during earlier measurements, or perhaps most likely, that both the samples, and all the structures present on them, had degraded.

The details of the surface passivation present on the samples, if any, is currently unknown. After the completion of measurements for the technique development work in January 2017, and beginning the cryostat work in July 2018, the samples were stored in air at room temperature in wafer boxes. An ageing effect such as sample surface degradation due to contamination, could therefore have caused the increase in signal noise and voltage dependent leakage.

To improve the signal to noise ratio of the subsequent $Y-f-V$ measurements, the oscillation voltage was increased to 50 mV, and the CV measurement was conducted at 200 Hz in addition to the 20 Hz measurement. The increase from 20 mV to 50 mV should not be too large, when compared to a room temperature thermal voltage of 26 mV (kT varied from 7 - 35 mV as temperature was increased from 80 to 400 K). Comparisons between measurements made with structures using a 20 mV and 50 mV oscillation frequency showed that the extracted mobility was not adversely affected.

It was not possible to use the AWE Asp accelerator neutron source for irradiation, discussed in Chapter 5, because it was taken off-line shortly after that work was completed. For the study described in this chapter the 14 MeV neutron source at the Ion Beam Laboratory (IBL), SNL, Albuquerque, was used. Samples 1 and 2 were irradiated at IBL to a neutron fluence of 3×10^{12} n/cm^2 over a period of 'a few days' in early September 2018.

For the post-irradiation measurements, due to time constraints caused by delays in sample shipments, it was necessary to increase the step size from 20 K to 40 K.

The assistance of Dr H. Chandrasekar is gratefully acknowledged in setting up the cryostat, and for performing a subset of the device characterisations before irradiation.

4.5.2 Model improvements for wide temperature range and noisy data fitting

To mitigate effects of increased low frequency noise and increased leakage currents present in the large reverse bias measurements, modifications were made to the equivalent circuit model and data-fitting algorithm used to extract electron mobility from $Y-f-V$ data. Improvements were also made to the fitting algorithm, including a change to the expression for C_{DOS}, which removed the need to manually determine whether data from weak- or strong-inversion was being processed. The changes are detailed in this section. Measurement data gathered earlier, during technique development using Sample 1, did not exhibit problematic noise or leakage current effects, and so was not re-processed using the updated algorithm.

During the technique development detailed earlier in this chapter, the expression for the component of capacitance due to the density of states was determined by $C_{\mathrm{DOS}} = \mathrm{A_i} \times \mathrm{q} \times \mathrm{n_{2DEG}}/\frac{\mathrm{2kT}}{\mathrm{q}}$ in strong inversion, and $C_{\mathrm{DOS}} = \mathrm{A_i} \times \mathrm{q} \times \mathrm{n_{2DEG}}/\frac{\mathrm{kT}}{\mathrm{q}}$ in weak inversion. The transition was set manually to the weak inversion case at low channel density to better represent the physical situation and consequently to improve the fit to the data. More recently, Waller derived an analytic expression for the density of states as a function of channel carrier density [99], given by

$$C_{\mathrm{DOS}} = q^2 \frac{m_e^*}{\pi \hbar^2} \frac{\exp\left(\frac{q\phi}{kT}\right)}{1+\exp\left(\frac{q\phi}{kT}\right)} \tag{4.19}$$

where ϕ is found by rearranging the expression for channel carrier density,

$$\begin{aligned} n_{\text{2DEG}} &= kT\frac{m_e^*}{\pi\hbar^2}\ln\left(1+\exp(\frac{q\phi}{kT})\right) \\ \phi &= \frac{kT}{q}\ln\left(\exp\left(\frac{n_{2DEG}\pi\hbar^2}{kTm_e^*}\right)-1\right) \end{aligned} \tag{4.20}$$

In order to use Equation 4.19 to fit the measurement data across the 80-400 K temperature range required a temperature dependent effective mass term. The electron effective mass in $Al_{0.72}Ga_{0.28}N$ was determined to be 0.336 m_e by Schöche *et al.* [100], who estimated the effective mass in AlN by extrapolating from their data to be 0.376 m_e. Hofmann *et al.* found a 300 K effective mass of $(0.36 \pm 0.03)m_e$, increasing from $(0.22 \pm 0.01)m_e$ at 1.5 K for a $Al_{0.25}Ga_{0.75}N$ HEMT [101]. Given the agreement, within error bounds, of the 300 K effective mass values for the two different alloy compositions, the temperature dependent effective mass data in [101] was digitised, and used to produce Equation 4.21, below.

$$\begin{aligned} m_e &= 9.19\times10^{-31}\,[\text{kg}] \\ m_e^* &= m_e \times \left(0.219 + 1.117\times10^{-4}\left(\text{abs}\left((T-81.7)^{1.323}\right)\right)\right) \end{aligned} \tag{4.21}$$

This equation was used to find effective mass from 80-300 K, and to estimate it by extrapolation from 300 and 400 K. This enabled the calculation of 2DEG mobility from the $Y-f-V$ data across the entire measured temperature range. The above expressions were used to modify the code so that the $Y-f-V$ data could be fitted continuously across the entire temperature and n_{2DEG} range.

The algorithm was adjusted to calculate n_{2DEG} at each voltage using a C-V curve composed of the capacitance values measured at 200 Hz during each $Y-f$ measurement. This was done to remove the influence on calculated n_{2DEG} values, and hence μ values, of the low frequency noise that developed on the 20 Hz dedicated C-V measurements. The algorithm was also adjusted to only use data from 200 Hz to 2 MHz during the μ fitting calculations. Subsequent test fits using known-good data showed that the extracted mobility values were almost identical to those obtained using the original 20 Hz - 2 MHz data sets, except at the lowest n_{2DEG} values. The increased leakage current and signal noise affected low frequency measurements to the greatest extent, this is because the impedance of the capacitor elements decreases with increasing frequency as $Z = R + \frac{1}{i\omega C}$, and so dominates the total conductance ($1/Z$) at higher frequencies. The higher frequency data, which represent the high channel carrier density region (G_p/ω peak is at higher frequency for higher number density), are therefore relatively unaffected by the low frequency noise and leakage current. The maximum mobility, and open channel mobility (at maximum n_{2DEG}), should therefore be accurate. To avoid any spurious fits to low n_{2DEG} data, in the following sections we will consider only μ for n_{2DEG} values of $10^{11}\,\text{cm}^{-2}$ and greater.

In addition to the changes already listed, it was necessary to remove the effect of the spurious low frequency and large reverse bias leakage current on the higher frequency data. To do this

the leakage conductance at each disc-annulus voltage was defined as the mean conductance measured below 200 Hz at that disc-annulus voltage. Three different methods of removing the effect of the leakage conductance on the extracted mobility values were then tested to cover the apparent physical explanations for the leakage:

1. An element-wise Schottky contact leakage model. In this case, the equivalent circuit model was modified so that each finite element had a conductance element parallel to the series capacitors. The value of each conductance was determined by the element's area as a fraction of the low frequency conductance. This model accounted for the potential increase in Schottky contact leakage.

2. A surface leakage model. In this case the equivalent circuit model was modified to include a parallel leakage conductance from the disc contact to the annulus contact. Its value was set as the average leakage current defined above.

3. Simple subtraction. In this case, the leakage conductance value was simply subtracted from the conductance value measured at each frequency prior to fitting the data with the usual equivalent circuit model.

It was found that the third approach of simply subtracting the leakage conductance from the conductance used in the fitting procedure, was the most effective method for enabling the algorithm to fit noisy data. It also produced extracted mobility values consistent with the original fitting algorithm when tested on low noise data for comparison.

4.5.3 Results of temperature dependence and irradiation testing

In this section we will see how the 2DEG density ($n_{2\mathrm{DEG}}$), and electron mobility vary from 80 K to 400 K in Samples 1 and 2. We will also see how irradiation to $3 \times 10^{12}\,\mathrm{n/cm^2}$ affects those properties and the scattering mechanisms.

The 2DEG density in both samples was found to increase with increasing temperature, prior to and following irradiation, as visible in Figure 4.10. Two distinct regions of temperature dependence were apparent in the data for both samples, with $n_{2\mathrm{DEG}}$ displaying a weak temperature dependence between 80 K and around 150 K, which then increases as temperature is increased further. Examination of the $n_{2\mathrm{DEG}} - \mathrm{T}$ data, shown in Figure 4.10, reveals that it is likely that a systematic error has affected the Sample 1 200-300 K measurements prior to irradiation, and that there is data missing from the Sample 2 measurement series taken prior to irradiation in the range 200-280 K. The Sample 1 200-300 K $n_{2\mathrm{DEG}}$ data measured prior to irradiation was therefore excluded from the channel carrier density model fitting, discussed below. $n_{2\mathrm{DEG}}$ was found to increase from $(0.957 \pm 0.002) \times 10^{13}\mathrm{cm^{-2}}$ in Sample 1, and $(1.147 \pm 0.002) \times 10^{13}\mathrm{cm^{-2}}$ in Sample 2 at 80 K, to $(1.10 \pm 0.02) \times 10^{13}\mathrm{cm^{-2}}$ and $(1.50 \pm 0.04) \times 10^{13}\mathrm{cm^{-2}}$ at 400 K.

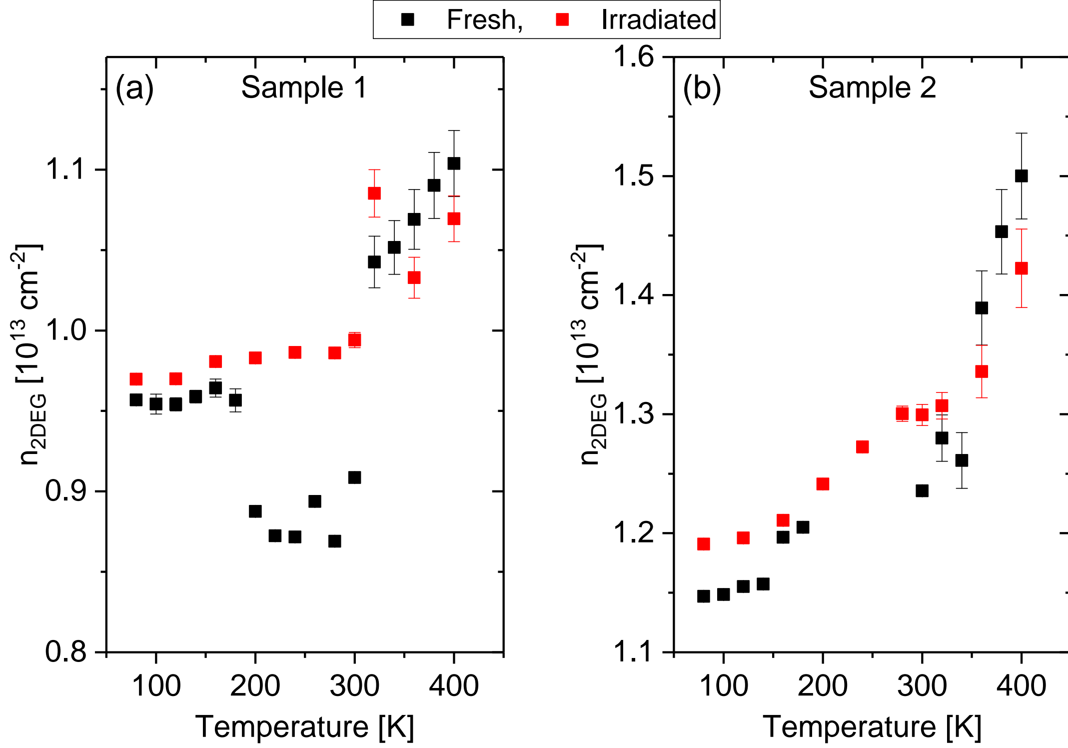

Figure 4.10: Channel 2DEG density, n_{2DEG}, in Sample 1 (a) and 2 (b), as measured before and after irradiation, plotted against temperature.

Irradiation was found to affect the temperature dependence of n_{2DEG}. At low temperatures (80-160 K), the carrier density was found to be higher after irradiation. Conversely, at the highest temperatures tested (360-400 K), the opposite behaviour was observed. At the low temperature 80 K extreme, in Sample 1 and Sample 2, n_{2DEG} increased to $(0.970 \pm 0.001) \times 10^{13}\text{cm}^{-2}$ and $(1.191 \pm 0.001) \times 10^{13}\text{cm}^{-2}$, respectively. Whereas at 400 K the respective decreased n_{2DEG} levels in the two samples were $(1.07 \pm 0.01) \times 10^{13}\text{cm}^{-2}$ and $(1.42 \pm 0.03) \times 10^{13}\text{cm}^{-2}$.

In Figure 4.11 Arrhenius plots for n_{2DEG} are presented for Sample 1 and Sample 2. If a single Arrhenius-type process as described by Equation 4.18 were supplying the carriers for n_{2DEG}, with temperature-independent C and E_a, then the plots would show one straight line for each data series, corresponding to a single activation energy. It can be seen in the figure that a single process as described by Equation 4.18 can not adequately represent the temperature dependence of n_{2DEG} across the measured 80 K to 400 K temperature range. Surface states can provide a temperature-independent source of source of carriers for the 2DEG, as discussed in Chapter 2. To fit the data, a temperature-independent term was therefore added to Equation 4.18 to give

$$n_{2DEG}(T) = C \exp\left(\frac{-E_a}{kT}\right) + n_{2DEG,0} \tag{4.22}$$

where $n_{2DEG,0}$ represents the low temperature limit of the carrier density in the samples, E_a is

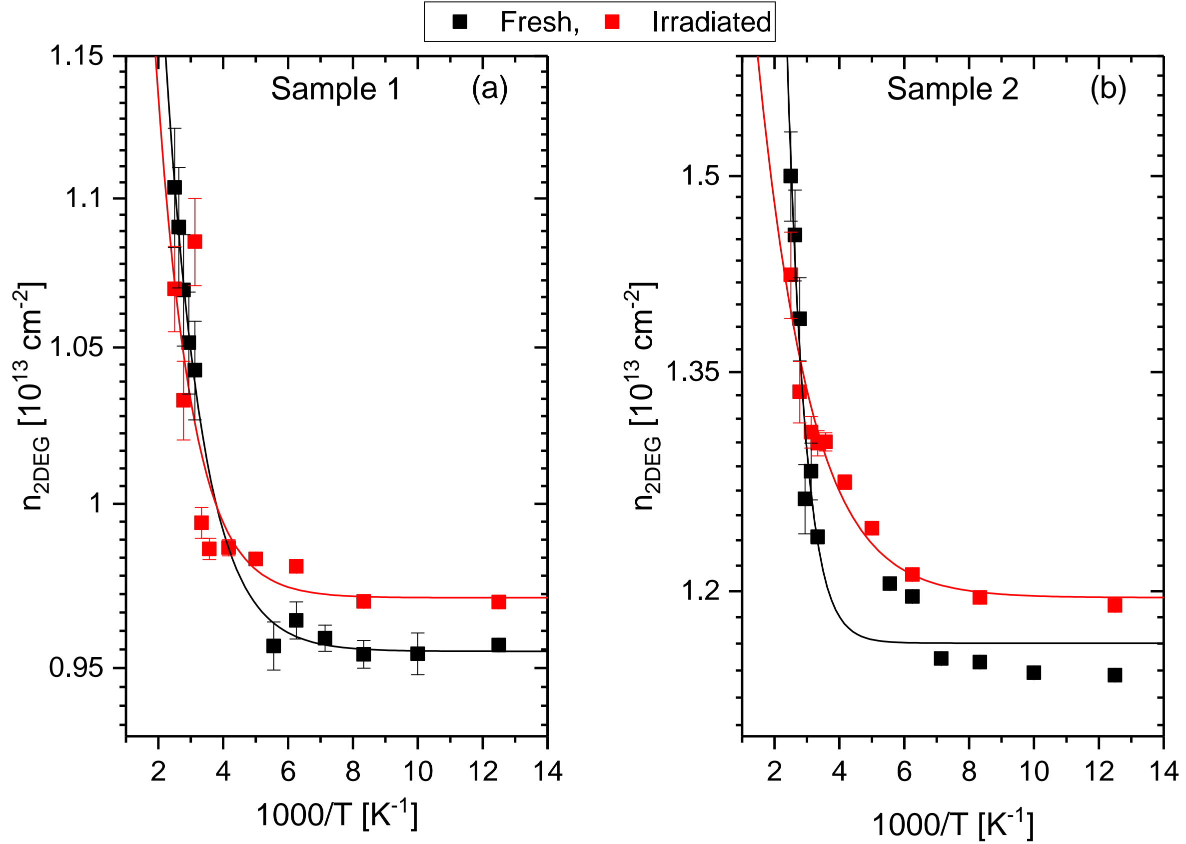

Figure 4.11: Arrhenius plot showing $n_{2\text{DEG}}$ plotted on a logarithmic scale against reciprocal temperature. Points are data for Sample 1 (a) and Sample 2 (b), as measured before and after irradiation. Lines are fits to the data using Equation 4.22. Note: The Sample 1 200 K to 300 K subset of the fresh data is excluded.

Parameter	Sample 1		Sample 2	
	Fresh	Irradiated	Fresh	Irradiated
E_A [meV]	81 ± 6	85 ± 48	174 ± 29	60 ± 12
$n_{2\text{DEG},0}$ [$10^{12}\,\text{cm}^{-2}$]	9.55 ± 0.02	9.71 ± 0.15	11.7 ± 0.11	12.0 ± 0.12
C [$10^{12}\,\text{cm}^{-2}$]	16 ± 3	12 ± 17	540 ± 468	11.3 ± 4.2
Adj. R^2	0.996	0.618	0.944	0.941

Table 4.2: Table of model parameters for the source of the 2DEG, found by fitting Equation 4.22 to the temperature-dependent $n_{2\text{DEG}}$ data shown in Figure 4.11 for Samples 1 and 2, before (fresh), and after irradiation.

the characteristic activation energy associated with the temperature-dependent source of carriers, and C is a constant with dimensions of reciprocal area. The solid lines in Figure 4.11 are fits of Equation 4.22 to the measurement data. The fitting parameters are listed in Table 4.2 along with the adjusted coefficients of determination (Adj. R^2). The decrease in the quality of the Sample 1 fit observed after irradiation is due to the high 320 K mobility measurement point.

(a) Fresh Sample No.	μ (max) [cm^2/Vs]			μ (open channel) [cm^2/Vs]		
	80 K	300 K	400 K	80 K	300 K	400 K
1	238 ± 2	159 ± 0.3	118 ± 24	166 ± 5	125 ± 3	90 ± 2
2	228 ± 2	161 ± 4	88 ± 14	148 ± 5	104 ± 3	57 ± 2

(b) Irradiated Sample No.	μ (max) [cm^2/Vs]			μ (open channel) [cm^2/Vs]		
	80 K	300 K	400 K	80 K	300 K	400 K
1	266 ± 5	183 ± 3	126 ± 7	186 ± 5	130 ± 3	94 ± 2
2	224 ± 3	145 ± 6	100 ± 10	143 ± 5	99 ± 3	68 ± 2

Table 4.3: Peak and open channel mobility at 80, 300, and 400 K, before a), and b) after irradiation.

In Figures 4.12 (a) and (b), the $\mu - n_{2DEG}$ curves for Samples 1 and 2 are plotted for three temperatures, 80, 300, and 400 K, for the measurements made before and after irradiation. The maximum and open channel mobilities (μ at maximum n_{2DEG}) corresponding to Figure 4.12 are given in Table 4.3. For both tested epitaxies the mobility for carrier densities above $10^{12}\,\text{cm}^{-2}$ decreases with increasing temperature. This trend is also followed after irradiation. At lower carrier densities, prior to irradiation the 400 K mobility is shown to be greater than the 300 K mobility for some regions of the $\mu - n_{2DEG}$ curves. After irradiation the low n_{2DEG} mobility appears to increase with temperature for Sample 1. However, considering the increased uncertainty in the measured mobility values in that n_{2DEG} range, which is more susceptible to distortion due to leakage currents, this trend may be an artefact. In contrast, for Sample 2 the low n_{2DEG} mobility decreases with increasing temperature.

The complete set of measured maximum and open channel mobilities are plotted in Figure 4.13. Parts (a) and (b) of the figure show that the measured mobility of Samples 1 and 2 displays a weak temperature dependence at the lower measurement temperatures. As the temperature is increased further, the mobility begins to sharply decrease. Consistent with this trend, here the scattering mechanisms limiting mobility will be considered into two groups, one temperature-independent and one temperature-dependent, following the approach used in [102]. The temperature-dependent scattering mechanisms are taken to follow a power law, so that total mobility is given by

$$\mu_{\text{total}}^{-1} = \mu_0^{-1} + \left(\beta \times T^{-\gamma}\right)^{-1} \tag{4.23}$$

where the constant first term on the right represents the low temperature mobility, and the second term represents the contribution to mobility that varies across the measured temperature range. The second term would be due to several individual scattering processes, which in the following analysis are considered together. The solid lines in Figure 4.13 are fits of Equation 4.23 to the data. The fitting parameters are given in Table 4.4. There were no differences between the fitted temperature-dependent parameters after fitting uncertainty was accounted for. In all cases, the temperature dependent contribution to peak and open channel mobility in Equation 4.23 was found to vary approximately as T^{-3}.

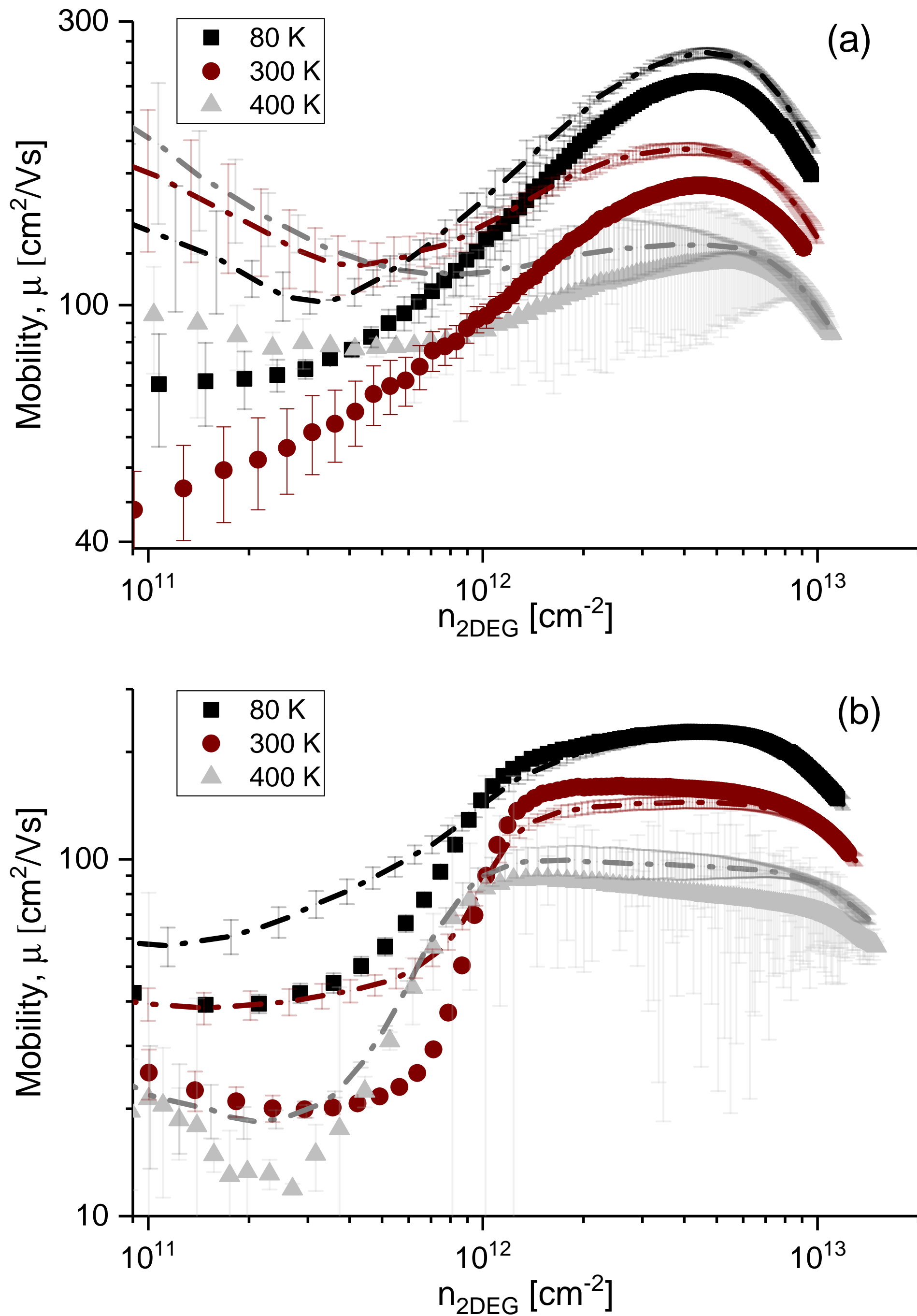

Figure 4.12: Mobility plotted against channel carrier density at 80, 300, and 400 K for Sample 1 (a), and Sample 2 (b). Symbols show the fresh device data, and the dash-dot lines of matching colour show the corresponding mobility after irradiation.

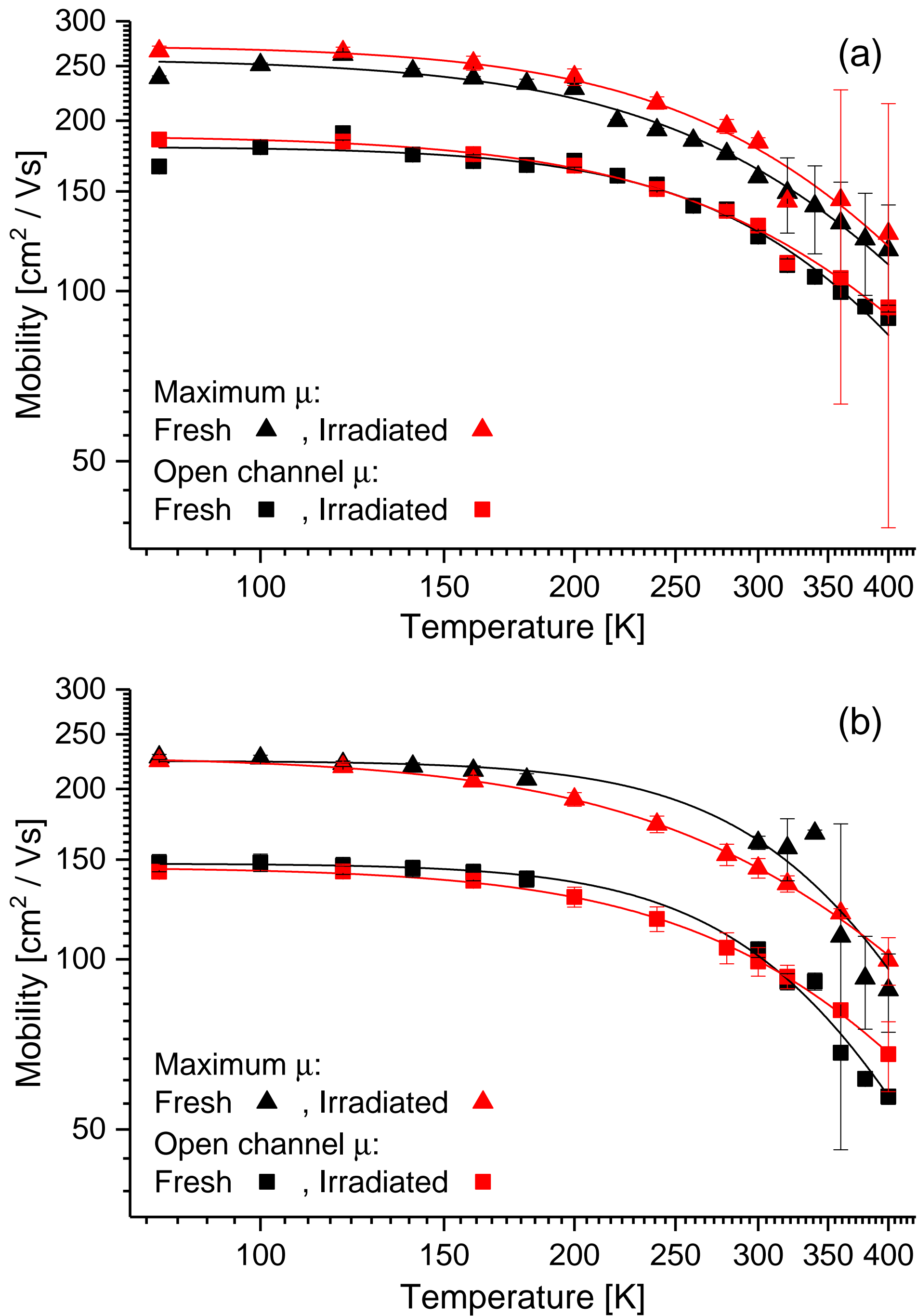

Figure 4.13: Mobility plotted against temperature prior to and following irradiation for Sample 1 (a), and Sample 2 (b). Triangles show maximum mobility in the $\mu - n_{2DEG}$ curve at each given temperature, squares denote open channel mobility ($V_{disc-annulus} = 0\,V$). Lines are fits to the data using Equation 4.23.

(a) Parameter	Sample 1 Fresh	Sample 1 Irradiated	Sample 2 Fresh	Sample 2 Irradiated
μ_0 [cm^{2}V^{-1}s^{-1}]	258 ± 6	272 ± 9	224 ± 9	229 ± 2
β [$\times 10^{10}$]	0.7 ± 1.7	1.8 ± 7.4	3400 ± 78000	0.18 ± 0.12
γ	2.9 ± 0.4	3.0 ± 0.7	4.3 ± 3.8	2.7 ± 0.1
Adj. R^2	0.976	0.969	0.937	0.999

(b) Parameter	Sample 1 Fresh	Sample 1 Irradiated	Sample 2 Fresh	Sample 2 Irradiated
μ_0 [cm^{2}V^{-1}s^{-1}]	180 ± 4	188 ± 4	148 ± 3	146 ± 1
β [$\times 10^{10}$]	29 ± 125	0.7 ± 1.6	1700 ± 15000	1.6 ± 1.5
γ	3.6 ± 0.7	2.9 ± 0.4	4.3 ± 1.5	3.1 ± 0.2
Adj. R^2	0.965	0.988	0.989	0.998

Table 4.4: Model parameters for the temperature dependence of (a) peak mobility, and (b) open channel mobility, found by fitting Equation 4.23 to the data shown in Figure 4.13.

The final quantity included in this results section is sheet resistance, which is given by

$$R_{\text{sheet}} = \left(\mu q n_{\text{2DEG}}\right)^{-1} \tag{4.24}$$

where the channel density and mobility are the open channel values, and q is the electronic charge. Figure 4.14 shows the sheet resistance values as a function of temperature extracted for Samples 1 and 2, for the fresh and irradiated cases. Sheet resistance is shown to increase with increasing temperature from around 3500 ohms/square at 80 K to 6000 ohms/square at 400 K. At 300 K we see that R_{sheet} is around 4700-5000 ohms/square, around an order of magnitude greater than would be expected for a HEMT 2DEG at an AlGaN/GaN heterojunction.

4.5.4 Discussion of temperature- and irradiation-dependent results

The results presented in this section demonstrate that the density of electrons in the 2DEG formed at the interface of AlGaN/AlGaN is temperature dependent. From 80 K to around 150 K the source of electrons contributing to n_{2DEG} was found to be temperature-independent. This is consistent with surface states as the source of carriers for the 2DEG in the low temperature regime, as discussed in Chapter 2, and included in Equation 2.4. The intrinsic carrier density of a semiconductor sample is given by

$$n_i = (N_v N_c)^{1/2} \exp(-E_g/2kT) \tag{4.25}$$

where N_v and N_c are the effective density of states for the valence and conduction bands, and E_g is the band gap. Due to the UWBG of the AlGaN barrier approaching 6 eV, its intrinsic carrier density available to contribute to the 2DEG will be negligible. The temperature-dependent contribution to n_{2DEG} is therefore most likely to be ionised donors in the barrier layer. The ionisation energies listed in Table 4.2, with the exception of Sample 2 before irradiation, are of

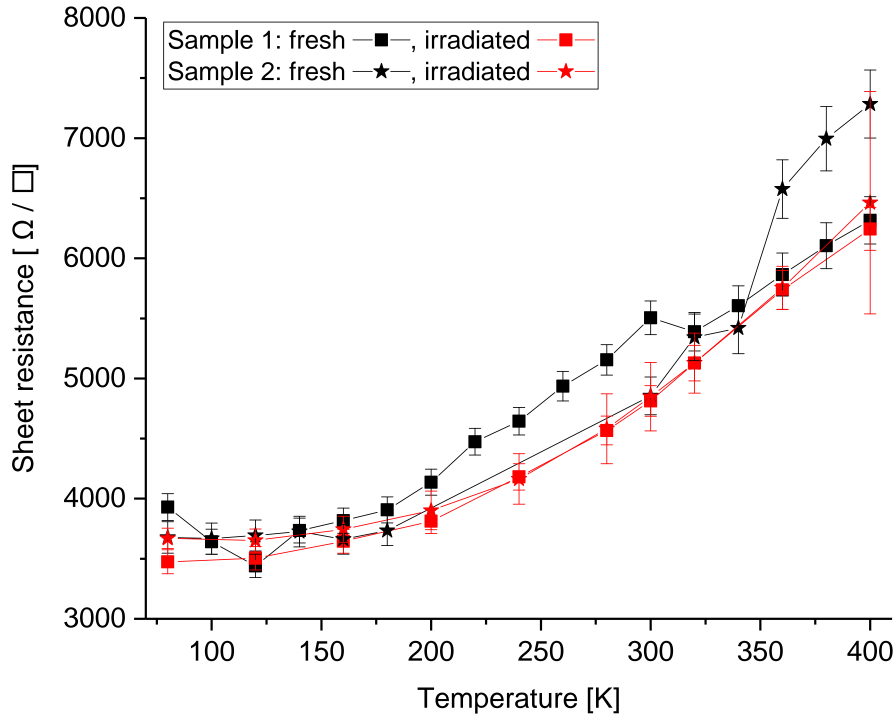

Figure 4.14: Sheet resistance in ohms per square, plotted against temperature in Kelvin for Samples 1 and 2. Connecting lines are a guide for the eye.

comparable magnitude to the (63.5 ± 1.5) meV reported in [103] for the donor ionisation energy of silicon in aluminium nitride. This suggests that the temperature-dependent contribution to the 2DEG density may be ionised silicon donor sites in the AlGaN barrier layer. The $10^{18}\,\mathrm{cm}^{-3}$ silicon doping density in the 40 nm and 50 nm barrier layers of Sample 1 and Sample 2, respectively, could provide maximum contributions to their 2DEG of $4 \times 10^{12}\,\mathrm{cm}^{-2}$ and $5 \times 10^{12}\,\mathrm{cm}^{-2}$, respectively. The observed n_{2DEG} increase in the samples was approximately $1.5 \times 10^{12}\,\mathrm{cm}^{-2}$ and $3.5 \times 10^{12}\,\mathrm{cm}^{-2}$, respectively, which confirms that the thermally activated component of n_{2DEG} could plausibly be due to the silicon doping in the buffer.

The increase at low temperatures, but decrease at high temperatures, of n_{2DEG} following irradiation, visible in Figure 4.10, may indicate an interesting defect compensation behaviour due to the neutron displacement damage induced defects. However, the observed post-irradiation changes were small, and all within 5% of their fresh levels. A follow-up study, potentially conducted at AWE's Asp accelerator to higher neutron fluence levels, would enable this effect to be studied further, and would enable an increase in understanding of UWBG/WBG semiconductor mobility response to harsher radiation environments.

In both tested epitaxies, before and after irradiation, mobility was found to decrease with increasing temperature. The decrease with increasing temperature is particularly steep at around room temperature and high temperatures, consistent with the Monte-Carlo calculations reported

by [98]. Taking the mobility to be limited by two independent scattering processes that combine via Matthiessen's rule, it was found that the temperature dependent contribution to total mobility varied approximately as T^{-3}. Optical phonon scattering scales as $T^{-3/2}$, and alloy scattering [92] as $T^{-1/2}$. Interface roughness and ionised impurity scattering are temperature-independent. This is suggests that mobility was being limited by a combination of optical phonon scattering and alloy scattering processes across the wide 320 K temperature range studied. In the first part of this chapter we saw that from 300 K to 350 K peak mobility varied as $T^{-0.86}$, suggesting alloy scattering as the dominant mobility-limiting mechanism. However, the data presented in this section show that no one power-law representation for an individual scattering process can explain the 2DEG mobility-limiting mechanisms occurring within AlGaN/AlGaN heterostructures across the entire 80 K to 400 K range.

In his book [76], Johnson shows how a model based on impurity scattering can be used to model the effect of displacement damage on mobility as

$$\frac{\mu_0}{\mu} = 1 + \beta\Phi \tag{4.26}$$

where Φ is the fluence of incident particles causing displacement damage [$n \cdot cm^{-2}$], β is a damage constant for the particulars of the process and material being studied which can be seen to have the dimensions of [$cm^2 n^{-1}$], and μ_0 represents the mobility prior to irradiation. This simple model is equivalent to the Messenger-Spratt model, described by Equation 2.48, if mobility is substituted for gain and setting $k = \beta/\mu_0$. The damage constant for mobility changes is typically smaller than for majority carrier removal by trapping at the displacement damage-induced defect sites, and is orders of magnitude smaller than for minority carrier lifetime reduction [62]. Given the sub-5% changes in carrier removal, no changes in mobility would be expected according to this model. The data presented in Table 4.3 for Sample 2 are consistent with this expectation. However, the mobility for Sample 1 can be seen to have increased following irradiation by around 12% for μ(max) at 80 K. The increase in mobility is greatest at lower temperatures, and for peak mobility, rather than open channel mobility. The data as a function of channel density can be seen in Figure 4.12, and for all measured temperatures in Figure 4.13.

In Section 4.4 we saw how the peak in Sample 1 mobility is more sensitive to ionised defect scattering than Sample 2, which appears to be primarily limited by interface roughness scattering. This suggests that the increase in peak mobility seen for Sample 1 after irradiation is due to a decrease in ionised impurity scattering. The low n_{2DEG} mobility curves for both epitaxies can be seen to have increased after irradiation in Figure 4.12, which supports this suggestion.

The primary effect of displacement damage is to create point defects and defect clusters, which behave as defect scattering centres when ionised. The increase in the peak mobility of Sample 1, and in both samples at low n_{2DEG} levels, therefore suggests that the defects introduced following irradiation have caused a net reduction in ionised defect scattering. This can be explained by the irradiation-introduced defects compensating the native defects. At the high channel densities

which determine open channel mobility, the electrons in the channel largely screen Coulomb scattering from ionised defects, which explains why the changes in mobility due to irradiation for the open channel case, where alloy scattering dominates, are smaller.

At the beginning of this chapter we saw how conductivity determines resistive energy losses due to Joule heating, and that it increases with the product of carrier density and mobility. Carrier density and mobility are affected by temperature, and both are also known to be sensitive to displacement damage. Sheet resistance is a function of both of these properties, and so is a useful indicator of device performance. In [104] Kaplar *et al.* reported for a similar epitaxy 4200 ohms/square and $n_{2\mathrm{DEG}} = 6 \times 10^{12}\,\mathrm{cm}^{-2}$. This compares well to the 4700-5000 ohms/square demonstrated in this chapter as shown in Figure 4.14. Due to the experimental spread in the μ and $n_{2\mathrm{DEG}}$ values, it is difficult to draw conclusions about the effect of the low neutron fluence irradiation on the sheet resistance values in the figure. What is clear, however, is that increasing temperature increases the sheet resistance of the two-dimensional electron gas at the hetero-interface of the tested AlGaN/AlGaN samples.

4.6 Conclusions

In this chapter we have seen how a new method to measure 2DEG mobility effectively without Ohmic contacts was developed, and demonstrated with ultra-wide band-gap AlGaN/AlGaN heterostructures. The technique was also demonstrated on a second UWBG material, with a thinner buffer layer, but thicker barrier. This revealed that despite the higher carrier density present in the thicker barrier material (Sample 2), mobility was in fact lower in that material. The decrease in mobility may be due to an increase in interface roughness scattering, or an increased dislocation defect density due to the thinner buffer.

We then saw how mobility varied across a wide temperature range (80-400 K), following a power law, $\mu_{\mathrm{total}}^{-1} = \mu_0^{-1} + \left(\beta \times T^{-\gamma}\right)^{-1}$, with $\gamma \approx 3$. We have also seen how different regions of the $\mu - n_{2\mathrm{DEG}}$ curve are affected by temperature and 14 MeV neutron irradiation to a fluence of $3 \times 10^{12}\,\mathrm{n/cm}^{-2}$. Neutron irradiation at this low level would not be expected to produce changes in (ultra)wide band-gap compound semiconductor heterostructures. However, because of the ability of the Ohmic contact-free mobility measurement technique to determine mobility across a wide $n_{2\mathrm{DEG}}$ range, we have been able to probe the peak-mobility and low-$n_{2\mathrm{DEG}}$-mobility regimes. In those regions, when mobility is limited by ionised defect scattering in fresh devices, we find evidence that suggests displacement damage, caused by neutron irradiation in this case, may actually cause an increase in mobility. A plausible explanation for the apparent neutron-induced mobility increase is the electrical compensation of the ionised scattering centres by the defects introduced by the irradiation. This is consistent with displacement damage causing a semiconductor to become more intrinsic in nature, a well-established radiation effect.

Chapter 5

Neutron-induced charge trapping effects

Crystallographic defect sites which enable trapping of charge carriers within HEMTs (traps), can result in reduced output power and switching speeds, increased leakage currents, and changes in device parameters such as threshold voltage. All semiconductors contain defects, but for WBG materials the densities are typically higher than competing materials, due in part to challenges associated with their growth and non-native substrates. For these reasons there is a clear need to understand trapping effects in WBG semiconductor devices. Crystallographic point defects include vacancies, interstitials, antisites, foreign atomic species, and defect complexes formed from those, as discussed in Chapter 2. These defects can produce allowed energy levels in the band structure of the semiconductor, which when located within the band-gap form acceptors, donors, amphoteric defects, and generation-recombination centres. Defect levels that are close to a band-edge, relative to kT, are easily thermally ionised so act as donors or acceptors of charge depending on the nature of the particular defect. When intentionally added, such defects are known as dopants. Defects with energy levels at the centre of the band-gap, where charge exchange with the valance and conduction bands is equally likely, act as generation-recombination centres. Traps are formed by the defects intermediate to these two extremes - they have energy levels deep compared to kT, but are not at the centre of the band-gap. This property of traps causes them to have a low probability of ionisation in response to an applied electric field, and so they can be slow to respond to a change in Fermi level caused by an applied electrical bias. This in turn leads to undesirable device characteristics including the ‘kink effect’, and a time-varying on-state resistance following changes to electrical biasing conditions. This latter phenomenon, known variously as dynamic-R_{on}, drain- and gate-lag, is the subject of this chapter. Analysing the time-varying currents associated with this effect can provide valuable information on the traps (Chapter 3), and is known as CTS. An important

advantage of using CTS to study trap effects is that it is possible to perform CTS studies on real devices - its applicability is not limited to specially constructed test structures or diodes, unlike e.g. Deep Level Transient Spectroscopy (DLTS). This means that the technique can be widely applied, and quickly related to real world performance.

Semiconductor device operation depends critically on the electronic band structure within the device. The effect that trapped charge within a device can have on its band structure can be appreciated by considering Poisson's equation,

$$\frac{d^2\phi}{dx^2} = -\frac{\rho(x)}{\epsilon_0\epsilon_r} \tag{5.1}$$

where ϕ is the electrostatic potential, ρ is the charge density at a point, and ϵ_0 and ϵ_r are the permittivity of free space and the relative permittivity of the material, respectively. Equation (5.1) shows that trapped charge in a device alters the band bending within it, which directly affects the operation of the device. Traps can also provide conduction pathways for electrical currents. This can lead to undesirable effects like increased leakage currents due to trap-assisted-tunnelling, and increased off-state leakage currents, increasing power losses and reducing efficiency in application circuits.

In this chapter we continue the approach begun in Chapter 4 of considering the cumulative displacement damage effects of neutron exposure on AlGaN/GaN HEMTs, rather than transient radiation or Single Event Effects (SEE), which are considered later in this thesis. Displacement damage and NIEL effects in semiconductors due to fast neutrons scattering from atoms in the lattice include the creation of point defects including vacancies, interstitials, Frenkel pairs and defect-impurity complexes, as reviewed for the case of silicon by Srour *et al* [105]. These defects can affect HEMT operation in addition to, or in combination with, the pre-existing native defects. Displacement damage testing is typically performed for optoelectronics, sensors, and bipolar technologies. However, previous studies have shown that irradiation of AlGaN/GaN HEMTs with 2.8×10^{11} n/cm^2($\langle E \rangle = 9.8$ MeV) can cause a 10% reduction in drain-source current (I_{DS}) [106], and irradiation by 1.6×10^{12} n/cm^2 (1 MeV equivalent) [107] was found to cause increases in gate leakage current via trap-assisted tunnelling in the AlGaN gate region. A higher neutron fluence study found reductions in I_{DS} and transconductance (G_m), but not cut-off frequency after exposure to 10^{15} n/cm^2($\langle E \rangle = 1$ MeV) [108]. Conversely, AlGaN/GaN HEMTs degraded by prior electrical stress have shown partial recovery of I_{DS} following irradiation with thermalised Am-Be neutrons to 6×10^{11} n/cm^2 [109]. Consequently, the impact of neutron irradiation on the switching and transient recovery characteristics of HEMTs remains unclear. In this chapter we will see how by applying CTS to trapping in HEMTs, we can measure the effect of neutron irradiation on the HEMTs ability to switch current quickly and efficiently.

This chapter contains significant amounts of material expanded from that previously published in IEEE Transactions on Nuclear Science [110].

5.1 Details of UMS devices studied with CTS

The HEMTs used in the study reported in this chapter were kindly provided by Dr Benoit Lambert of United Monolithic Semiconductors (UMS), Villebon-sur-Yvette, France. The devices were AlGaN/GaN HEMTs grown on SiC substrates, and packaged in Egide ceramic RF packages. Detailed development process and electrical characterisation information on these UMS GH25-10 devices can be found in [111].

In order to enable the damage calculations and trap density extraction discussed later in this chapter, it was necessary to obtain information on the total HEMT width and physical configuration. By combining the details in [111], and the results of electrical characterisation performed on the tested devices, the gate length was determined to be $L_G = 0.25\ \mu m$. The source-drain distance for the tested HEMTs was $L_{SD} = 2.75\ \mu m$, and the gate-drain distance was $L_{GD} = 1.7\ \mu m$. Gate width was $W_G = 800\ \mu m$. Threshold voltages were ≈ -3.3 V, and peak transconductance was ≈ 0.17 Siemens (213 mS/mm). Device parameters are nominal as-designed values.

5.2 Experimental details

Three HEMTs were irradiated at AWE's ASP accelerator [112, 113], where 14 MeV neutrons were generated by deuterium-tritium (D-T) fusion: the dominant reaction is

$$^{2}_{1}\mathrm{H} + ^{3}_{1}\mathrm{H} => \mathrm{n} + ^{4}_{2}\mathrm{He} + 17.62\ \mathrm{MeV} \quad (5.2)$$

In this reaction, the emitted alpha particle has energy $E_\alpha = 3.5$ MeV, and the neutron has $E_n = 14.1$ MeV. HEMTs were un-powered during irradiation, and stored in conducting foam to mitigate charging effects. Exposure was uniform across the HEMT surface (< 1% variation). Three HEMTs were irradiated to neutron fluences of 2.1×10^{13} n/cm^2, 1.24×10^{14} n/cm^2, and 7.82×10^{14} n/cm^2. The average rate of irradiation was 4.3×10^{13} n/cm^2/day (ASP was operational for up to 8 hours per day). Due to safety controls in place for the handling of radioactive components, post-irradiation electrical testing was conducted 4 days after the maximum neutron fluence was reached. At least 10% of the fluence for the 7.82×10^{14} n/cm^2 irradiation was due to 2.45 MeV neutrons from deuterium-deuterium (D-D) fusion [114], because of deuterium build-up and tritium depletion in the ASP targets during operation.

To enable electrical connection to the packaged HEMTs, a test jig was designed, which was then manufactured by the Physics Workshop. To perform electrical tests, the HEMTs were mounted into a recessed well which had a changeable printed circuit board mounted on top. This enabled different test modes to be conducted by changing the PCB as required. To ensure a good electrical connection was maintained, the HEMT gate and drain contact tabs were then pressed onto the PCB connection pads by a top mounted plastic frame. This ensured good electrical conduction, and avoided exposing the devices to the thermal stresses that can be caused by repeated cycles of soldering, removal, and re-soldering. This also helped to keep exposure to

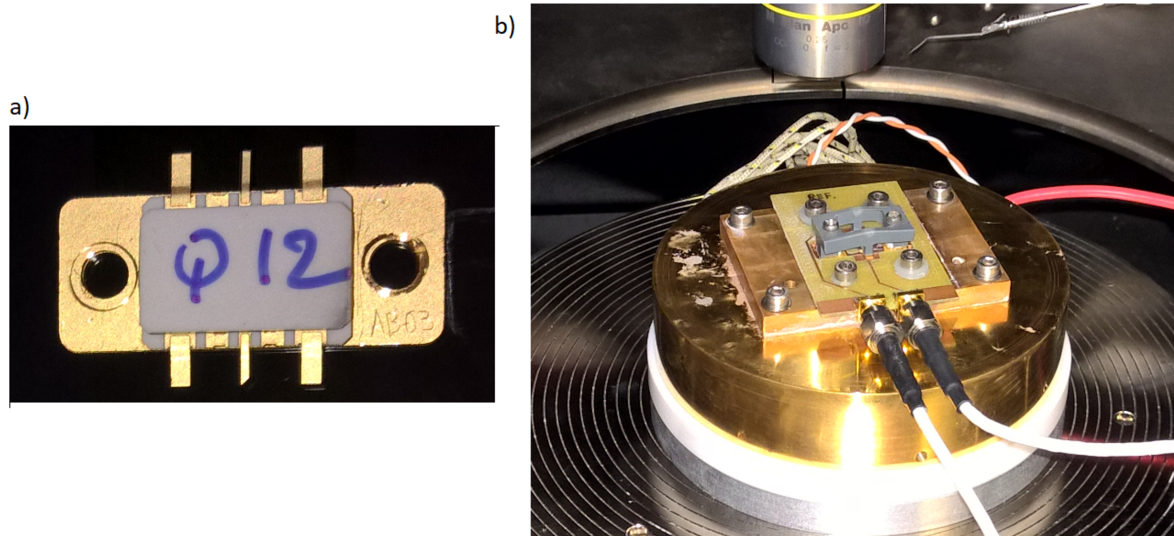

Figure 5.1: a) UMS GH-25 HEMT in Egide radio frequency (RF) package. b) HEMT installed in test fixture and mounted onto temperature control chuck.

ionising radiation as low as reasonably practicable when working with the components after neutron irradiation when they were radioactive. The jig itself was manufactured from copper to ensure excellent thermal conductivity to mitigate against self-heating effects during testing, and enable testing at a range of different temperatures, if required. In-line SMA connectors were mounted to the front of the PCB, which enabled electrical connection to the Keithley SMUs, described in Chapter 3. The test fixture, and a packaged HEMT can be seen in Figure 5.1 mounted onto a PID controlled hot check that was also produced for this work.

The HEMTs were characterised before and after irradiation using drain current (I_D) transient spectroscopy of gate-lag measurements. In this chapter we will see a method for analysing current transient spectroscopy data beyond the standard approach that was introduced in Chapter 3. The first step in measuring each HEMT I_D transient was to apply an off-state trap filling bias of gate voltage (V_G) = -10 V, drain voltage (V_D) = 0.5 V using Keithley 4200 Semiconductor Characterisation System source-measure units. V_G was chosen to ensure that the channel would be fully pinched off even if the threshold voltage changed after irradiation. The duration of off-state bias applied prior to each on-state transient measurement, t_{fill}, was varied from 10^{-2} s to 10^{2} s in decade steps, enabling investigation of the filling time dependence of trap occupancy. Next, HEMTs were switched to $V_G = 0$ V, $V_D = 0.5$ V for 1800 s to measure the on-state I_D transient in the linear regime of operation (where $V_{drift} = \mu E$). Measurement stage temperature was maintained at 25°C throughout the testing by using a hot chuck with cartridge heaters operated by a PID controller with thermocouple temperature feedback, visible in Figure 5.1-b. Prior to each measurement, a bias of $V_G = 0.7$ V, $V_D = 0$ V was applied to the devices for 10 minutes, resetting devices sufficiently for repeatable I_D transients.

5.3 Method of determining trapped charge density

In Chapter 2 we saw how trapped charge density is conventionally taken to be a linear function of HEMT output current, $I_D(t)$. Here we will see that output current is in fact a non-linear function of the trapped charge density in a HEMT. This approach was used in [110], where it is shown that the charge density trapped in the region of interest is higher than that which would need to be trapped if the whole channel were depleted.

To estimate the trapped charge density from CTS measurements we first note that the 2DEG density in the HEMT channel varies with the position of the Fermi level, polarisation, and the occupation of surface donors [41], barrier traps, and buffer traps. During the off-state biasing applied to the HEMT prior to measuring each transient, potential gradients exist that cause electrons to be injected into available states in surface regions. This electron trapping produces a virtual gate [115, 116, 117], as shown in Figure 5.2-(a) extending from W_1 to W_2. Because the -10 V bias applied to the gate throughout the duration of the off-state biasing (t_{fill}) was below the threshold voltage of the HEMTs, it fully depleted the 2DEG under the gate and also depleted the bulk (Al)GaN vertically and laterally to generate a screening charge. Bulk trapping of charge injected from the gate is likely in those regions indicated by the dark shading in Figure 5.2-(a). To estimate the lateral extent of the depletion into the drain and source access regions of the HEMT TCAD drift-diffusion simulations were performed using Silvaco Atlas [118]. An (unknown) background donor density of 5×10^{16} cm^{-3} was set in the simulations. The lateral extent of the depletion region estimated from these calculations was 100 nm. The channel length probed by the off-state pulse was then $L_P = 2 \times 100\,\mathrm{nm} + L_G = 0.45\,\mu$m. During on-state biasing trapped charge is redistributed, and the 2DEG density in the HEMT channel recovers towards its original value. Because the off-state bias only changes the charge state of traps located within the depletion region under the gate (Figure 5.2-(a)), the conventional approach of assuming that charge trapping affects the entire HEMT channel underestimates the trapped charge density in the depletion region.

To derive an expression to estimate the actual trapped charge density in the HEMT we make use of the following considerations:

1. During the off-state electrical stress applied prior to measuring the transient current, charge trapping occurs primarily within the high electric field depletion region of the HEMT, not uniformly throughout.

2. The region of the HEMT 2DEG channel affected by charge trapping is one element in series with the complete measurement circuit that includes the channel regions unaffected by the electrical stress, the source and drain contacts ($2R_C$), and the cable resistances (R_{cables}).

3. The Keithley SMUs enable four-wire Kelvin measurements, however, the part of the current path from where the Egide package contacts the PCB to the Keithley Remote Bias Tees

is a two-wire measurement, as apparent in Figure 5.1, so cable resistance must also be considered by setting a total extrinsic resistance, $R_{ext} = 2R_C + R_{cables}$.

For the HEMTs tested here, R_{ext} was similar to the channel resistance at 10^4 s, defined as $t = \infty$, and so cannot be ignored. By utilising the length of the depletion region L_P, the channel length L_{SD}, and the extrinsic resistance R_{ext}, and noting that $R_{sheet} = \frac{1}{\mu q n_{2DEG}}$ and therefore $R = \frac{L}{W\mu q n_{2DEG}}$, an equation was derived for the non-linear relationship between the 2DEG density within the region probed by the off-state pulse and the measured current as follows:

$$R_{ext} = 2R_C + R_{cables} = \frac{L_{SD}}{W\mu q n_{2DEG}(t=\infty)} \tag{5.3}$$

The portion of the channel unaffected by the off-state pulse, R_u, is given by

$$R_u = \frac{L_{SD} - L_p}{W\mu q n_{2DEG}(t=\infty)} \tag{5.4}$$

The resistance of the channel region probed by the off-state gate pulse, R_p, is time-dependent, and depends on the trapped charge due to its modulating effect on n_{2DEG}. It is described by

$$R_p(t) = \frac{L_p}{W\mu q n_{2DEG}(t)} \tag{5.5}$$

where $n_{2DEG}(t)$ is the channel density at time t in the region probed by the off-state gate pulse. We can now write the measured current as

$$I_{DS}(t) = \frac{V_{DS}}{R_{ext} + R_u + R_p(t)} \tag{5.6}$$

By normalising $I_{DS}(t)$ by the maximum extrapolated drain current reached at 10^4 s following an off-state pulse, $I_D(t=\infty)$, we have

$$I_{norm}(t) = \frac{I_{DS}(t)}{I_{DS}(t=\infty)} = \frac{R_{ext} + R_u + R_p(t=\infty)}{R_{ext} + R_u + R_p(t)} \tag{5.7}$$

By substitution of the above simultaneous equations into Equation (5.7), and re-arranging for $n_{2DEG}(t)$, we have our result below for the general case (left), and for $R_{ext} \approx R_{HEMT}(t=\infty)$ (right)

$$n_{2DEG}(t) = \frac{I_{norm}(t) L_P\, n_{2DEG}(t=\infty)}{R^*(1 - I_{norm}(t)) + I_{norm}(t)(L_P - L_{SD}) + L_{SD}} = \frac{I_{norm}(t) L_P\, n_{2DEG}(t=\infty)}{2L_{SD} - I_{norm}(t)(2L_{SD} + L_p)} \tag{5.8}$$

where $R^* = R_{ext}\, W\, \mu\, q\, n_{2DEG}\,(t=\infty)$. W is total HEMT width, μ is mobility and taken as 1400 cm^2/Vs, and q is the electronic charge. Figure 5.2-(b) shows the non-linear relationship between $I_{norm}(t)$ and $n_{2DEG}(t)$, demonstrating that local changes in n_{2DEG} are much larger than the measured change in I_D. Accounting for the limited extent of the charge trapping region in the HEMT in this manner enables semi-quantitative analysis of trap densities from I_D current transients.

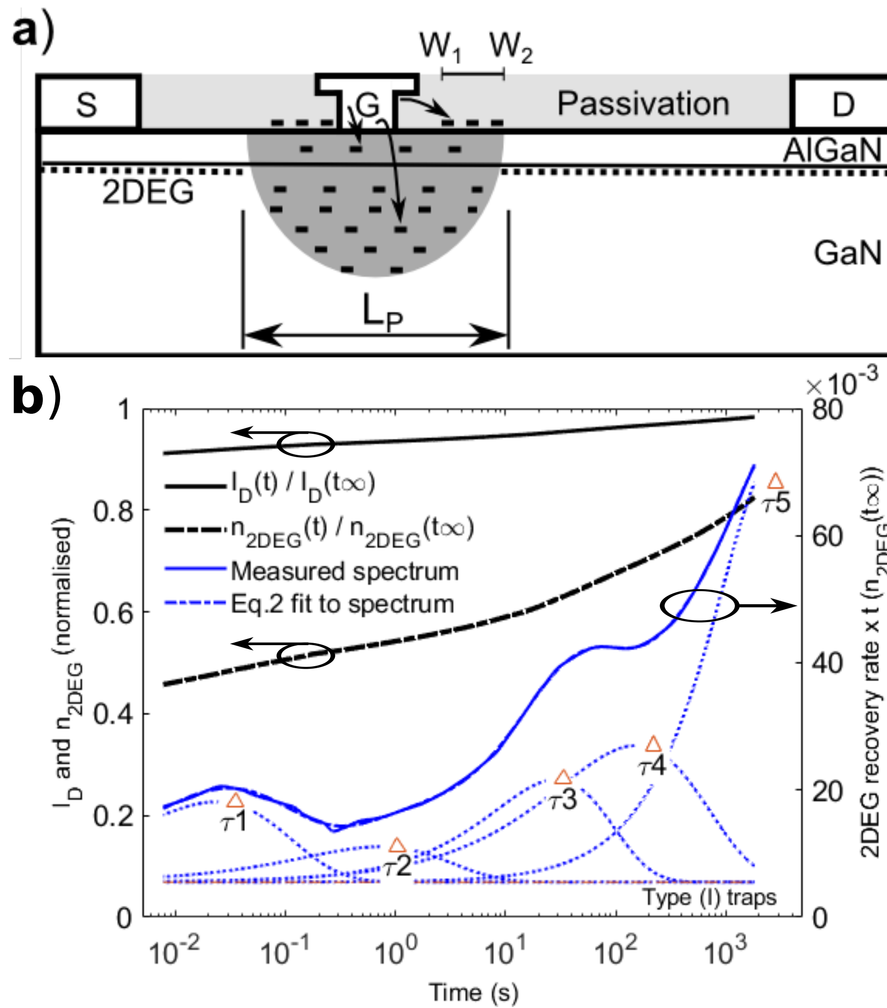

Figure 5.2: (a) Schematic of a lateral HEMT used in this work. Negative charge trapped by off-state bias depletes the 2DEG within L_P. Trap locations shown for Type (I) traps (likely in the passivation layer, passivation/AlGaN surface, AlGaN barrier); and Type (II) traps (dominant in GaN bulk). (b) un-irradiated HEMT normalised $I_D(t)$ for t_{fill} = 100 s, corresponding normalised $n_{2DEG}(t)$, and detrapping spectrum fit using five Type (II) trap terms. Reproduced from [110].

5.4 Producing current transient spectra

Transient spectra were produced by differentiating $\frac{n_{2DEG}(t)}{n_{2DEG}(t=\infty)}$ with respect to $\ln(t)$ (equivalent to t x 2DEG density recovery rate, Equation (5.9) below), then plotting against $\log_{10}(t)$, as shown in Figure 5.2-(b). Plotting and processing the spectra in this manner enables traps acting with vastly different time constants, and effective charge emission rates, to be easily compared in one figure, and it aids the non-linear numerical fitting required to determine discrete trap densities, discussed below. Efficacy of 2DEG depletion varies with trapped charge location [119] depending on whether its image charge resides completely in the channel or also resides partially in the metal contacts, hence the integrated recovery rate is the effective trapped charge emitted during the integration period.

$$\frac{\partial n_{2DEG}(t)}{\partial \ln(t)} = \frac{\partial n_{2DEG}(t)}{\partial t}\frac{\partial t}{\partial \ln(t)} = \frac{\partial n_{2DEG}(t)}{\partial t}\left(\frac{\partial \ln(t)}{\partial t}\right)^{-1} = t\frac{\partial n_{2DEG}(t)}{\partial t} \tag{5.9}$$

To analyse the spectra transient changes of n_{2DEG} were considered to be due to I) traps with a continuously varying time constant within the limits of the measurement, and II) traps with discrete time constants. A constant density of traps over some range of tunnelling distances from the gate (W_1 to W_2 as shown in Fig.5.2-(a)), with time constants that lie within the measurement window, will exhibit charge capture or emission current decreasing with time as 1/t [120], i.e.

$$\frac{dn_{trapped}(t)}{dt} = \frac{n_{trapped}(t_0)}{t} \qquad \text{(Type (I) traps)} \tag{5.10}$$

This appears as a constant baseline on the I_D transient spectra. Conversely, such a distribution of slow traps can also cause noise that decreases with frequency i.e. flicker (1/f) noise [121] due to carrier number fluctuations. Application of the Dutta-Horn model [122] to 1/f noise in GaN has been used to estimate the defect energy distributions in GaN devices [123, 124]. The slow traps responsible for these effects could be located in the passivation, or on the surface forming a virtual gate, or in the AlGaN barrier. Trapped charge current to/from Type (II) traps, assumed to be primarily located in the bulk GaN, was considered using stretched exponential functions [125, 74]. This treatment is appropriate for independent traps such as non-interacting point defects, and for clusters of traps, including those generated by energetic displacement damage cascades, where trap depth is modified by an occupancy dependent Coulomb potential. Active trap density (effective density acting within the measurement time window), and time constants were found by fitting each spectrum with the function:

$$\frac{\partial n_{2DEG}(t)}{\partial \ln(t)} = A + \Sigma_{i=1}^{N} D_i\, e^{\left(-\frac{t}{\tau_i}\right)^{\beta_i}} \qquad \text{(Type (I) + Type (II) traps)} \tag{5.11}$$

where A is the effective charge density at the start of the transient (t_0) in Type (I) traps, $n_{trapped}(t_0)$. Charge emission from N species of Type (II) traps is described by the summation term, where the τ_i are the emission time constants of each trap species. The coefficients, $D_i = \beta_i\, n_{trapped,i}(t_0)\left(\frac{t}{\tau_i}\right)^{\beta_i}$, where $n_{trapped,i}$ is the normalised effective charge density in the ith discrete

trap, and β_i is the stretch parameter which can vary from 1.0 to 0.6 in the fit. To properly define the time constant for each stretched exponential process term, an average time constant was required, as described by [126]

$$<\tau>=\frac{\tau}{\beta}\Gamma\left(\frac{1}{\beta}\right). \tag{5.12}$$

This is necessary because when the stretch parameter, β, is decreased below 1, the fraction of detrapping due to that trap that occurs after the peak in its $\frac{\partial n_{2\mathrm{DEG}}(t)}{\partial \ln(t)}$ function increases. Figure 5.2-(b) shows an example of a fit of Equation (5.11) to a $n_{2\mathrm{DEG}}(t)$ transient, where five discrete trap species ($N = 5$), and a continuum trapped charge source are apparent.

5.5 The 'range' of active trap density as a damage measure

Absolute trap density (or density per eV in the band gap), can be used to estimate the extent that defects in a device or material will affect its electronic properties, and can be used to assess displacement damage effects or material quality. However, the absolute trap density does not necessarily indicate how a semiconductor device will operate in a circuit application. A parameter which is indicative of the overall extent to which traps are affecting device performance would therefore be useful.

Varying the off-state duration applied to a HEMT prior to measuring a transient (t_{fill}) can change the active trap density observed during the recovery transient. The active trap density is limited by the absolute trap density, and by the rate of off-state conduction to the traps in the material, and by the subsequent detrapping rate. Conduction pathways to traps include extended defects like dislocations, and variable range hopping along point defects. Displacement damage and electrical stress can alter those pathways. By measuring transients following a pre-defined set of t_{fill} values, a set of active trap density values will be produced.

The range of active trap density, defined here as the difference between the maximum and minimum active trap density (the range) in that set, is here proposed as a parameter that could be used to assess the extent that trapping is adversely affecting device operation. The range of active trap density is sensitive to changes in trap density, cross sections, and conduction pathways to traps due to e.g. the creation of shallow defects. It is therefore indicative of the potential change in HEMT performance in circuit applications, and may provide a valuable measure of the extent of damage in a HEMT as manifested in real device performance. The range of active trap density is used later to compare measured changes in HEMTs following irradiation to displacement damage estimates based on radiation transport calculations.

5.6 Results

Transient drain current, $I_D(t)$, increased quasi-linearly with the logarithm of measurement time for all tested HEMTs prior to irradiation, as shown in Figures 5.3(a), (b), and (c). Little device-

to-device variation in the extent of the I_D increase during the transients or its t_{fill} dependence was observed. Increasing trap filling time, t_{fill}, was found to cause a small reduction of $I_D(t)$ from $t = 10^{-1}$ s to $t > 1.8 \times 10^3$ s, indicating a small increase in the effective density of negative trapped charge in the HEMTs. At times less than $t = 10^{-1}$ s, $I_D(t)$ varied non-monotonically with t_{fill}, increasing until $t_{fill} = 1$ s, then decreasing for larger t_{fill} values. This non-monotonic t_{fill} dependence suggests the presence of discrete traps responding more quickly than the shortest measurement times. One second after switching to the on-state (t = 1 s), the mean $I_D(t)$ was $(95 \pm 1)\%$ of $I_D(t\infty)$.

After irradiation, HEMT $I_D(t)$ sensitivity to changes of t_{fill} had increased, as is apparent in Figures 5.3(d), (e), and (f). Averaged over the three irradiation levels, mean $I_D(t)$ at $t = 1$ s was $(94 \pm 2)\%$ of $I_D(t = \infty)$. Transients measured after irradiation to a fluence of 7.8×10^{14} n/cm^2 are displayed in Figure 5.3(f) where it can be seen that for $t_{fill} = 100$ s, I_D at the start of the transient was 75% of $I_D(t = \infty)$, whereas prior to irradiation (Figure 5.3(c)), it was 91%. This suggests an irradiation-induced increase in effective negative trapped charge density.

Five Type (II) trap terms labelled $\tau 1 : \tau 5$, were required for a satisfactory fit of Equation (5.11) to the experimental data. These traps were enhanced by irradiation, obscuring, and in some cases suppressing the Type I traps with an apparent continuum of time constants. Time constants for traps $\tau 1 : \tau 5$ for the un-irradiated HEMT transients were: $\tau 1 = (0.036 \pm 0.013)$s, $\tau 2 = (0.37 \pm 0.24)$s, $\tau 3 = (11 \pm 9)$s, $\tau 4 = (107 \pm 43)$s, and $\tau 5 = (2910 \pm 1117)$s (see Figures 5.2(b) and 5.4(a)). The large uncertainties suggest that this is not a unique trap attribution, however it provides a valuable means of comparing and analysing responses.

Figure 5.4 illustrates how the effect of increasing t_{fill} on transient spectra depends on neutron exposure. Prior to irradiation (Figure 5.4(a)), increasing t_{fill} above one second monotonically increased the 2DEG recovery rate observed for $t \geq 1$ s during the transient measurements for all tested HEMTs. Changes in the HEMT transient recovery rate and t_{fill} dependence are clearly apparent after irradiation (Figures 5.4(b), (c), and (d)). However, the trend is not fully clear, especially given that only one HEMT could be tested at each neutron fluence.

The normalised active density of all traps in the 10^{-2} s to 10^3 s time window ($\tau 1 : \tau 5$ and the continuum trap) was found by fitting Equation (5.11) to the experimental data in Figure 5.4 and integrating under the curves. This is plotted in Figure 5.5. For the un-irradiated devices, increasing t_{fill} from 10^{-2} s to 1 s lowered the total active trap density by reducing the combined $\tau 1$ and $\tau 2$ contributions. A total active trapped charge density of $\approx 0.38\, n_{2DEG}(t\infty)$ was approached at high t_{fill}. After irradiation, maximum active trap density increased, as did the maximum change in active density obtained by varying t_{fill} (the range). For the 7.8×10^{14} n/cm^2 case, net positive charge emission was apparent during the $t_{fill} = 10$ ms and 100 ms transients.

The DC drain-source current (I_{DS}) and gate-source current (I_{GS}) characteristics for the HEMTs are shown in Figure 5.6 for each of the un-irradiated and irradiated cases. Curves were measured using double V_{GS} sweeps (reverse then forward). Following irradiation changes

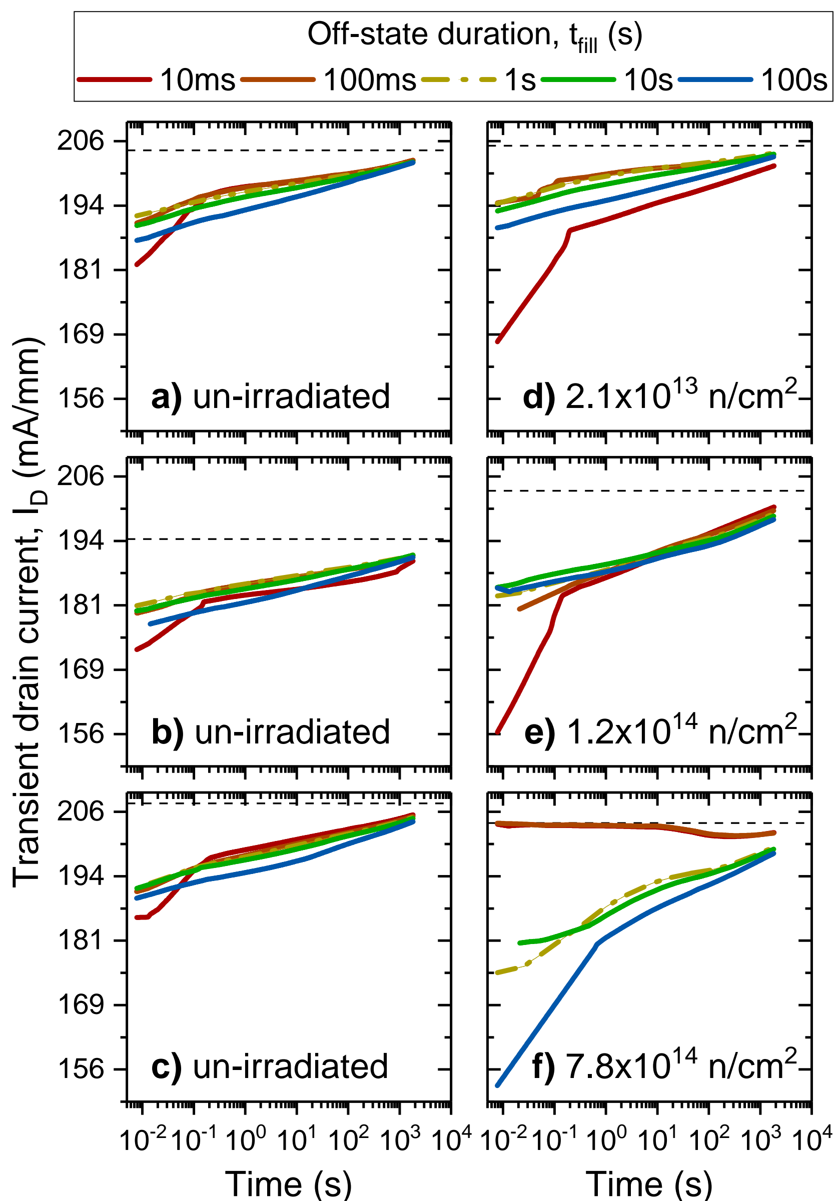

Figure 5.3: Drain current transients after t_{fill} of 10 ms to 100 s in decade steps, prior to irradiation (a, b, c), and for corresponding HEMTs following neutron irradiation to fluences of: 2.1×10^{13} n/cm^2 (d), 1.2×10^{14} n/cm^2 (e), and 7.8×10^{14} n/cm^2 (f). The dashed lines indicate $I_D(t = \infty)$. Values are normalised by gate width ($W_G = 800$ μm). Adapted from [110].

were present in the magnitude and the hysteresis of the I_{DS} curves, suggesting altered trapping behaviour, as shown in the figure. However, as is the case for the changes in the spectra shown in Figure 5.4, a clear trend is not apparent in the DC measurement results.

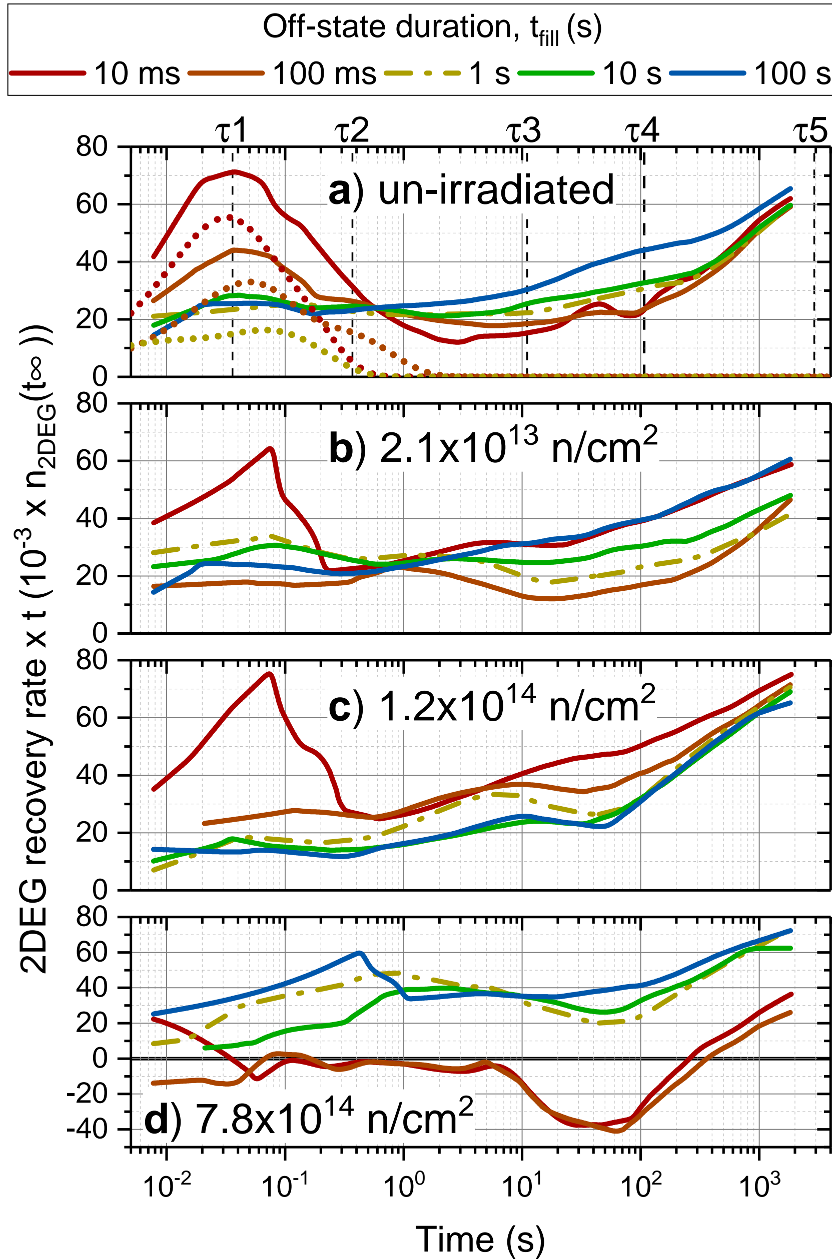

Figure 5.4: Measured transient spectra for all t_{fill} values before irradiation (a), and as a function of increasing neutron fluence: (b), (c), and (d). The time constants for the five fitted Type (II) traps are shown. To fit the 10 ms and 100 ms spectra in (d) required a negative baseline. Dotted coloured lines in a show the sum of the fitted $\tau 1 + \tau 2$ components for $t_{fill} = 10$ ms, 100 ms, and 1 s. (a) and (b) are the same device before and after irradiation. Reproduced from [110].

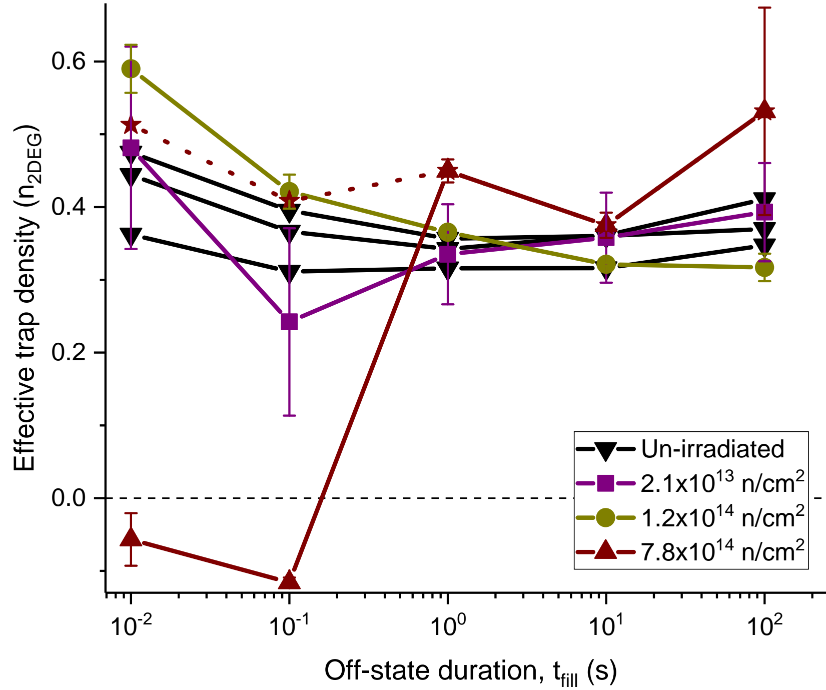

Figure 5.5: Effective density of trapped negative charge within the depletion region emitted during the measurement, plotted against off-state duration as a function of neutron fluence. Densities were found by integrating fits of the 2DEG recovery rates of the depletion region in Fig. 5.4. Starred points connected by dots show the maximum fluence case after subtracting the positive charge emission found by fitting Equation (5.11). Connecting lines are a guide to the eye. Adapted from [110].

5.7 Damage modelling

In order to estimate the displacement damage produced by the neutron irradiation, radiation transport calculations were performed [127] using the Monte Carlo particle radiation transport code MCNP6 [128]. The results of those calculations showed that differences in the number and energy spectra of primary knock-on atoms (PKAs) produced in the HEMT semiconductor regions due to 14 MeV DT neutrons and 2.45 MeV DD neutrons were minimal. The variation in the incident neutron energy spectrum with time, described earlier, can therefore be disregarded in this analysis. PKA density was calculated to be between 1×10^{-7} and 8×10^{-7} $\text{cm}^{-2}/(\text{n/cm}^2)$, with the highest densities expected in the gate-drain and gate-source access regions due to higher energy PKAs from the SiN passivation entering the barrier.

The stable defect densities resulting from the irradiation were estimated by using the modified Kinchin-Pease model [57] and setting mean damage energy equal to the calculated primary recoil energy in each spectrum division. Defect densities calculated in this work are for indication only because of the inherent difficulties involved [105] when considering displacement damage in binary and ternary alloys with widely differing atomic numbers and the uncertain influence of

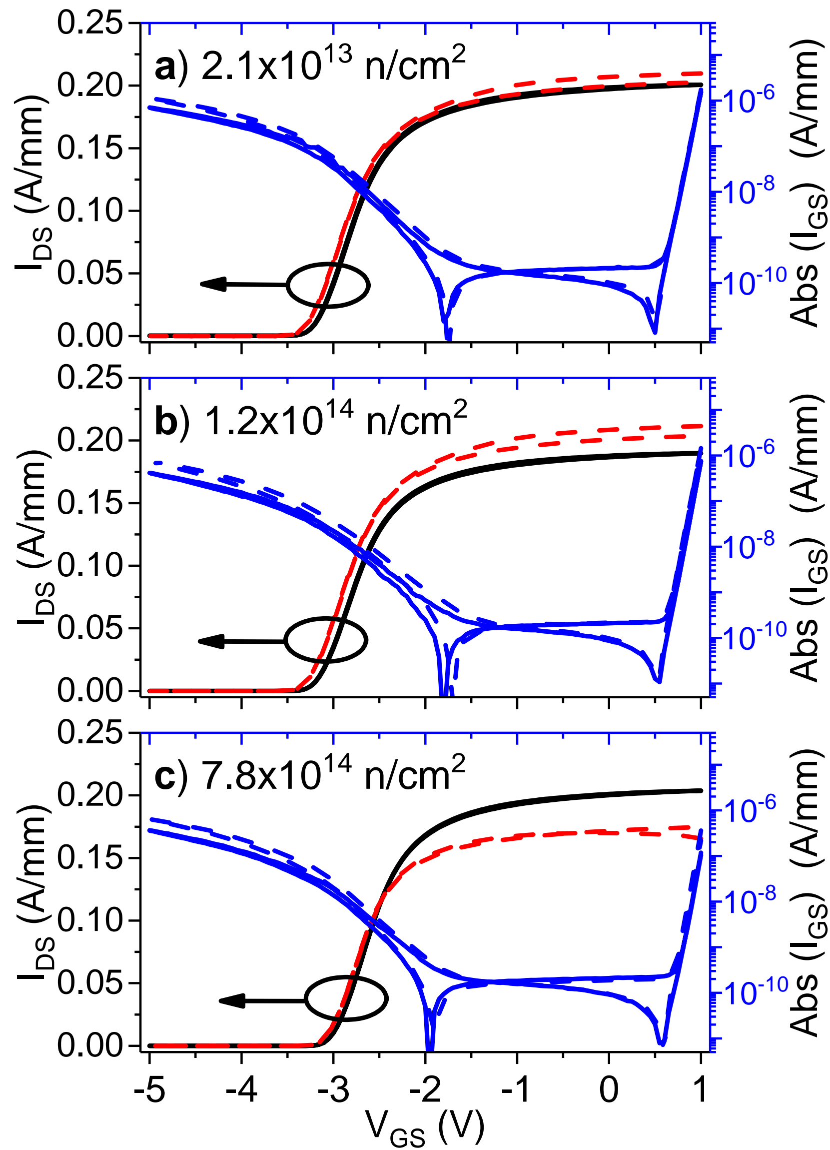

Figure 5.6: Drain-source current (I_{DS}) and gate-source current (I_{GS}) each normalised by gate width (W_G = 800 μm), are shown plotted against gate-source voltage (V_{GS}). Drain-source voltage was V_{DS} = 0.5V. (a), (b), and (c) show un-irradiated (solid lines), and corresponding irradiated (dashed lines) characteristics for each HEMT. Reproduced from [110].

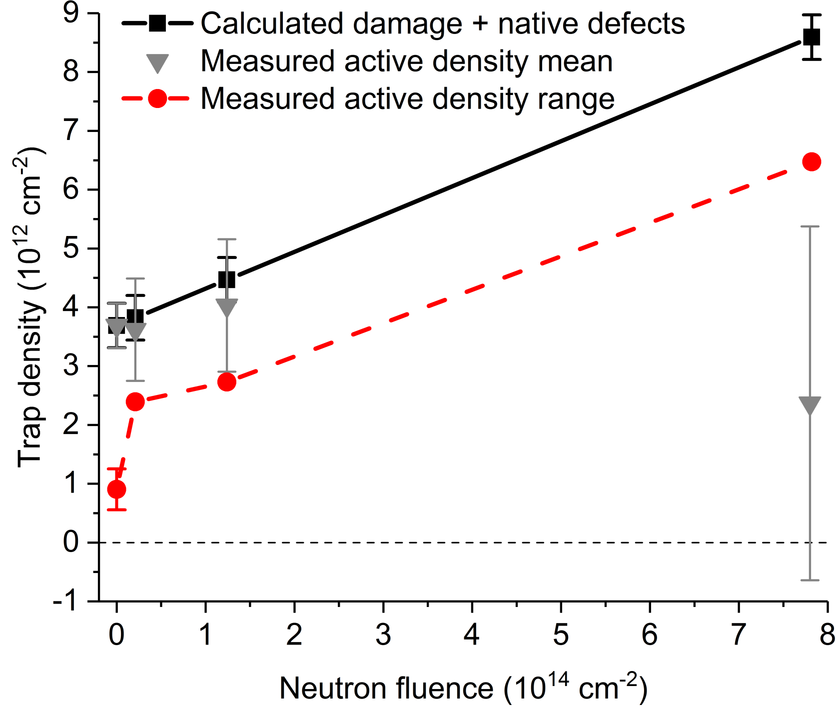

Figure 5.7: Sum of calculated irradiation-induced stable defect density and measured native density against neutron fluence. The active trap density in the depletion region, and the maximum change in active density by varying t_{fill} (the range), found by fitting Equation (5.11) to the current transient spectra and assuming a nominal $n_{2DEG}(t=\infty) = 10^{13}\,\text{cm}^{-2}$ are shown for comparison. Connecting lines are a guide to the eye. Reproduced from [110].

clustering at the high peak PKA energies considered (MeV). The calculated defect densities under the gate are $2.81 \times 10^{-4}\,\text{cm}^{-2}/(\text{n/cm}^2)$ in AlGaN and $3.77 \times 10^{-3}\,\text{cm}^{-2}/(\text{n/cm}^2)$ in GaN. In the access regions, defect densities of $4.53 \times 10^{-3}\,\text{cm}^{-2}/(\text{n/cm}^2)$ in AlGaN and $4.52 \times 10^{-7}\,\text{cm}^{-2}/(\text{n/cm}^2)$ in GaN were calculated. The expected stable defect densities within the HEMT depletion regions, as plotted in Fig.5.7, were calculated using these values and setting $n_{2DEG}(t=\infty) = 10^{13}\,\text{cm}^{-2}$.

By assuming that all calculated defects within the region bounded by L_P and extending throughout the GaN buffer are electrically active, it was calculated that approximately one third of the measured trapped charge would be expected to be located in each of three HEMT regions, 1) the AlGaN in the access regions on the source and drain sides of the gate, 2) the bulk GaN in the access regions, and 3) the GaN under the gate. Surprisingly, only around 3% of the trapped charge would be expected to be stored in the AlGaN under the gate. GaN buffer defects would therefore account for around two thirds of the measured traps.

Considering the approximate nature of the calculation described above, it is encouraging that the measured active trap densities, and their range probed by varying t_{fill}, are less than, but broadly comparable to, the defect densities expected from the damage modelling (Figure 5.7). It is possible that the trapped charge changes measured following irradiation are due to changes in

pre-existing traps, however this calculation confirms that the trap density changes can plausibly be attributed to displacement damage.

5.8 Discussion of the neutron testing results

Prior to neutron irradiation, little device-to-device variation in trapping was observed using drain current transient spectroscopy, as seen in Figures 5.3, 5.5, and 5.7. The measured active trap density range found by varying t_{fill} was $(9.0 \pm 3.5) \times 10^{11}$ cm^{-2} prior to irradiation; it more than doubled to 2.4×10^{12} cm^{-2} after irradiation to 2.1×10^{13} n/cm^2, and increased further with increasing neutron fluence. The HEMT 2DEG channel density transients, $n_{2DEG}(t)$, calculated from $I_D(t)$ by accounting for the limited depletion region contribution to the extrinsic HEMT drain-source resistance, are reasonably well fitted using Equation (5.11), suggesting that the model is credible.

Damage constants for mobility reduction due to displacement damage in compound semiconductors are expected to be several orders of magnitude lower than for carrier lifetime reduction [76], as discussed in Chapter 4. As shown by the dashed lines in Figure 5.3, $I_D(t = \infty)$ levels are largely unchanged after irradiation. It is expected, therefore, that neutron-induced mobility reduction is not significant in the results presented in this chapter.

There is an expectation that Type (II) trap occupancy depends exponentially on t_{fill} under low trapping conditions, or has a logarithmic t_{fill} dependence under high trapping conditions [129]. However, the sum of the active density of $\tau 1$ plus $\tau 2$ in the un-irradiated HEMTs decreased as t_{fill} was increased from 10 ms to 1 s, shown by the dotted coloured lines in Figure 5.4(a); whereas the active density of slower traps ($\tau 3$, $\tau 4$, and $\tau 5$), increased monotonically with increasing t_{fill}. Total active trap densities (Figure 5.5), show a non-monotonic dependence on t_{fill}. This is surprising since active trap density is a function of occupancy, and should therefore increase or saturate with increasing t_{fill}, but not decrease. This observation can be explained if trap occupancies are coupled.

A mechanism for the trap coupling suggested by the non-monotonic t_{fill} dependence of active trap density would be charge migrating to more energetically favourable locations during long periods of off-state biasing: either to traps with time constants outside the measurement range, or to regions where it is less effective at depleting n_{2DEG} (e.g. migrating from the GaN buffer, where the 2DEG is the only screening conductor, to the AlGaN barrier under the gate where image charge will partially reside on the gate). Two distinct peaks in a HEMT I_D transient spectrum can also be caused by two rate limiting conduction pathways from a single trap [130]. Given the apparent coupling and lack of straightforwardly extractable time constants, it is not possible to attribute the defects to those listed in papers such as [74, 124].

After irradiation the active density of all traps displayed a non-monotonic dependence on t_{fill} (Figure 5.4(b), (c), and (d), with the resulting overall increase in coupling and device-to-device

variation apparent in Figure 5.5. Maximum active trap densities also increased after irradiation to a fluence of 1.2×10^{14} n/cm^2 and above. This could be caused by displacement damage affecting conduction pathways by altering the potential distribution in the bulk as it charges, or by enhancing inter-trap coupling because of its increased density. The baseline of Type (I) traps was suppressed for the highest irradiation level (where calculated damage density exceeded native trap density) followed by measurement at short fill times (Figure 5.3(f)). This suggests that either 1) Type (I) traps were actually a superposition of discrete traps, and irradiation caused the traps to change to respond outside the measurement time window or 2) the continuum trap was screened by the enhanced charge in Type (II) traps, i.e. another coupling mechanism. The increased range of active trap density achievable by varying t_{fill} after irradiation (Figure 5.7), could be due to coupling to traps with time constants outside the measurement window, and an increased density of traps with time constants within the measurement window, as expected from the displacement damage calculations.

Iron (Fe) doping is used in these devices to achieve semi-insulating GaN buffers and to eliminate punch-through effects [131]. This is known to make GaN n-type, unless excess carbon renders the GaN p-type [132], although other intrinsic defects such as vacancies and interstitials are likely to be present, as discussed earlier, and would contribute to the effective doping. Bardeleben et al. [133] found that particle irradiation can generate a split nitrogen interstitial defect (ambipolar, acting as a deep acceptor at $E_c - 1.0$ eV in n-type GaN and as a deep donor in p-type GaN), at a rate close to that of the generation of nitrogen interstitials (acceptors in n-GaN [134]). In p-type GaN the nitrogen vacancy, a donor, has the lowest formation energy [135], whereas in n-type GaN the gallium vacancy is most likely and acts as an acceptor. The net effect of these defects is likely to increase the intrinsic nature of the GaN by compensation, thus reducing conductivity, although hopping conduction can lead to an increase in leakage current under reverse bias. These mechanisms are illustrated in Figure 5.8(a) for band-edge transport where a net increase in trapped negative charge occurs. Donors, which are positioned deep in the buffer, are neutralised by electron capture, and holes are emitted by acceptors. In Figure 5.8(b) trapped negative charge is shown to be emitted into the channel and gate by ionising deep donors and by hole current flowing into the buffer. Therefore, it is plausible that displacement damage defects, the approximate densities of which were given above, are responsible for the observed changes in HEMT switching and transient recovery characteristics.

The transient recovery of HEMT output current following off-state biasing has a complex dependence on biasing conditions after irradiation: changes can vary from an apparent complete suppression to a major enhancement of active trap density, increasing gate lag and resulting in slower overall I_D recovery. This demonstrates that AlGaN/GaN HEMT neutron damage susceptibility is more complex at these irradiation levels than suggested by previous reports of either neutron-induced defect suppression [109], or output degradation [106, 108].

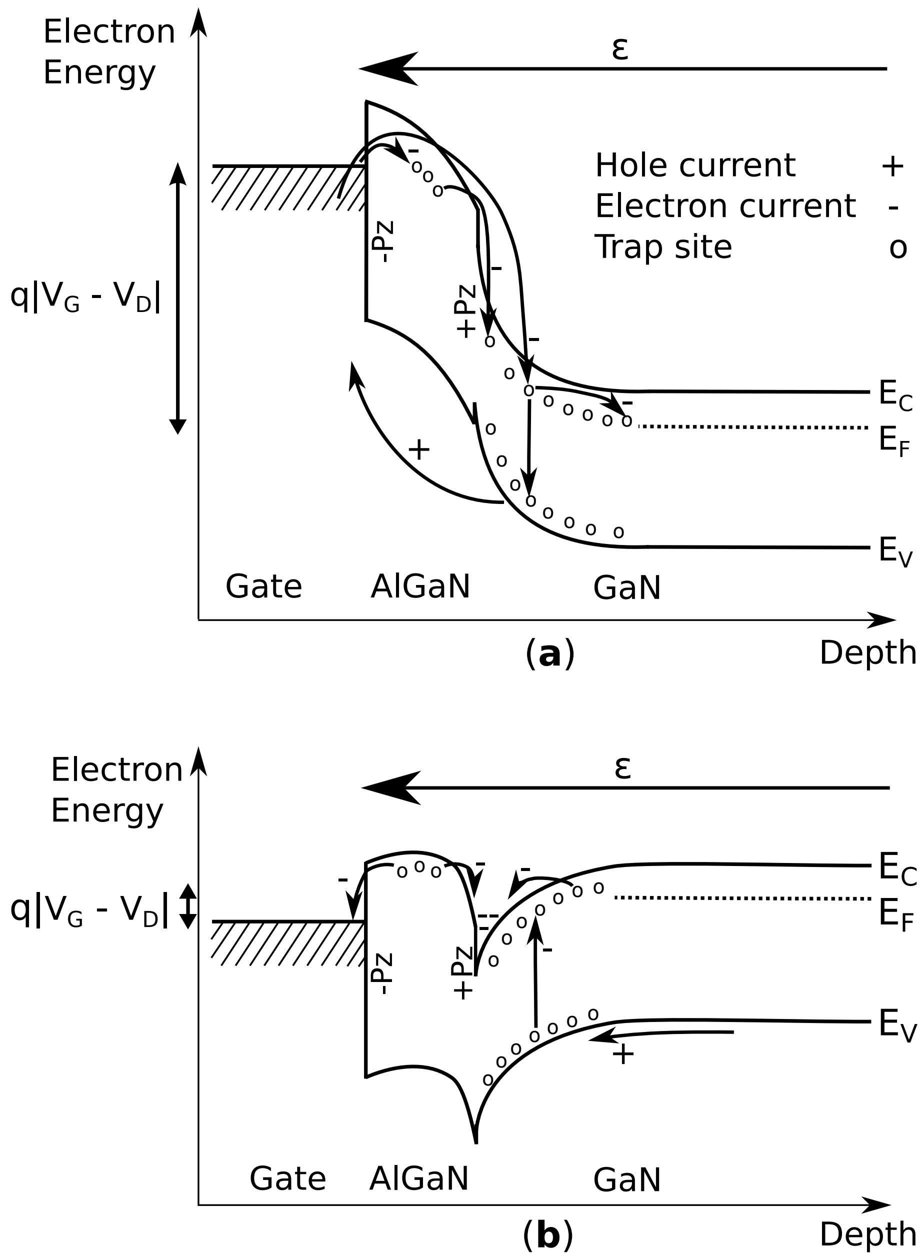

Figure 5.8: Band diagrams showing charge (de)trapping currents for the region under the HEMT gate during: (a) off-state ($V_g = -10\,V$, $V_d = 0.5\,V$), and (b) on-state biasing ($V_g = 0\,V$, $V_d = 0.5\,V$). Modified from the equivalent figure presented in [110].

5.9 Conclusions

In this chapter, we have seen that despite the well-known insensitivity of AlGaN/GaN HEMT DC characteristics to neutron irradiation when compared to competing technologies, 14 MeV neutron irradiation of 2×10^{13} n/cm^2 and beyond can alter the magnitude and duration of AlGaN/GaN HEMT switching transients. The changes to the transient switching behaviour of the HEMTs have been shown to be due to not only increases in trap density, they have also been shown to be due to inter-trap coupling.

The recovery rate of 2DEG density, and therefore drain current, following off-state to on-state switching was shown to decrease or increase after irradiation, depending in a complex manner on trap filling conditions. This was reflected in the DC Vg-Id characteristics. The complex 2DEG density recovery rate dependence on trap filling conditions merits further research to better understand the implications for using AlGaN/GaN HEMTs in radiation environments where displacement damage is likely. However, the increased range of active trap density that can be observed by varying off-state duration prior to switching HEMT was found to increase monotonically with the neutron irradiation fluence that the HEMTs were exposed to, suggesting that the range of active trap density might be a useful damage measure.

It is unlikely that simulations of HEMT performance after irradiation based on testing a small set of biasing conditions and using simple charge trapping models such as Equation (5.11) would capture the complex emergent trap coupling behaviour that has been shown in this chapter. Since the trap coupling behaviour affects HEMT output current stability, an important consideration in circuit applications, HEMT transient characteristics should be considered in addition to DC parameters when assessing and certifying components for use in harsh neutron radiation environments.

We have now seen that effects of neutron irradiation on WBG/UWBG structures and devices can be observed *ex-situ*. Knowledge of these changes can aid semiconductor device design, and can be used to design electronic systems that are tolerant to parameter changes after exposure to displacement damage-causing radiation fields. We have not yet considered what happens in semiconductors, and their devices, *during* irradiation. Aside from the interesting device physics of transient radiation effects, such understanding is particularly important for designers of safety critical systems, and will be explored in the next chapter.

CHAPTER 6

PULSED INERTIAL CONFINEMENT FUSION (ICF) NEUTRON EFFECTS

In this chapter, we consider the *in situ* effects of short busts of neutrons upon HEMTs. Unlike the cumulative displacement damage effects due to neutrons discussed in Chapters 4 and 5, the effects of exposing HEMTs to short bursts of neutrons can be transient or permanent in nature. Pulsed ICF neutron sources make it possible to measure the DUT response to neutrons, without the radiation effects due to delayed decay components of materials in the test area, and those due to background radiation fields, which can be present at reactor facilities and accelerator-based sources. Developing and demonstrating effective methods for radiation effects testing at pulsed ICF neutron sources acts as a proof of principle for neutron-effects testing using such facilities. Because of the neutron fluence achievable within a single pulse of an ICF source, of the order of $10^{11}\,\mathrm{n\,cm^{-2}}$ within hundreds of pico-seconds, multiple neutron interactions in a DUT can be expected within a single short irradiation pulse. As discussed earlier in this thesis, each neutron-induced PKA scattering event can cause a cascade of thousands of secondary events within the active region of the semiconductor DUT, causing a complex pattern of ionisation and displacement damage. By measuring how semiconductor devices respond to pulsed ICF neutron environments, the transition from SEEs to 'dose rate' effects can be understood. This environment, therefore, provides a means of determining whether DUT radiation response in high flux environments can be predicted by modelling it as a sum of SEEs.

The Omega laser [136] at the Laboratory for Laser Energetics, University of Rochester, NY, USA, provided the pulsed ICF neutron environment used here. Omega's 60 beams deliver up to a total of 30 kJ of ultraviolet laser light directly onto a deuterium and tritium (D-T) filled target capsule. The direct laser-drive heats the capsule, releasing X-rays, ejecting capsule material, and causing an implosion of the D-T fuel. For a short time, this creates the conditions necessary for

nuclear fusion within the capsule. The onset of the nuclear fusion burn of the D-T fuel is known as ‘Bang Time’. Development of diagnostics to monitor ICF experiments are an area of active research, and can utilise monitoring of the gamma rays which are emitted from a small fraction of the D-T fusion reactions within the implosion [137]. Figure 6.1 shows the relative timing at the Target Chamber Centre (TCC), where the 60 laser beams are incident upon the D-T filled capsule, of the X-ray production due to the laser heating of the capsule, and the subsequent gamma output used to monitor nuclear fusion. During D-T fusion an excited $^{5}\mathrm{He}^{*}$ nucleus is initially produced, which can decay by several branches. The most likely branch, discussed earlier in this thesis, results in the production of a 3.5 MeV alpha particle ($^{4}\mathrm{He}$), and a 14.1 MeV neutron. Alternatively, however, a gamma ray can be released instead of a neutron,

$$\mathrm{D}+\mathrm{T} \rightarrow {}^{5}\mathrm{He}^{*} \rightarrow {}^{5}\mathrm{He}+\gamma(16.75\,\mathrm{MeV}). \tag{6.1}$$

Other gamma production reactions are also possible. The total gamma-to-neutron branching ratio for D-T fusion has been reported [138] to be $(4.2 \pm 2.0) \times 10^{-5}$. The mean free path, λ, for a 16.75 MeV gamma photon in GaN, calculated using the $0.03092\,\mathrm{cm^{2}\,g^{-1}}$ total interaction cross-section taken from [139], and the $6.15\,\mathrm{g\,cm^{-3}}$ density of GaN, is 5.26 cm. 14.1 MeV neutrons in GaN have $\lambda \approx 10\,\mathrm{cm}$ (Chapter 2). This means that the gamma-to-neutron interaction ratio in GaN should be around 8×10^{-5}. The maximum possible ionisation caused by each 16.75 MeV gamma photon is of the order of 10x that due to neutron elastic scattering (see Table 2.1), giving an expected gamma-to-neutron ionisation ratio, in GaN, of ≈ 0.001. Ionisation due to the gamma field caused by the ICF burn at Omega will, therefore, be disregarded below.

Knock-on ions generated by neutron interactions within passivation layers, and metal contacts, can enter the semiconductor regions, deposit charge, and potentially cause SEEs. Displacement damage from these interactions was apparent in the results presented in Chapter 5. However, Bazzoli *et al.* [32] found that 14 MeV neutron irradiation did not cause Single Event Burnout in GaN HEMTs. They also did not observe single event breakdown events during irradiation with ion sources providing either LET=$1.8\,\mathrm{MeV\,cm^{2}\,mg^{-1}}$ or LET=$18.5\,\mathrm{MeV\,cm^{2}\,mg^{-1}}$. However, a destructive event was observed during ion irradiation with LET=$60\,\mathrm{MeV\,cm^{2}\,mg^{-1}}$, suggesting a threshold LET exists for the onset of breakdown in GaN HEMTs. Neutrons down-scattered in energy by surrounding materials can be captured by nuclei in the GaN due to (n,α) reactions. The probability for such reactions involving low energy neutrons scales as $\sigma \propto v^{-1} \propto E^{-1/2}$. where v and E are neutron velocity and energy, respectively. The subsequently emitted high energy alpha radiation can have energies in the MeV range, which could cause SEE to be observed at Omega.

The Omega laser experiments, discussed below, were conducted with the following objectives. Firstly, to observe fast neutron-induced SEEs in GaN-based HEMTs. These effects include catastrophic failure due to Single Event Gate Rupture (SEGR) [140], and transient switching from off- to on-state, known as Single Event Switching (SES) [141]. Secondly, to observe any displacement damage-induced effects, including output current degradation, and increases in charge trapping. The final objective was to establish whether neutron effects testing of GaN

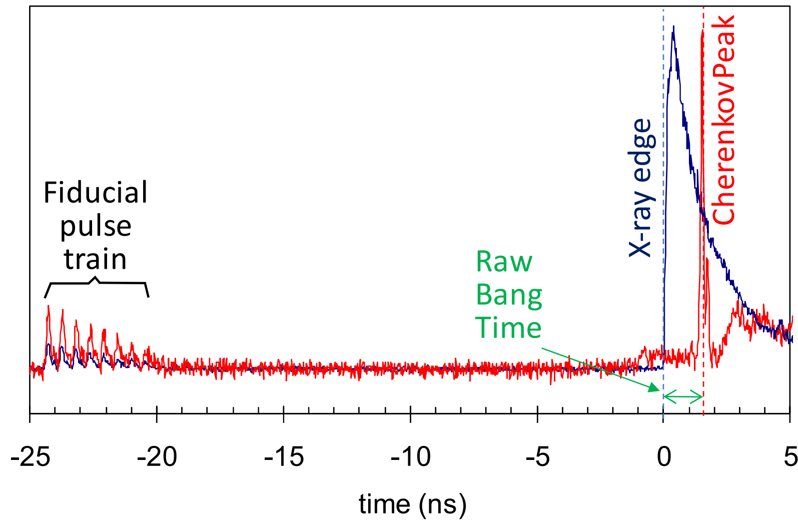

Figure 6.1: The relative timings, at TCC, of X-ray and neutron outputs during an Omega laser ICF burn. X-rays are generated by the interaction of the 60 beams of the Omega laser with the ICF capsule located at TCC. The red line is the output from a gas Cherenkov detector, which converts gamma rays emitted by nuclear fusion into UV and visible photons, which are detected with their number recorded as a function of time. The portion of the red line labelled Cherenkov Peak, indicates the time of the peak in nuclear fusion rate. Figure reproduced from [137].

HEMTs could be successfully conducted using the Omega laser ICF source. In support of these objective, three separate trials were performed at Omega. On each return the measurement setup was improved with an emphasis on reducing electrical noise, and improving neutron effects measurement fidelity. The attempts at noise reduction and test setup optimisation were partially successful, and for this reason an abridged account of the work is provided here.

6.1 Experimental Details

6.1.1 Devices tested

All devices tested at Omega were provided by NXP (now Nexperia). They were GaN-on-Si HEMTs, in two nominal sizes of gate width, $W_G = 400\,\mu$m, and $W_G = 50\,$mm. Here, these are referred to as small (S-Type), and large (L-Type), respectively. Large devices were fielded with either Schottky gates (L-Type), or metal-insulator-semiconductor (MIS) gates (M-Type). S-Type devices were fielded with Schottky gates only. Nominal source-drain separation for all devices was $L_{SD} = 12\,\mu$m. Measured device characteristic curves for L-Type and M-Type devices are shown in Figure 6.2. Large power devices are of particular relevance to power switching applications, and were tested here to present a large cross sectional area to the incident neutrons. For a nominal Omega shot and the TCC-DUT distance used for this work, tens of PKA interactions would be expected within the sensitive volume of an S-Type HEMT, and thousands would be expected within the

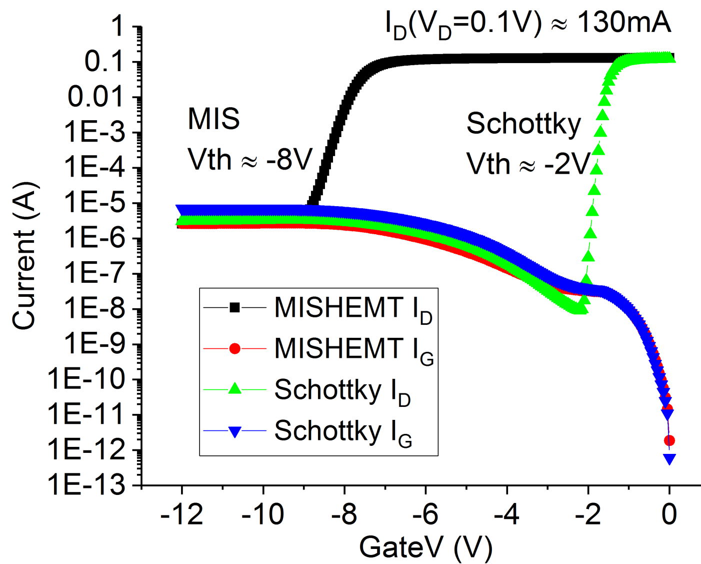

Figure 6.2: Characteristic curves for large Schottky-gate HEMTs (L-Type), and MIS HEMTs (M-Type) fielded at Omega. Important device parameters are indicated.

sensitive volumes of L-Type and M-Type HEMTs, based on calculations performed for the work in Chapter 5.

6.1.2 Omega laser ICF test series and output

Three ICF neutron trials were conducted at the Omega laser. The first was in May 2016, where a small number of shots were conducted to test the response of 400 μm Schottky gate HEMTs (S-Type), and to test the feasibility of developing measurements using the facility. During the second trial, conducted during October 2016, 50 mm Schottky and MISHEMTs (L-Type and M-Type), and a small number of 100 mm MISHEMT were fielded in addition to S-Type HEMTs. These first two trials exposed some technical challenges associated with fielding powered semiconductor device tests at the Omega ICF facility, and also provided some initial results, summarised below. The final Omega trial was conducted during April 2017, where S- L- and M-Type devices were fielded, with an increased through-shot bias maximum bias of 150 V available, and several improvements to the test fixture, circuit, and cabling arrangements. The April 2017 data are the focus of this analysis.

During the April 2017 shot day, the average bang time and width were (1261 ± 90) ps and (132.1 ± 8) ps, respectively. The average neutron fluence delivered to each HEMT by an Omega shot was $(9.2 \pm 0.5) \times 10^{10}$ n/cm^2, with a total ionising dose from all prompt and delayed sources of (0.49 ± 0.05) Gy(Si). An absolute time reference to compare measured data to $t = 0$, as shown in Figure 6.1, was not available. Future test data capture arrangements should incorporate a

fiducial signal with a fixed relation to $t = 0$ at TCC, as shown in the figure. Instead, $t = 0$ in the following results has been placed at the start of apparent X-ray-induced signal, and is at the same fixed position for all shots, consistent with the triggering arrangements for the data capture hardware.

6.1.3 Test circuit and measurements made

Devices under test were mounted on custom made PCBs, which were fixed into a motherboard at the end of a Nuclear Effects Diagnostic (NED), as shown in Figure 6.3(a). The NED is an air-tight metal enclosure, designed by Sandia National Laboratories, to field diagnostic experiments at Omega. The NED was sealed to form a Faraday cage, with the exception of the shielded electrical connection ports at its rear. The NED was contained with a Target Insertion Module (TIM), which was fitted into the Omega target chamber. This enabled the NED to be positioned correctly within the Omega target chamber, avoiding the incident laser beams, and presenting the front face of the NED where the HEMTs were at a nominal distance of 11.4 cm from the TCC. Power and signal cables connected to the bottom of the NED were connected to an electrical interface at the rear of the TIM via 64"(1.63 m) cables. Connections to the outside of the interface were then routed through conduits along a 100 feet (30.48 m) cable run to instrumentation racks within the diagnostic control room known as 'La Cave'. This is where device biasing was applied, and signals were monitored and captured using digital storage oscilloscopes. Electrical biasing was applied to the HEMTs during each shot of the Omega ICF facility. HEMTs were tested in an either on-state ($V_G = 0\,V$), an off-state ($V_G < V_{th}$), or an intermediate state where the channel was partially depleted ($V_{th} < V_G < 0\,V$).

Three sets of transient data were captured during each Omega shot by using three sets of oscilloscopes in the instrumentation rack. They spanned different timescales from fast (10^{-10} to 2×10^{-6} s), intermediate (10^{-7} to 2×10^{-2} s), and slow (10^{-3} to 2×10^{2} s). Current viewing resistors (CVRs) were used in series with the HEMT drain connections, effectively putting the HEMT into a low-side switch configuration. CVRs were also used to monitor current on the gate connections. Differential voltage measurements were made across these in addition to node to facility ground voltage measurements. These signals were used for intermediate and slow timescale measurements, to investigate delayed effects after the fast measurement timescale of the differential RF transformer signals, described below, had ended. Testing of DC HEMT parameters, and dynamic iV analysis (DiVA) tests, were performed to characterise the HEMTs before irradiation, and afterwards.

The final test circuit PCB, fielded during the April 2017 trial, featured capacitors placed across the power lines of the DUT to decouple the response from the long cable run to the PCB. A low-pass filter was included to protect the HEMT gates from damage by electrical transients induced on the gate bias cable by neutron-induced ionisation effects and X-ray induced photo-ionisation effects. The magnitude of such unwanted transients depends on the conductor and

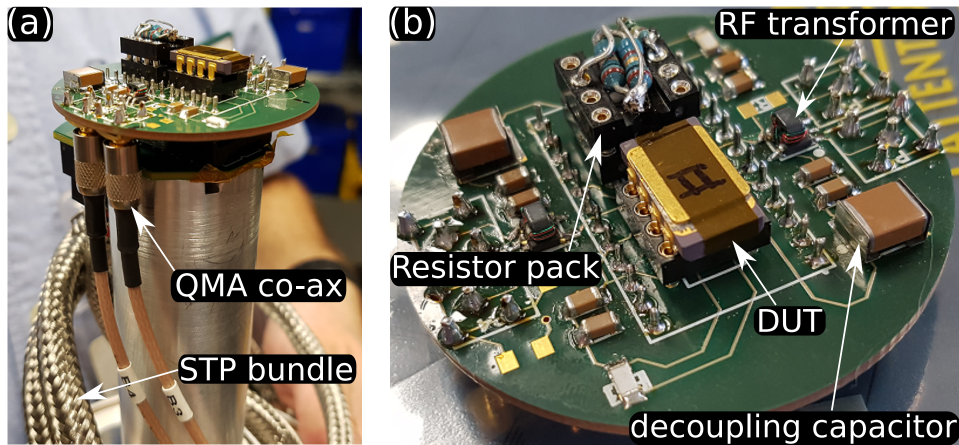

Figure 6.3: Final Omega Laser test PCB design. (a) NED cover removed to show resistor pack and DUT fitted to an Omega test PCB. The small motherboard is beneath the test PCB. The high-bandwidth co-ax cables shown were used for fast measurement of drain current transients, and were connected to the PCB using push to fit QMA connectors. Also visible is the external shield of the shielded twisted pair (STP) cable bundle, used to bias the DUTs. (b) Close up view of a test PCB with one DUT fitted. In the second DUT slot, a resistor pack has been fitted for use as an experimental control. Decoupling capacitors, filter resistors, and equivalent centre-tapped RF transformers are visible.

dielectric materials used in the cables, and on their location and biasing. During Omega ICF shots these signals can generate hundreds of mV across a 50Ω termination, even when unbiased [142]. Such a signal could cause a change in drain current output which could be misinterpreted as an irradiation effect on the DUT. For the 2017 circuit design, to enable low-noise drain current transient measurement in the presence of radiation-induced signals on the test fixture ground and cables, a common-mode noise cancelling arrangement was used. This was achieved by using a transmission line transformer in combination with a DC block to form a circuit equivalent to a centre-tapped RF transformer in series with the ground connection for the decoupling capacitors. By digitally subtracting the two outputs of the transformer, after data capture by measuring the voltage across 50Ω terminations fitted to the oscilloscopes, common-mode noise was removed from the drain current transient signal.

6.1.4 Electrical noise challenges and characterisation at ICF neutron sources

During an Omega Laser ICF neutron shot, there are many sources of electrical noise which can interfere with a measurement. The noise sources include the electro-magnetic pulse (EMP) from the accelerating charges in the implosion experiment; the EMI from the electrical power systems of the laser banks as they fire; the photo-currents induced by the X-rays emitted from interaction between the laser beams and the target capsule; the effects of the emitted gamma

rays and those due to emitted charged particles. Noise couples to experiments within a NED via system-generated electromagnetic pulse (SGEMP), and via signals injected from the cable run connected to the NED. Transient signals can be generated on co-axial cables due to X-rays liberating charge from their constituent conductors. EMP can couple to exposed conducting surfaces and ground planes, thus inducing signals into the measurement system. The neutrons themselves also induce electrical currents in the cabling connected to the DUTs, as discussed in [142]. Signals are expected to be measured due to the X-ray and neutron pulses, followed by signals due to the above sources of noise and interference coupling to the cables connected to the DUTs. Signal reflections will also occur at the interfaces along the cable run, as will signal oscillations, due to the reactive elements present in the measurement circuits. For this reason, only fast measurement system data for the period before $t = 0$ and for approximately 20 ns afterwards will be analysed in detail.

To reduce and control the above noise effects during the April 2017 trial the following features were used. Co-axial cables were introduced for as many lines as possible at the time. Shielded twisted pair cables were used where co-axial was not available, and were fielded in balanced signal transmission mode where possible. Care was taken to optimise grounding arrangements to minimise noise pickup, and allow fast signal transmission. Common-mode noise cancellation techniques were also employed, as discussed above. The entire cable run was routed inside an overall shield. Measurements were made throughout the evolution of the test setup to characterise the electrical noise.

The results of a dedicated noise measurement fielded during the April 2017 shot day are shown in Figure 6.4. A resistor pack was installed in place of a HEMT on a test PCB and exposed to an Omega shot. The resistor values were chosen to mimic a HEMT biased in the off-state. An equivalent on-state measurement was also performed, however, there was a problem with the data capture on that shot, and so the results are unavailable. In the figure the X-ray flash and Bang Time are shown, based on average values for the day because the Gamma Reaction History (GRH) diagnostic data for this particular shot were unavailable at the time of writing. GRH data was, however, available for most shots, and was used to produce the figures shown in the Results section below. Peak 1 is indicated as the peak which appears to result from the X-ray flash. The highlighted X-ray and neutron regions on the figure were calculated by using the average duration of the laser firing and the nuclear fusion burn, along with the respective times of flight from TCC to the PCB for photons and neutrons, and estimates for the signal broadening effect of the cable run and diagnostic systems. After an initial signal is produced by the decoupling capacitor current, indicating a change of voltage across the DUT, a return current will flow to recharge them. The return current is seen as the negative-going signal after Peak 1. This would be expected to quickly decay to zero in the absence of further energy input to the system. Peak 2 immediately follows this, however. Peak 2 is tentatively attributed to neutron-induced effects upon the test PCB and DUT. Further oscillations and signals are apparent after Peak 2, some of

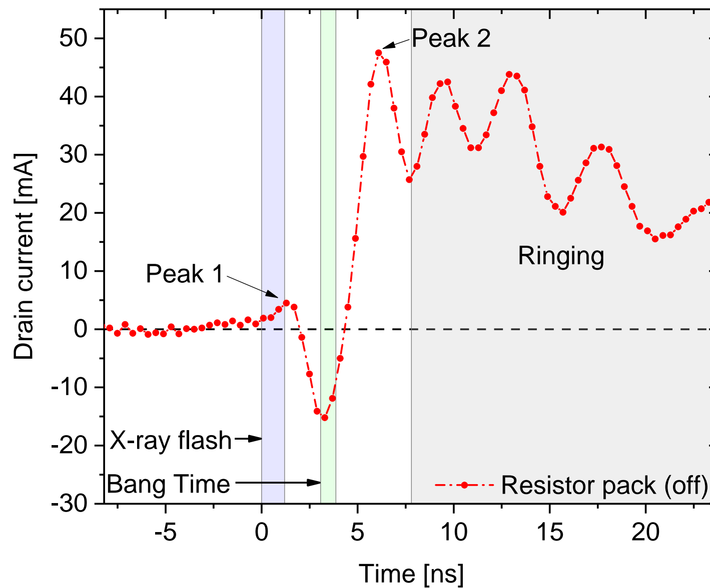

Figure 6.4: Omega facility noise and cable pickup measurement using an off-state resistor pack. The resistor pack was fitted into a socket normally occupied by the DUT, on the PCB at the end of the NED. The blue shaded region beginning at $t = 0$ marks the time that X-rays, generated by the Omega laser drive upon the ICF capsule at TCC, will be incident upon the DUT. The second highlighted region, in green, marks the time when neutrons produced at bang time at TCC will reach the DUT. The resistor pack connections were biased with $V_G = -3\,V$, $V_D = 50\,V$. Note: the displayed X-ray and neutron signal measurement regions are broadened due to the effect of the measurement system bandwidth and the approximately 32 m long cable run from the DUT to the instrumentation rack.

which may be due to irradiation effects on the cable run.

6.2 Results

6.2.1 Summary and discussion of May 2016 and October 2016 trial results

During the first two Omega trials no SEGR events or other catastrophic failures were observed. Permanent device parameter degradation was also not observed following HEMT exposure to the Omega ICF neutron pulse. However, the maximum permissible drain bias for the first two trials was 50 V, far below the designed 200 V operating capability of the devices. Transient response was found to depend on the applied electrical biasing, and upon W_G. Off-state testing produced a noisy fast transient response following the Omega pulse, and then a fast return to off-state operation for all tested devices. On-state testing revealed that large devices recovered their output current to the DC level set prior to irradiation within $\approx 10\,\mu s$. Small devices, however were found to switch off, or decrease their drain current to a near zero, in response to the Omega pulse. The transient recovery of the drain current was found to take tens of seconds to complete. When

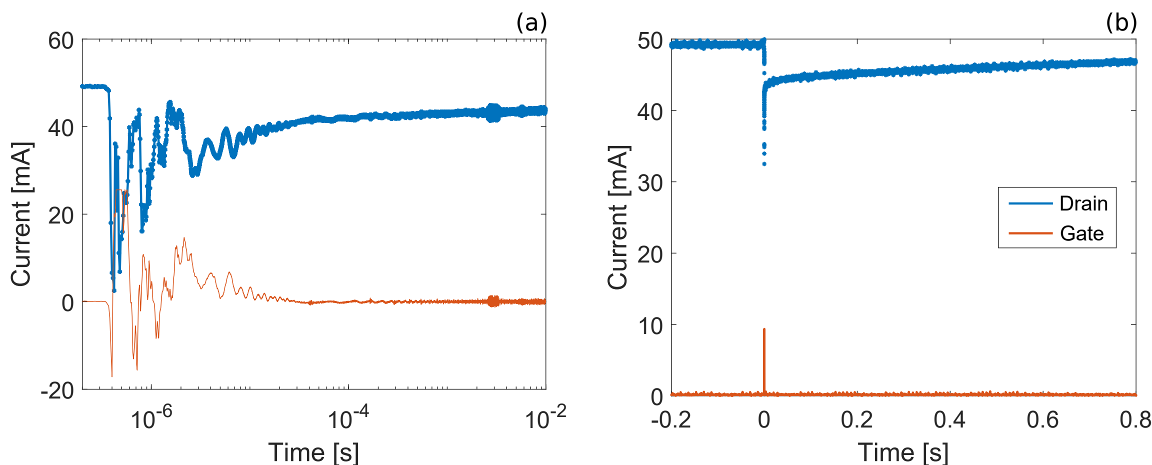

Figure 6.5: On-state current transients due to exposure to an Omega laser ICF neutron pulse. $V_G = 0\,\mathrm{V}$, V_D was set at the PSU to obtain the DC current of approximately 50 mA shown. Measurement perfomred during the October 2016 trial. (a) Intermediate timescale measurement data. Drain current switch-off is visible immediately following the Omega ICF neutron pulse, followed by signal oscillations superimposed upon a recovery transient. A large transient is also visible on the gate signal. (b) Slow timescale measurement for the same Omega shot. Gate current settled back to 0, but the drain current recovery is still continuing with a time constant of the order of seconds.

irradiating HEMTs with an intermediate bias, ($V_{th} < V_G < 0\,\mathrm{V}$), all three device types, S- L- and M-Type, displayed a transient drain current reduction followed by a recovery period. The time constant for the larger devices' recovery was of the order of 10s of μs, whereas it was seconds for the S-Type devices.

Figure 6.5 shows the transient response of an S-Type device to an Omega ICF neutron pulse. The late-time noise apparent at around 0.003 s in this example, occurred for several S-Type devices, often at later times. The slow recovery of the drain current apparent in part (b) of the figure is similar to the switching transients studied in Chapter 5, which resulted from trapped charge following a gate voltage pulse. The transient reduction and subsequent slow on-state recovery of drain current may have been a neutron effect, but could plausibly be explained by an electrical pulse on the gate contact caused by radiation-induced electrical noise pickup on the test cables. The 2016 trials did not feature gate signal filtering, and so to test the plausibility of this explanation, low-pass gate filtering was introduced on the test PCB for the April 2017 trial.

6.2.2 April 2017 Omega trial

The improvements made to the test setup, listed above, made it possible to begin to study the HEMT through-pulse response, and to investigate its bias-dependence. Examples of the transient response of HEMTs to irradiation whilst biased in the off-state are shown here first, followed by on-state examples. Plots of the extracted Peak 1 and Peak 2 magnitudes as a function of biasing

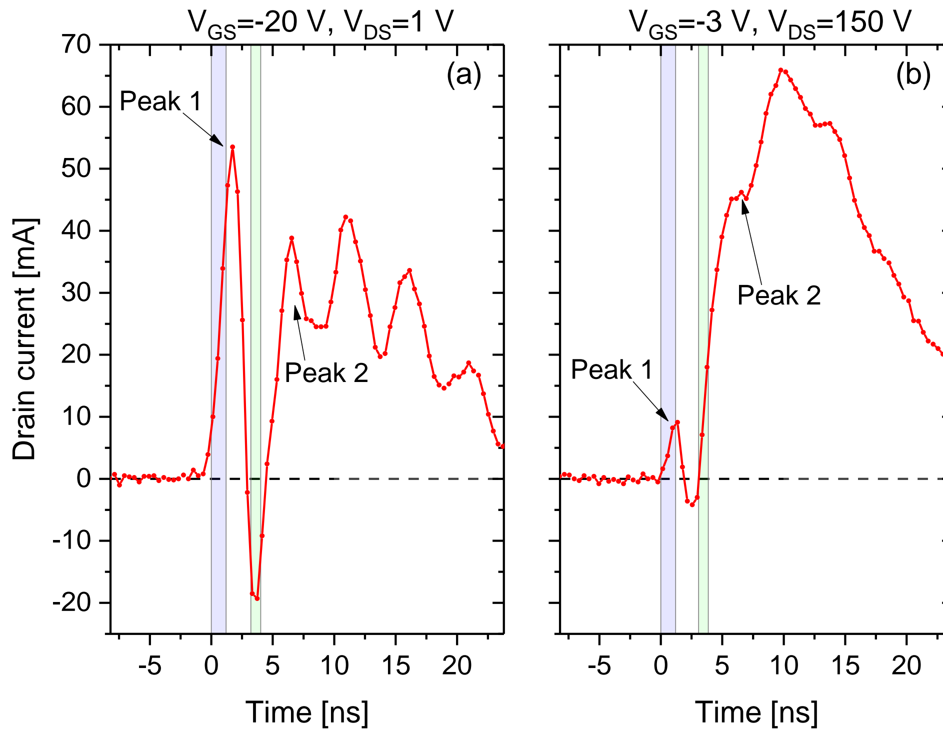

Figure 6.6: Drain current transients measured during exposure to an Omega laser ICF burn. (a) Drain current transient measured for an L-Type HEMT biased with $V_{GS} = -20\,V$, well below threshold, and a small drain bias of $V_{DS} = 1\,V$ applied. (b) Drain transient measured for an L-Type HEMT biased with $V_{GS} = -3\,V$, just below threshold, and a large drain bias of $V_{DS} = 150\,V$. Note: Green shaded neutron signal regions are determined from the bang time and burn width as measured by Omega facility diagnostics for each individual shot.

conditions are then given. The time taken for circuit behaviour to relax back to it's pre-irradition DC value, the settling time, are given next. Finally, a summary of the results of the pre- and post-irradiation characterisation tests for all samples irradiated during the April 2017 trial are shown.

In Figure 6.6 (a) a drain transient measured for an L-Type HEMT with a gate bias applied well below its threshold voltage (hard off) is shown. A drain bias of only 1 V was also applied to the HEMT. In the figure it can be seen that the magnitude of Peak 1 has increased dramatically in response to the increase in negative gate bias, as compared to the control measurement shown in Figure 6.4. Because there is no connection other than a shared ground plane between the gate bias line, and the drain current monitoring lines, this is likely to be a real radiation effect in the HEMT. In part (b) of the figure, for a test with a HEMT biased just below threshold voltage (off), but with a large drain voltage applied, Peak 1 has dramatically reduced, but Peak 2 has increased in magnitude. The ringing occurring immediately after Peak 2, from $t = 7-20\,ns$, is suppressed by the large transient response and decay signal.

The fast timescale results of on-state HEMT Omega irradiation tests are shown in Figure

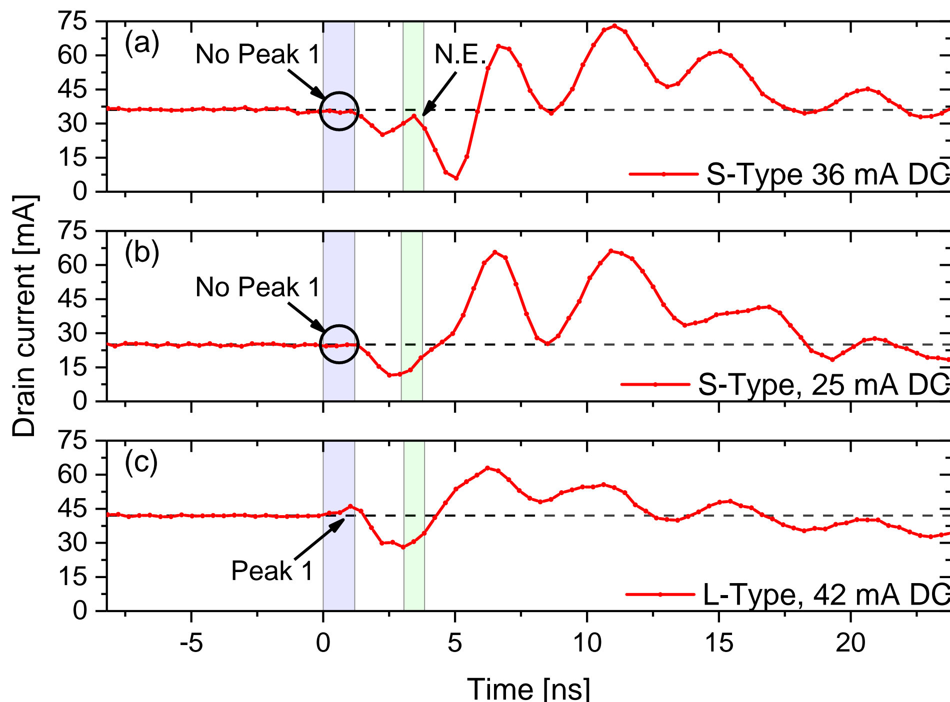

Figure 6.7: On-state HEMT drain current transients measured during exposure to Omega laser ICF burn shots. In all cases $V_{GS} = 0\,V$, and V_{DS} was set at the PSU to produce the indicated DC drain-source currents. (a) S-Type HEMT with Peak 1 absent. A possible neutron-induced transient signal is labelled N.E. (b) S-Type HEMT with Peak 1 absent. (c) L-Type HEMT with small Peak 1 present. Note: Green shaded neutron signal regions are determined from the bang time and burn width as measured by Omega facility diagnostics for each individual shot.

6.7. In the figure it can be seen that Peak 1 is absent for the S-Type devices, this was true for 2/3 measurements performed. In part (c) of the figure a small Peak 1 can be seen to be present for the L-Type device under test. In part (a) of the figure a potential neutron-induced signal is present which differs from the response seen in the other measurements. The presence of the negative-going return current signal, despite the absence of Peak 1 signals, suggests that the irradiation effect on the S-Type HEMTs alters the usual transient current flow within the test circuit. In Figure 6.8 the slow timescale measurements are shown which correspond to the fast data shown in Figure 6.7. Part (b) of Figure 6.8 shows that L-Type on-state response is to return to full output drain current quickly after irradiation, as was seen in the earlier testing. S-Type drain current is also now seen to return to its full value shortly after irradiation, although some late-time instability is apparent. The intermediate biasing case shows an interesting switch-off and recovery behaviour. Part (a) of the figure shows that gate current stabilised back to zero shortly after irradiation for all devices.

The Peak 1 and Peak 2 current magnitudes are plotted as functions of V_{GS} and $V_{DS} - V_{GS}$, in Figure 6.9 and Figure 6.10, respectively. In Figure 6.9 it can be seen that L-Type Peak 1 drain

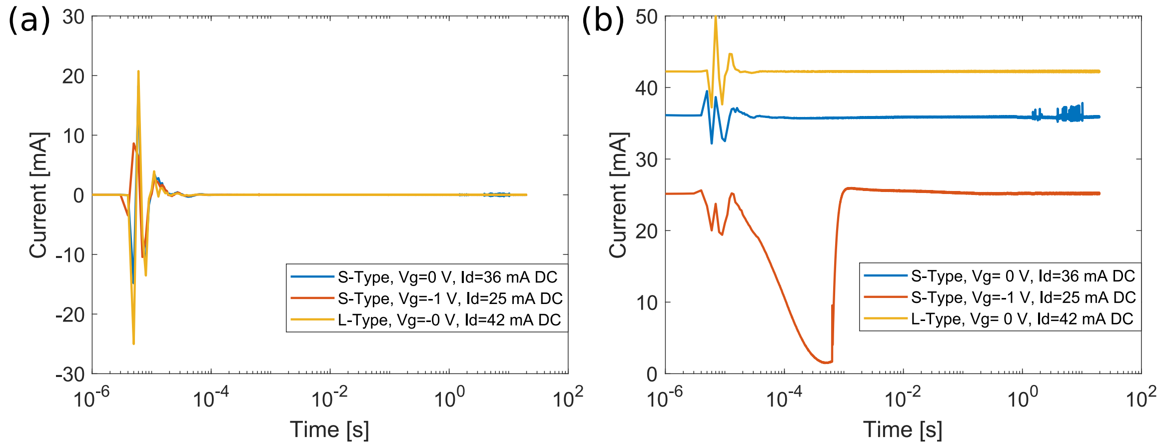

Figure 6.8: On-state long duration transient measurements corresponding to the fast measurement data shown in Figure 6.7. t_0 occurs at approximately 3×10^{-6} s on this plot. (a) gate current transients. (b) drain current transients.

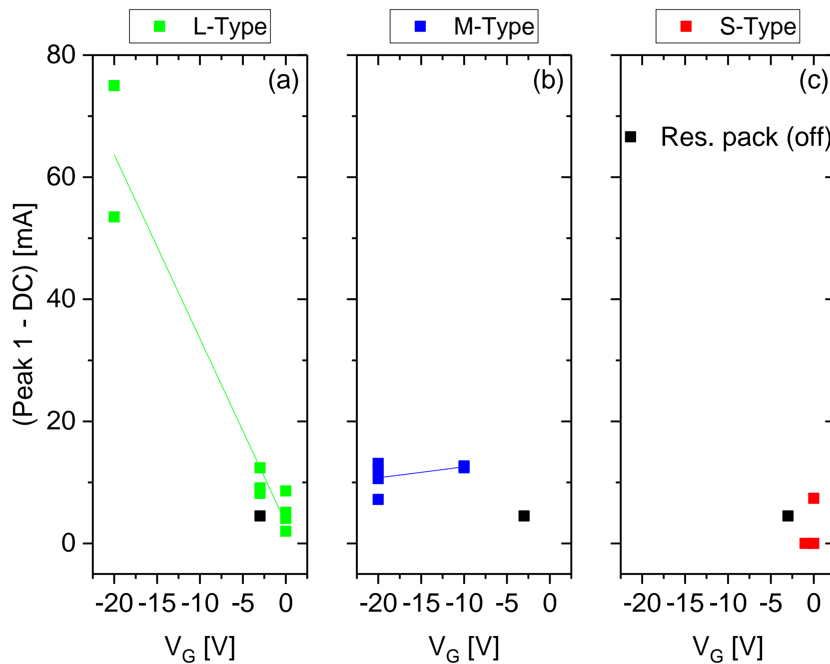

Figure 6.9: Peak 1 drain current magnitude shown as a function of gate bias, V_{GS}.

current magnitude depends on gate bias, indicating an irradiation effect in the HEMTs. Peak 1 magnitude was found to be independent of drain bias. In Figure 6.10, the magnitude of Peak 2 above the DC current operating point is apparent for all devices.

The time for the drain current of L-Type, and M-Type HEMTs to settle back to within 2% of their pre-irradiation levels are shown in Figure 6.11, for various electrical biasing conditions. No difference was found between M-Type HEMTs output settling time and that of the resistor pack

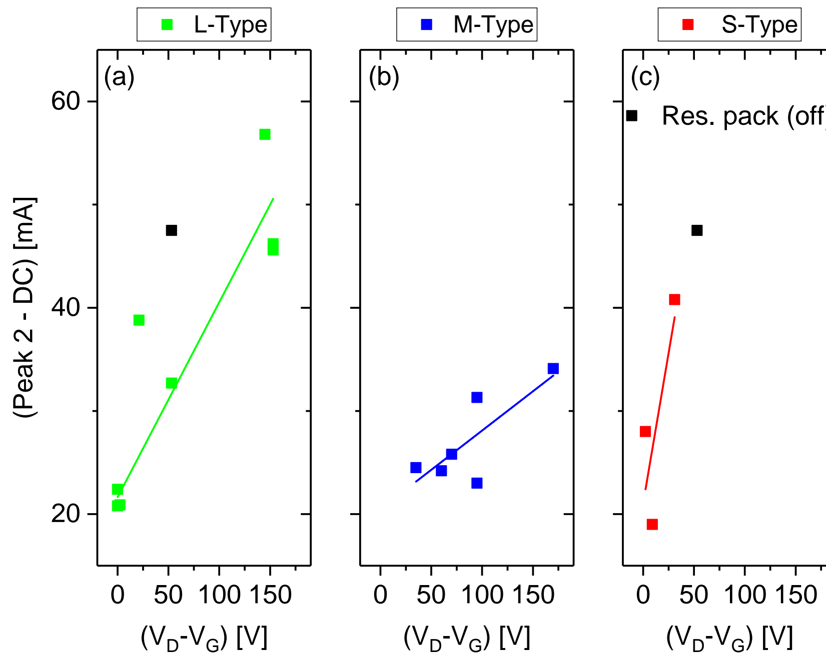

Figure 6.10: Peak 2 drain current magnitude shown as a function of $V_{DS} - V_{GS}$.

control. L-Type settling time was shorter than the control when biased hard off. When irradiated in the on-state L-Type settling times were found to be up to a few tens of micro-seconds. The settling time for an S-Type HEMT irradiated with $V_G = -1\,\text{V}$ was $870\,\mu\text{s}$, shown in Figure 6.8(b). In the on-state it was $> 20\,\text{s}$, if output instability is considered.

DC and pulsed characterisation of HEMT characteristics was performed before and after each irradiation. The results of these characterisation measurements are given in Figure 6.12. In the figure it can be seen that no permanent significant shifts in parameter values was found for L-Type and M-Type devices. For S-Type devices, however, there are indications of increased off-state gate leakage current, and increases in maximum transconductance and on-state drain current, with a slight negative shift in threshold voltage.

6.3 Discussion

The increased output current and transconductance of the S-Type HEMTs, after ICF neutron irradiation at Omega, may be due to a slight apparent decrease in HEMT threshold voltage. Alternatively, the increased transconductance and drain output current may be caused by the increased leakage current through the gate contact, enabling faster de-trapping of trapped charge during characterisation testing, and thus enabling an increase in 2DEG density. An increase, due to neutron irradiation, of the recovery rate of the 2DEG after switching was shown in Chapter 5, suggesting that this mechanism is credible.

One possible explanation for the lack of catastrophic SEE damage by devices during exposure

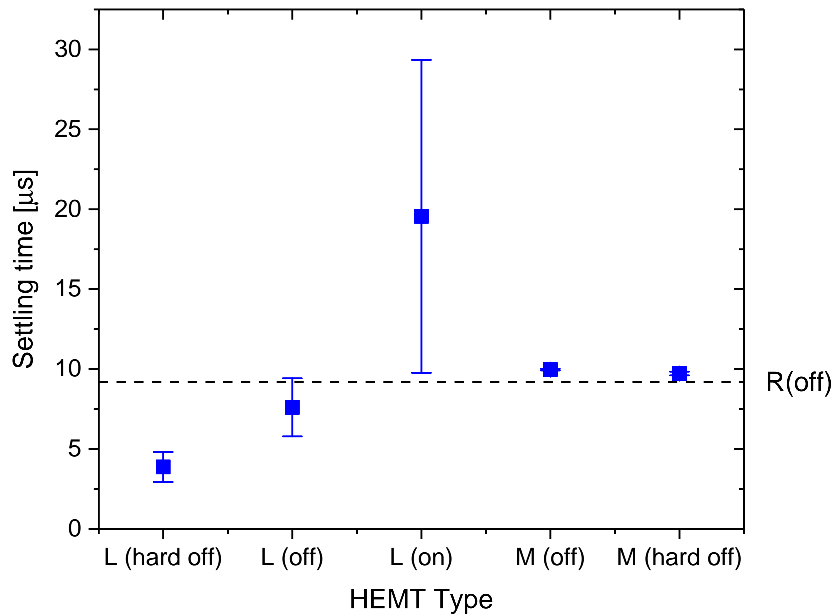

Figure 6.11: Time for drain current to settle to within 2% of its pre-irradiation level after exposure to an Omega ICF neutron pulse, shown for each tested HEMT type, except S-Type. Electrical bias condition is indicated within parentheses. The settling time for a resistor pack in place of a HEMT within the NED is indicated by the dashed line, labelled R(off).

to ICF neutron sources, being discussed by other workers in the field, is that the bulk ionisation created by the X-ray flash which precedes the neutron pulse may be protecting the DUTs from the effects of the localised ionisation caused by the neutron effects. The concept is that the increased bulk conductivity reduces the peak current along knock-on ion tracks crossing device regions at different potentials, and so prevents catastrophic failure due to localised Joule heating along those tracks. Such an effect is certainly possible. However, for the particular devices and test conditions used here, the e-h pair density caused by the X-ray pulse would be of the order $10^{15}\,\mathrm{cm}^{-3}$, equivalent to a low doping level, whereas the charge density along an ionisation track would be several orders of magnitude higher. Considering the results presented here in the light of the reports of GaN HEMT insensitivity to the ion LET values caused by 14 MeV neutron irradiation, discussed earlier, suggests that in this case the technology is not vulnerable to SEGR when biased within its safe operating region, as it was for all tests shown here. Future improvements to the test setup and measurement circuit, particularly increased temporal resolution achieved by decreasing the length of the cable run, may enable the short lived transient conduction events to be discriminated from the overall device irradiation response even without SEGR occurring.

The transient on-state and off-state testing results revealed that for L-Type and M-Type devices after the X-ray and neutron fields have passed, no device response was measurable above the test system noise level. For S-Type devices, late-time drain current output showed signs of instability when biased in the on-state. This instability could be caused by the possible increase

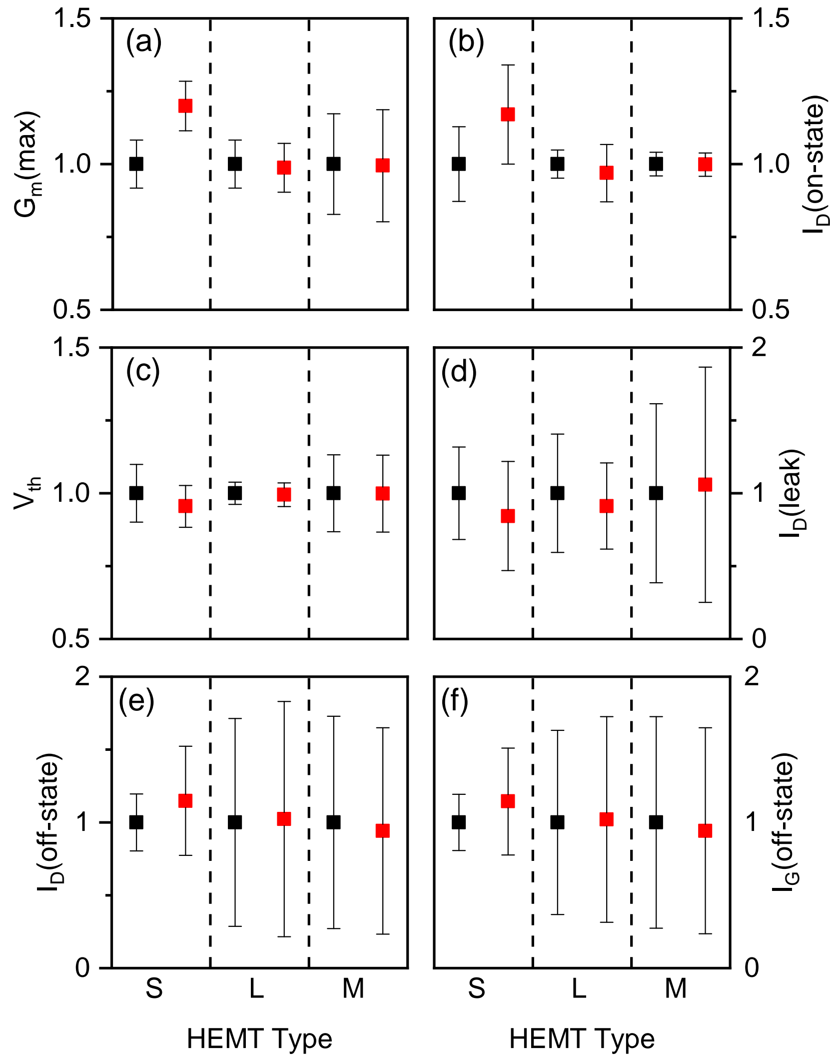

Figure 6.12: HEMT DC parameters as measured before irradiation (black squares), and after (red squares), during the Omega laser 2017 ICF neutron tests. Values are normalised by their respective before irradiation levels, and shown with associated normalised uncertainties for S-Type (S), L-Type (L), and MIS-Type (M) structures. (a) is maximum transconductance Gm; (b) is on-state drain current with $V_G = 0\,V$ and $V_D = 0.1\,V$; (c) is the threshold voltage (V_{th}); (d) I_D(leak) is the drain current measured with $V_D = 0.1\,V$ and V_G set below the respective V_{th} for each type (-3 V and -20 V); (e) I_D(off-state) and I_G(off-state) (f) are drain and gate currents measured with $V_D = 50\,V$, and $V_G = -10\,V$ for S- and L-Type Schottky gate HEMTs, and $V_G = -20\,V$ for MIS-Type insulating gate HEMTs, well below the V_{th} for each type.

in gate leakage current, and related device parameters, discussed above. The results of tests using gate filtering, introduced to stop charge injection on the gate contact during the irradiation event, were successful in demonstrating that the GaN-on-Si HEMTs tested here do not suffer from a transient switch-off due to irradiation in the Omega laser ICF neutron environment. The observed on-state late-time instability and intermediate-bias switch-off and recovery of S-Type devices suggests that gate width may be a factor in determining radiation hardness of HEMTs. The intermediate bias switching event appears to be an inverse form of SES, i.e. switching from on- to off-state, followed by rapid recovery. These results indicate that an irradiation damage mechanism exists to which the larger devices are invulnerable. Because of their smaller gate area, and thus smaller absolute value of gate leakage current, the S-Type HEMTs are more sensitive to changes in gate leakage current caused by neutron irradiation-induced defects.

L-Type Schottky gate devices were found to show the largest dependence on gate bias of their initial transient drain current peak, tentatively attributed to X-ray pulse response. The apparent strong X-ray sensitivity of the large area reverse biased HEMTs suggests that they may be of use in X-ray detection applications. The gate reverse bias sensitivity, and drain bias insensitivity, of the Peak 1 magnitude supports the suggestion that the signal is created in the depletion region beneath the HEMT gate contact. The insulating gates of the M-Type devices are likely to be the cause of their Peak 1 signal V_{GS} insensitivity. The rapid settling times, of the order of $10\,\mu$s, of all tested device types when irradiated with off-state biasing, with applied drain voltages of up to 150 V, suggests that the irradiation-induced excess carriers rapidly recombine or are swept out of the active device regions. The absence of Peak 1 in the transient response of 2/3 S-Type devices tested in the on-state is interesting, especially when given the presence of the apparent return current in all cases. This suggests that the X-ray interaction does occur in S-Type devices. The effect itself must be either too small to detect with the present test setup, but large enough to cause the return current to flow, revealing its presence. Or it may be that the effect causes an alternative current path to flow, connecting the HEMT channel and gate contact in a manner which causes the observed drain channel measurement. The possible neutron effect observed in one case may have been caused by either a temporary increase of the HEMT conductivity, i.e. SES, or it was simply the collection at the drain contact of the charge deposited by the neutron irradiation.

The Peak 2 signal magnitude dependence on $V_{DS} - V_{GS}$ is clear in Figure 6.10 for all device types, and is consistent with an irradiation-induced transient increase of conductivity within the HEMTs. However, further data is needed to demonstrate that the effect on Peak 2 HEMT conductivity is measured distinctly from the irradiation effects on the PCB and cabling.

6.4 Conclusions

The above results and discussion indicate that SEEs, possibly in the form of SES, may have been observed in GaN-on-Si HEMTs during Omega laser pulsed ICF neutron testing. Two possible SEEs were observed in S-Type HEMTs. Post-irradiation device parameter changes were present in S-Type devices, consistent with displacement damage effects, and consistent with behaviour observed in GaN-on-SiC HEMTs following accelerator based irradiation, as described in Chapter 5. Catastrophic failures, including SEGR, were not apparent in the test results. However, drain bias testing was not increased beyond 150 V, due to technical challenges which arose during the test day, and so all devices were irradiated within their rated safe operating areas.

To mitigate the challenging effects of the electrically noisy environment at Omega it has been necessary to implement several shielding and noise reduction methods. These have been partially successful, and the feasibility for neutron effects testing that the facility has been demonstrated. It was necessary to low-pass filter gate connections at the DUTs to protect them from electrical transients. The transient turn-off and recovery behaviour observed prior to this measure, and subsequently mitigated by the filtering, could perhaps have been misinterpreted as an irradiation effect under different circumstances. This is in part a cautionary tale for when developing radiation effects test platforms. The effectiveness of the test PCB gate low-pass filter at reducing the on-state switch-off and slow recovery effect demonstrates that gate injection of charge causing slow switching transients was occurring, and may be a vulnerability for similar devices in radiation environments where fast transients couple into the gate connections.

The on-PCB differential current transformer arrangement produced usable data, with less noise than was present using earlier test circuit designs. If further Omega trials were to be conducted, the system would benefit from further optimisation to reduce noise pickup and oscillations, to increase bandwidth, and to reduce signal reflections at interfaces in the cable chain. A fiducial signal should be incorporated into the data capture system to provide an unambiguous measure of $t = 0$. The inevitable signal peak broadening caused by the long cable run limits the potential for discriminating single, or multiple closely spaced, neutron-induced SEEs from bulk ionisation effects. Such discrimination could be achieved by developing a compact instrumentation electronics box, to field adjacent to the Omega test chamber. The proposed system could use a digitiser housed near the outside end of a TIM to measure the required electrical signals. Because of the greatly reduced length of cable run, measured electrical pulse shapes would be a more accurate representation of those found within circuits exposed to short pulse irradiation. The proposed new test system should also feature removable X-ray shielding in front of the experiment, and should enable TCC to DUT distance to be varied, as discussed further below.

Combined neutron and photon environment testing has been conducted in the past using flash X-ray machines in combination with pulsed neutron reactors [143]. Such tests revealed surprising device behaviour which would not have been predicted by testing in either environment

in isolation. In that example MMICs recovered their output current state five times faster, in 20 ms rather than 100 ms, when irradiated by a combined neutron and photon field, than when irradiated with photons only. To progress development of ICF neutron source testing, and potentially discover further synergistic effects and interesting device physics, it will be important to distinguish between X-ray and neutron-induced effects, and to understand how they interfere. Where possible, it may be simplest to vary the X-ray shielding in the front of the NED, which is ineffective at shielding fast neutrons, to determine the relationship between X-ray and neutron flux effects whilst keeping the neutron flux constant. Firing shots with increasing TCC to DUT separations will enable the time of flight difference of the photons and neutrons to be exploited to discriminate between their effects on devices, and to study how the interfere. This method, however, has the undesirable side effect of reducing the neutron fluence the DUT is exposed to.

In this chapter we have seen that Shottky gate HEMTs are more sensitive to the X-ray and neutron environment at the Omega laser ICF facility than MIS gate devices are. We have also seen how GaN-on-Si HEMTs are able to return to their unperturbed operating points within times less than 10 μs, under certain operating conditions. These results confirm the potential of this technology for use in harsh radiation environments. In the next Chapter, we shall continue to study *in situ* irradiation effects. We will see how photo-ionisation can be used as a surrogate for aspects of the neutron irradiation effects studied in this chapter. We will also see how HEMTs respond to the effects of two closely separated, but distinct, pulses of localised ionisation.

6.5 Acknowledgements

Dr David Cussans of the University of Bristol is acknowledged for generously sharing his time to discuss Omega measurement circuit development ideas on several occasions. Mr Alex Salmon is thanked for transforming my schematic designs into highly viable production-ready PCB layouts.

CHAPTER 7

Pulsed ionisation effects using femto-second lasers

Radiation effects testing, although an essential prerequisite for many applications, is often a costly undertaking. To test semiconductor devices and subsystems across a range of radiation environments, that adequately represent the conditions they may be exposed to in applications, requires experimental trials at multiple radiation effects simulators, often situated across geographically separate locations. The logistic effort, cost, and time commitment of such a trials campaign can be significant. Where testing is to be performed using neutron sources, such as nuclear reactors, test equipment may become radioactive, known as 'activation', and contamination controls may also be necessary. Ideally, testing would be performed by fielding the electronic systems in the radiation environment of interest. Clearly, this is neither practical, nor possible for many applications. The key task then, is to determine which aspects of the application radiation environments are most important to simulate for a given semiconductor technology. An example would be the electron-hole pair generation rate in the high electric-field region present at the interface of two difference semiconductor regions. Once these aspects are identified, a physical analogue for that environment must be sought, or developed.

An effect caused in semiconductors that is common to displacement damage environments including neutron, SEE environments, and X-ray and gamma irradiation environments, is ionisation. In the particle irradiation cases, ionisation is localised along the tracks of incident charged particles and secondary particles, created by neutron capture, for example, or along knock-on ion tracks following elastic scattering by energetic neutrons. In the photon irradiation cases, the ionisation is a bulk effect. In Chapter 6 the response of HEMTs exposed to near-simultaneous localised and bulk ionisation was presented. In this chapter the use of photons to create localised ionisation within semiconductors will be explored.

In comparison to using a particle accelerator, a nuclear reactor, or performing flight trials,

pulsed laser testing is relatively cheap, requiring only access to a suitable optics laboratory and instrumentation similar to that used for conventional transient radiation effects testing. Testing can be performed quickly, with minimal sample preparation, and does not produce radioactive waste or contamination that requires special procedures to handle. Laser testing enables precise control of the location of injected charge, and rapid characterisation. Unlike pulsed power radiation effects simulators, the shot-to-shot time can be almost arbitrarily short. High local ionisation densities are possible because photons are comparatively easy to produce. Laser effects testing also offers advantages in terms of reduced electrical noise compared to pulsed power radiation effects simulators. Although pulsed lasers do produce electromagnetic interference, it is orders of magnitude less than that produced at pulsed power facilities such as the Omega laser discussed in Chapter 6, or at pulsed nuclear reactors. This opens up opportunities to study the effects of small quantities of ionisation, or ionisation delivered over a short duration, to specified regions of semiconductor devices. In principle, the use of TPA in particular, enables probing of any region within a semiconductor device, because absorption of the light *en route* to the region of interest is negligible.

The tracks of ionisation resulting from particle irradiation are due to Coulomb interactions. The electrostatic attraction between the passing positively charged ion, and the electrons in the semiconductor, imparts kinetic energy to the electrons and results in a spatial charge distribution, whereas ionisation due to photon irradiation can be caused by a number of mechanisms. For the photon energies studied here, the creation of electron-hole pairs is most likely. In this case valance band electrons absorb the energy of the photon, and if sufficient energy is absorbed, are promoted to the conduction band. In an indirect band gap semiconductor a change of momentum may also be required. For the X-ray irradiation present in the testing in Chapter 6, the photoelectric effect and Compton scattering must also be considered. The spatial distribution of charge generated by particle ionisation and photo-ionisation is also clearly different. Given the different physical mechanisms and spatial profiles of the generated charge, it is important to determine a method of comparing ionisation caused by the two sources so that equivalent irradiation conditions can be determined.

An early evaluation of the potential for pulsed laser testing to be used to study fundamental mechanisms, and SEEs was produced by Melinger *et al.* [144] which covered many important aspects of the technique. More recently, Buchner *et al.* [145] reviewed the status of the pulsed laser testing technique for SEEs in particular. In those studies and elsewhere LET is used as a useful measure of ionisation caused by particle irradiation. The theoretical groundwork for an equivalent laser LET was put down by Pouget *et al.* in [146]. In that framework, a sensitive volume is defined, having a finite thickness, within which generated charge contributes to the radiation effect in the semiconductor device. The shape of the sensitive volume is taken to be a rectangular parallelpiped, hence this is known as the Rectangular Parallelpiped (RPP) model. The equivalent laser LET is then defined as the ion LET that would generate the same electrical

charge within the same sensitive region. Recent work by Hales *et al.* [147] has demonstrated a clear correlation between calculated laser-equivalent LET and heavy ion LET. The demonstration was experimentally validated for the case of a deep collection depth bulk silicon photo-diode, and for the case of charge collected from the drain of a 45 nm silicon-on-insulator (SOI) static random access memory (SRAM). The authors state that the ratio of the sensitive volume to the laser generated charge carrier profiles for these two cases are 10^8 and 10^{-5}, respectively. For the HEMTs studied here, however, the ratio of sensitive volume to laser focal spot size is closer to one, and so is a more complex case. In [148] analytic expressions were presented for the quantity of charge collected as a function of the relative sizes of the sensitive region and laser generated charge distribution region. In all cases for charge generation by TPA, collected charge was predicted to increase proportionally to the square of the laser pulse energy. That prediction is tested in this chapter.

In addition to deposited charge, other characteristics of the irradiated HEMT's response to the ionisation profiles which may be important in circuit applications are the peak voltage or peak current output generated, and the temporal shape of the photocurrent. Ildefonso *et al.* recently reported a method, based on varying pulse energy and focal spot size, for optimising the optical parameters of a pulsed laser irradiation system to better reproduce aspects of the output current and collected charge due to ion irradiation for SiGe HBTs [149]. However, as mentioned in [146], due to the lower peak charge density of a laser generated charge deposition profile when compared to an ion track, there is a reduced chance of laser irradiation reproducing the funnelling effect [150], also known as enhanced charge collection. For the same reason catastrophic breakdown effects are also less likely to occur with laser irradiation. The ion induced shunt effect [151], may be more significant than the funnelling effect in GaN-on-SiC devices due to the insulating substrates. However, a complete experimental simulation of the ionisation effects of particle irradiation would need to be able to reproduce all of these effects. These aspects are explored later in this chapter.

The aim of this work is to improve understanding of the conditions under which laser testing can be used to simulate particle irradiation, and having demonstrated that laser irradiation can simulate aspects of the effects of particle irradiation, to provide some insights into the potential *in situ* particle irradiation response of HEMTs. The work described below attempts to further elucidate some of the charge deposition and collection dependencies on incident light intensity, electrical biasing conditions, doping level, and PRF. The PRF dependence explored below is particularly interesting and is important for any testing performed using a continuous train of pulses. Here it is shown to be an important factor that should be considered when interpreting tests and modelling of multiple ions strikes or high irradiation dose rate environments. The dependence on laser focal spot position of the measured electrical effects is also shown to be of use for understanding electrical field distributions within operating HEMTs to aid design and analysis, calibrating TCAD simulations, and identifying regions most at risk of damage due to

irradiation.

7.1 Experimental details

The laser testing setup that was developed and constructed for the work described in this chapter is detailed in Chapter 3. Information on the specific test conditions and devices used for the work described below is provided here.

Electrical contact to the HEMTs tested here was achieved without sawing and packaging individual devices by probing on-wafer using RF GSG probes. These probes enabled a continuous $50\,\Omega$ impedance from the contact pads into the coaxial cables used to connect the probes to the bias tees used in the setup. The bias tees were used to apply DC bias to the HEMTs from a programmable PSU whilst allowing a low-voltage, high-bandwidth measurement path for the transient signals resulting from the laser irradiation. The transient signals were monitored on a digital storage oscilloscope where they were terminated in a $50\,\Omega$ impedance. Focal spot position was determined by the motorised microscope stage position. Control of the laser pulse picker, microscope stage position, and data capture system was achieved using custom LabVIEW software produced for this study.

Semiconductor devices tested

The semiconductor devices used in this study were drawn from three different wafers. Each of the three wafers employed SiC as a substrate material, GaN for the buffer, and AlGaN for the barrier layer. All the wafers were likely to have an approximately 100 nm thick AlN nucleation layer between the substrate and GaN layers. The wafers will be referred to as Wafer A, Wafer B, and Wafer C. Wafers A and B were produced by IQE, and are described in some detail in [152]. However, their properties that are relevant to the work described in this chapter are provided here. Wafer C was produced by United Monolithic Semiconductor (UMS). Wafers A and B had a common iron (Fe) doping profile of $3 \times 10^{18}\text{cm}^{-3}$ peak density deep in the GaN layer, decreasing in concentration exponentially with distance towards AlGaN interface where the concentration was around $1 \times 10^{16}\text{cm}^{-3}$. Wafers A and B also had a 200 nm thick unintentionally doped channel layer nearest the AlGaN interface where the carbon density was $5 \times 10^{16}\text{cm}^{-3}$. The principal difference between Wafers A and B is the carbon doping in the buffer layer beneath the channel layer. The available details of the three wafers that have not already been discussed are provided in Table 7.1.

Each of the wafers had a mirror finish polished back surface. However, Wafers A and B had a thin metal layer covering their back surfaces, presumably to act as a ground plane for high frequency operation. Initial testing showed that despite a semi-transparent appearance, due to light reflection from the covering metal, it would not be possible to image effectively through the

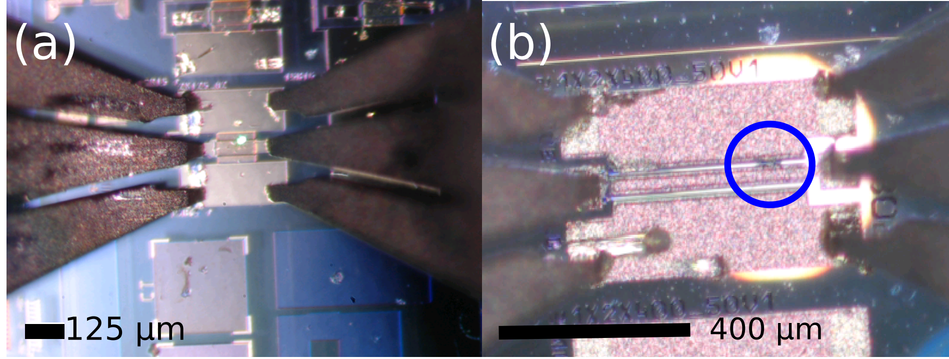

Figure 7.1: Top side images of HEMTs used for laser testing. (a) Wafer A&B HEMT layout. The green laser spot is visible through the gap in the contacts adjacent to the upper gate finger after transmission through the substrate. (b) Wafer C HEMT layout. The ground-signal-ground probes visible on the left in each image are making contacting with the two gate fingers; the probes on the right connect to the drain of each HEMT. The blue circle indicates the region where burnout occurred during laser irradiation.

coating. The metallisation was chemically removed, as described in Chapter 3, leaving an optical surface suitable for the measurements described below.

Wafer label	Substrate	Buffer		Barrier
	Thickness	Thickness	Doping	Thickness
A	-	$> 1.4\mu m$	Common Fe profile, C: $(3 \pm 1) \times 10^{17} cm^{-3}$	-
B	-	$> 1.4\mu m$	Common Fe profile, C: $2 \times 10^{16} cm^{-3}$	-
C	$\approx 500\mu m$	$\approx 1.4\mu m$	Common Fe profile*,	20-30 nm

Table 7.1: Details of wafers used for femto-second laser studies. *Doping is unknown, but Fe doping similar to Wafers A and B would be consistent with this technology, and is expected here.

All of the testing reported here used two-finger HEMTs available on the three wafers. Images of the types of HEMTs tested are visible in Figure 7.1. The HEMTs on Wafer C had widths of $2 \times 400\,\mu m$. The HEMTs on Wafers A and B had widths of $2 \times 125\,\mu m$, gate of $0.25\,\mu m$, a source-drain gap of $4\,\mu m$, and a source-gate gap of $1\,\mu m$. Prior to each laser test HEMT electrical characteristics were measured using the DC programmable power supply used to bias devices probed in the femto-second laser setup. Typical characteristics were $V_{th} = -2.3\,V$, and $I_D = 140\,mA$ with $V_{DS} = 2.0\,V$ and $V_{GS} = 0.0\,V$.

Laser spot

The dimensions and intensity profile of the laser focal spot achievable inside a semiconductor device depend on the optical characteristics of the illumination system used, and on the optical properties of the sample under investigation. In order to estimate the lateral size of the focussed laser spot achievable without the aberrations caused by transmission through the substrate,

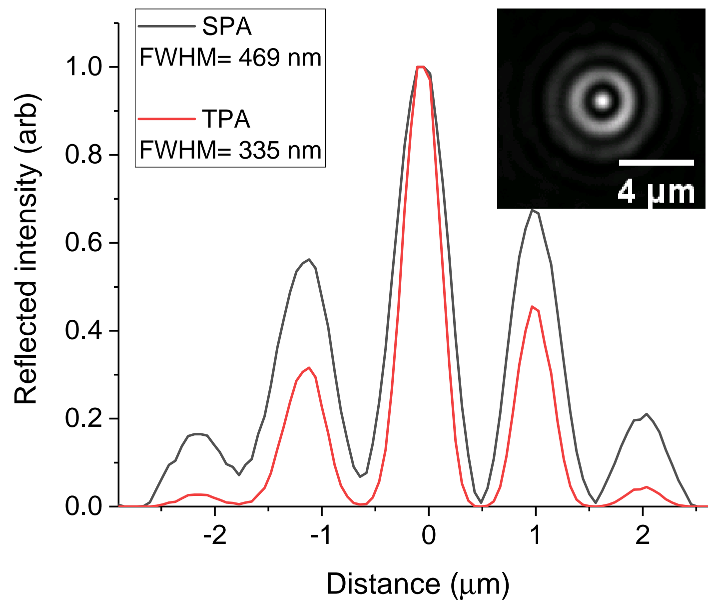

Figure 7.2: Normalised intensity profile of laser spot reflected from back surface of wafer, labelled SPA, and its square, labelled TPA. Inset: Image of laser spot used for intensity profile.

it was first focussed onto the back surface of a wafer. A travelling knife edge measurement is conventionally used to measure the width of a laser spot, however that was not practical with the setup that had been developed. An equivalent measurement was performed by focusing through the sample substrate onto the reflective straight edge of an electrical contact. The microscope stage position was moved, and the reflected intensity measured at each position. However, the results were unsatisfactory due to the minimum step size of the microscope stage being limited to 200 nm at that time . Instead, the reflected spot was imaged using the microscope camera and the magnification of the microscope objective lens and the pixel size of the sensor were used to calculate its size. In Figure 7.2 we see a line profile of the reflected laser intensity taken through the centre of the reflected spot when focussed on the back surface. The central peak was fitted with a Gaussian function to find the FWHM expected from any Single Photon Absorption (SPA), as was the squared profile for TPA. The bright central Airy disc is visible in the inset. The pixel size in the captured image is ≈ 60 nm. For the measurements presented later in this chapter, the relative magnitude of the side bands was decreased, thus increasing the fraction of the available energy in the central Airy disc. This was accomplished by improvements made to the beam expansion and periscope systems system which resulted in improved collimation and transmission though the microscope onto the wafer.

Here the reflectivity of the surface of the sample under the optical conditions used for the subsequent testing is determined. A first estimate of the reflection losses can be made for the

case of normal incidence, assuming a well polished 'mirror finish' as

$$R = \left[\frac{n_1 - n_2}{n_1 + n_2}\right]^2 \tag{7.1}$$

where n_1 and n_2 are the refractive indices of air and the SiC substrate, respectively. This suggests reflective losses of around 21%. As described by Fresnel's equations, the reflectivity of the surface depends on the angle of incidence of the laser beam, which varies across the radius of the laser spot. However, the maximum angle of incidence for a marginal ray in the setup used here is 48.6°, and because the energy distribution profile across the incident waterfront is weighted towards the centre, marginal rays are less important. It is therefore a reasonable approximation to use the above expression to estimate losses due to reflection at the air-sample interface.

The output of the laser used here was linearly polarised normal to the plane of the optical bench. Here we consider the implications of linearly polarised light incident on the entry pupil at the back of the objective lens. Light passing directly through the centre of the pupil will be will be incident normal to the wafer surface, and so is entirely p-polarised. Light originating at increasing radial distances from the centre of the pupil acquires an increasing s-polarisation component, and decreasing p-polarisation component, as it is rotated by the lens in order to form a focus. However, applying the same reasoning as before, this effect can be neglected here. After focussing through the circularly symmetric objective lens any off-axis light will have the p-component of its polarisation rotated about the propagation axis to an extent determined by its radial position. Given that SiC is a birefringent material, this may be an important factor to consider for more sophisticated models of this optical system. However, due to the large change in refractive index that the air-wafer interface, spherical aberration will be the dominant effect here and it is discussed further later in this chapter.

To put an experimentally measured upper limit on the reflective losses a measurement of the transmitted optical power was made. First, to mimic the experimental test conditions used throughout this chapter, the system was brought to a focus, imaging from the back side through the substrate, on a HEMT gate. Next the stage was moved laterally so that the beam was passing through a region with no top side metallisation, to allow maximum transmission at the focus used for the subsequent measurements. A laser power meter was then positioned facing the top side of the wafer such that all the light passing through the wafer was incident on the sensor's active surface. Laser power was measured across a range of microscope stage positions in order to assess the sensitivity of the transmission to focus position. In Figure 7.3 the 0 μm position is the separation of best optical focus, which corresponds to moving the sample approximately 165μm closer than the separation required for focus on the wafer back surface. In the figure we see that the transmitted power varied sinusoidally with sample-lens separation, which may be due to interference effects caused by the variation of the optical path length. Note that when the laser was focussed on the backside of the wafer transmitted power was 50.0 mW (49%).

The inset reflected laser spot images in the figure show how the focussed spot altered with focal depth. An asymmetry in spot focus with changes in separation is apparent, whereby it

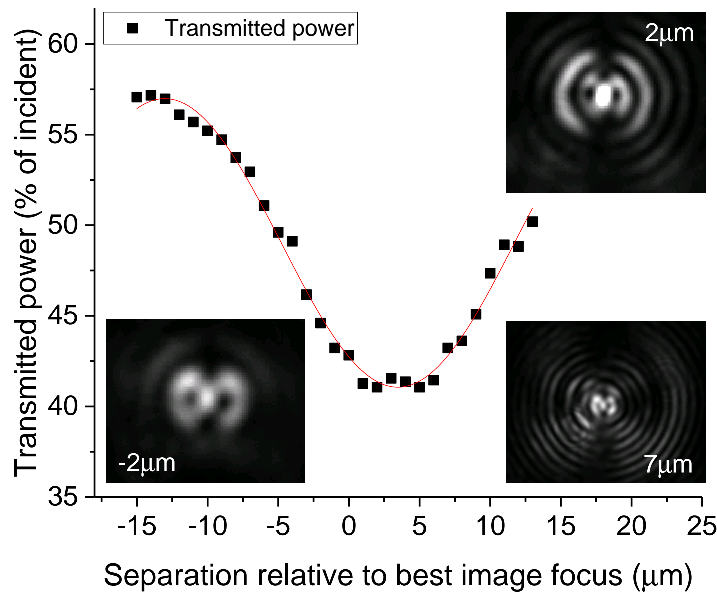

Figure 7.3: Measured transmittance plotted against change in semiconductor-objective lens separation. The red line is sine function fit to data. Images show reflected spot appearance at the three different separations given in each image. Positive numbers correspond to an increase in separation.

remains sharp for increasing separation, but is rapidly blurred with decreasing separation. This can be explained by the expected depth dependence of focus due to aberration by refraction at the air-sample interface, as discussed later and illustrated in Figure 7.7.

In order to assess the impact of intensity-dependent absorption, transmitted optical power was measured as a function of incident power. The results of the measurements can be see in Figure 7.4. For this test the separation was set to the position corresponding to best visible focus - close to the position for optimum TPA. The data in the figure show that transmittance was constant across the range of tested incident intensity.

7.2 Charge deposition due to a representative knock-on ion

The radial charge density profile generated within a semiconductor by the passage of an energetic ion typically has a characteristic radius of tens of nanometres to around one hundred nanometres. In contrast, the smallest radius of charge deposition achievable due to laser irradiation typically has a characteristic scale comparable to the wavelength of the light i.e. several hundred nanometres or greater. This limitation can be overcome by employing super-resolution techniques, where, for example, a binary amplitude mask is used to control the interference of a large number of beams with the result that a sub-wavelength focal spot is produced. In principle there are no lower limits on the focal spot size achievable using this technique, and imaging with a resolution of $\lambda/6$ has already been demonstrated [153]. Although super-resolution techniques

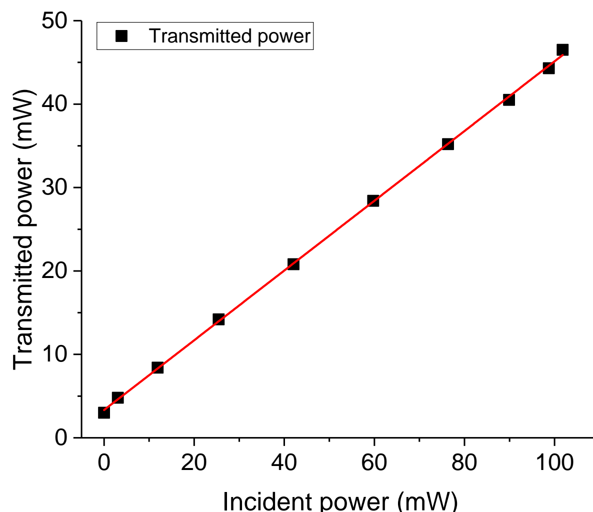

Figure 7.4: Measured transmitted power plotted against incident laser power. The red line is a straight line fit to the data, with slope 0.418 ± 0.003 (Adj. $R^2 = 0.9996$). The non-zero intercept of the fit is due to the apparent 3 mW noise floor of the laser power meter.

are extremely promising, for the laser irradiation approach used here, the large amounts of light energy directed into the side lobes or side bands, as compared to the focal spot, may be problematic. The characteristic axial lengths of the charge generation profiles resulting from ion- and photon-irradiation, however, can be comparable.

Here PKAs due to elastic collisions with incident neutrons will be considered. Higher energy ions generated by the capture of thermalised neutrons will be neglected here because of their low likelihood. Taking the peak in the PKA spectra in GaN found by the MCNP calculation of 14 MeV neutrons incident on GaN discussed in Chapter 5 to be around 1 MeV, a calculation of the expected ionisation and its depth profile was performed using TRIM [154, 155]. TRIM uses a Monte Carlo approach to calculate the transport of the ions, accounting for elastic and inelastic interactions between the incident ion and the target electrons and nuclei in the GaN. The transport of secondary knock-on atoms, and the ionisation due to them, was also accounted by performing a 'full recoil cascades' calculation. A plot of the ion tracks and recoil cascades due to 15 incident Ga ions is shown in Figure 7.6 (a). A limitation of TRIM is that the target material is treated as amorphous, so effects due to the crystal structure of the target material, such as channelling, are not accounted for. A transport code such as Marlowe [156], which uses the binary collision approximation [157] can be used to simulate irradiation of targets accounting for their crystal structure. The results of the TRIM calculation are given in Figure 7.5, where the calculated ionisation profile caused by a 1 MeV gallium (Ga) ion impinging into a GaN target is shown. The ionisation due to the incident ions, and due to recoiling knock-on ions are plotted separately. The figure shows the sum of ionisation from all lateral distances plotted against depth. In the figure the characteristic longitudinal length scale of the ionisation profile is seen

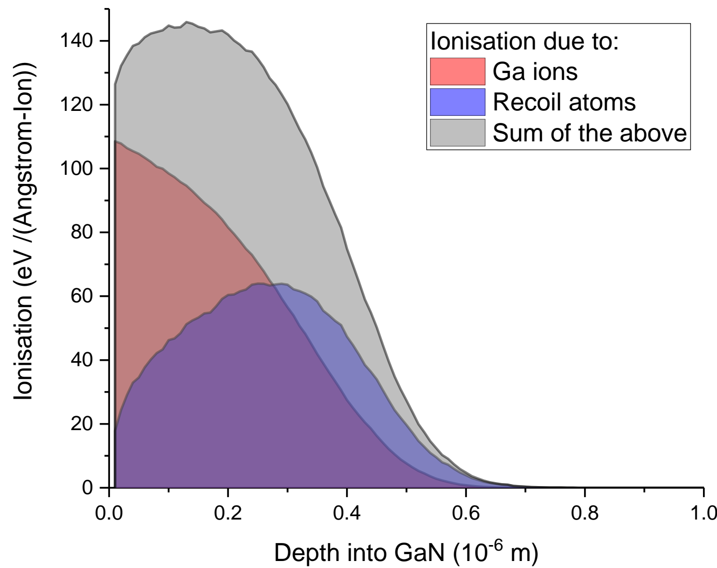

Figure 7.5: 1-D projection of a TRIM calculation of the average ionisation caused by 1 MeV Ga ion irradiation of GaN. The components of the total ionisation due to the passage of the incident ion, and due to secondary recoil atoms which have been knock-on by collisions are shown.

to be around $0.5\,\mu$m. The lateral ionisation profile is shown plotted in Figure 7.6 (c) where the characteristic length scale can be seen to be on the order of tens of nanometres. The average energy deposited per incident ion was estimated from the TRIM calculation to be $\approx 571\,$keV.

The average electron-hole pair creation energy in GaN is required in order to estimate the charge generated by the ionising energy loss calculated using TRIM. The electron-hole pair creation energy can be considered to consist of the band-gap energy, the energy losses to optical phonons, and the residual kinetic energy of the carriers, as described by Klein [158]. In that work the average electron-hole pair creation energy was found to be $\frac{14}{5}\mathrm{E_G} + \mathrm{r}(\hbar\omega_\mathrm{R})$, where $\mathrm{E_G}$ is the band-gap energy, $\hbar$ is Plank's constant over 2π, ω_R is the phonon frequency due to Raman scattering, and r is an adjustable parameter in the fit. Using that model a value for the creation energy of around 9.4 eV is found. However, because of deviation in measured creation energies from the main trend predicted by that model for a number of semiconductors, including AlN [159], here the value of 8.9 eV reported in [160] and [21] will be used. For the 1 MeV Ga PKA ion irradiation under consideration, this leads to the generation of around 64000 electron-hole pairs, or $2 \times 1.0 \times 10^{-14}\,$C of charge split equally between the two species. Due to the field funnelling effect discussed earlier, the charge collected at the contacts of a HEMT is likely to be larger this calculated value for the direct ionisation deposited by the ion itself.

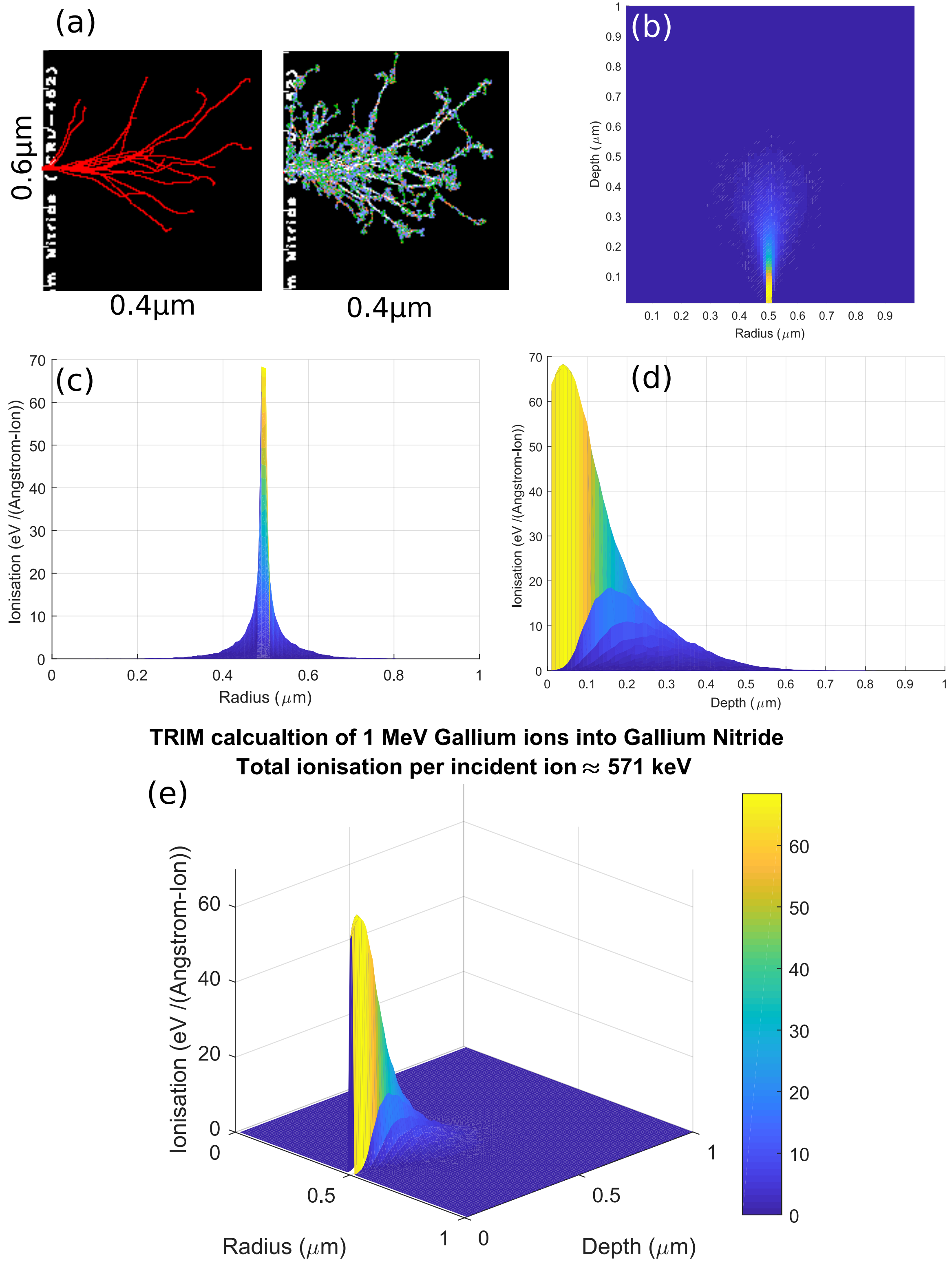

Figure 7.6: TRIM calculation of the ionisation caused by 1 MeV Ga ion irradiation of GaN. (a) The first image shows 15 ion tracks in red, the second shows the full recoil cascades. The extent of the axes are shown. (b) Plan view of average ionisation due an ion entering at 0.5 μm. (c) and (d) show the corresponding radial and longitudinal ionisation profiles. (e) 3D view of the ionisation.

7.3 Charge generation by sub-band-gap laser illumination

Illuminating a semiconductor sample using light with a photon energy smaller than the material band-gap allows the light to propagate though the material without absorption, except where the light couples to defect states of sub-band-gap energy. This transparency permits the optical probing of any region within the material, provided the external surfaces are transparent. In many semiconductor devices, optoelectronics being an exception, electrodes are usually opaque metals connected on the top-side of the device (particularly HEMTs). Therefore in the following illumination is performed from the backside of the device, through the substrate, enabling optical access to the entire active semiconductor region of the device. Useful information on the local condition of the semiconductor can be obtained by studying light emitted from the illuminated region. Examples include the temperature, found by analysing Raman scattered (inelastic) incident light from phonons with a well understood temperature dependence [161], or the electric-field magnitude within it due to Electric-Field Induced Second Harmonic Generation (EFISHG) [162, 163]. However, to simulate the effects of ionisation caused by exposure to a radiation environment at an arbitrary location within a semiconductor, multi-photon absorption is needed.

7.3.1 Two-photon absorption

Multi-photon absorption requires an atom, or in the case of a bulk semiconductor, a defect state or an electron in the valance band, to undergo successive photon absorption events until it is promoted to the conduction band. The absorption of the successive photons must occur within a short enough time period so that there is no intervening decay to a lower energy state, or movement away from the region under consideration due to drift or diffusion. The probability of each absorption event is proportional to the light intensity at that point in the material, I, so the probability of two photons being absorbed within the required time period is given by the product of the individual probabilities. This results in an intensity-squared dependence of TPA in light intensity, $P_{\text{TPA}} \propto I^2$. It is clear that to optimise charge generation by TPA, pulse duration and focal region size must be minimised, and pulse energy must be maximised.

Calculation of the exact rate of TPA can be performed using several different approaches, as discussed further in Chapter 2. For convenience we state here the result obtained by using second-order perturbation theory that the number of two-photon absorption events per unit volume, per unit time, as reported by Bechtel and Smith [164] is:

$$W^{(2)} = \frac{(2\pi)^3}{n^2 c^2 \hbar^2} \left(\frac{I}{\hbar}\right)^2 \sum_f |M_{fg}|^2 \delta(w_{fg} - 2\omega) \tag{7.2}$$

where n is the refractive index of the semiconductor, c is the speed of light in vacuum, $\hbar$ is Plank's constant over 2 Pi, I is the irradiance (power per unit area), ω is the angular frequency of the incident light, and ω_{fg} and ω_{ig} are the difference in angular frequency of the final and ground,

and intermediate and ground states, respectively. f is the number of possible final states, and the summation should also be performed over all the possible ground states, g. In the above,

$$M_{fg} = \frac{e^2}{m^2\omega^2} \sum_i \frac{\vec{\mathbf{p}}_{fi} \cdot \hat{a} \vec{\mathbf{p}}_{ig} \cdot \hat{a}}{\omega_{ig} - \omega} \tag{7.3}$$

where $\hat{a}$ is the unit vector describing the direction of polarisation of the incident light, and $\vec{\mathbf{p}}_{fi}$ and $\vec{\mathbf{p}}_{ig}$ are the elements of the momentum operator connecting the final, initial, and ground states. From Equations 7.2 and 7.3 it is clear that a peak in TPA rate ($W^{(2)}$), would be expected when the incident photon energy is precisely equal to half the band-gap energy, E_g. However, TPA is possible whenever the sum of the two incident photon energies is equal to, or greater than the E_g. From inspection of Equation 7.3 an anisotropy of the TPA rate with respect to the incident polarisation of the incident light might also be expected. For simplicity we will neglect that complication for the time being. One further assumption in the above is that the incident light intensity is low enough so that free hole absorption is negligible.

The attenuation of the light pulse normal to the x-y plane as it propagates through the semiconductor material in the z-direction can be described by

$$\frac{dI}{dz} = -\alpha I - \beta I^2 \tag{7.4}$$

where α and β are the one- and two-photon absorption coefficients, respectively. Since we are considering illumination by sub-band-gap light, any one-photon absorption will be due to interaction of the light with defect states of some concentration in the semiconductor and can be described by the Beer-Lambert law represented by the first term in the above. The two-photon absorption coefficient is given by

$$\beta = \frac{2\hbar\omega W^{(2)}}{I^2} \tag{7.5}$$

A simplified method of estimating the TPA coefficient, β, was devised by Van Stryland *et al.* [165], who found that in direct band-gap semiconductors, β scaled as $\beta \propto E_g^{-3}$. The TPA coefficient for GaN was determined for incident light with photon energy close to half the band gap energy by fitting photocurrent measurements to that model [166]. Following that work [167] a value for β of 2.5 cm/GW is taken here.

The transmitted irradiance as a function of position, sample thickness, and time can then be described by

$$I(r,l,t) = -\frac{(1-R)^2 I(r,0,t) e^{-\alpha l}}{1 + \beta(1-R) I(r,0,t)(1-e^{-\alpha l})/\alpha} \tag{7.6}$$

where R is the reflectivity of the semiconductor, t is the time, l is the sample length, and r is the position.

7.3.2 Optical factors influencing charge generation

Charge generation within the semiconductor region of interest can be achieved by bringing the incident light to a focus within the material at that region. Due to the intensity-squared

dependence of charge generation by TPA, the generated charge is strongly localised in the focal region. If we consider a typical Gaussian beam intensity profile in the focal region, and assume a small fraction of the incident light flux is absorbed in the focal region, this would result in a Gaussian-squared charge generation profile due to TPA. Any charge generation by defect states would have a linear intensity dependence, and so would be less concentrated in the focal region. The difference in spatial distribution can be quantified by considering the FWHM of the Gaussian profile, and the squared profile. The FWHM of a Gaussian function can be described by $\text{FWHM(Gauss)} = 2\sqrt{\ln(2)}$, and the FWHM of its square, e^{-2x^2}, can be shown to be $\text{FWHM(Gauss}^2) = 2\sqrt{\frac{ln(2)}{2}}$. The FWHM of the TPA distribution would therefore be $\text{FWHM(Gauss}^2) = \frac{\text{FWHM(Gauss)}}{\sqrt{2}}$. So by using TPA rather than single photon absorption, not only is access obtained to the entire active region of a HEMTs by back-side illumination, but also the linear dimensions of the resulting charge deposition profile are reduced by a factor of $1/\sqrt{2} \approx 0.71$.

To estimate the achievable focal region size, and thus the charge generation, we must account for the refraction of incident light at the air-sample interface from across the entire objective lens. This can be done by using the formulae derived by Everall [168], who considered the focal point of rays from across the entire objective lens due to the effect of refraction at the air-sample interface, and used a ray tracing analysis to produce the Equations (7.7) and (7.8), shown below. The second important correction described by Everall is for z-scan measurements. In that case, when the objective lens-semiconductor sample distance is altered to determine the depth-dependence of a signal e.g. TPA charge generation, the effects of refraction need to be accounted for to avoid an inaccurate depth-signal profile.

The Depth of Field (DoF), defined in [168] as the difference in focal point depth for a ray from the centre of the objective lens, and another ray originating at the edge of the lens, is given by

$$\text{DoF} = \Delta\left(\left(\frac{\text{NA}^2(n^2-1)}{1-\text{NA}^2} + n^2\right)^{1/2} - n\right) \tag{7.7}$$

where n is the refractive index of the of the semiconductor sample, NA is the numerical aperture of the objective lens, and Δ is the nominal focal point distance below the sample surface. Δ remains a fixed distance from the objective lens when the objective lens to sample distance is changed. This equation shows that focusing deeper within a semiconductor sample will also cause the undesirable effect of increasing the depth of focus. As an example, back-side illumination through a 500 μm 4-H silicon carbide (SiC) substrate (n=2.69), using an NA=0.75 objective lens, would result in a depth of field of around 200 μm longitudinal extent. However, the optical energy density distribution is not longitudinally symmetric throughout the depth of field. Adapting the approach in [168] we note that for a ray tracing analysis with a fixed density of rays per unit area incident of the objective lens, the number of rays originating from a given fractional radius, $m = r/r_{\text{max}}$, is proportional to that radius (area $= 2\pi r \cdot dr$), the intensity of light originating from that radius will be equal to a the radial distribution function at the lens multiplied by the radius, $I(m) = m \cdot f(m)$ where $f(m)$ is the radially symmetric light intensity profile across the objective

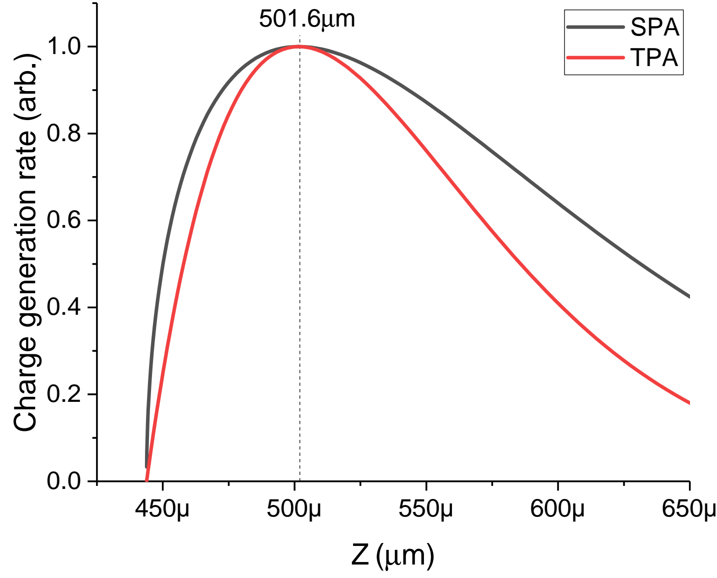

Figure 7.7: Expected asymmetric charge generation as a function of depth due refraction at the air-semiconductor interface, from i) a Single Photon Absorption (SPA) process, and ii) a Two Photon Absorption (TPA) process. The dashed line indicates the depth of the generation rate maxima for both curves. Negligible beam attenuation is assumed.

lens. In the experimental configuration used here the rear entry pupil of the objective lens was slightly over-filled. So the input Gaussian laser spot intensity profile can be considered as a truncated Gaussian, giving a normalised radial intensity distribution function of $I(m) = e^{-2m^2}$. Because of the quadratic dependence of the TPA charge generation on intensity, the characteristic width of the light distribution might expected to reduce further still. Figure 7.7 shows two calculated $I(m)$ curves plotted against depth below the semiconductor surface (Z_m), calculated using Equation (7.8), for a nominal focal depth of $\Delta = 165\,\mu$m and using the optical parameters for the experimental setup used herein. The SPA curve is the normalised irradiance (optical power per unit area), and the TPA curve is its square. Z_m as a function of m was calculated using

$$Z_m = \Delta \left[m^2 \frac{\mathrm{NA}^2(n^2-1)}{1-\mathrm{NA}^2} + n^2 \right]^{1/2} \tag{7.8}$$

To move the focal point from the back surface of the UMS GaN-on-SiC sample, through the substrate and on to the active device layer within the sample, required a microscope stage movement of $165\,\mu$m. Because of the refractive effects described above, that stage movement was sufficient to cause the focal point within the semiconductor sample to move to the active device layers, located around $500\,\mu$m below the surface. This corresponds to the peak in the calculated charge generation rate, as shown in Figure 7.7. The asymmetric depth dependence of charge generation is also apparent, as is the increased confinement of charge generation due to the quadratic irradiance dependence of TPA when compared to processes that depend linearly on

irradiance: the FWHM of the SPA curve is 181 μm, whereas the FWHM of the TPA curve is 128 μm (a reduction factor of $\sqrt{2}$). It should be noted that because the total wafer thickness was a little over 500 μm, except for charge generated by a small fraction of the light which is reflected back into the sample at the top side air-semiconductor or air-metal interface, charge generation which would have been caused by light coming to a focus at points deeper than 500 μm will not occur.

Recently published results by McMorrow *et al.* [169] for Z-scan TPA charge collection measurements using diodes have found an asymmetric dependence of collected charge on sample-lens separation (Fig. 5 in that paper), that closely resembles the calculated focal depth response shown in Figure 7.7. In [169] to explain the discrepancy between their calculated and measured Z-scan profiles, the authors mention that their depth profiles could be caused by a focal region more axially elongated than considered in their simulations. The calculation performed above, based on Everall's model (Fig. 7.7), demonstrates that focal region elongation should be expected, and so their results can plausibly be explained by the effect described above. This suggests that it is reasonable to apply the Everall model analysis for the TPA measurements discussed here.

Inspection of Equation 7.8 above, shows that reducing the depth of substrate material that illumination is performed through, for example, by thinning the substrate material prior to performing TPA charge generation, would decrease the longitudinal FWHM of the charge deposition profile. Using a lower Numerical Aperture (NA) lens would reduce the DoF, and the FWHM, but that would be at the expense of increased diffraction, thus reducing lateral resolution. Another option for reducing the depth-of-field would be to use a Solid Immersion Lens (SIL) in between the objective lens and the semiconductor surface. The SIL would reduce aberration due to the effects of refraction at the air-semiconductor interface, resulting in better axial focus (smaller DoF), and increased peak intensity in the focal region, as discussed in detail by, for example, Pomeroy *et al.* [170]. This would enable greater spatial resolution of depth profiling (Z-scan) measurements, and, for a given laser source, the generation of a wider range of deposited charge densities due to the greater accessible peak intensity in the semiconductor.

To determine whether it is necessary to account for refraction at the SiC-GaN interface, refraction at the air-SiC interface is first considered. At that interface marginal rays incident from the 0.75 NA objective lens will have an angle of incidence, $\theta_i = \sin^{-1}(0.75/1) = 48.6°$. From Snell's law, this leads to an angle of refraction within the SiC of $\theta_r = \sin^{-1}(1 \times \sin(48.6)/2.69) = \sin^{-1}(\mathrm{NA}/n_{\mathrm{SiC}}) = 16.2°$. Refraction into the GaN at the SiC-GaN interface would then be at an angle of of $\theta_r = \sin^{-1}(2.69 \times \sin(16.2)/2.4) = 18.2°$. Given the small change in the propagation angle of marginal rays, the effects of refraction at that interface on the part of the focal spot contained within the GaN layer can be neglected in subsequent calculations.

Given the small angles of incidence of the light in the focal region we can calculate reflection for the case of normal incidence, as done above for light incident at the air-semiconductor interface. Reflectivity at the SiC-GaN interface is then $R = |\frac{2.69-2.4}{2.69+2.4}|^2 = 0.0032$, and so can be neglected.

Due to the high transmissivity at the SiC-GaN interface any light propagating beyond the end of the GaN layer, shown to the right of the vertical dotted line in Figure 7.7, will not contribute further to charge generation within the semiconductor layers.

Due to the high density of rays in the focal region within the material, mutual interference will cause diffraction to put a lower limit on the lateral dimension of the focal region. An estimate of the best case spot size achievable can be made using the diameter of the Airy disc, $\frac{1.22\lambda}{\mathrm{NA}}$ where NA is the numerical aperture, equal to $n \cdot \sin(\theta)$, where n is the refractive index of the medium, and λ is the wavelength of the light. For the 517 nm incident light and the NA=0.75 objective lens used here, this places a lower limit on the achievable spot size of 841 nm in air ($n = 1$). The spot sizes achievable within the SiC and GaN layers if an immersion lens is used are smaller than those in air due to the increased acceptance angle in the high n materials because refraction at the air-sample interface is reduced by the SIL, giving rise to a larger effective NA. The beam waist is the minimum diameter of the focal spot of the beam where irradiance is at its highest, and so is where TPA is most probable. An estimate for the diffraction-limited beam waist diameter using the objective lens and wavelength described above can be made taking the lateral FWHM as [171]

$$\mathrm{FWHM} = 0.51\frac{\lambda}{\mathrm{NA}} \approx 352\,\mathrm{nm} \tag{7.9}$$

By discarding the part of the focal region which would have occurred beyond the top surface of the wafer, we expect an achievable focal region profile with a lateral FWHM of 352 nm and a full length of 58 μm.

7.3.3 Calculating charge generation

The charge generated by TPA for a particular optical configuration and target material can be calculated by using the optical and physical principles outlined above. A rigorous calculation would necessitate the solution of a coupled set of non-linear equations to include the effects of self-focusing, optical limiting, and free-carrier absorption. Calculations including those effects could be performed using a Beam Propagation Method approach as implemented in the software package NLO_BPM [172]. The non-linear optical effects mentioned here dominate beam propagation and absorption in many cases. However, here the simplifying assumption is made that the most significant factor contributing to the intensity profile within the focal region, and hence the charge generation there, for the optical configuration used in this study, is the aberration due to refraction at the air-semiconductor interface. This is justified by the calculated extent of the focal region elongation due to the large thickness of SiC substrate that the focus must be formed through, as shown in Figure 7.7.

Proceeding with this assumption in mind, the charge generation calculation was conducted as follows. Firstly, the measurement of the reflected image of the laser spot formed at the GaN-passivation or GaN-metallisation interface, depending on location of interest, as imaged through the SiC substrate, was used to determine the beam waist diameter and the lateral intensity profile

across the focal region. This is physically reasonable because the majority of charge generated comes from that region due to the I^2 dependence discussed above. The longitudinal stretching of the focal region due to refraction at the air-semiconductor interface, and the resultant depth-intensity profile, was accounted for as described above. By combining these two spatial weighting distributions numerically, a matrix of relative light intensity was created corresponding to the lateral and longitudinal focal spot extent within the semiconductor. To simplify the calculation, it was assumed that, relative to the incident intensity, there was negligible light absorption during beam propagation. By setting the SPA absorption coefficient in Equation 7.4 equal to zero, the charge density creation rate at each element in the matrix could then be found from the attenuation of the light due to TPA by

$$\frac{dN}{dz} = \frac{\lambda}{2hc}\beta I^2 \tag{7.10}$$

where N is the generated electron-hole pair density, λ is the wavelength of the incident light, h is Plank's constant, c is the speed of light *in vacuo*, and I is the light intensity at the time step being calculated at the position being considered.

The laser power incident at the back surface of the SiC was found by measuring the power exiting the objective lens using a laser power meter with the incident PRF set to 75 MHz. The energy per pulse was found by dividing this measured power by the PRF, with losses due to reflection accounted for during each calculation. The objective lens was considered to be optimally over-filled at the entry pupil, so the intensity distribution across the radial profile exiting the lens would be a truncated Gaussian. This profile was used to calculate the longitudinal extent of the focal spot using Equation 7.8. Next, the total power in a laser pulse was taken to be equal to the integral of the intensity across the laser spot area.

$$\int_{m=0}^{m=1} I(m)\cdot dA = P \tag{7.11}$$

where, as before, m is the fractional radius, and $dA = 2\pi m \cdot dm$. The radial intensity distribution $I(m)$, has a truncated Gaussian form, and so the peak intensity, I_0, and average intensity measured with the power meter are related by

$$P = \frac{I_0\pi}{2}\left(1-e^{-2}\right) \tag{7.12}$$

For each radial position a circumference was calculated, and the area of the corresponding annulus was found. The charge generation density matrix was then integrated, first over the area normal to beam propagation, and then along the direction of beam propagation, the $z-$axis. The integration along the $z-$axis used the correct values for β at each spatial position included in the calculation. The lower limit of integration in z was taken to be the minimum of the focal depth in the SiC substrate, and the upper was set as the end of the GaN layer, a nominal 2μm thickness.

The instantaneous intensity used above to calculate the rate of charge generation at each point in time during the laser pulse was determined from a Gaussian temporal beam profile with

a FWHM equal to 118 fs, as discussed in Chapter 3. The peak intensity was determined from the FWHM similarly to the radial intensity profile described above. The total charge generated was found by integrating over the instantaneous values for each point in time from a period from -2×118 fs to $+2 \times 118$ fs, with the peak intensity of the pulse at t=0.

We scale I at each z value by the effect of refractive focal plane elongation discussed above by using Equation 7.8, and then integrate dI with respect to sample depth (dz). In this manner a depth-radius map of charge generation density from TPA is produced, as shown in Figure 7.8(b,c). By integrating over both radial and axial spatial dimensions of the map we obtain the charge density deposited by the laser pulse, shown in part (a) of the figure.

The calculation was performed for incident laser pulse energies from 0.196 nJ to 1.96 nJ, the maximum pulse energy achieved experimentally. The results of these calculations are given in Figure 7.8. In the figure the total generated charge throughout the focal region can be seen to increase with the square of the laser pulse energy, as expected. Free carrier absorption and self-focusing due to refractive index changes were neglected in the calculations presented here, so optical saturation and limiting effects are not accounted for. The equation for the best fit to the data is

$$\mathrm{Q} = 2.14 \times 10^{6} \times \mathrm{PE}^{2} \tag{7.13}$$

where Q is the sum of the charge generated across the laser focal region in Coulombs, and PE is the laser pulse energy in Joules. The maximum charge generated by TPA according to the calculation is 8.2×10^{-12} C, whereas the maximum possible for zero reflective losses, and 100% conversion efficiency using an e-h pair creation energy of 8.9 eV would be 1.8×10^{-10} C.

At a sufficiently high carrier density excitons are no longer a physically realistic way to model e-h pairs generated by the irradiation because the density of the e-h pairs means their average separation is comparable to or smaller than the Bohr radius of the excitons. At such high densities electrons and holes are no longer uniquely paired, hence the free carriers should be considered as an electron-hole plasma (EHP). To estimate the critical carrier density the approach suggested by Klingshirn [173] is adopted, by setting

$$a_B^3 \cdot n_{\mathrm{e-h\,pairs}} \approx 1 \tag{7.14}$$

where a_B^3 is the Bohr radius, which varies from around 1 nm to 50 nm in semiconductors [173], and $n_{\mathrm{e-h\,pairs}}$ is the critical electron-hole density. Using the above equation thus provides a density range of $8 \times 10^{21}\mathrm{m}^{-3} < n_{\mathrm{e-h\,pairs}} < 1 \times 10^{27}\mathrm{m}^{-3}$ for the onset of a high-density regime where electrons and holes are no longer uniquely paired, and hence the free carriers should be considered as an EHP. To estimate the average electron-hole pair density in the focal region, the spatial distribution of the charge generation profile shown in Figure 7.8 (b) and (c) can be used. From the figure, a focal volume of $\pi \times \left(0.25 \times 10^{-6}\right)^2 \times 50 \times 10^{-6} = 9.8 \times 10^{-18}\,\mathrm{m}^3$ is taken, which combined with the total charge calculated above gives an average carrier density of around $5.2 \times 10^{24}\,\mathrm{m}^{-3}$. The carrier density in the GaN regions would be higher than this figure. During

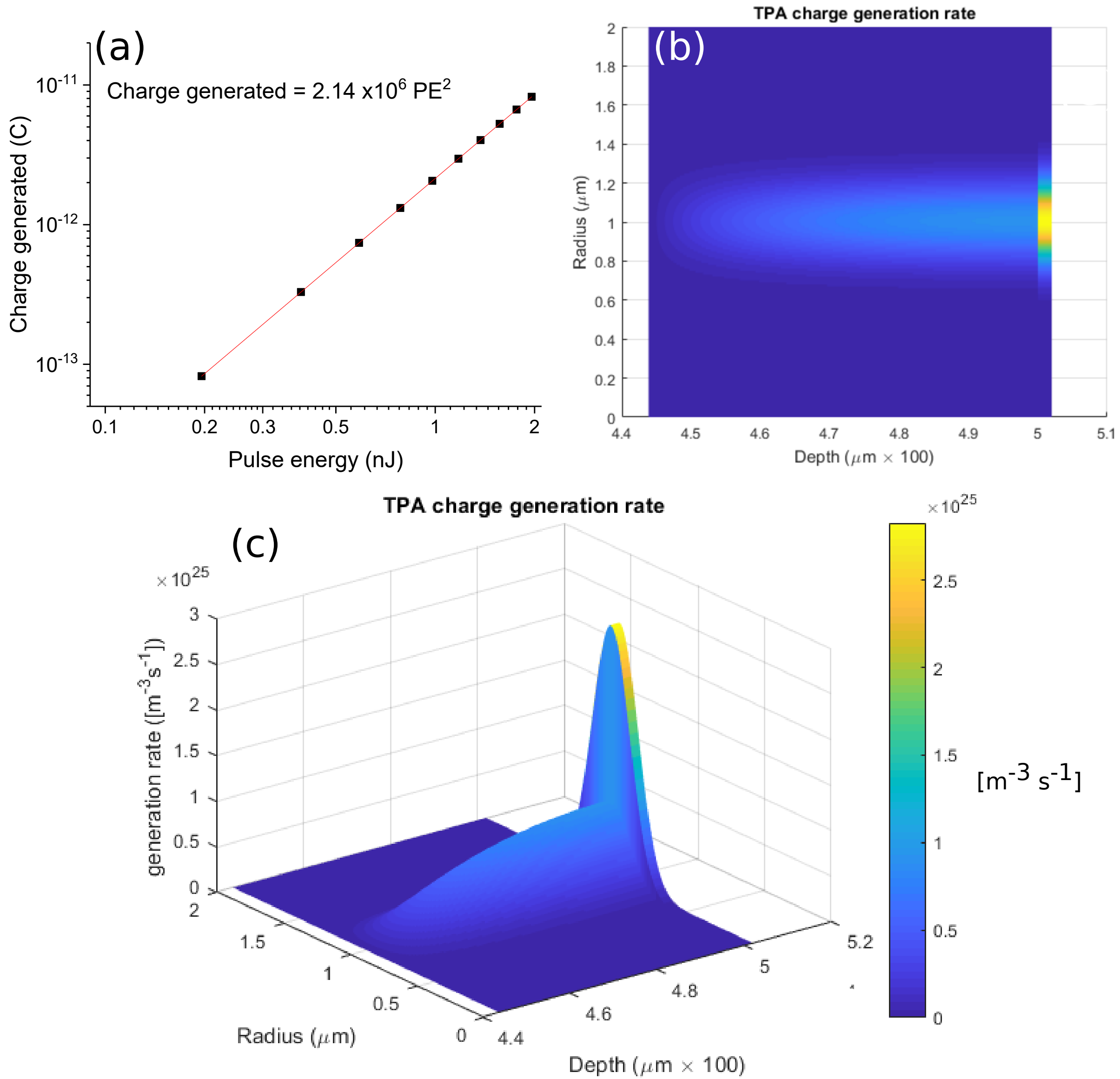

Figure 7.8: a) Total charge generated within the focal region as a function of incident laser pulse energy. The red line is a power law fit to the data. The fitted equation is shown, where PE is the pulse energy in Joules. b) and c) show the rate of charge density increase at the time of peak laser pulse intensity. The discontinuity at 500 μm is due to the increased TPA coefficient in GaN as compared to SiC.

and immediately after the laser pulse the charge density in the focal region will be sufficient to cause the generated electrons and holes to exhibit properties of collective EHP behaviour - the material will behave like a plasma. For comparison, taking average values calculated for the spatial profile of the ionisation due to a PKA created by a 14 MeV neutron collision, shown in Figure 7.6, gives an average carrier density of $1.6 \times 10^{25}\,\mathrm{m}^{-3}$. The charge density produced by the laser pulse is therefore of comparable magnitude to that due to PKAs in a fast neutron irradiation environment, suggesting that pulsed laser induced TPA is a credible surrogate for the ionisation aspects of 14 MeV neutron irradiation.

7.4 Measurements of charge collection and enhancement

In this section, following the discussion above, the scaling of collected charge, peak current, rise times and FWHM of the signals at the gate and drain contacts of HEMTs exposed to a single laser pulse are investigated with respect to the applied electrical biasing and laser pulse energy. The measurements reported in this section were produced by aiming the laser spot at the gate position, and then fine-adjusting position and focus to maximise the electrical signal. Unless stated otherwise, laser pulse energy was set to the minimum level which would produce a clear signal for each individual test. Signals measured at the Schottky gate contact, with zero applied drain bias, are presented first. These measurements provide valuable information on the basic charge deposition and collection mechanisms for a HEMT with a quasi-symmetrical electric field distribution under the gate contact. Following those results, the more realistic usage case of simultaneously applied gate and non-zero drain biasing is presented.

The results in this section show that the variation of peak transient electrical current, and collected charge, with respect to electrical biasing and laser intensity are non-trivial. The charge collected at the drain contact will be seen to be greater than that generated by TPA according to the calculations above. Similarities of the HEMT response to pulsed laser irradiation, to the funnelling- and ion-shunt effects due to ion irradiation, are explored. The effect of buffer doping on the above is also presented.

7.4.1 Results

Gate transients with zero drain bias

Photocurrents could be observed with no external electrical biasing applied, as shown in Figure 7.9, where a HEMT gate contact photocurrent can be seen. The time delay between the photodiode and the HEMT signals is primarily due to the difference in optical path length for the two devices, and also due to electrical path length differences to the digital storage oscilloscope. The time delay of 7.3 ns suggests a combined delay equivalent to a free space optical path difference of around 2.19 m, which is similar to the path difference present in the setup, as shown in Chapter 3.

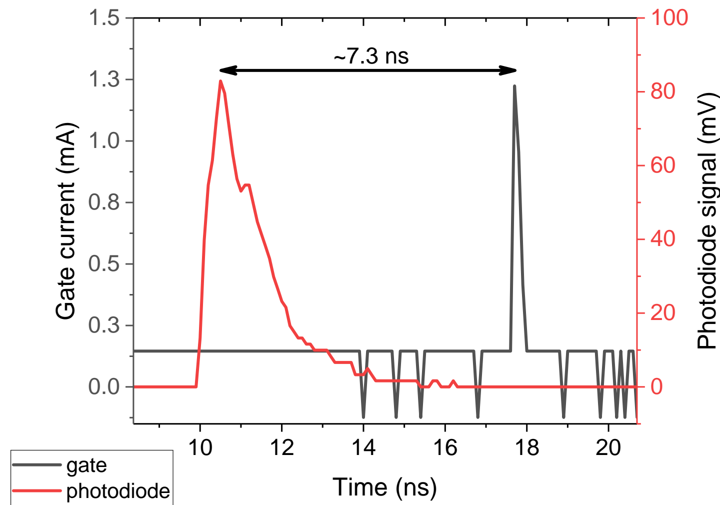

Figure 7.9: Gate photocurrent transient observed from a HEMT on Wafer C with no external electrical bias applied ($V_{GS} = V_{DS} = 0$V). The displayed signal is the average of 64 individual transient measurements, shown along with the associated photodiode signal used to trigger data capture. The HEMT to photodiode signal peak-to-peak delay time is indicated. The quantization of the gate signal is due to a limitation of an early version of the data capture software, which recorded an insufficient number of significant figures in the measurement data file.

Next the results are shown of tests performed with a gate bias applied, but with the drain-source voltage, V_{DS}, held at 0 V. The results of these tests are shown in Figure 7.10 (a) and (b) for the gate and drain currents, respectively. As is visible in the figure, the rising edge of the transient signal typically consisted of only one data point, due to the approximately 100 ps minimum sample separation achievable with the oscilloscope used in the measurement system. For the zero drain bias transients displayed here the FWHM of the signals can be seen to be < 0.5 ns. The magnitude of the measured transients increased as gate-source voltage, V_{GS}, was decreased from 0 V to -10 V. The source current could not be measured directly. However, since drain current is of a almost identical magnitude but opposite sense to the gate current, from conservation of charge the source current must be negligible in this case. From the figure it is apparent that positive charge was collected at the gate contact, and negative charge at the drain contact.

Further measurements were performed with zero drain bias, but using smaller increments in V_{GS}, and centred around the unbiased point, as shown in Figure 7.11. The measurements were performed on Wafer C with zero applied drain bias, as before. A change from positive to negative charge carriers, holes to electrons, is apparent as V_{GS} is made increasingly positive. The hole signal seen for negative values of V_{GS} can be seen to have a shorter FWHM than the electron signal that manifests for sufficiently large positive values of V_{GS}.

By taking the complete data set corresponding to the transient measurements shown in Figure 7.11, the peak currents and charge collected at the gate and drain contacts were determined.

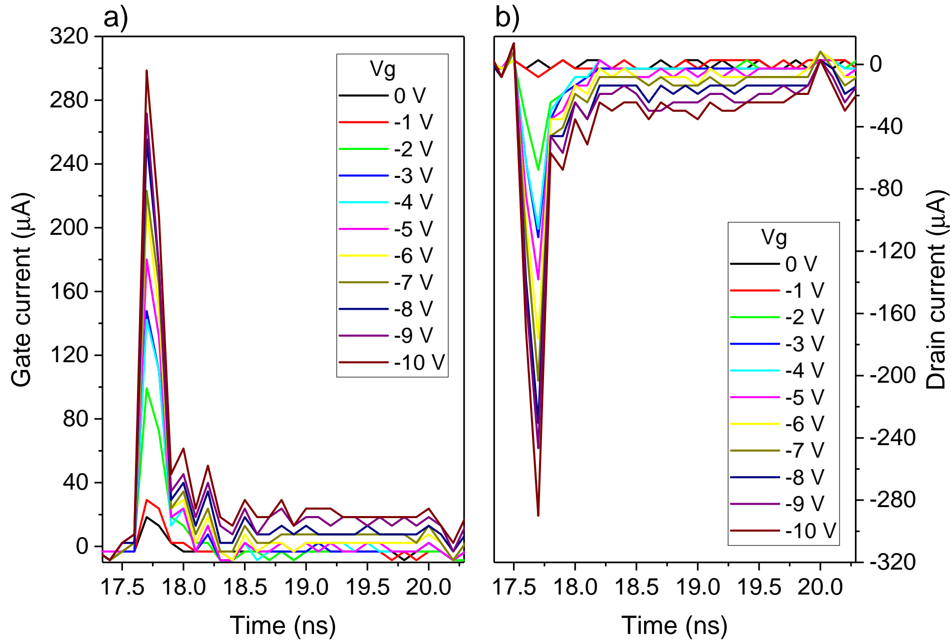

Figure 7.10: (a) Gate, and (b) drain, photocurrent transients as a function of applied gate bias, measured from a HEMT on Wafer C. In each case $V_{DS} = 0\,\text{V}$. The signs of the currents correspond to the measured voltage across the $50\,\Omega$ oscilloscope termination. The plots are 64 sample averages. The quantization of the signals is due to a limitation of an early version of the data capture software, which recorded an insufficient number of significant figures in the measurement data file.

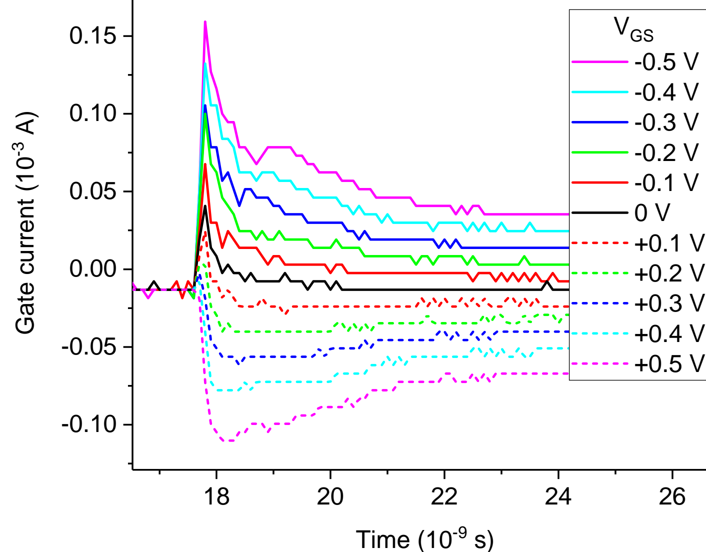

Figure 7.11: Gate current against time as a function of gate-source voltage. The full measurement range was for V_{GS} from -1.0 V to +0.7 V, however, for clarity in the figure the displayed range is from -0.5 V to +0.5 V. The apparent non-zero gate current prior to the transients is an artefact caused by an oscilloscope offset.

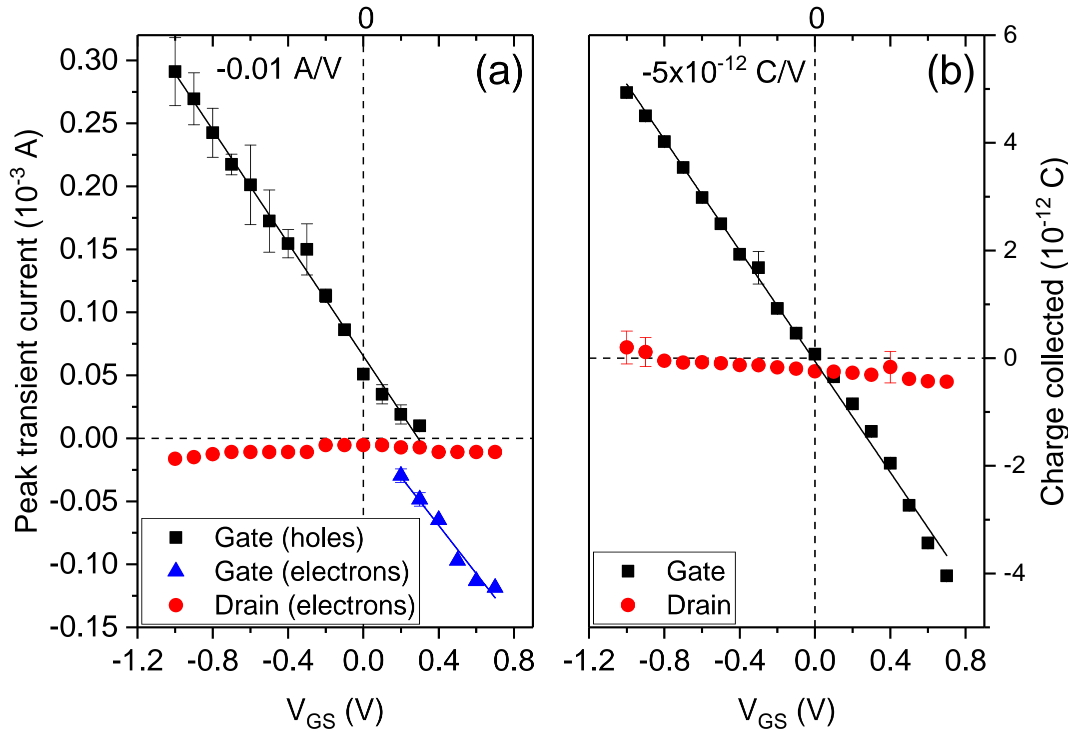

Figure 7.12: (a) Peak transient current, and (b) charge collection, measured at the gate and drain contacts with zero drain bias ($V_{DS} = 0\,V$). Solid lines are fits to the data. Note the non-zero hole current at the gate for $V_{GS} = 0\,V$.

These are shown as a function of gate bias in Figure 7.12. In part (a) of the figure a non-zero hole current measured at the gate contact for $V_{GS} = V_{DS} = 0\,V$ is present. From the fit to the gate hole data, the V_{GS} value corresponding to zero hole current was found to be $(0.33 \pm 0.03)\,V$. The slope of the fits to the hole and electron currents measured at the gate are similar, at $(12 \pm 0.9)\,mA/V$ and $(9 \pm 1)\,mA/V$, respectively. Negligible drain currents were observed in these measurements. In part (b) of the figure the charge collected at the gate contact, found by integrating the measured transient currents with respect to time, passes through the origin with a slope equal to $(-5.15 \pm 0.08) \times 10^{-12}\,C/V$. The magnitude of charge collected is consistent with the calculation of charge generation due to TPA shown in Figure 7.8(a).

Simultaneous gate and drain bias

The results presented above have helped to establish the nature of the photocurrent and collected charge dependence on the applied V_{GS}. Here the complicating effect of an applied drain bias is presented. Figure 7.13 shows the peak currents and the charge collected during the transient measurement as a function of V_{GS} but with an applied drain bias of $V_{DS} = 2\,V$. For comparison, a small number of measurements with $V_{DS} = 0\,V$ are also presented in the figure. In parts (a) and (c) of the figure the peak gate current, and the charge collected at the gate contacts are found

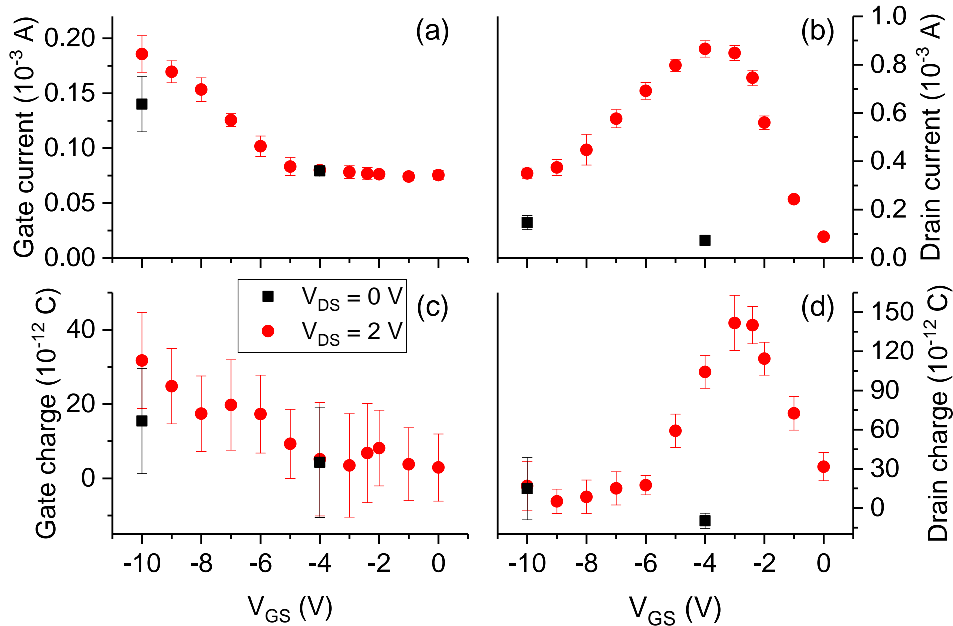

Figure 7.13: Peak current (a, b), and total charge collected (c, d), as measured at the gate and drain contacts respectively as a function of gate-source voltage for Wafer B. Drain quantities were multiplied by -1.

to increase monotonically as V_{GS} is made increasingly negative. In contrast to this trend, the equivalent plot for the drain values shown in parts (b) and (d) of the figure show a non-monotonic dependence on V_{GS}. The peak in the drain signals occur for $V_{GS} \approx -3$ V, they then decrease as reverse gate bias is increased.

The effect of increasing electrical bias and laser pulse energy

Here the effect of increasing drain bias, V_{DS}, towards the usual operating level is shown, along with the effect increasing laser pulse energy. In Figure 7.14, gate bias is held constant at $V_{GS} = -4$ V. V_{DS} is increased, as shown in the figure, from 0 V to 20 V for the lower pulse energy tests, and from 0 V to 30 V in the case of the higher pulse energy tests. Taking the lower pulse energy case first, there is a sharp increase in peak current and charge collected at the gate and drain when $V_{DS} = -V_{GS} = 4$ V. For small V_{DS} values, drain current is less than gate current. However, the situation is reversed as V_{DS} is increased sufficiently. The same magnitude trend is followed by the collected charge, where positive charge is collected at the gate, and negative charge at the drain. The data for the ≈ 2x higher pulse energy case is quite different. In that case the peak drain currents, shown in part (b) of the figure, quickly become much larger than the gate current, in contrast to the lower pulse energy results shown in part (a). Positive charge was collected at the drain contact for several of the V_{DS} values tested at the higher pulse energy. When compared to the lower pulse energy testing, the collected charge resulting from high pulse

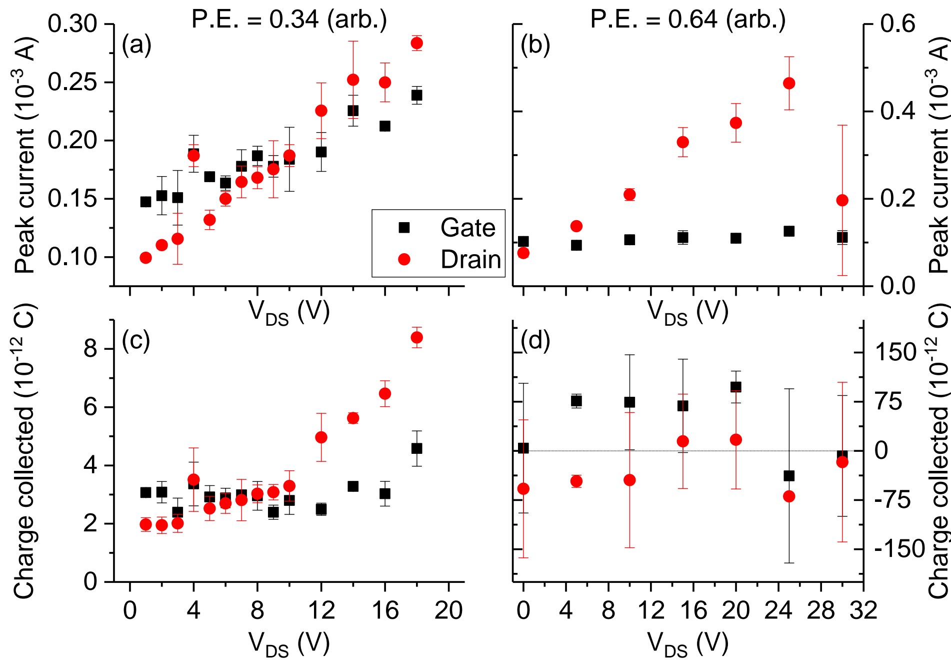

Figure 7.14: Peak gate and drain currents (a, b), and charge collected (c, d), plotted as a function of V_{DS}. Laser pulse energy was 0.34 (arb.) for (a, c), and 0.64 (arb.) for (b, d). Measurements were performed on Wafer B. Drain quantities were multiplied by -1.

energy testing demonstrated an increased shot-to-shot variation, and was around an order of magnitude larger in quantity.

Above, we saw how key aspects of HEMT transient response depend on the electrical biasing applied during pulsed femto-second laser irradiation. We are now, therefore, in a position to explore the important question of the laser pulse energy dependence. Peak currents and collected charge, as a function of laser pulse energy, are shown in Figure 7.15. In the figure, power law fits to the data of the form $y = a \times \text{P.E.}^b$ are plotted, where P.E. is laser pulse energy, and a is a constant. b values, uncertainties, and quality of fit parameters are provided in the figure adjacent to the line to which they relate. In part (a) of the figure, peak gate current is seen to vary as P.E.^{3}, once increased beyond a threshold level. The peak drain current, however, appears to split into two distinct regimes, as shown in part (b) of the figure: in the low P.E. regime, where peak gate current was insensitive to P.E., peak drain current increases as approximately P.E.^{3} to P.E.^{4}; in the high P.E. regime, where peak gate current increased as P.E.^{3}, peak drain current increases as P.E.$^{1.2}$ to P.E.$^{1.5}$, where the higher power was found for the high V_{DS} tests. Drain collected charge followed the same trend as peak drain current, but with slightly reduced b values. The charge collected at the gate contact, shown part (c) of the figure, does not display a clear trend, and is larger than the calculated charge deposition, suggesting that laser shunt or funnelling effects are taking place, as discussed earlier.

Results from pulse energy dependence testing of Wafer B are shown in Figure 7.16. In part

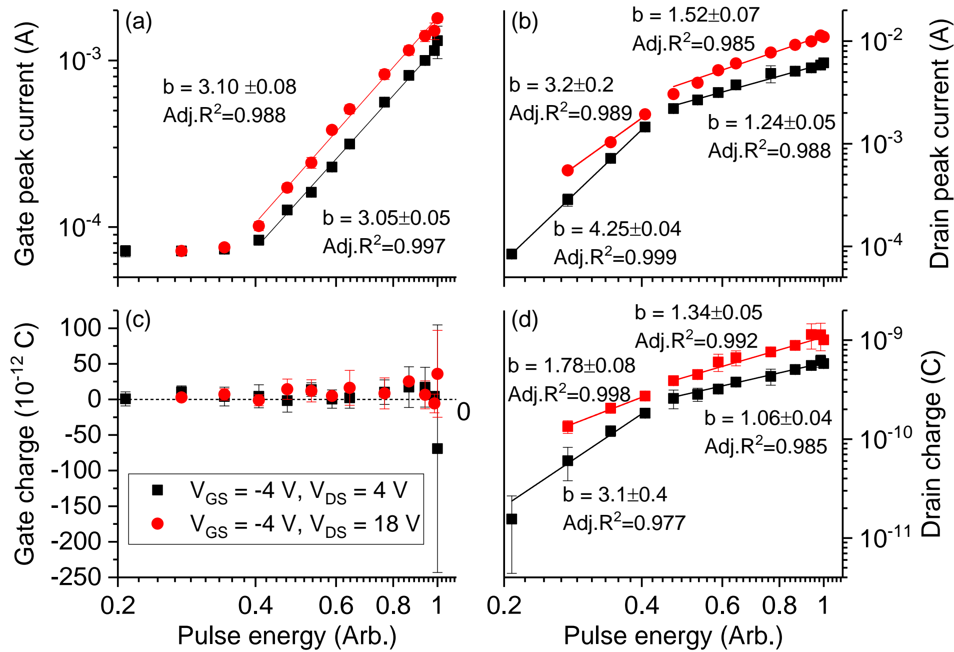

Figure 7.15: Wafer A peak gate and drain currents (a, b), and charge collected (c, d), plotted as a function of laser pulse energy. Biasing conditions tested: $V_{GS} = -4\,V$, $V_{DS} = 4\,V$ and $V_{GS} = -4\,V$, $V_{DS} = 18\,V$. Solid lines are power law fits to the data. Drain quantities were multiplied by -1.

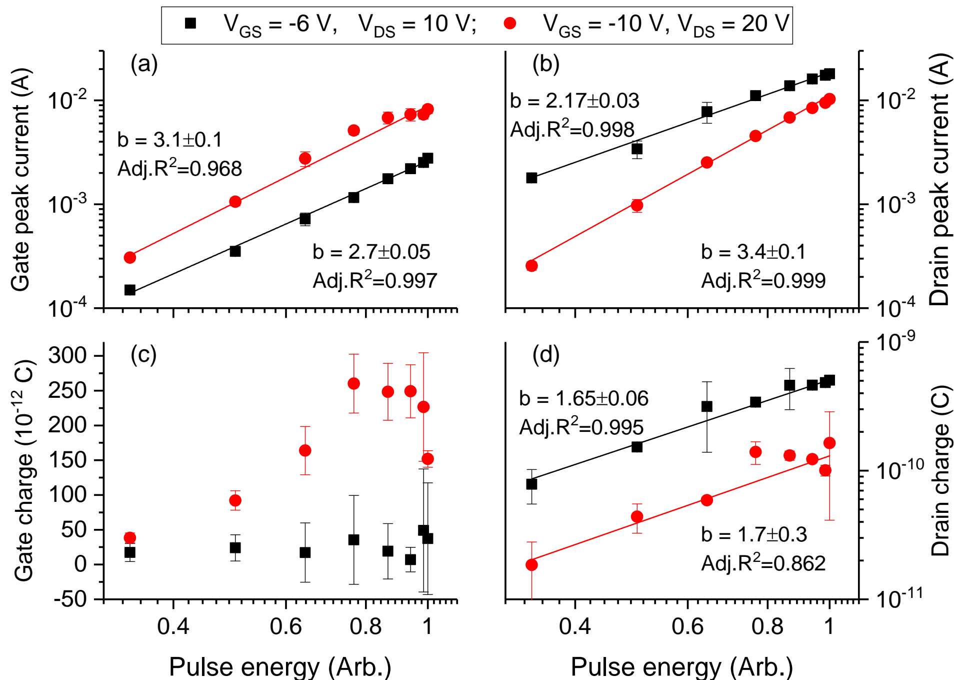

Figure 7.16: Wafer B: peak gate and drain currents (a, b), and charge collected (c, d), plotted as a function of laser pulse energy. Biasing conditions tested: $V_{GS} = -6\,V$, $V_{DS} = 10\,V$ and $V_{GS} = -10\,V$, $V_{DS} = 20\,V$. Solid lines are power law fits to the data. Drain quantities were multiplied by -1.

(a) of that figure, peak transient gate current can be seen to increase approximately as P.E.^{3}, similarly to Wafer A. The charge collected at the gate contact, shown in part (c), is similar to Wafer A for the lower electrical bias case, but for the high bias case, $V_{DS} = 20\,V$ and $V_{GS} = -10\,V$, gate collected charge increases with increasing pulse energy until saturating at around 250 pC. An interesting trend is apparent in the drain signals shown in parts (b) and (d), where the peak drain current and charge collected are smaller than for the lower bias case. As was seen for Wafer A, the power law fits for the Wafer B drain signals, shown in the figure, are all super-linear.

7.4.2 Discussion

Gate transients with zero drain bias

The measurements displayed in Figure 7.9 show that it is possible to measure a gate photocurrent from a HEMT even with no externally applied electrical bias. The photocurrent must therefore be due to either diffusion of carriers generated near the gate electrode, or drift of carriers due to the built-in field present in the space charge region that exists in the AlGaN barrier layer. Next, a gate bias was applied, with the drain held at 0 V, with the aim of producing a simplified quasi-symmetric electric field profile centred around the gate. By increasing the reverse bias (negative V_{GS}) on the HEMT gate, the size of the depletion region is increased in order to provide sufficient carriers to screen the applied electric field. When free carriers are generated by the laser pulse in the increased size depletion region, they are exposed to the larger electric field there. So increasing the applied reverse bias increases the volume of semiconductor material that charge is collected from, and increases the rate at which it is collected. Figure 7.17 (b) graphically shows how the extent of the high electric field region under the gate is increased with reverse bias as extracted from a Silvaco Atlas simulation for a representative structure. In part (c) of that figure the increased electric-field magnitude in the AlGaN barrier, and increased depth into the GaN buffer of the electric field are apparent. Part (d) of the figure is the corresponding band diagram extracted from the simulation for the $V_{GS} = -6\,V$ case.

A change was observed from hole current to electron current measured at the gate contact, shown in Figure 7.11, as V_{GS} was made increasingly positive. This can be explained by the hole current into the gate contact being enabled by the valence band profile as shown in Figure 5.8 (b) in Chapter 5. Because the source and drain contacts were held at the same voltage, the apparent negligible source current in Figure 7.10 suggests an asymmetric electric field profile within the HEMT when a gate voltage is applied. This is likely to be caused by field plates connected to the contacts, and designed to minimise the peak electric field magnitude on the drain side of the gate.

The non-zero hole current measured at the gate when ($V_{GS} = V_{DS} = 0$V), seen in Figure 7.12, suggests the presence of a built-in field within the HEMT. The built-in field, which could be due to the intrinsic polarisation, is causing free holes to drift out of the gate. The magnitude of the potential difference across the HEMT barrier, due to the built-in field, was found to be (0.33 ± 0.03)V from the fit to the hole current shown in that figure. In Fig.12a of [44], Ambacher

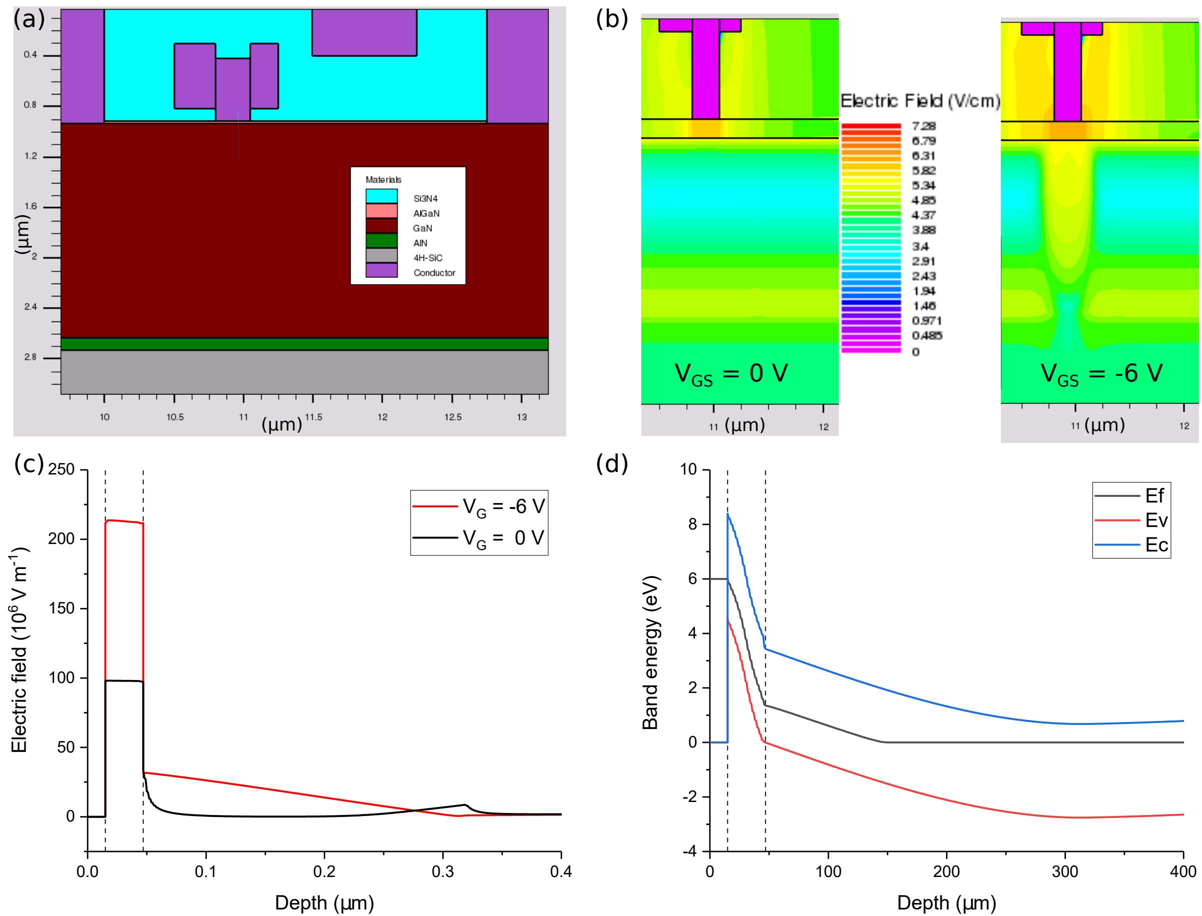

Figure 7.17: Electric field maps and band diagrams extracted from Silvaco Atlas TCAD simulations. (a) Layout of simulated structure. (b) Electric field distribution directly beneath the gate for, left $V_{GS} = 0\,\mathrm{V}$, and right $V_{GS} = -6\,\mathrm{V}$, note the enlarged vertical scale and logarithmic colour scale. The AlGaN barrier layer is delineated by the horizontal solid black lines. (c) Electric field magnitude extracted from a cut line taken vertically through the centre of the gate contact. Dashed lines indicate the edges of the AlGaN barrier. (d) Band diagram for the $V_{GS} = -6\,\mathrm{V}$ case.

provides a comprehensive model developed in that paper for Schottky gate on AlGaN/GaN structures like those tested here. In the model, the penetration of the conduction band edge below the Fermi level is shown to be $\approx 0.30\,\mathrm{eV}$. Once experimental uncertainty is considered, this matches the value of positive bias shown in Figure 7.12 (a) needed to completely suppress the hole current, shown by the x-intercept of the fit to the hole data, suggesting that the model is applicable to the structures tested here. The linear dependence of the peak currents, and integrated charge collected, on V_{GS} suggest that the charge conduction mechanism between the photo-generated charge and the gate contact is Ohmic in nature. The negligible peak drain currents shown in the figure suggest that the photocurrents were flowing between the source and gate for those small V_{GS} tests. This then indicates that for small V_{GS}, the field plates proposed to explain the apparent lack of a source current for the larger V_{GS} measurements shown in Figure

7.10, are ineffective.

Simultaneous gate and drain bias

Peak transient gate current can be seen to increase with increasing $-V_{GS}$, as shown in Figure 7.13 (a). In the figure, the slope of the peak gate current versus $-V_{GS}$ curve can be seen to increase once $-V_{GS}$ is decreased below around -5V. The charge collected at the gate contact also demonstrates an inflexion point at the same V_{GS} value, seen in part (c) of the figure. These increases are largely consistent with the transient photocurrent expected from a reverse biased diode. However, the inflexion point near $V_{GS} = -5$V, more than 2V below the HEMT threshold voltage, V_{th}, is not. Turning to the drain current and charge measurements in part (b) and (d) of the figure respectively, a clear non-monotonic dependence on V_{GS} is apparent.

Increasing V_{GS} increases the electric field under the gate, causing electrons and holes generated by the laser irradiation to separate more quickly by drift. This enables a greater proportion of the charge carriers generated by the laser pulse to be collected before they recombine. The gate bias causes drift of holes towards the gate, whereas the electrons move towards the 2DEG that is present adjacent to the charge generation volume, and are subsequently collected at the drain contact. The charge collected at the drain contact, however, reached around 150 fC at its maximum. That is around an order of magnitude greater than the maximum charge deposition expected from the calculations described above. It is also several times larger than that collected at the gate contact. This high level of charge collection at the drain is consistent with the plasma generated by the laser irradiation temporarily creating a high conductivity region that connects the source and drain contacts. This suggests that pulsed lasers can simulate the analogous ion shunt effect, discussed earlier.

As V_{GS} was increased further below V_{th}, the 2DEG would have been increasingly depleted laterally. The increasing lateral extent of the depletion region would, provided that the laser focal region did not encompass it, increase the time taken for the generated electrons to scatter into the 2DEG. The increased gate bias would also enable the depletion region to be re-established more quickly. The net effect would be an increase in peak gate current, and a decrease in peak drain current and charge collected. Which is what is shown in Figure 7.13. Part (d) of the figure, where, despite a non-zero peak current, the collected charge is near zero. Comparing Figures 7.13 (a) and (b) it can be seen that even at $V_{GS} = -10$V, the peak drain current remains larger than the peak gate current. The increased reverse gate bias therefore reduces the 'laser shunt effect', but does not suppress it completely.

Figure 7.18 shows the graphical results from simulations performed using Silvaco Atlas TCAD software to demonstrate the plausibility, for the case of AlGaN/GaN HEMTs of the funnelling, 'laser shunt', and the depletion region recovery effects, discussed above. The femto-second laser pulse was simulated in Atlas by defining a spatially- and temporally-dependent charge generation source, as calculated using the methods described earlier in this chapter. Part (a) of the figure

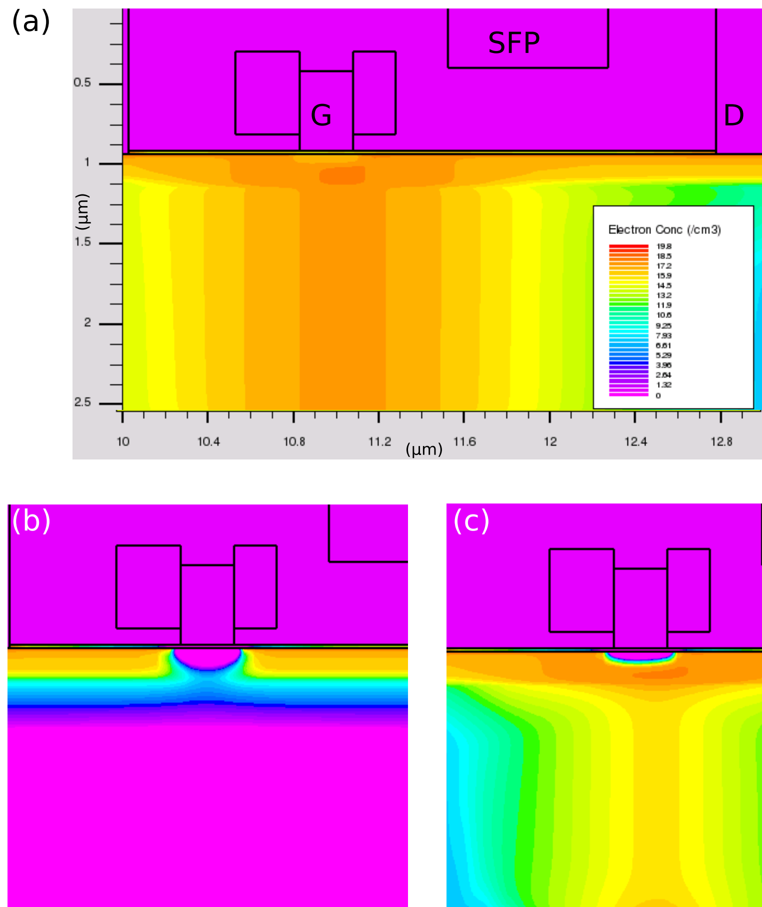

Figure 7.18: Electron concentration within a HEMT calculated using Silvaco Atlas TCAD software, (a) during, (b) before, and (c) 10×10^{-12} s after the femto-second laser pulse. In the simulation $V_{GS} = -6$ V, and $V_S = V_D = 0$ V 'G' indicates the gate contact, 'SFP' is a source-connected field plate, and 'D' indicates the drain contact. Note the logarithmic colour scale.

shows the electron concentration during the laser pulse in the HEMT structure. The depletion region is clearly visible under the gate contact in part (a) of the figure, before the laser pulse. In part (c) of the figure, 10 ps after the laser pulse, the depletion region can be seen to be re-establishing, however the 2DEGs on either side of the depletion region are shown to be linked by a non-negligible electron concentration below the depletion region. This is the conduction path corresponding to the 'laser shunt' effect. The funnelling effect is enabled by the electric field penetration into the buffer enabled by the vertical extent of the high electron concentration region, shown in part (c) of the figure.

The effect of increasing electrical bias and laser pulse energy

The lower pulse energy test data shown in Figure 7.14 shows that peak gate and drain currents increased monotonically with increasing drain bias, with the exception of the case where the

gate bias screens the drain bias from the source at $V_{DS} = -V_{GS} = 4\,V$. The rate of increase of drain current with respect to V_{DS} is greater than that for the gate current. This fact, combined with the observation that the quantity of charge collected at the drain became larger than that collected at the gate at high V_{DS}, suggests that the 'laser shunt effect' provided a source-drain conduction path. For the ≈ 2X higher pulse energy case, where the TPA charge generation would be ≈ 4X larger, the apparent source-drain laser shunt effect increased considerably. In that case the peak drain current reached up to ≈ 4X larger than the gate current. Net positive charge collection was observed at the drain contact, and the quantity of charge collected at both contacts was ≈ 10X larger than for the lower pulse energy case. During the high pulse energy tests at the maximum V_{DS} value tested, 30 V, the HEMT under test suffered irreversible damage. The impact of the damage was that the channel could no longer be closed by applying reverse gate bias, as is apparent from the peak current data shown in the figure. This demonstrates that pulsed femto-second laser radiation effects testing can cause gate breakdown effects.

It was shown earlier that charge generation by TPA follows an intensity-squared power law. It can be seen in Figure 7.15 that the peak transient current and collected charge resulting from a femto-second laser pulse may not follow that simple power law in a HEMT. Results were shown above that suggested the creation of a region of high conductivity within the HEMT, activating conduction pathways from the source to the drain and the gate, and in some cases from the gate to the drain. The power law fits plotted in the figure show that for Wafer A, as laser pulse energy is first increased, peak drain current is strongly coupled to the quantity of charge deposited by the laser pulse, increasing with the third or fourth power of pulse energy. Beyond a threshold level, however, peak drain current continues to increase with increasing pulse energy, but the coupling is reduced to a power of 1.2 to 1.5, suggesting it becomes limited by a different physical mechanism. It is unlikely that the observed behaviour was due to carriers generated by SPA at defect sites because of the super-linear power law fits obtained from the measured data, although a combination of SPA and TPA is possible. At that point, peak gate current increases with the third power of laser pulse energy. To understand this behaviour one may consider that at lower pulse energies, peak drain current increases faster than the charge collected at the drain, shown in part (d) of the figure. Whereas at higher pulse energies, peak drain current and collected charge scale almost identically with pulse energy. Given that the quantity of charge collected at the drain contact is larger than that calculated in Section 7.3 to be deposited by the laser pulse, this suggests that the initial rapid rise in peak drain current is primarily source-drain conduction as a result of the increasing transient conductivity in the focal region caused by the TPA-generated free carriers, and that the slower rate of drain current increase as pulse energy continues to rise is due to the resistivity of the intrinsic HEMT or the electrical contacts made to it.

The power law fits to the tests results from Wafer B, although conducted with larger bias applied, are largely consistent with the results found from Wafer A. The reduction seen in peak

drain current and drain charge collected when V_{DS} is increased from 10 V to 20 V can be explained by the increase of negative V_{GS} from -6 V to -10 V. It can be seen that for the larger bias case, gate and drain peak currents are of similar magnitudes, and that the charge collected at the gate is larger than collected at the drain. A transient source-gate conduction path is therefore created under these biasing conditions during laser irradiation.

Under normal operating conditions, increasing the drain-source voltage applied to a HEMT would be expected to increase the output drain current. Increasing the drain-gate voltage might also be expected to increase the photocurrent response of the region between those two contacts, by increasing the drift velocity of the photo-generated electron-hole pairs, allowing more to be collected at the contacts before recombination. However, the results given above shown that increasing drain-gate and drain-source voltage applied to a HEMT does not necessarily increase the size of the irradiation response.

7.4.3 Conclusions

Irradiation of the gate region of the HEMTs caused a photocurrent to flow between the gate and drain contacts, not the gate and source, suggesting that field plates create an asymmetric electric field distribution within the devices. This response to localised TPA is likely to be representative of the nature of the HEMT electrical transients caused by exposure to a radiation environment. Under very low biasing conditions, however, the photocurrent flowed between gate and source contacts, indicating the existence of a threshold gate bias, below which the field plates are ineffective. Without a drain bias applied, peak photocurrent and total charge collected at the contacts, increased linearly with increasing reverse gate bias, suggesting that conduction was dominated by electrical drift from the focal spot region. If this suggestion is correct, then these results show that increasing volume of the depletion region under the gate, by increasing the reverse gate bias, did not determine the magnitude of the transient radiation effects. It is likely that the extent of the depletion region for small values of reverse bias is large enough to completely enclose the charge generation, as shown by comparison of Figures 7.8 (b,c) and Figures 7.18 (b,c). Because the density of charge created by the laser pulse temporarily created a plasma within the focal spot region, it was the rate of charge collection from that plasma due to drift, caused by the combination of the built-in and applied electric fields, that determined the extent of the transient radiation effect.

The results presented above for the simultaneous gate and drain bias tests indicate that the plasma generated in the laser spot focal region is sufficiently dense to enable a ‘laser shunt effect’, analogous to the ‘ion shunt’ radiation effect. In this effect conduction from the source to drain, normally prevented by the off-state gate bias, is enabled by the transient high conductivity region under the gate. Pulsed femto-second laser testing may therefore be suitable for screening devices where that SEE would be a concern in an application. Furthermore, the measurements also suggest that increasing gate bias causes the depletion region to be re-established more

quickly, reducing the duration of the source-drain current flow. Clearly then, when testing HEMTs using TPA under biasing conditions which enable this 'laser shunt effect' to occur, a pulse energy-squared, or intensity-squared dependence of collected charge should not be expected.

7.5 A pulse repetition frequency (PRF) effect

It is often experimentally advantageous to use averaging techniques to improve the signal to noise ratio of small signals, or repetitive signals. Quantities of charge as low as femto-Coulombs may be generated by low LET PKAs within sensitive regions of HEMTs, so there is a clear case for the use of averaging or lock-in techniques to improve measurement signal fidelity when detecting or simulating signals generated by the passage of such ions. The response of a semiconductor device to a high radiation flux environment, or an environment where multiple radiation events occur within the device over an extended period, is comparable to testing using averaging or lock-in techniques. This raises the question of whether the response of a semiconductor device can be considered as a sum of SEEs.

In radiation detection the phenomena of 'pulse pile up' and the 'pulse height defect' are well known. In the pulse pile up effect, when PRF is sufficiently high the signals generated in a detector in response to the discrete pulses will overlap. This can shift the baseline of the detector output, and cause an erroneous pulse height measurement. In the pulse height defect, a detector can measure the deposition of a different quantity of charge from two ions with identical LET values, but different mass. Three factors affect the pulse height defect: i) ions of differing mass depositing differing proportions of their energy in the window, packaging, or dead zone of the detector; ii) heavier ions losing energy via nuclear collisions in addition to electronic interactions; and iii) the high rate of electron-hole pair recombination within the dense core of the plasma track along an ions path, particularly near the Bragg peak at its end. The severity of the pulse height defect can be reduced by increasing the electrical bias applied to the radiation detector. This has the effect of decreasing the proportion of generated electron-hole pairs that can recombine before reaching the electrical contacts.

In this section, the effect of varying the PRF used when performing TPA laser testing of HEMTs will be explored. The question as to whether high PRF testing can be used to increase the fidelity of transient radiation effects simulation will be answered. It will be shown that considering the radiation response of a HEMT in a high radiation flux environment to be a sum of SEEs over-estimates the radiation response of the HEMT under test. Using high PRF testing to measure the response of a HEMT to a single impulse should be used with caution where device electrical response is of interest.

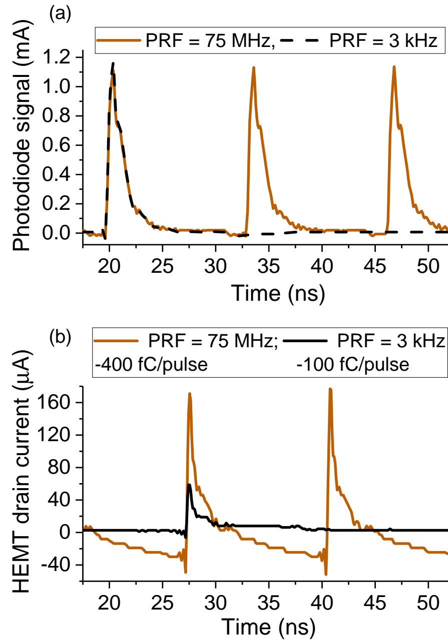

Figure 7.19: a) Photodiode signals, used to monitor incident laser pulse energy, shown for two different pulse repetition frequencies (PRFs). b) corresponding HEMT drain current transients exhibiting a PRF dependent amplitude - the PRF effect. The quantization of the 75 MHz signal in b) is due to a limitation of an early version of the data capture software. HEMT biasing was $V_{GS} = -4$ V and $V_{DS} = +4$ V. Plotted signals are 512 sample averages.

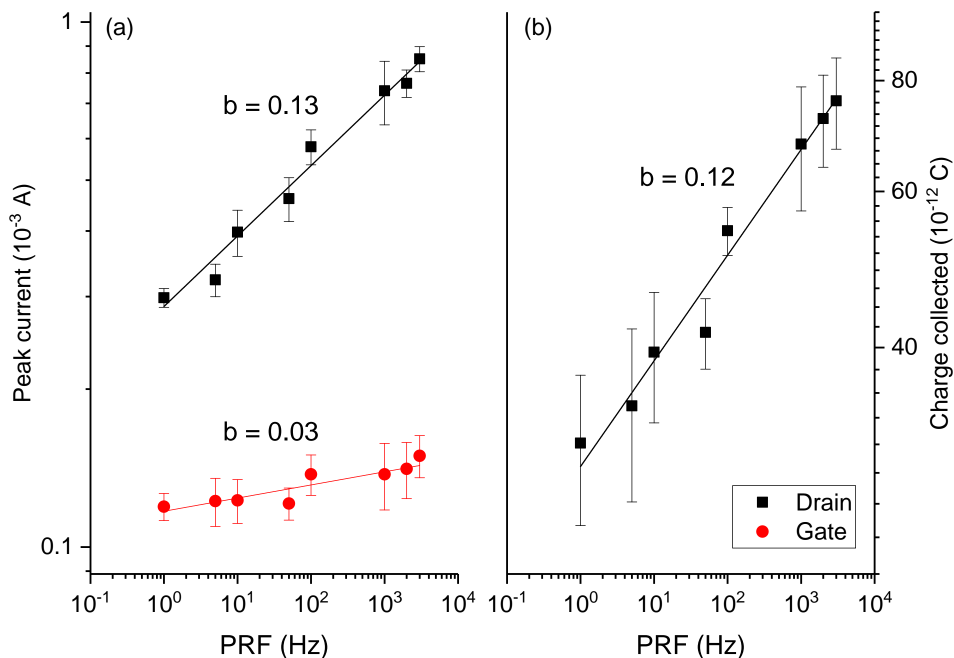

Figure 7.20: Peak drain current (a) and collected charge (b) plotted against laser pulse repetition frequency (PRF). Solid lines are power law fits to the data, with the power, b, shown. Data obtained for a HEMT on Wafer B, biased with $V_{GS} = -4$ V and $V_{DS} = +4$ V.

7.5.1 Results

The signal from the photodiode used to monitor laser pulse energy is plotted in Figure 7.19 (a), for measurements performed using the native 75 MHz output PRF of the femto-second oscillator, and for those recorded when using a 3 kHz PRF produced using the Pockels Cell pulse picker. The 75 MHz PRF was achieved by inserting a $\lambda/2$ plate in between the first Glan laser prism and the Pockels cell, having the effect of rotating the polarisation of the light by 90° so that the entire pulse train could propagate through the Pockels Cell. The photodiode signals shown demonstrate that the pulse energy propagated to the pulse picker had been carefully adjusted to ensure that the pulse energy directed on to the HEMTs under test was the same for both PRFs. In part (b) of the figure, HEMT drain current transients resulting from irradiation at the two different PRFs are shown. Two effects are clear in the figure: a baseline shift, and a large change in signal amplitude. The charge collected in a single pulse is also shown in the figure - increasing the PRF from 3 kHz to 75 MHz increased the charge collected in each pulse to 400 fC, a factor of four increase. The peak current amplitude can also be seen to have increased by a similar factor. This PRF effect was observed during testing of all three wafers.

For Wafer B, the peak gate and drain current, and the charge collected at the drain contact, increased with increasing PRF, as shown in Figure 7.20. The plotted quantities were seen to follow a power law, as shown by the fits indicated by solid lines. This was then investigated for slightly different optical conditions below, where Wafers A and B are compared directly. A comparison is presented, in Figure 7.21, of how the PRF effect manifests itself when testing HEMTs on Wafers A and B. In parts (a) and (b) of the figure the peak drain currents measured on both wafers at $V_{DS} = 4\,V$ and $V_{DS} = 18\,V$, respectively, can be seen to increase with the logarithm of the PRF, once it is increased beyond around 10 Hz. In the figure, the slope of the peak current increase with log(PRF) can be seen to be steeper for Wafer A than Wafer B. Wafer A also displays a higher peak drain current at low PRF values. Peak drain current was increased approximately linearly with applied drain bias at all tested PRF values, consistent with the single shot data presented earlier. When $V_{DS} = 4\,V$ the charge collected at the drain contacts for Wafer B is only slightly lower than the Wafer A case, seen in parts (e) and (f) of the figure, despite the FWHM of drain transients on Wafer B being two orders of magnitude longer than those measured on Wafer A. By increasing the drain bias to $V_{DS} = 4\,V$ the FWHM of all the drain transients was reduced, to the point that Wafers A and B are almost equal for low PRF values. For higher PRF values, however, transients on Wafer B were around an order of magnitude longer than on Wafer A. The quantity of charge collected at large drain bias, shown in part (f), was clearly incrased for Wafer A, but decreased for Wafer B, under low PRF irradiation. The difference between the charge collected from the two wafers decreased as PRF was increased.

Drain current transients measured with a PRF of 3 kHz are shown in Figure 7.22. The figure shows how the peak current measured in response to the pulsed laser irradiation of Wafer A is greater than for Wafer B, as described above. After this prompt radiation response, however,

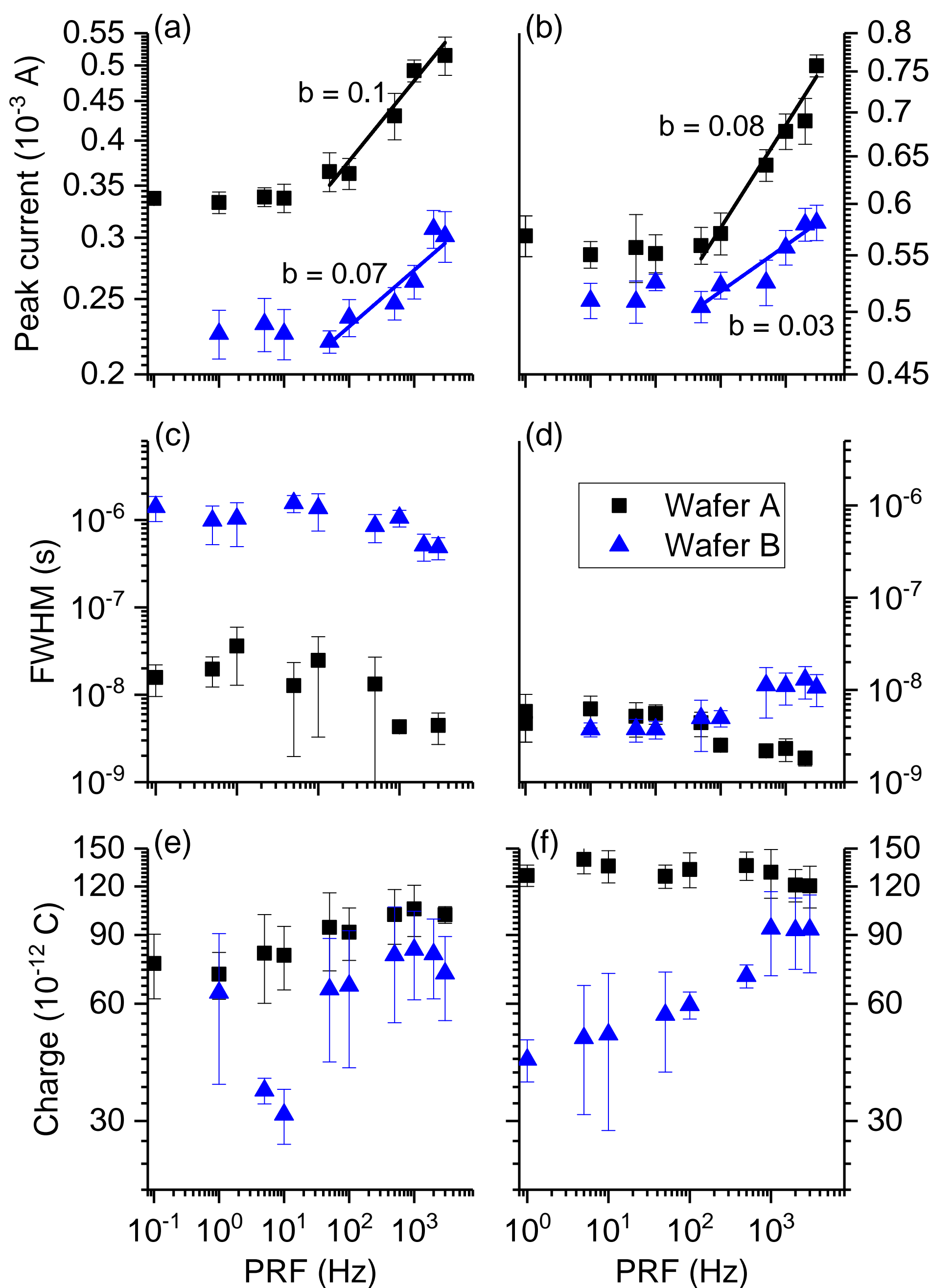

Figure 7.21: Pulse repetition frequency, PRF, effect on Wafers A and B. Drain peak current, FWHM, and collected charge are plotted against PRF for $V_{DS} = 4\,V$ (a,c,e), and for $V_{DS} = 18\,V$ (b,d,f). In all cases $V_{GS} = -4\,V$. Absolute drain values plotted.

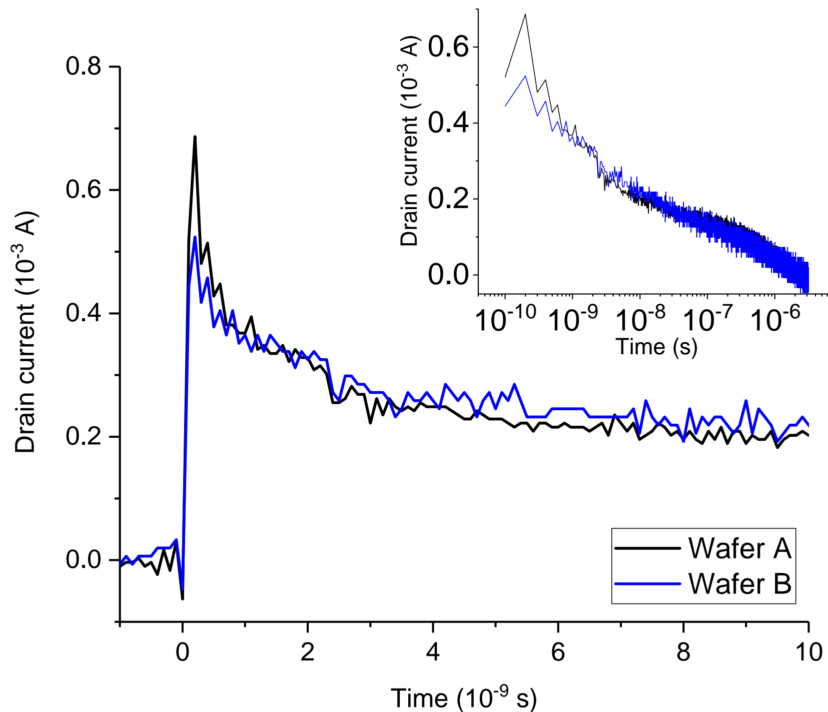

Figure 7.22: Drain transients measured on Wafers A and B at 3 kHz. Inset: Drain current plotted against log(time). In both cases $V_{GS} = -4\,V$ and $V_{DS} = 18\,V$. Absolute drain values are plotted.

the delayed drain current is seen to be almost equal in this case. The inset shows the how the delayed effect similarity continues over several orders of magnitude in time.

7.5.2 Discussion

The baseline shift visible in Figure 7.19, is in the opposite sense to that which would be expected from a pulse pile up effect. The baseline shift can be explained by considering the electrical connections to the HEMT. The bias tees used in the setup include a capacitor element to isolate the high bandwidth connection to the oscilloscope from the DC component of the signal. Therefore, there can be no net flow of charge between the oscilloscope and the isolated side of the bias tee. Because the pulse period is around 13 ns for the 75 MHz PRF data shown in the figure, the return component of the displacement current pulse must occur before the next pulse, making it visible within the time scale shown. The baseline is therefore negatively shifted to ensure that the integral of the curves is zero. The limits of integration used to calculate deposited charge elsewhere in this thesis were carefully chosen to ensure they avoided the return component of the transient signal.

The existence of the PRF effect demonstrated here shows that, during irradiation by train of pulses with a PRF of around 10 Hz or greater, the response of HEMTs to each ionising radiation event is not independent. The size of the PRF effect did not grow during repeat measurements

whilst the HEMTs were continuously exposed to a train of laser pulses. This suggests that the system was in a state of dynamic equilibrium - a steady state. The PRF effect is, therefore, determined by the combined effect of a finite number of the preceding irradiation events. In other words, the PRF effect depends on the sum of a quickly convergent infinite series. The implication of this is that the magnitude of the effect is determined by the period of time elapsed between the measurement pulse and the one that immediately preceded it, not the number of pulses that preceded the measurement.

Because the PRF effect can be observed from 10 Hz and upwards, the physical mechanisms which could plausibly be responsible for it are limited to those that can persist for times of up to around 100 ms following a previous laser pulse and transient current measurement. The most likely candidates are an elevated temperature due to localised heating, or charge storage either in traps at defect sites or by an electrostatic mechanism. As discussed earlier in this thesis, elevated temperature has the effect of increasing carrier density in a semiconductor, which can increase conductivity, provided that mobility is not adversely affected by increased scattering *cf* Chapter 4. Charge storage due to a preceding laser pulse can affect the electrical transients during the measurement pulse either by i) coupling with the incident laser light in a manner than increases the charge generation rate, or ii) by electrically enhancing the effect of the usual amount of charge generated by a laser pulse. Because all excess carriers will contribute either to electrical conduction, or band bending, the possible photo-enhancement mechanism will be neglected here. Trapped charge can locally alter the band bending in a semiconductor, with the result of changing the 2DEG concentration in a HEMT and thus its conductivity, *cf* Chapter 5. Trapping of positive carriers, holes, could explain the observed measurements, if an increased 2DEG channel conductivity were the cause. On the other hand, if charge storage in the form of an increased excess bulk carrier density was responsible for the enhancement of the electrical signals observed, then it is plausible that carriers of either sign could contribute to a net increase of bulk conductivity.

The measured quantity displaying the clearest PRF effect is peak drain current. Here, a minimal model will be proposed for the PRF effect. The peak current is directly linked to the bulk conductivity of the material surrounding the focal region, given by Equation 4.1. Because of the likely large hole current into the reverse biased Schottky gate, bulk conduction causing the apparent laser shunt effect due to electrons will be considered. If excess electrons have a certain probability of recombination per unit time, then their density will decrease as

$$\frac{dn}{dt} = -r\,n \tag{7.15}$$

where r is the rate of electron recombination [s^{-1}], and n is the excess electron density [cm^{-3}]. Separating variables and integrating, we find the solution for the excess electron density at time, t, since the preceding irradiation event, as

$$n(t) = n_0\,e^{-r\,t} \tag{7.16}$$

where and the excess electron concentration, created by the preceding radiation pulse, is n_0 at $t = 0$.

The measurements of peak drain current as a function of PRF fitted a power law equation of the form $\mathrm{I} = a \times \mathrm{PRF}^b$, where b was found to be around 0.1. Outside of the plasma region, if peak current is via bulk conduction through the semiconductor then

$$I = A V q \mu_e n_0 e^{-rt} = a \times \mathrm{PRF}^b \tag{7.17}$$

where A is a constant determined by the geometry of the current flow, V is the voltage across the conducting region, μ_e is the bulk electron mobility, a is constant for a given sample and test conditions with units of current, and b describes the strength of the PRF effect. Equation (7.17) shows that where this minimal model is applicable, for given experimental conditions, b and r vary inversely. The greater the excess carrier recombination rate, r, the lesser the effect of increasing PRF will be on enhancing current transients. This suggests that material with increased defect density, such that caused by neutron irradiation displacement damage, would be less sensitive to the PRF effect than higher quality material.

The two parts to the drain current transients, prompt and delayed, as shown in Figure 7.22, show that there is a large fast current component, followed by a smaller, but longer lasting component to the transients. Hsieh *et al.* 1981 [150] suggested that the higher the substrate doping level, the faster the recovery of a depletion region after an ion strike where charge funnelling occurred. It was shown earlier how very high carrier densities are created by ion strikes, and by the laser pulses used here to simulate some of their effects. The transient high carrier densities cause a collapse of the electric field profile under an off-state bias gate, allowing the electric field lines to penetrate much deeper into the structure than it was previously, as in the ion funnelling case. Once the carrier density has decayed back to its previous level the usual electric-field profile and depletion region are restored. For two samples with equal decay or recombination rates, but different doping levels, the more highly doped sample will be returned to its usual condition more quickly. It should be noted here that Wafer A had an around ten times higher carbon doping level in the buffer layer than that Wafer B had. According to this model, Wafer A should recover its pre-irradiation electric field profile more quickly. This is what was observed.

7.5.3 Conclusions

In this section, an irradiation pulse repetition frequency (PRF)-dependent response was presented. The nature of the effect is that observed radiation response increases as a sub-unity power of the PRF of the incident radiation. The effect is distinct from the well known phenomena of the pulse pile up effect and the pulse height defect effect. A minimal model was used to suggest that the PRF enhancement factor, b, would vary inversely to the irradiation-generated excess carrier recombination rate, r, and so could be used to measure material quality or the extent of

displacement damage. Increasing V_{DS} was found to decrease the recombination rate-to-PRF ratio. This is consistent with the applied electric field separating charge carriers from recombination sites.

The implications of this effect are firstly that high PRF testing, often used to detect small signals on noisy backgrounds, should be used with caution if the quantities of interest are discrete events. The second implication concerns the use of semiconductor devices in radiation environments: the impact of a second radiation strike will be larger than a first strike with identical characteristics, if it occurs within a certain time period. For the devices tested here, modelling the charge deposition due to multiple secondary ions or a high flux radiation environment, as a sum of SEEs, would produce erroneous results. Finally, the results presented in this section suggest that during irradiation, HEMTs with increased buffer doping levels may experience higher peak with shorter duration than those found in lesser-doped devices. This suggests an avenue to be explored in hardening-by-design studies, and in circuit radiation hardening.

In the next section of this chapter an optical delay stage is used to split one laser pulse into two equal parts, to elucidate some of the dynamics of multiple radiation events in HEMTs as a function of their separation in time.

7.6 Simulating a double ion strike

The PRF effect, a power law dependence on PRF of semiconductor device radiation response, demonstrates that the effects on a device of multiple irradiation events in a continuous pulse train are not independent of each other. It is entirely possible for multiple secondary ions following a single event to pass through the same region within a device, and in the case of an intense radiation pulse, as discussed in Chapter 6, for example, multiple individual radiation events will occur inside the device during the radiation pulse. In practise, to estimate the response of a semiconductor device to such an environment where testing is not possible or practical, it could be considered as a sum of single event effects. However, as demonstrated earlier, this may produce erroneous conclusions for a pulse train environment. Considering the PRF effect in this context raises the question of how a device would respond to two closely spaced, but discrete, radiation strikes. Would the effect simply be a sum of the individual responses, would an electronic or optical process act as a limiting mechanism as appears to be the case with the PRF effect where recombination rate was found to increase with increasing PRF, or conversely would there be some form of amplification? In this section, the range of validity of the sum of SEEs approach is tested, and an attempt is made to clarify the nature of the semiconductor device response to a simulated multiple ion strike.

7.6.1 Experimental details

The pump-pump technique used here employed an optical variable delay stage. The layout and details of the system are described in Chapter 3. Briefly, a polarising beam splitter was used to split an individual laser pulse after it was picked by a pulse picker consisting of a Pockels cell and Glan laser polarisers. By varying the position of the retro-reflectors in the optical delay stage, the optical path length for one part of the beam was varied. The direct and delayed components of the beams were then recombined, again using a polarising beam splitter, and then directed to the sample though the microscope, as is common with the rest of the work described in this chapter.

Measurements made using the double pulse consisted of the direct and delayed components of the beam. To monitor the effect of non-perfect optical alignment anywhere in the measurement system, periodically measurements were also made where the direct and delayed beams were alternately blocked off. The data from those measurements provides a check on the system behaviour as the retro-reflector position, and hence the delay time, was varied. This allows changes in semiconductor device response, due to unintentional minor changes in optical focusing of the component beams, to be distinguished from the effects of changing delay time between the two component pulses of the double pulse irradiation.

The direct and delayed beam components were carefully aligned in an attempt to achieve coaxial propagation through the microscope and as close to identical focal spot position within the device as practically possible. Figure 7.23 shows the close degree of overlap achieved. During intial setup for each double pulse test, the combined laser spot was aimed within the HEMT at a region near a gate edge where a clear transient signal was produced. The focus depth was adjusted from the optical best focus, to a position that produced the largest peak current. This position was typically within a few microns of the best optical focus. The final optical adjustment made was the rotation of the half wave plate installed immediately in front of the first polarising beam splitter. This altered the polarisation of the beam that propagated to the polarising beam splitter, enabling fine adjustment of the optical power in each beam path. Because of the different attenuation in each beam path, the half wave plate was adjusted to the angle which made the transient electrical signals from the HEMT, due to isolated direct and delayed beams, as close as possible to equal.

The results of variable delay double pulse testing of Wafer A are reported below. The electrical biasing conditions used were $V_{GS} = -4\,V$; $V_{DS} = +18\,V$. Maximum laser power was selected using the half wave plate which immediately follows the second harmonic generator. This was required to permit clear signals to be measured despite the extra losses incurred by the polarising beam splitters, the second half wave plate, and the additional mirrors present in the double pulse setup. The additional optics in the double pulse setup decreased total optical power at the sample surface to around 41% of the single pulse setup level.

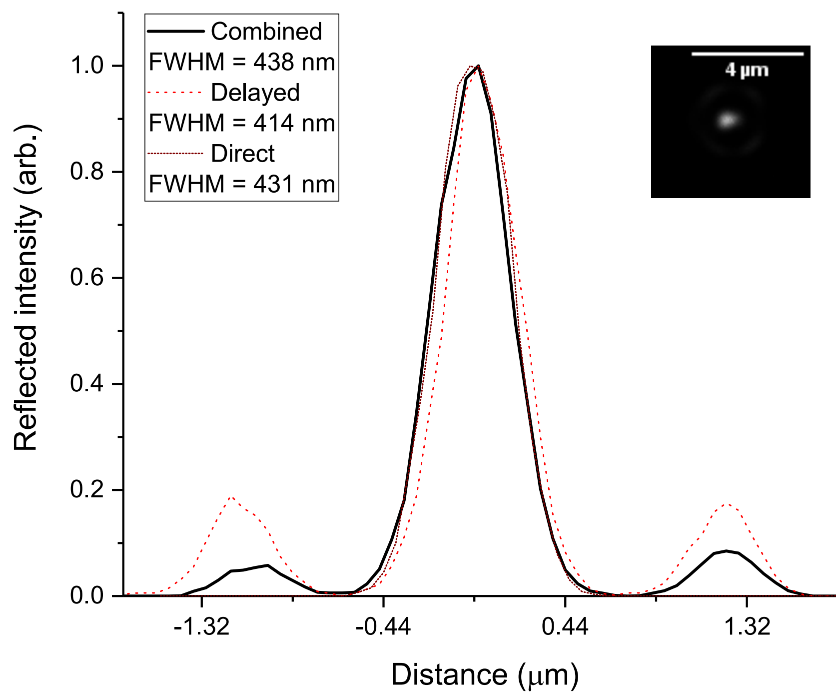

Figure 7.23: Normalised intensity profiles of the direct, delayed, and combined beams, imaged through the backside of the wafer when focused on, and reflecting from, the semiconductor-contact interface. The full width at half maximum of each beam is indicated. Inset: image of combined beams.

7.6.2 Results

A drain current transient resulting from the irradiation of a HEMT by a double laser pulse is shown in Figure 7.24. The rising edges of the HEMT transient response to the direct and delayed irradiation components of the double pulse are too fast to resolve fully with the current measurement setup, as was the case with the single pulse irradiation, discussed earlier. The irradiation pulses are effectively Dirac delta functions when compared to the response time of the measurement system. The effect of the second irradiation pulse can be seen to combine constructively with the decaying transient due to the first pulse. The slope of the transient decay immediately after the peak of the first pulse, and after the peak of the second pulse, can be seen to differ from the slope for the following two decades of time. This indicates that the transient signal due to the laser irradiation is composed of distinct prompt and delayed components.

To study how semiconductor device response to a double pulse depends on the separation in time between the two incident irradiation pulses, it was necessary to determine the exact retro-reflector position that corresponded to the direct and delayed beam paths having the same optical path length. To find that position the rise time of the combined double pulse drain signal was used. Here that is defined as the difference in time between the 10% amplitude point on the rising edge of the drain signal due to the faster pulse, and the 90% amplitude point on the rising edge of the drain signal due to the slower pulse. For the test conditions used, the rise time of the drain signal was always shorter than the limit of the oscilloscope's temporal resolution, and so was a suitable candidate signal. In the optical delay stage built for this experiment, each light pulse travels the retro-reflector movement distance four times on its inbound path, and a further four on its outbound path. So a retro-reflector movement of one millimetre will increase the optical path length for the delayed beam by eight millimetres. The double pulse combined rise time is plotted against retro-reflector position in Figure 7.25. The minimum in the plot of the combined rise time should correspond to the condition where the delayed and direct beams have equal path lengths. To calibrate the distance scale, the straight line fit shown was used to calculate the speed of light:

$$\begin{aligned} c &= \frac{8\times 10^{-3}\,\mathrm{m}}{(26.76\pm 0.09)\times 10^{-12}\,\mathrm{s}} \\ c &= (2.990\pm 0.010)\times 10^{8}\,\mathrm{m/s} \end{aligned} \tag{7.18}$$

The accepted value for c, 2.998×10^{8} m/s, is 0.27% higher than the value reported here and lies within its range of uncertainty. This confirms that the distance scale on the delay stage used to position the retro-reflectors is well calibrated, and that the rise time measurements are consistently determined. From the straight line fit shown in the figure, the retro-reflector position corresponding to coincidence of the two split components of the laser pulse was found to be (29.98 ± 0.28) mm. This gives an uncertainty in the coincidence time of 0.94×10^{-12} s.

In addition to the double pulse measurements, the electrical signals from the HEMTs due to the direct and delayed beams in isolation were measured. This was achieved by placing a beam

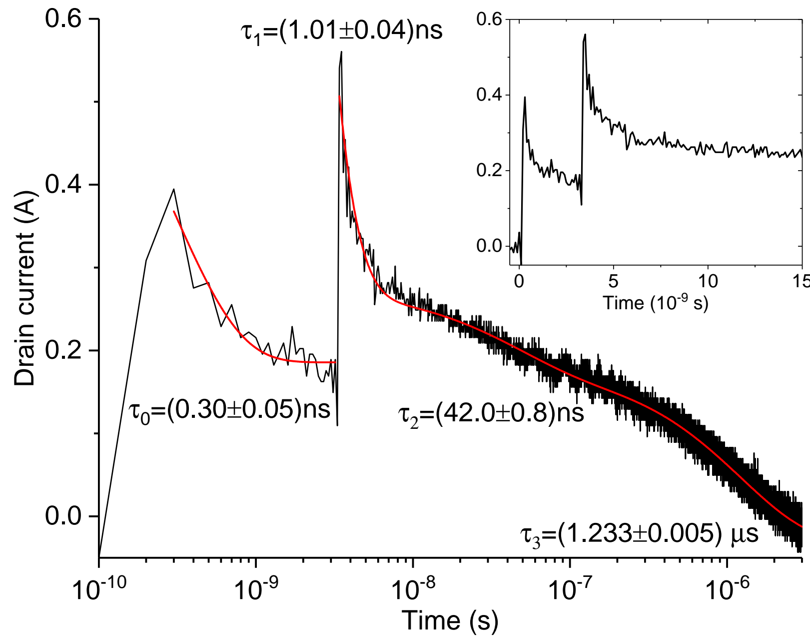

Figure 7.24: Drain current transient measured using a HEMT irradiated with a double laser pulse. The two laser pulses were separated by 3.212×10^{-9} s. Measurements performed on Wafer A. Red lines show exponential decay fits to the transient curves, with time constants indicated. Inset: Linear scale plot of the time during and immediately after the two pulses.

blocker in the path of one of the two beams, performing a measurement, then repeating with the other beam blocked. This process was repeated at many of the retro-reflector positions used for the double pulse measurements. Any changes in the sum of the effects due to the two independent beams indicates a change in the optical laser focus at the HEMT. These measurements, therefore, act as a control that enable effects due to changes in delay time to be distinguished from the effect of small deviations in the optical focus due movement of the retro-reflector. Despite achieving a good alignment and recombination of the two beam paths, due to the extreme sensitivity of HEMT response to laser focal spot position and optical properties, the signals were found to have a dependence on retro-reflector position in some cases. However, after taking into account these effects by using the control measurements, clear changes were observed in HEMT double pulse irradiation response due to altering the second pulse delay time. These are discussed below.

The total charge collected at a drain contact during a transient measurement is shown plotted against the time delay between the direct and delayed components of the incident laser pulse in Figure 7.26. In part (a) of the figure, the increase in the charge collected from two individual pulses as the delay time is decreased from around 4 ns to around 300 ps, the experimental control, suggests that the slope in the double pulse data in that region is due to the extreme sensitivity of the transient signals to the small optical changes caused by moving the retro-reflectors in the optical delay stage. Within that range of delay times, the charge collected due to a double laser

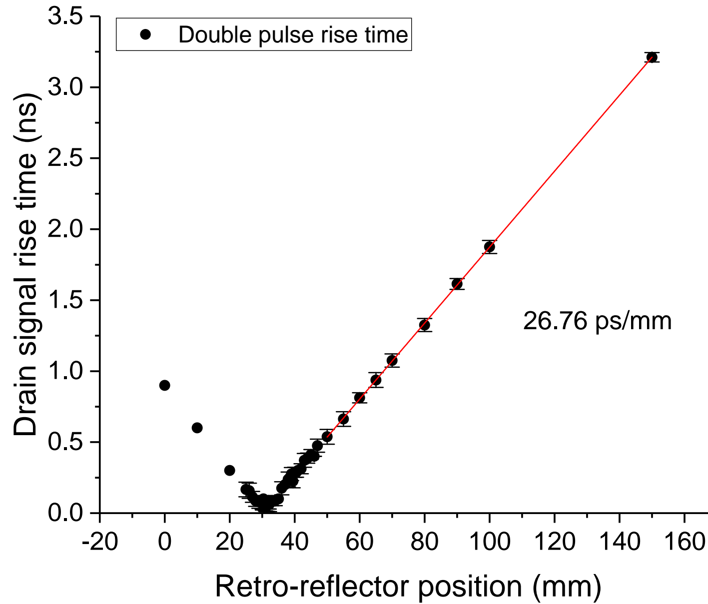

Figure 7.25: Double pulse rise time obtained from drain transient signals, given by the time difference between when the leading edge of the first pulse reached 10% of its maximum value, and the time when the second pulse reached 90% of its maximum value, plotted against retro-reflector position. The red line indicates the straight line fit used to find the position which would produce simultaneous direct and delayed laser pulse arrival on a HEMT target. The slope of the fit was used to calculate the speed of light, in order to calibrate the distance scale.

pulse is seen to be similar to that collected from the two constitutive pulses performed in isolation. The measurements for a delay time of around 27 ps, seen most clearly in part (b) of the figure, suggest that for a particular delay time, near to the calculated zero delay point, there may be no difference between the charge collected following a double pulse, and that due to two isolated pulses. For all other measured delay times smaller than around 300 ps, the charge collected at the drain contact following a double laser pulse was less than the sum of the charge collected due to each of the individual pulses delivered in isolation. In Figure 7.27, the difference between the charge collected due to a double pulse and that due to the sum of the two pulse components delivered in isolation, $Q_{\text{double}} - (Q_1 + Q_2)$, is plotted against the time separation between the double pulse components. The figure shows a clear transition in behaviour near $\delta t = 300\,\text{ps}$.

The peak currents measured at the gate and drain contacts, as a function of second pulse delay time, δt, are presented in Figure 7.28. The measured peak drain current values, shown in parts (c) and (d), of the figure show a similar dependence on δt as the collected drain charge. However, the peak gate current values, shown in parts (a) and (b) of that figure, behave differently. The sum of the peak gate currents due to individual direct and delayed pulses for $\delta t \gtrapprox 300\,\text{ps}$ is around twice the peak gate current measured for the double pulse case. As δt is reduced below $\lessapprox 300\,\text{ps}$ however, the double pulse peak current increased until it was approximately equal to

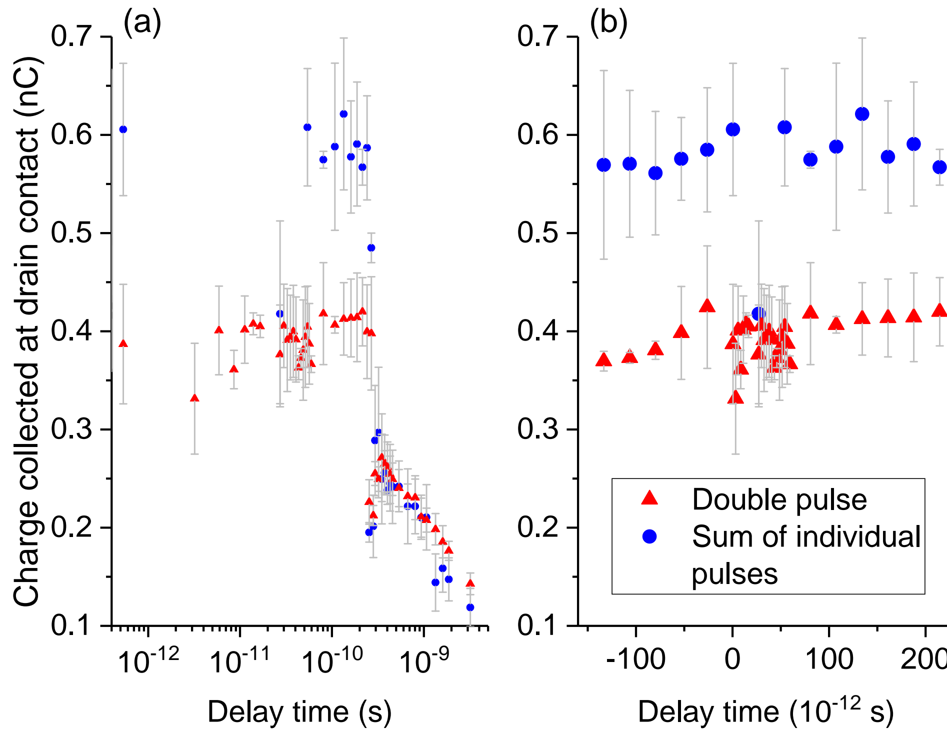

Figure 7.26: Charge collected at a HEMT drain contact following a double pulse irradiation, plotted against the second pulse delay time. Also plotted are the sum of charges collected due to direct and delayed pulses measured in isolation at the corresponding retro-reflector positions. (a) shows data plotted against log(delay time), and (b) shows results obtained for positive and negative delay values near the zero delay point.

the sum of the individual components measured in isolation.

7.6.3 Discussion

The drain current transients caused by localised irradiation that are discussed in this chapter have been shown to consist of prompt and delayed components. This can be seen by the change of slope in the plot of drain current against the logarithm of time since the irradiation pulse in Figure 7.24. The prompt effect can be seen to have a sub-nanosecond timescale. The delayed effect persists for around 3 μs, for the particular biasing and irradiation conditions used with the HEMTs tested here. The the PRF effect discussed above must therefore be due to the delayed, not prompt effect. Varying the delay time between the pulses, δt , determines whether the second pulse interferes with the prompt or delayed component of the transient caused by the first pulse. If the physical mechanisms that cause the prompt and delayed components of the transients are different, then the outcome of interference of a second irradiation pulse with the first may depend on δt. Earlier, the funnelling and shunt effects were discussed. The funnelling current to the gate contact will have a characteristic time determined by the time taken to restore the depletion

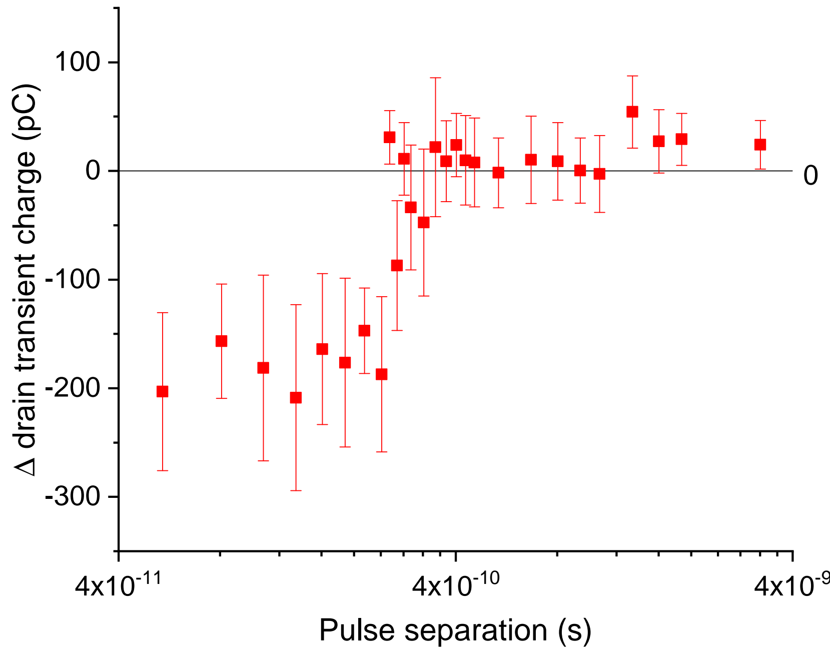

Figure 7.27: Plot showing the difference between the charge collected at the drain contact during exposure to a double irradiation pulse, and that due to the sum of the two pulse components delivered in isolation, $Q_{\text{double}} - (Q_1 + Q_2)$. Values are plotted against the time separation between the double pulse components. Note: only values corresponding to positive delay times are shown, and only for the delay times where both sets of measurement data are available.

region immediately beneath the gate contact under reverse bias. Whereas the bulk conductivity that circumvents the gate control of the channel, known as the shunt effect, will continue until the carrier concentration profile throughout the bulk region beneath the gate has been restored to its pre-irradiation condition.

The charge collected at the drain contacts due to a double laser pulse for $300\,\text{ps} \lessapprox \delta t \lessapprox 4\,\text{ns}$ was approximately equal to the sum of charge collected from the individual pulses performed in isolation. No net charge collection at the gate contacts was apparent above the background noise level. This suggests that the conduction path to the drain originated at the source contact, and may therefore be due to the enhanced charge collection phenomena of funnelling or 'laser shunt' bulk conduction. The FWHM of drain transients for Wafer A with $V_{DS} = 18\,\text{V}$ was shown to be between 1 and 10 ns in the PRF section. Therefore, the excess carriers, and hence conductivity, generated by the first irradiation pulse, may simply combine with that due to the second pulse for such δt values. However, for $\delta t \lessapprox 300\,\text{ps}$ the charge collected at the drain contact due to a double radiation pulse was less than that collected by the sum of two isolated pulses (Figure 7.27). This suggests that either i) an extrinsic factor prevented the collected charge following a double pulse matching the level of two isolated pulses; or ii) that charge generation or conductivity increase in the focal spot region was saturated; or iii) a limiting process reduced the effect of the delayed

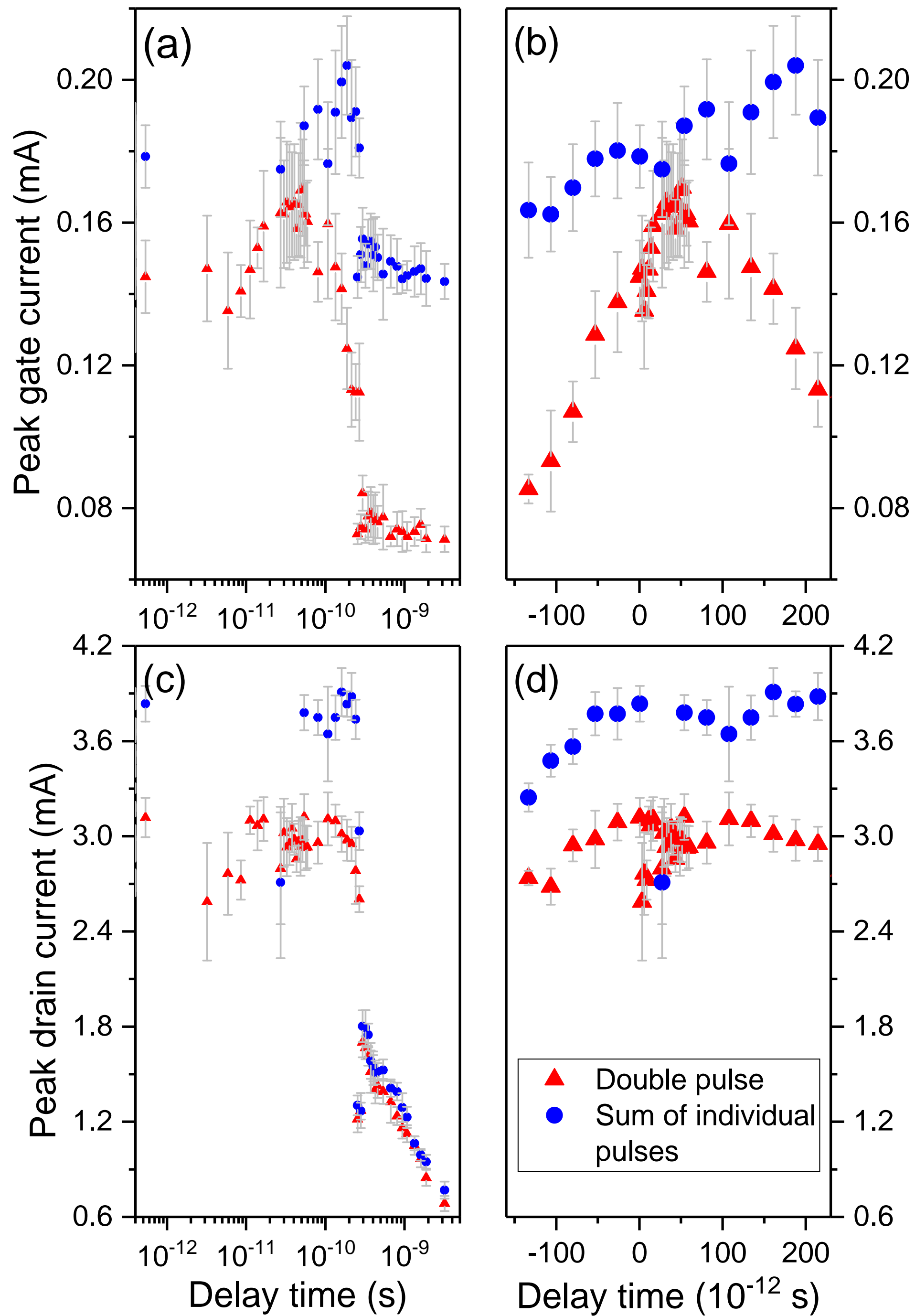

Figure 7.28: Peak current measured at the gate contacts (a) and (b), and drain contacts (c) and (d), plotted against the second pulse delay time. Also plotted are the sum of charges collected due to direct and delayed pulses measured in isolation at the corresponding retro-reflector positions. (a) and (c) show data plotted against log(delay time), whereas (b) and (d) show results obtained for positive and negative delay values near the zero delay point.

pulse compared to its effect in isolation.

Peak current is representative of the prompt component of the irradiation effect when a single pulse is considered in isolation. In the case of a double irradiation pulse, the peak current is usually the peak due to the interaction of the second irradiation pulse with the residual conditions it encounters within the HEMT due to the first pulse. For the drain signal, the peak current followed a similar trend to the collected charge: for $300\,\mathrm{ps} \lessapprox \delta t \lessapprox 4\,\mathrm{ns}$ the double pulse value was approximately equal to the sum of individual pulse peak currents; and for $\delta t \lessapprox 300\,\mathrm{ps}$ double pulse peak current was less than the sum of the direct and delayed irradiation effects measured in isolation, as shown in Figure7.28 (c), (d). The one exception to this trend was the data measured at 27.3 ps, where the double pulse peak current was equal to the sum of peak currents due to individual pulses. The second irradiation pulse of a double pulse exposure was found to interfere constructively, in a quasi-linear manner, with the delayed component of a HEMT's response to a previous pulse. However, when a second pulse irradiated a HEMT during the prompt stage of its drain current transient, $\delta t \lessapprox 300\,\mathrm{ps}$, the effect of the second pulse was smaller. For such short pulse separations, the interference between the two irradiation pulses was sub-linear. This suggests that a mechanism exists within the semiconductor which limits the generation of charge by a second radiation pulse, or its conduction to the drain contact, when the separation in time between the two radiation pulses is shorter than around 300 ps. Because the peak current levels are a few mA, much smaller than typical operating levels or measurement circuit capability, the limiting mechanism is not the intrinsic device or measurement circuit.

There was no interference apparent between the peak gate current due to direct and delayed irradiation pulses for $\delta t \gtrapprox 300\,\mathrm{ps}$. The peak gate current due to a double irradiation pulse for $\delta t \gtrapprox 300\,\mathrm{ps}$ was approximately half of the sum of the individual pulses measured in isolation. Both of these observations indicate that the FWHM of the gate transient signals were shorter than 300 ps. Because of the large reverse bias applied to the gate contact, the portion of the depletion region immediately below it re-establishes very quickly after irradiation. In the example simulation shown in Figure 7.18 (c), that part of the depletion region is shown to have re-established in less than 10 ps after the irradiation pulse. For $\delta t \lessapprox 300\,\mathrm{ps}$ however, as $\delta t \rightarrow 0$ the peak gate current due to a double irradiation pulse was found to converge with the sum of peak current due to isolated pulses, as apparent in Figure 7.28 (b). This demonstrates that the gate electrical signals resulting from two individual laser pulses superpose constructively and linearly. Therefore, the charge collected at the gate due to the delayed laser pulse is not limited by the residual effects of the first pulse. If this behaviour is maintained across the entire laser focal spot, then the mechanism limiting peak current and charge collection at the drain for $\delta t \lessapprox 300\,\mathrm{ps}$ must be conduction. If conduction processes are limiting the effects of a second irradiation pulse, not the specific charge generation mechanism, then the observed behaviour may also occur during irradiation by charged particles or secondary ions.

Here it is shown that changes in focal region opacity are unlikely to limit the effect of the

second irradiation pulse. In Chapter 2 it was shown that the plasma frequency can be described as

$$f_p = \sqrt{\frac{e^2 n}{m_e \epsilon_0 \epsilon_{GaN}}} \tag{7.19}$$

where the symbols have their usual meaning. Equation 7.3.3 can be used to calculate n for the first pulse by taking the pulse energy to be a maximum of 41% of the nominal maximum value, and assuming the same generation volume as above. As a worst case estimate it is assumed that no carrier drift or diffusion has occurred. The plasma frequency in the focal region due to the first laser pulse would then be approximately $f_p = 1.7 \times 10^{13}$Hz. The green light used for both laser pulses has a frequency of $f = 5.8 \times 10^{14}$Hz. This suggests that the plasma density generated by first pulse is inadequate to limit the propagation of the second pulse, so opacity is not the limiting effect.

Continuing the above reasoning, the mechanism which limits conduction to the drain contact must persist for a time scale of up to a few hundred pico-seconds only. It must limit bulk conduction from the source contact which bypasses the gate control region, the 'laser shunt' effect, and it must limit charge collection at the drain contact due to the funnelling effect. From the minimal model based on excess carrier concentration developed when considering the PRF effect, the delayed component of conductivity observed in the transients would be expected to equal the sum of its parts. This may explain why the drain effects due to a double pulse, and the sum of two isolated pulses are equal for $300\,\mathrm{ps} \lessapprox \delta t \lessapprox 4\,\mathrm{ns}$. For shorter delays, the prompt component of the transient effect dominates the device response. The prompt component is likely to be dominated by the non-equilibrium conditions within the focal spot region during and immediately after irradiation. Partial screening of the drain electric field by electrons generated by the first pulse would reduce the drift velocity of charge generated by the second irradiation pulse, and may contribute to the limiting effect. A reduction in bulk electron mobility within the focal spot region, due to the first irradiation pulse, may also explain the observed limiting effect upon the second pulse. Bulk heating of the focal spot region by the first pulse could cause a maximum temperature increase of around 0.5 K, and so can not be responsible for a mobility reduction sufficient to cause the observed limiting effect. However, some of the charge generated by the first pulse will scatter in the generation region, generating a non-equilibrium population of phonons, known as hot phonons. Thermalisation of the generated charge into phonons occurs on pico-second (ps) timescales, and higher charge density causes shorter hot phonon lifetimes [174]. Shorter hot phonon lifetimes result in higher hot-electron drift velocities. For the plasma densities considered here, hot phonon lifetime would be between around 1 ps and 10 ps, after which the hot phonons thermalise. It is possible that the electrons generated by the delayed irradiation pulse are scattered by the elevated thermal phonon population remaining after the first irradiation pulse. This could result in a reduced mobility, and hence lower peak current and charge collection.

7.6.4 Conclusions

The response of HEMTs to exposure to two successive irradiation pulses was investigated in this section. Maximum collected charge and peak current was not found to exceed the sum of those due to two individual irradiation pulses. For the conditions used here, gate transient current signals consisted of a prompt component only. This is likely to be because the depletion region immediately below the gate contact re-establishes very quickly due to the large reverse bias applied to it. It was found that peak gate current due to a double irradiation pulse is equal to the sum of that due to two isolated pulses, provided that the two irradiation events occur within the FWHM characteristic of the gate signal. The gate signal can therefore be considered as a sum of SEEs. Similarly, the drain transient caused by a second irradiation pulse superposed onto the first when it struck the HEMT during the delayed component of its response to the initial pulse, corresponding to time delay of $\delta t \gtrapprox 300\,\mathrm{ps}$. This superposition is consistent with the minimal model based on excess bulk conductivity used to explain the PRF effect earlier. However, when the second pulse struck whilst the HEMT was still in the prompt part of its response, $\delta \mathrm{t} \lessapprox 300\,\mathrm{ps}$, its effect was limited. Under those conditions, the peak current and charge collected at the drain contact, due to a double irradiation pulse, was less than that due to the sum of two isolated pulses. The mechanism limiting the double pulse effect for small δt values is likely to be either a partial screening of the drain bias within HEMTs by the charge deposited by the first irradiation pulse, or a reduction in local bulk mobility due to electron scattering caused by thermalised hot phonons. This limiting effect does not appear to be specific to laser irradiation, and so it may also occur during ion or neutron/PKA irradiation. This understanding of how component response scales as the time between charge packet deposition is reduced, or equivalently as effective irradiation flux is increased, may aid understanding of the device physics occurring at very fast switching speeds, and will be of use for designing and certifying electronic systems for use in harsh SEE and high dose rate radiation environments.

7.7 Irradiation location sensitivity and electric-field profile

In this final section of results obtained using femto-second laser irradiation, the effects of varying irradiation location are presented. The motivation for this study is twofold. Firstly, when radiation effects testing is performed using localised irradiation, such as an ion beam with a diameter comparable to the electronic device feature size, or a laser source, an initial spatial scan might be performed to determine the most sensitive region, and so to fix the irradiation location. To determine the safe operating area, the electrical bias that can be applied to a device when operating in a radiation field without causing failure, the bias would next be increased. Irradiation would be repeated, and the process repeated until the failure bias was found. The derating required to use the component in a radiation environment would then be known. This method assumes that the position of the most sensitive region within a device does not change

with increasing bias. This assumption is tested below, to determine whether this approach is valid. The second motivation for this study is to qualitatively determine the electric field distribution within working HEMTs. Highly localised peaks in electric field reduce device lifetime by causing hot spots where the increased Joule heating accelerates failure mechanisms, decreasing operating lifetime and reducing reliability. Charge trapping is also increased by regions of high electric-field concentration, limiting switching and recovery speeds as discussed earlier in Chapter 5. By measuring the spatial variation of the electric field *in situ* it is possible to assess different designs of transistors, so that reliability may be improved, and so that trapping effects may be reduced, improving switching efficiency.

It was shown earlier that increasing the electric bias applied to a contact increases the electrical signal due to irradiation measured at that contact. It was also shown that there are distinct prompt and delayed parts to the resulting electrical transients. The prompt signal component is represented by the peak current measured, which is likely to have a closer link to E-field in the focal spot region than the delayed component, which can be represented by the charge collected at the contacts, and is affected by bulk residual excess carrier concentration. Below, the peak current will be used as a qualitative indicator of relative electric field magnitude within HEMTs. It is well known that the peak electric field in a lateral HEMT will be found at the edge of the gate on the drain side, due to electrostatic considerations. Simulations have shown that there should also be a region of high potential gradient under the drain contact in biased HEMTs [175]. Simulations have also been used to show that the peak electric field position within HEMTs is closer to the gate edge for a double field plate than for a single field plate [176]. A literature search failed to find reports of the experimental verification of the effects predicted by these simulations. In the following, the spatial dependence of irradiation-induced transient signals will be shown as a function of applied electrical bias for two different wafers, and qualitative measurements of the electric field distribution within biased devices are presented.

7.7.1 Experimental details

The operating parameters of the motorised microscope stage were tested and carefully tuned to achieve best performance, positional reproducibility, and to avoid slippage. A maximum movement speed of $250\,\mu$m/s was used along with a maximum acceleration of $1000\,\mu$m/s^2. Stage position encoders were used to achieve maximum precision. Minimum step size achieved was around 100 nm. Backlash correction was enabled. In order to overcome drift during extended duration measurements servo control was enabled to maintain the stage at the desired position. At each measurement position, a minimum of five repeat measurements were performed to determine the reproducibility and variance of the measurements. Line scans were always performed in the same direction to avoid systematic errors caused by any residual differences in stage movement step size or slippage.

The measured signals were found to vary in magnitude as focal depth was adjusted, as

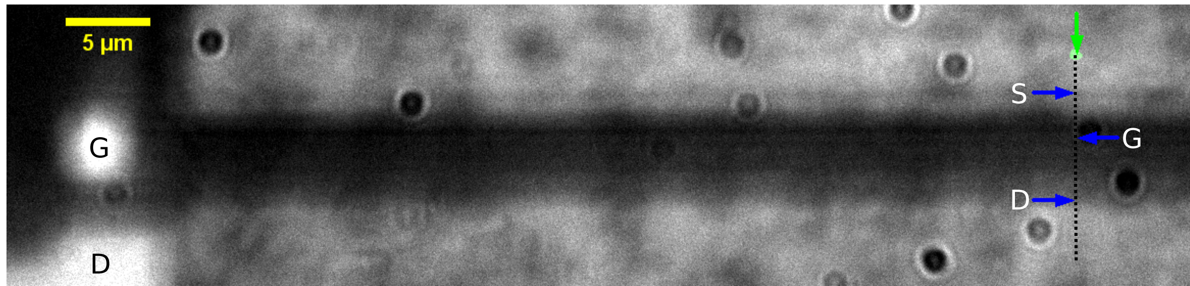

Figure 7.29: Composite visible light image, taken via the backside, through the substrate, of the source-drain gap in a HEMT used for this study, and the laser spot focused at the finish position of a scan. The grey scale indicates reflected light intensity. The false colour green spot is the laser spot, indicated by the green arrow. Blue arrows indicate the positions of the metallisation of the edge of the source, S, the centre of the gate, G, and the edge of the drain, D. The 'G' and 'D' white regions at the far left indicate the position of the contacts. The dashed line shows the path of the line scan. The dark circles are caused by debris within the imaging microscope, and are not present in the laser irradiation beam path.

expected from the discussion in the first half of this chapter. Two peaks in magnitude were apparent as the objective lens-sample separation distance was decreased. The first peak is likely to correspond to the focal spot becoming optimally positioned with respect to the barrier-buffer interface and depletion region extent below. The second peak may be due to constructive interference of out of focus light reflecting from the contact metal layers. In the work below all measurements were made with the laser focussed at a constant depth position corresponding to the first peak in the depth-signal profile.

The LabVIEW programme developed to control the experimental setup automatically labelled each transient measurement file with the co-ordinates reported by the microscope stage. Images were taken of the start and finish positions of each line scan, which were then matched up to the co-ordinates saved in the measurement files. This enabled the positions of important features within the devices to be matched up with the spatial positions of the electrical measurements. An example image is shown in Figure 7.29. In the image the positions of the key features are shown. The results below show the position of these features with respect to the measurement data. This enabled repeat maps performed using different biasing to be aligned, overcoming the potential problem of stage slippage when resetting for repeat scans.

An Atomic Force Microscope (AFM) measurement of the topology of an area covering a Wafer B $2 \times 125\,\mu$m HEMT source-drain gap was performed. The AFM scan rate used was 0.2 Hz, with 1024 samples and a scan range of $20.0000\,\mu$m.

7.7.2 Results

In Figure 7.30 measurements of peak transient current and charge collected are presented spanning the entire source-drain gap across the gate fingers of HEMTs from Wafers A and B.

When irradiating under the source contact of devices on Wafer A, charge collection of up to around 200 pC was measured at the drain contact, but very little peak drain current, and near zero gate signal were observed. Increasing the drain bias from 4 V to 18 V caused the entire spatial profile to broaden and to shift towards the drain contact, causing a non-negligible drain signal to be generated when irradiating under the drain contact. The peak drain current and collected charge increased across the entire HEMT profile when the drain bias was increased. The peak gate current behaved similarly, with the profile broadening and shifting by around 1 μm towards the drain contact when drain bias was increased. However, whereas for the $V_{GS} = -4$ V, $V_{DS} = 4$ V case peaks were exhibited in the gate current signal when irradiated on either side of the gate, when biasing was changed to $V_{GS} = -4$ V, $V_{DS} = 18$ V, the peak closer to the drain contact increased and the peak closer to the source contact decreased, reversing the relative sizes of the two peaks. The peak drain current approximately doubled when drain bias was increased, whereas charge collected at the drain contact increased by around half. Turning now to Wafer B, it can be seen the at the spatial profile and response to increasing drain bias were distinctly different from Wafer A. The most striking difference was the presence of a peak in drain and gate signals when the HEMTs were irradiated beneath the source contact. Secondly, increasing drain bias did not cause a shift in the position of the drain signal profile for Wafer B. However, it did cause a small drain current signal of around 200 μA and charge collection of around 50 pC to emerge when irradiating beneath the drain contact. Increasing drain bias caused the peak drain current to more than double, however the maximum charge collected at the drain contact increased by only around a quarter. The largest peak in the gate signal was observed to shift towards the drain contact by approximately 1 μm for the $V_{GS} = -4$ V, $V_{DS} = 18$ V case, and broadened to fill almost the entire source-drain gap.

An AFM height profile measurement was made using a HEMT from Wafer B to confirm the presence of field plates apparent from backside imaging, and to determine device metallisation dimensions. The height profile generated by the AFM measurement, given in Figure 7.31, shows regions elevated regions where metallisation material has been deposited on top of the HEMT structure. The electrical contacts are visible in the optical image (a), and can be seen to correspond to the raised regions at the edges of the AFM profile (b). The raised regions in between the contacts are the likely location of field plates and the gate contact.

7.7.3 Discussion

Earlier in this chapter, the prompt component of irradiation-induced current transients measured at a HEMT contact, as represented by the peak current, was seen to increase monotonically as electrical bias applied to the contact in question was increased. See Figure 7.14 (a,b), for example. Because of this dependence, the peak current measured measured as a function of position can be considered to indicate electric field magnitude at the irradiation location. The general spatial dependence of the electric field data would be expected, from simulations and

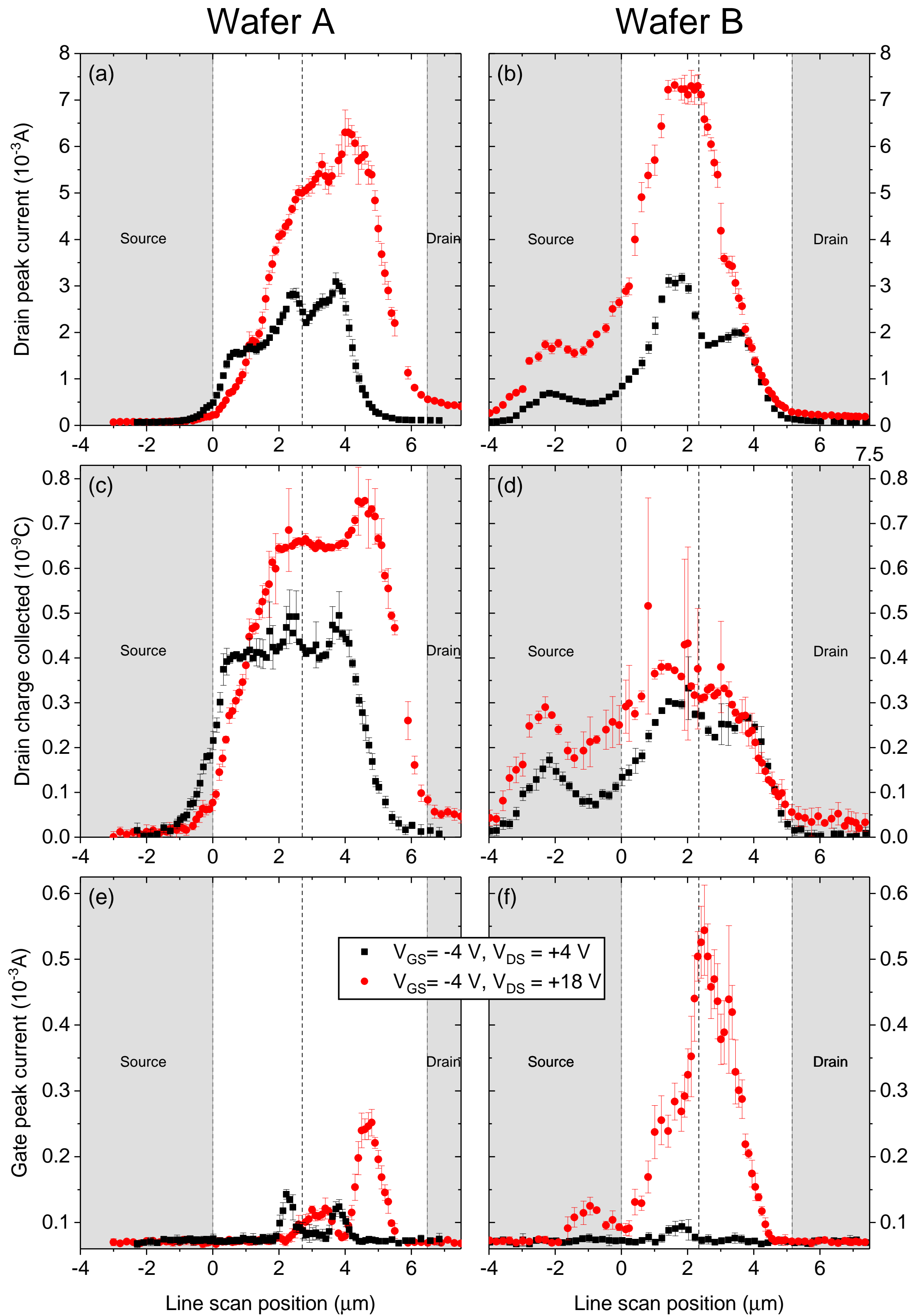

Figure 7.30: Drain peak current and charge collected, and gate peak current, for Wafers A (a,c,e), and B (b,d,f), respectively. Data are shown for two bias conditions, where $V_{GS} = -4\,V$, $V_{DS} = 4\,V$, black squares, and $V_{GS} = -4\,V$, $V_{DS} = 18\,V$, red circles. Source and drain contact positions are shaded grey, with the origin set as the edge of the source contact. The dashed lines near the gap centres indicate the gate contacts.

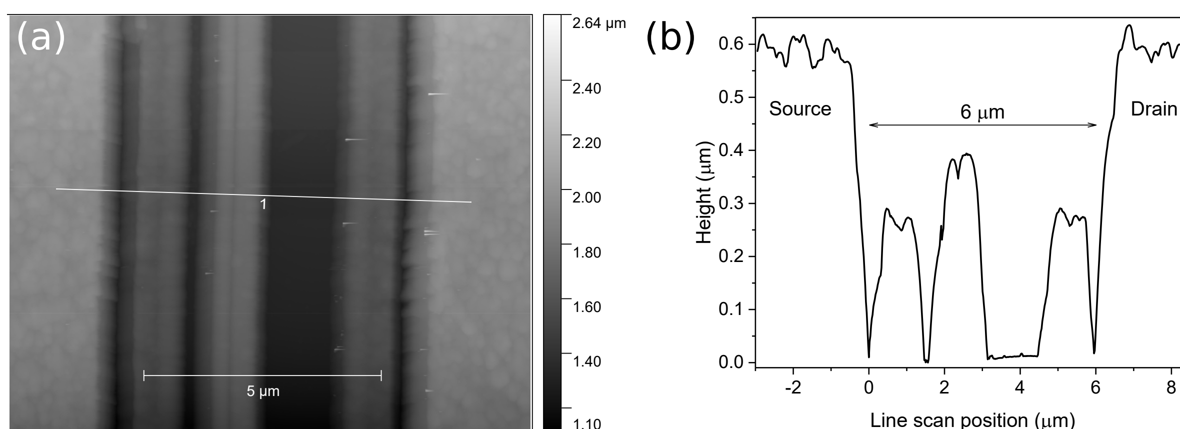

Figure 7.31: Surface topography of a HEMT as measured with an atomic force microscope (AFM). (a) Height map. Source contact is on the left, and drain contact is on the right of the image. Approximate position of AFM line scan is indicated. (b) Surface height line scan extracted from AFM map. The origin is the edge of the source contact. Measurements performed on a 2x125 μm finger HEMT on Wafer B. Ms Hannah Morgan-Cooper and Dr Filip Gucmann are thanked for their assistance with the AFM measurements.

electrostatic considerations, to reach a maximum near the drain side edge of the gate contact. The data shown in Figure 7.30 broadly confirm that expectation. However, it is apparent in the data that there is a split in the E-field profile near the peak, most clearly visible in the $V_{GS} = -4$ V, $V_{DS} = 4$ V profiles. The separation between the two parts of the peaks is around 1.3 μm for Wafer A, and 1.8 μm for Wafer B. Comparison with the AFM height profile shown in Figure 7.31, shows that the closest edges of the central raised area in the source-drain gap, and the raised area adjacent to the drain, are separated by around 1.3 μm. This suggests that the central peak in the E-field profile is associated with the gate field plate, and that the E-field peak closer to the drain contact is associated with a second field plate. For lateral FET structures a peak in E-field at the edge of the drain contact in addition to the gate edge peak, has been anticipated by simulations for some time, see [175] for an example in the case of GaAs MESFETs. The data presented above suggest the field plates in these HEMTs are effective at causing peak E-field to be shared between two peak regions, each associated with a field plate when operating at low electrical bias. The changes observed in the Wafer A E-field profiles when the bias was increased to $V_{GS} = -4$ V, $V_{DS} = 18$ V are consistent with the apparent field plate nearest the drain causing a greater potential gradient beneath it as drain bias is increased. The E-field profiles of Wafer B, however, show that the field plate is less effective in moving the peak E-field region away from the gate edge as drain bias is increased. The HEMTs from Wafers A and B were nominally identical, with the exception of the buffer doping. The ideal flat E-field distribution in the channel region [45], is more closely realised by the higher buffer doping concentration in Wafer A, enabling better field plate operation. Devices produced with a Wafer A-type buffer may therefore have reduced peak channel temperatures, and hence greater lifetime and reliability

than those produced with Wafer B-type buffers. For the same reasons, Wafer A-type buffer devices would also be expected to produce smaller peak currents under the localised irradiation caused by ions, or PKAs and secondary ions resulting from nuclear scattering or capture, thus demonstrating improved performance in radiation environments.

A somewhat speculative explanation for the above result, which merits further investigation, is that the lower doping concentration of Wafer B results in a larger depletion region penetrating deeper into the buffer under the gate in devices on that wafer. The broader gate E-field profile of Fig. 7.30 (f) compared to (e) is consistent with this claim. Under ideal field plate operation, when drain bias is increased, the charge at the edge of the 2DEG adjacent the pinched-off region is compensated by a charge in the field plate above. As drain bias is increased the coupling between the field plate 2DEG and is maintained, and an increasing extent of the 2DEG becomes depleted due to an increasing compensating charge on the field plate. Because of the potentially deeper field penetration within the buffers within Wafer B HEMTs, less compensating charge may be produced on the field plate, and hence the peak electric field region remains closer to its original position.

The distributed lateral resistance which exists beneath contacts, as mentioned in Chapter 4, will generate an electric field in that region due to the current flow there. Due to the positive potential of the drain contact, a spatially varying negative charge accumulation would also be expected to occur there. The measurement of a small peak drain current when irradiating the HEMTs beneath the drain contacts, Fig. 7.30 (a,b), and subsequent charge collection, Fig. 7.30 (c,d), is therefore not unexpected. However, the apparent peak in E-field beneath the source contact measured for Wafer B has not been anticipated by simulations published in the literature. The peak was also present in repeat measurements made using a second test structure on the same wafer. The apparent E-field peak beneath the source is smaller in magnitude than the peaks near the gate and field plate in the source-drain gap, and in a less critical location, and so may have a small effect on device lifetime. Comparison with part (d) of the figure reveals that almost as much charge is collected when irradiating the source region as the gate and field plate regions. The smaller apparent E-field, but similar charge collection, suggests that the delayed conduction mechanism, attributed to a bulk conductivity process earlier in this chapter, is the cause of the charge collection when irradiating beneath the source contact. In application circuits sensitive to irradiation-induced charge collection, the increase of sensitive area by a third for Wafer B devices, due to the source contact peak, would need to be considered when calculating expected radiation effect upsets due to SEEs, and potentially bulk irradiation environments.

The calculations of expected charge generation by each laser pulse presented earlier in this chapter showed a maximum of around 8 pC per pulse. To put an upper bound on the possible charge generation, if 100% light to charge conversion efficiency occurred, then around 180 pC could be generated within the HEMTs per laser pulse. The charge collected at the drain contact as a function of position, shown in Figure 7.30 (c,d), reached values of up to around 800 pC. This

confirms the claim made earlier that laser irradiation activates conduction pathways within the HEMTs, known in the radiation effects literature as 'enhanced charge collection', enabling more charge to be collected at contacts than was deposited by the irradiation event itself. It can be seen in Figure 7.30 that increasing the drain bias from 4 V to 18 V increased peak drain current, by a factor of ≈ 2 for Wafers A and B, close to the ratio $\frac{\sqrt{18}}{\sqrt{4}}$. In a junction device with 2-D symmetry about a line passing through the junction, the depletion region width scales with $\sqrt{V}$, suggesting a model based on similar geometric considerations may be appropriate to describe the prompt component of the localised irradiation-induced current transients in HEMTs. However, the charge collected at the drain contact for the two wafers increased by smaller proportions, 1.5 and 1.25, respectively, supporting the suggestion that different conduction mechanisms are responsible for the prompt and delayed transient current components.

From a radiation effects testing perspective, changes in biasing altering E-field profile shape within HEMTs presents a problem. It is common practice to set irradiation parameters to simulate a particular environment or test standard, and to then increase biasing until the radiation effect on the component under test exceeds some predetermined level, or until a catastrophic failure occurs. This is appropriate for diode structures with 2-D symmetry about a line through the junction. In this manner a safe operating area can be determined, and appropriate derating applied to the component in circuit applications. For devices without such symmetry, increasing biasing can cause the most sensitive region to move away from the irradiation location. Such changes in profile shapes and peak positions, apparent in the data shown above, means that where irradiation is localised to a region narrower than the peak widths in the E-field profiles, this test method would determine larger safe operating areas than are actually the case. One solution to this problem would be to use low pulse energy laser testing to identify the regions within which the peak E-field moves as biasing is increased. Then when performing, for example, ion beam testing or well collimated neutron beam irradiation at a facility such as Isis at the Rutherford Appleton Laboratory, to ensure that the irradiation region covers the identified sensitive region at a flux and duration sufficient to ensure a representative test.

7.7.4 Conclusions

Peak current caused by femto-second pulsed laser irradiation was used to qualitatively infer electric-field magnitude within operating AlGaN/GaN HEMTs. By scanning across the source to drain region, profiles of E-field magnitude were produced as a function of electrical bias for samples with nominally identical layout, taken from two different wafers with differing buffer doping. Peaks were were found in the E-field profiles consistent with the expected gate peak, and a field plate peak near the drain edge was also observed. This technique could be used to qualitatively map the effectiveness of different field plate designs in increasing uniformity of E-field distribution along the channel to avoid hot spots. It is not currently clear how to perform a point calibration to enable quantitative E-field maps to be obtained from this test data. The

profile shape dependence on biasing shows that changing buffer composition affects electric field distribution within operating HEMTs. In Wafer A, which has over ten times greater carbon doping concentration in its buffer than Wafer B, peak E-field was more effectively moved away from the gate region as drain biasing was increased. An unexpected peak in E-field was found beneath the source contact of Wafer B devices, which merits further investigation. This additional peak would increase the effective surface area of devices generating undesirable current transients when irradiated with localised or bulk irradiation fields. This, combined with the more effective E-field redistribution of Wafer A devices under increasing drain bias, suggests that HEMTs produced from Wafer A epitaxy would be superior for use in a radiation environment. It was demonstrated that pulsed laser testing can produce an 'enhanced charge collection' effect, similar to that due to ion irradiation, and necessary for radiation environment simulation. Finally, the peak E-field region was shown to move as biasing was increased. Safe operating area tests must therefore ensure that either the irradiation beam is wide enough, and delivered at sufficient flux, to cover the entire region that the E-field peak moves within as biasing is increased. Or, if using a highly collimated and tightly focussed irradiation source, that as bias is increased it is moved to follow the peak region, which can be established as a function of electrical bias by using low power pulsed laser irradiation beforehand.

7.8 Summary

The work described in this chapter was performed using a femto-second pulsed laser TPA-based Optical Beam Induced Current (OBIC) system which was constructed and optimised for these studies. This included mechanical, electrical, optical, and computer control aspects. By using this system it was found that charge deposition by sub-band gap femto-second duration laser pulses can deposit sufficient charge to simulate the charge deposited by ions resulting from irradiation by, for example, 14 MeV neutrons. It was demonstrated that the confinement of the charge generation region was sufficient to enable the measurement of line profiles of irradiation sensitivity within the active region of HEMTs. It was demonstrated that an 'enhanced charge collection' process, similar to that caused by ion irradiation, can be triggered by laser irradiation. It was shown that peak transient current, and charge collected at contacts as a result of irradiation, can display a power law dependence on laser pulse energy, but that due to the interaction of at least two demonstrated distinct conduction mechanisms contributing to the transients, the power can vary from between one and three, depending on irradiation and electrical biasing conditions. A pulse repetition frequency effect was discovered where the peak transient current and charge collected at the contacts of HEMTs due to pulsed irradiation increased with a sub-unity power of the PRF. Because of this PRF effect, high repetition rate irradiation should not be used with averaging techniques to increase signal to noise unless the quantities of interest are known to be insensitive to it. For example, the PRF effect would cause erroneously high charge deposition measurements

in a radiation detection or spectroscopy application.

By constructing and using a system to simulate the effects of a double ion strike, it was shown that the time delay between irradiation events determines the manner in which they interfere. When the delay between two irradiation events is short enough, within a few hundred pico-seconds for the devices tested here, the radiation effect due to two pulses will be smaller, in terms of transient current and charge collected, than would be expected by adding up individual effects produced in isolation. The implication of this finding is that HEMTs are less vulnerable to multiple PKA effects due to SEEs and high neutron dose rate environments, than would be expected by summing the SEEs. It was demonstrated that the constructed system could produce line profiles of irradiation response across the active region of the devices. By taking the peak transient current as a qualitative measure of electric field magnitude at each point, it was found that position of greatest electric field within HEMTs, and therefore the position of greatest vulnerability to irradiation effects, moved as the applied electrical bias is increased. Pulsed laser testing could, therefore, be used to map the position of peak vulnerability as a function of electrical bias, enabling subsequent ion beam irradiation, for example, to be precisely directed to improve the accuracy of safe operating area testing. The next step for this work will be to construct TCAD models to explore the experimental results that were presented, and to disseminate the findings to the community.

CHAPTER 8

Summary and conclusions

Wide band gap semiconductors, particularly those based on the group III-Nitrides, have many impressive performance characteristics, including irradiation tolerance. These characteristics are apparent in the results presented in this thesis. Throughout this work, techniques have been developed and applied to better measure these characteristics, and to further understanding of the limits of device performance in challenging radiation environments. In so doing, the aim has been to create techniques of general applicability, and to discern trends which may also aid understanding of radiation effects and device performance in other technologies. Understanding the performance limiting mechanisms in devices based on WBG materials, which offer many efficiency advantages, may also aid the development of future technologies to reduce electrical power usage, and hence atmospheric carbon emissions.

With the above objectives in mind, AlGaN/AlGaN and AlGaN/GaN devices were studied. Techniques were developed to measure mobility and charge trapping effects, both of which directly influence device performance and efficiency. To understand how devices perform when they are operated during irradiation, further techniques were developed to measure the transient response of HEMTs *in situ*. The aim of this work was to determine the physical processes taking place within the operating devices, and how those effects might depend on irradiation and electrical conditions. Where neutron testing was performed it was restricted to quasi-monoenergetic 14 MeV irradiation. The reasons for this were the applicability of 14 MeV neutron test results to multiple real world radiation environments, and the expectation that elastic scattering would dominate over effects like (n, p) reactions from neutron capture, which are more common when irradiating using a reactor spectrum neutron field. A summary of the results of these efforts is given below, along with recommendations for future work.

An admittance-based method was developed to measure 2DEG mobility effectively, with-

out Ohmic contacts. Using the developed technique, the mobility in ultra-wide band-gap AlGaN/AlGaN heterostructures was measured from 80 K up to 400 K. The structures were drawn from samples with two different epitaxies, which differed only in terms of barrier and buffer thicknesses. It was found that the expitaxy employing a 50 nm barrier displayed a higher carrier density, and a lower 2DEG mobility, than the 40 nm barrier material. This decrease in mobility could plausibly be attributed to an increase in interface roughness scattering, due to 2DEG confinement increasing and moving closer to the heterointerface. Two different charge carrier populations were evident, one temperature-dependent, and the other temperature-independent, consistent with surface states. The activation energy of the temperature-dependent component of the 2DEG was found to be broadly comparable to the energy of a silicon donor in AlN. The temperature-dependent component of the 2DEG mobility, at its maximum or in the open channel condition, was found to follow a power law with temperature, $\mu_{\text{total}}^{-1} = \mu_0^{-1} + \left(\beta \times T^{-\gamma}\right)^{-1}$, with $\gamma \approx 3$. Finally, a tentative neutron effect on 2DEG mobility was found. In the low 2DEG density threshold region, a small increase in mobility was observed after neutron irradiation, which may be related to neutron-induced displacement damage compensating native ionised defects. However, this latter effect must be confirmed by higher neutron fluence follow up tests in order to clarify the presence of the trend.

A current transient spectroscopy technique was developed to study charge trapping effects in HEMTs. The technique was demonstrated on AlGaN/GaN HEMTs, which were found to be vulnerable to increases in trapping related degradation of their switching characteristics due to neutron irradiation to a fluence of $2 \times 10^{13}\,\mathrm{n\,cm^{-2}}$ and greater. This finding contrasts with the widely reported insensitivity of AlGaN/GaN HEMT DC characteristics to neutron irradiation as compared to, for example, Si or GaAs technologies. Two mechanisms contributing to the performance degradation were identified: increases in trap density, and changes to inter-trap coupling behaviour. These changes decrease the output current stability of HEMTs.

Testing in the pulsed ICF neutron environment of the Omega laser was highly challenging. This was due to the long cable runs and the electrically-noisy environment, the latter due in large part to the interaction of the radiation field with the test setup fixtures and cabling. The test setup was refined over three iterations, resulting in the collection of the data reported in this thesis. Completely unambiguous through-pulse data was not obtained, however, the feasibility of neutron effects testing at Omega was demonstrated. Schottky gate HEMTs were found to be more susceptible to deleterious radiation effects in the Omega ICF pulsed neutron environment than MIS gate HEMTs. Evidence was also found that smaller Schottky gate HEMTs are more vulnerable to neutron-induced SEEs than larger devices. HEMTs were irradiated whilst electrically biased with up to 150 V applied to the drain, with no catastrophic damage observed. The HEMTs were also found to be able to return to their pre-irradiation operating points within 10 μs after irradiation, depending on electrical biasing. Recommendations were made for improvements to the Omega ICF radiation effects test setup, which would increase the

fidelity of future measurements, and increase X-ray and neutron effects discrimination. These findings will be of use for designing circuits for use in neutron radiation environments, they suggest avenues to be explored by further follow-up testing, and they demonstrate that the Omega test platform merits further development.

The development of a pulsed femto-second laser test system, based on TPA, for simulating irradiation-induced SEE, and probing internal HEMT E-fields during operation, proved to be highly successful. It was found that the constructed setup could trigger enhanced charge collection effects, similar to those caused by ion irradiation. The transient response of devices to pulsed laser irradiation displayed a power law dependence on pulse energy, with the power found to depend on biasing and irradiation conditions. At least two distinct conduction processes were found to be triggered by laser irradiation - a prompt and a delayed response, both of which are important for determining the overall radiation effect in devices. The PRF effect, where HEMTs display an increased response to an individual pulse within a pulse train as PRF is increased, is interesting in that the mechanism is not immediately clear, although the sub-unity power law dependence on PRF suggests excess carrier lifetime and defect density may be controlling factors. From a practical perspective, it demonstrates that high repetition rate testing is not suitable to directly determine SEE response. It was also found that the time delay between two discrete radiation pulses determines the manner of the combined response of a DUT in a non-trivial way. For a small enough delay, of the order of $\approx$100 ps, a limiting mechanism reduces the overall transient effect to less than that expected from the sum of the two constituent irradiation pulses. This double pulse effect has clear implications for device performance in high flux environments, will help to elucidate charge dynamics occurring within HEMTs under irradiation, and should be investigated further.

By using the TPA test system developed here, line profiles were obtained of the qualitative spatial dependence of the electric fields inside operating devices. The positions of the peaks in the E-field profiles, where devices are most vulnerable to damage due to irradiation effects or applied electrical stress, were found to move in response to biasing changes. This finding means that when using point irradiation sources such as ion beams or laser sources, safe operating areas cannot be determined by simply fixing an irradiation position and increasing the bias voltage until failure. Using pulsed laser testing to study radiation effects offers several advantages over using other radiation effects simulators, including high repetition rate and low cost, but it also presents some challenges when compared to more well established methods, such as establishing damage equivalency. Before laser testing can become a standard technique to screen components before use in radiation environments, such technical and theoretical challenges must be solved. However, it has been demonstrated that this method can expose the response mechanisms of HEMTs to pulsed irradiation, and can be used to probe their internal electric field distributions and vulnerabilities.

Publications and conference contributions

The following publications and conference contributions resulted from the work described in this thesis. It is anticipated that further contributions will result from the new results reported in Chapter 4 regarding temperature dependence of mobility and neutron effects, and the new findings pertaining to femto-second laser charge generation in HEMTs discussed in Chapter 7.

Publications

BUTLER, PA, UREN, MJ, LAMBERT, B, & KUBALL, M, 'Neutron irradiation impact on AlGaN/GaN HEMT switching transients'. IEEE Transactions on Nuclear Science, volume 65., Issue 12 pp. 2862-2869. Digital Object Identifier 10.1109/TNS.2018.2880287 (published online, 9th November, 2018, and in print December 2018).

Author contributions P.A.B. conceived the work, and developed and performed the measurements and analysis. P.A.B. wrote the manuscript with input from M.J.U., and M.K. B.L. provided the HEMT samples used in the study. All authors approved the final manuscript.

BUTLER, PA, WALLER, WM, UREN, MJ, ALLERMAN, A, ARMSTRONG, A, KAPLAR, R & KUBALL, M, 'Ohmic Contact-Free Mobility Measurement in Ultra-Wide Bandgap AlGaN/AlGaN Devices'. IEEE Electron Device Letters, vol 39., pp. 55-58, January 2018.

Author contributions P.A.B. and M.J.U. conceived the work. P.A.B and W.M.W. developed and performed the measurements. P.A.B. conducted the analysis. A. Allerman, A. Armstrong and R.K. produced the AlGaN material samples used in the study. P.A.B. wrote the manuscript with input from W.M.W., M.J.U., and M.K. All authors commented on and approved the final manuscript.

Conference contributions

PETER BUTLER (1,2), WILLIAM WALLER (1), MICHAEL J UREN (1), ANDREW ALLERMAN (3), ANDREW ARMSTRONG (3), ROBERT KAPLAR (3), MARTIN KUBALL (1), 'Ohmic contact-free measurement of mobility in ultra-wide band gap AlGaN/AlGaN structures'. (1) H.H. Wills Physics Laboratory, University of Bristol, Tyndall Avenue, Bristol, United Kingdom, (2) AWE Plc., Aldermaston, Reading, United Kingdom, (3) Sandia National Laboratories, Albuquerque, New Mexico, USA. 12th International Conference on Nitride Semiconductors (ICNS12) 24th-28th July 2017 Strasbourg, France. [Poster]

PETER BUTLER (1,2), MICHAEL J UREN (1), BENOIT LAMBERT (3), MARTIN KUBALL (1) (1) H.H. WILLS PHYSICS LABORATORY, UNIVERSITY OF BRISTOL, TYNDALL AVENUE, UNITED KINGDOM, (2) AWE PLC., ALDERMASTON, READING, UNITED KINGDOM, (3) UMS SEMICONDUCTORS, VILLEBON-SUR –YVETTE, FRANCE, '14 MeV neutron irradiation impact on AlGaN/GaN HEMT drain current transients'. 12th International Conference on Nitride Semiconductors (ICNS12) 24th-28th July 2017 Strasbourg, France. [Poster]

PETER BUTLER (1,2), (1) H.H. WILLS PHYSICS LABORATORY, UNIVERSITY OF BRISTOL, TYNDALL AVENUE, UNITED KINGDOM, (2) AWE PLC., ALDERMASTON, READING, UNITED KINGDOM, '14 MeV neutron irradiation impact on AlGaN/GaN HEMT drain current transients'. University of Bristol Physics Postgraduate Conference, 10th May 2017. Bristol, United Kingdom. [Talk]

PETER BUTLER (1,2), (1) H.H. WILLS PHYSICS LABORATORY, UNIVERSITY OF BRISTOL, TYNDALL AVENUE, UNITED KINGDOM, (2) AWE PLC., ALDERMASTON, READING, UNITED KINGDOM, 'Omega Testing and Neutron Certification Progress'. An inter-government laboratory conference, 8th December 2016. AWE, Aldermaston, United Kingdom. [Talk]

PETER BUTLER (1,2), (1) H.H. WILLS PHYSICS LABORATORY, UNIVERSITY OF BRISTOL, TYNDALL AVENUE, UNITED KINGDOM, (2) AWE PLC., ALDERMASTON, READING, UNITED KINGDOM, '14MeV Neutron Effects on AlGaN/GaN HFETs: Trap Filling-time-dependent Current Transient Spectroscopy'. An inter-government laboratory conference, May 2015. Washington DC, U.S.A. [Poster]

Bibliography

[1] International Energy Agency (IEA). *Global Energy & CO2 Status Report 2017*. Tech. rep. Organisation for Economic Co-operation and Development (OECD/IEA), 2018. URL: https://www.iea.org/publications/freepublications/publication/GECO2017.pdf.

[2] Intergovernmental Panel on Climate Change (IPCC). *Summary for Policymakers*. Tech. rep. 2018, 32 pp. DOI: 10.1017/CBO9781107415324. arXiv: 1011.1669v3.

[3] United Nations Environment Programme (U4E). *Accelerating the Global Adoption of Energy-Efficient Lightning*. Tech. rep. Paris, France: United Nations Environment Programme, 2017. URL: https://united4efficiency.org/resources/accelerating-global-adoption-energy-efficient-lighting/.

[4] J.L. Barth, C.S. Dyer, and E.G. Stassinopoulos. "Space, atmospheric, and terrestrial radiation environments". *IEEE Transactions on Nuclear Science* 50.3 (June 2003), pp. 466–482. ISSN: 0018-9499. DOI: 10.1109/TNS.2003.813131.

[5] E.G. Stassinopoulos, M.A. Xapsos, and C.A. Stauffer. *Forty-Year "Drift" and Change of the SAA*. Tech. rep. Greenbelt, Maryland 20771: Goddard Space Flight Center, National Aeronautics and Space Administration (NASA), 2015, p. 78.

[6] F.W. Sexton. "Destructive single-event effects in semiconductor devices and ICs". *IEEE Transactions on Nuclear Science* 50.3 (June 2003), pp. 603–621. ISSN: 0018-9499. DOI: 10.1109/TNS.2003.813137.

[7] D. Binder, E.C. Smith, and A.B. Holman. "Satellite Anomalies from Galactic Cosmic Rays". *IEEE Transactions on Nuclear Science* 22.6 (1975), pp. 2675–2680. ISSN: 0018-9499. DOI: 10.1109/TNS.1975.4328188.

[8] T.C. May and M.H. Woods. "Alpha-particle-induced soft errors in dynamic memories". *IEEE Transactions on Electron Devices* 26.1 (Jan. 1979), pp. 2–9. ISSN: 0018-9383. DOI: 10.1109/T-ED.1979.19370.

[9] J. F. Ziegler and W. A. Lanford. "Effect of Cosmic Rays on Computer Memories". *Science* 206.4420 (Nov. 1979), pp. 776–788. ISSN: 0036-8075. DOI: 10.1126/science.206.4420.776.

[10] M. Ackermann, M. Ajello, A. Allafort, L. Baldini, J. Ballet, G. Barbiellini, M. G. Baring, D. Bastieri, K. Bechtol, R. Bellazzini, R. D. Blandford, E. D. Bloom, E. Bonamente, A. W. Borgland, and S. Bottacin. "Detection of the Characteristic Pion-Decay Signature in Supernova Remnants". *Science* 339.6121 (Feb. 2013), pp. 807–811. DOI: 10.1126/science.1231160.

[11] J. F. Ziegler. "Terrestrial cosmic rays". *IBM Journal of Research and Development* 40.1 (Jan. 1996), pp. 19–39. ISSN: 0018-8646. DOI: 10.1147/rd.401.0019.

[12] S. Odenwald (NASA). *The Day the Sun Brought Darkness*. 2009. URL: https://www.nasa.gov/topics/earth/features/sun_darkness.html (visited on 04/01/2019).

[13] P. Cannon. *Extreme space weather: impacts on engineered systems and infrastructures*. Tech. rep. London: Royal Academy of Engineering, 2013, p. 70. DOI: 1-903496-96-9. URL: https://www.raeng.org.uk/publications/reports/space-weather-full-report.

[14] P. C. Anderson, F. J. Rich, and Stanislav Borisov. "Mapping the South Atlantic Anomaly continuously over 27 years". *Journal of Atmospheric and Solar-Terrestrial Physics* 177 (2018), pp. 237–246. ISSN: 13646826. DOI: 10.1016/j.jastp.2018.03.015.

[15] J.R. Letaw and E. Normand. "Guidelines for predicting single-event upsets in neutron environments". *IEEE Transactions on Nuclear Science* 38.6 (1991), pp. 1500–1506. ISSN: 00189499. DOI: 10.1109/23.124138.

[16] C.S. Dyer, A. Hands, K. Ford, A. Frydland, and P. Truscott. "Neutron-Induced Single Event Effects Testing Across a Wide Range of Energies and Facilities and Implications for Standards". *IEEE Transactions on Nuclear Science* 53.6 (Dec. 2006), pp. 3596–3601. ISSN: 0018-9499. DOI: 10.1109/TNS.2006.886207.

[17] ITER Organization. *What is ITER?* URL: https://www.iter.org/proj/inafewlines.

[18] M. Bagatin, A. Coniglio, M. D'Arienzo, A. De Lorenzi, S. Gerardin, A. Paccagnella, R. Pasqualotto, S. Peruzzo, and S. Sandri. "Radiation Environment in the ITER Neutral Beam Injector Prototype". *IEEE Transactions on Nuclear Science* 59.4 (Aug. 2012), pp. 1099–1104. ISSN: 0018-9499. DOI: 10.1109/TNS.2012.2187461.

[19] J.L. Bourgade, A.E. Costley, R. Reichle, E.R. Hodgson, W. Hsing, V. Glebov, M. Decreton, R. Leeper, J-L Leray, M. Dentan, T. Hutter, A. Moroño, D. Eder, W. Shmayda, B. Brichard, J. Baggio, L. Bertalot, G. Vayakis, M. Moran, T.C. Sangster, L. Vermeeren, C. Stoeckl, S. Girard, and G. Pien. "Diagnostic components in harsh radiation environments: Possible overlap in R&D requirements of inertial confinement and magnetic fusion systems". *Review of Scientific Instruments* 79.10 (Oct. 2008), 10F304. ISSN: 0034-6748. DOI: 10.1063/1.2972024.

[20] D. Lasi, M. Tulej, S. Meyer, M. Lüthi, A. Galli, D. Piazza, P. Wurz, D. Reggiani, H. Xiao, R. Marcinkowski, W. Hajdas, A. Cervelli, S. Karlsson, T. Knight, M. Grande, and S. Barabash. "Shielding an MCP Detector for a Space-Borne Mass Spectrometer Against the Harsh Radiation Environment in Jupiter's Magnetosphere". *IEEE Transactions on Nuclear Science* 64.1 (Jan. 2017), pp. 605–613. ISSN: 0018-9499. DOI: 10.1109/TNS.2016.2614040.

[21] J. Wang, P. Mulligan, L. Brillson, and L.R. Cao. "Review of using gallium nitride for ionizing radiation detection". *Applied Physics Reviews* 2.3 (Sept. 2015), p. 031102. ISSN: 1931-9401. DOI: 10.1063/1.4929913.

[22] J. Nord, K. Nordlund, and J. Keinonen. "Molecular dynamics study of damage accumulation in GaN during ion beam irradiation". *Physical Review B* 68.18 (Nov. 2003), p. 184104. ISSN: 0163-1829. DOI: 10.1103/PhysRevB.68.184104.

[23] J. Y. Tsao et al. "Ultrawide-Bandgap Semiconductors: Research Opportunities and Challenges". *Advanced Electronic Materials* 4.1 (2018). ISSN: 2199160X. DOI: 10.1002/aelm.201600501.

[24] B. Jayant Baliga. "Gallium nitride devices for power electronic applications". *Semiconductor Science and Technology* 28.7 (July 2013), p. 074011. ISSN: 0268-1242. DOI: 10.1088/0268-1242/28/7/074011.

[25] H. Amano et al. "The 2018 GaN power electronics roadmap". *Journal of Physics D: Applied Physics* 51.16 (Apr. 2018), p. 163001. ISSN: 0022-3727. DOI: 10.1088/1361-6463/aaaf9d.

[26] J. Millan, P. Godignon, X. Perpina, A. Perez-Tomas, and J. Rebollo. "A Survey of Wide Bandgap Power Semiconductor Devices". *IEEE Transactions on Power Electronics* 29.5 (May 2014), pp. 2155–2163. ISSN: 0885-8993. DOI: 10.1109/TPEL.2013.2268900.

[27] Y. Richard, M.A. Fernandez, J-L Issler, H. Guillon, P. Holsters, A. Barnes, and K. Mellab. "In-flight experience and results of the PROBA-V low cost X-Band HDR-TM Transmitter". *The 4S Symposium*. The European Space Agency, 2014.

[28] T.A. Mehlhorn. "National security research in plasma physics and pulsed power: Past, present, and future". *IEEE Transactions on Plasma Science* 42.5 (2014), pp. 1088–1117. ISSN: 00933813. DOI: 10.1109/TPS.2014.2310468.

[29] E. Normand and L. Dominik. "Cross Comparison Guide for Results of Neutron SEE Testing of Microelectronics Applicable to Avionics". *Radiation Effects Data Workshop (REDW), 2010 IEEE*. July 2010, p. 8. ISBN: 9781424484041. DOI: 10.1109/REDW.2010.5619496.

[30] F. Irom, T.F. Miyahira, D.N. Nguyen, I. Jun, and E. Normand. "Results of recent 14 MeV neutron single event effects measurements conducted by the Jet Propulsion Laboratory". *IEEE Radiation Effects Data Workshop* (2007), pp. 141–145. DOI: 10.1109/REDW.2007.4342555.

[31] C. Weulersse, N. Guibbaud, A-L Beltrando, J. Galinat, C. Beltrando, F. Miller, P. Trochet, and D. Alexandrescu. "Preliminary guidelines and predictions for 14 MeV neutron SEE testing". *IEEE Transactions on Nuclear Science* 64.8 (Aug. 2017), pp. 1–1. ISSN: 0018-9499. DOI: 10.1109/TNS.2017.2660583.

[32] S. Bazzoli, S. Girard, V. Ferlet-Cavrois, J. Baggio, P. Paillet, and O. Duhamel. "SEE sensitivity of a COTS GaN transistor and silicon MOSFETs". *Proceedings of the European Conference on Radiation and its Effects on Components and Systems, RADECS* (2007). ISSN: 0379-6566. DOI: 10.1109/RADECS.2007.5205553.

[33] J.L. Hudgins, G.S. Simin, E. Santi, and M.A. Khan. "An assessment of wide bandgap semiconductors for power devices". *IEEE Transactions on Power Electronics* 18.3 (2003), pp. 907–914. ISSN: 08858993. DOI: 10.1109/TPEL.2003.810840.

[34] T.F. Kuech. "III-V compound semiconductors: Growth and structures". *Progress in Crystal Growth and Characterization of Materials* 62.2 (June 2016), pp. 352–370. ISSN: 09608974. DOI: 10.1016/j.pcrysgrow.2016.04.019.

[35] A.G. Baca, B.A. Klein, J.R. Wendt, S.M. Lepkowski, C.D. Nordquist, A.M. Armstrong, A.A. Allerman, E.A. Douglas, and R.J. Kaplar. "RF Performance of $Al_{0.85}Ga_{0.15}N/Al_{0.70}Ga_{0.30}N$ High Electron Mobility Transistors with 80 nm Gates". *IEEE Electron Device Letters* 40.1 (2018), pp. 17–20. ISSN: 0741-3106. DOI: 10.1109/LED.2018.288042.

[36] D. Cherns, W. T. Young, M. Sanders, J. W. Steeds, F. A. Ponce, and S. Nakamura. "Determination of the atomic structure of inversion domain boundaries in α-GaN by transmission electron microscopy". *Philosophical Magazine A* 77.1 (Jan. 1998), pp. 273–286. ISSN: 0141-8610. DOI: 10.1080/01418619808214243.

[37] E. S. Hellman. "The Polarity of GaN: a Critical Review". *MRS Internet Journal of Nitride Semiconductor Research* 3.July 1998 (June 1998), e11. ISSN: 1092-5783. DOI: 10.1557/S1092578300000831.

[38] O. Ambacher, J. Smart, J.R. Shealy, N.G. Weimann, K. Chu, M. Murphy, W.J. Schaff, L.F. Eastman, R. Dimitrov, L. Wittmer, M. Stutzmann, W. Rieger, and J. Hilsenbeck. "Two-dimensional electron gases induced by spontaneous and piezoelectric polarization charges in N- and Ga-face AlGaN/GaN heterostructures". *Journal of Applied Physics* 85.6 (Mar. 1999), pp. 3222–3233. ISSN: 0021-8979. DOI: 10.1063/1.369664.

[39] J.F. Nye. *Physical Properties of Crystals*. Second Edition. Oxford University Press, 1985, p. 347. ISBN: 9780198511656.

[40] F. Bernardini, V. Fiorentini, and D. Vanderbilt. "Spontaneous polarization and piezoelectric constants of III-V nitrides". *Physical Review B* 56.16 (Oct. 1997), R10024–R10027. ISSN: 0163-1829. DOI: 10.1103/PhysRevB.56.R10024.

[41] J. P. Ibbetson, P. T. Fini, K. D. Ness, S. P. DenBaars, J. S. Speck, and U. K. Mishra. "Polarization effects, surface states, and the source of electrons in AlGaN/GaN heterostructure field effect transistors". *Applied Physics Letters* 77.2 (July 2000), pp. 250–252. ISSN: 0003-6951. DOI: 10.1063/1.126940.

[42] R. J. Kaplar, A. A. Allerman, A. M. Armstrong, M. H. Crawford, J. R. Dickerson, A. J. Fischer, A. G. Baca, and E. A. Douglas. "Review—Ultra-Wide-Bandgap AlGaN Power Electronic Devices". *ECS Journal of Solid State Science and Technology* 6.2 (Dec. 2017), Q3061–Q3066. ISSN: 2162-8769. DOI: 10.1149/2.0111702jss.

[43] B. J. Baliga. "Semiconductors for high-voltage, vertical channel field-effect transistors". *Journal of Applied Physics* 53.3 (Mar. 1982), pp. 1759–1764. ISSN: 0021-8979. DOI: 10.1063/1.331646.

[44] O. Ambacher, J. Majewski, C. Miskys, A. Link, M. Hermann, M. Eickhoff, M. Stutzmann, F. Bernardini, V. Fiorentini, V. Tilak, B. Schaff, and L.F. Eastman. "Pyroelectric properties of Al(In)GaN/GaN hetero- and quantum well structures". *Journal of Physics: Condensed Matter* 14.13 (Apr. 2002), pp. 3399–3434. ISSN: 0953-8984. DOI: 10.1088/0953-8984/14/13/302.

[45] W. Saito, I. Omura, T. Ogura, and H. Ohashi. "Theoretical limit estimation of lateral wide band-gap semiconductor power-switching device". *Solid-State Electronics* 48.9 (Sept. 2004), pp. 1555–1562. ISSN: 00381101. DOI: 10.1016/j.sse.2003.10.003.

[46] A. Fontsere, A. Perez-Tomas, V. Banu, P. Godignon, J. Millan, H. De Vleeschouwer, J. M. Parsey, and P. Moens. "A HfO_2 based 800V/300°C Au-free AlGaN/GaN-on-Si HEMT technology". *24th International Symposium on Power Semiconductor Devices and ICs*. June. IEEE, June 2012, pp. 37–40. ISBN: 978-1-4577-1597-6. DOI: 10.1109/ISPSD.2012.6229017.

[47] K.J. Chen, O. Haberlen, A. Lidow, C. lin Tsai, T. Ueda, Y. Uemoto, and Y. Wu. "GaN-on-Si Power Technology: Devices and Applications". *IEEE Transactions on Electron Devices* 64.3 (Mar. 2017), pp. 779–795. ISSN: 0018-9383. DOI: 10.1109/TED.2017.2657579.

[48] M. Micovic, D. F. Brown, D. Regan, J. Wong, Y. Tang, F. Herrault, D. Santos, S. D. Burnham, J. Tai, E. Prophet, I. Khalaf, C. McGuire, H. Bracamontes, H. Fung, A. K. Kurdoghlian, and A. Schmitz. "High frequency GaN HEMTs for RF MMIC applications". *2016 IEEE International Electron Devices Meeting (IEDM)*. IEEE, Dec. 2016, pp. 3.3.1–3.3.4. ISBN: 978-1-5090-3902-9. DOI: 10.1109/IEDM.2016.7838337.

[49] J. S. Blakemore. *Semiconductor Statistics*. Oxford: Pergamon Press, 1962. ISBN: 9780080095929. DOI: 10.1016/C2013-0-01678-7.

[50] J.R. Hook and H.E. Hall. *Solid State Physics*. Second Edition. Chichester: John Wiley & Sons, Ltd., 2003. ISBN: 0471928054.

[51] P. Siddiqua and S.K. O'Leary. *Electron transport within the wurtzite and zinc-blende phases of gallium nitride and indium nitride*. Vol. 29. 5. Springer US, 2018, pp. 3511–3567. ISBN: 0123456789. DOI: 10.1007/s10854-017-8324-1.

[52] S.K. O'Leary, B.E. Foutz, M.S. Shur, and L.F. Eastman. "Steady-State and Transient Electron Transport Within the III-V Nitride Semiconductors, GaN, AlN, and InN: A Review". *Journal of Materials Science: Materials in Electronics* 17.2 (Feb. 2006), pp. 87–126. ISSN: 0957-4522. DOI: 10.1007/s10854-006-5624-2.

[53] T. Ando, A.B. Fowler, and F. Stern. "Electronic properties of two-dimensional systems". *Reviews of Modern Physics* 54.2 (Apr. 1982), pp. 437–672. ISSN: 0034-6861. DOI: 10.1103/RevModPhys.54.437.

[54] B. K. Ridley, B. E. Foutz, and L. F. Eastman. "Mobility of electrons in bulk GaN and Al_xGaN_{1-x}/GaN heterostructures". *Physical Review B* 61.24 (June 2000), pp. 16862–16869. ISSN: 0163-1829. DOI: 10.1103/PhysRevB.61.16862.

[55] M.T. Robinson. "Basic physics of radiation damage production". *Journal of Nuclear Materials* 216 (Oct. 1994), pp. 1–28. ISSN: 00223115. DOI: 10.1016/0022-3115(94)90003-5.

[56] G.H. Kinchin and R.S. Pease. "The Displacement of Atoms in Solids by Radiation". *Reports on Progress in Physics* 18.1 (Jan. 1955), p. 301. ISSN: 00344885. DOI: 10.1088/0034-4885/18/1/301.

[57] M.J. Norgett, M.T. Robinson, and I.M. Torrens. "A proposed method of calculating displacement dose rates". *Nuclear Engineering and Design* 33.1 (Aug. 1975), pp. 50–54. ISSN: 00295493. DOI: 10.1016/0029-5493(75)90035-7.

[58] S. J. Pearton, Ya-Shi Hwang, and F. Ren. "Radiation Effects in GaN-Based High Electron Mobility Transistors". *JOM* 67.7 (July 2015), pp. 1601–1611. ISSN: 1047-4838. DOI: 10.1007/s11837-015-1359-y.

[59] C. Merckling. "Chapter 3 - Monolithic Integration of InGaAs on Si(001) Substrate for Logic Devices". *High Mobility Materials for CMOS Applications*. Ed. by Nadine Collaert. Woodhead Publishing Series in Electronic and Optical Materials. Woodhead Publishing, 2018, pp. 71–114. ISBN: 978-0-08-102061-6. DOI: https://doi.org/10.1016/B978-0-08-102061-6.00003-3.

[60] O.L. Curtis. "Radiation Effects on Recombination in Germanium". *Journal of Applied Physics* 30.8 (Aug. 1959), pp. 1174–1180. ISSN: 0021-8979. DOI: 10.1063/1.1735288.

[61] G. Messenger and J. Spratt. "The Effects of Neutron Irradiation on Germanium and Silicon". *Proceedings of the IRE* 46.6 (June 1958), pp. 1038–1044. ISSN: 0096-8390. DOI: 10.1109/JRPROC.1958.286841.

[62] G.C. Messenger. "A summary review of displacement damage from high energy radiation in silicon semiconductors and semiconductor devices". *IEEE Transactions on Nuclear Science* 39.3 (1992), pp. 468–473. ISSN: 15581578. DOI: 10.1109/23.277547.

[63] ASTM International. *Standard Guide for Measurement of Rapid Annealing of Neutron-Induced Displacement Damage in Silicon Semiconductor Devices*. Tech. rep. F980-10. ASTM International, 2003. DOI: 10.1520/F0980-16.

[64] ASTM International. *Standard Practice for Conducting Irradiations at Accelerator-Based Neutron Sources*. Tech. rep. E798-16. ASTM International, 2016. DOI: 10.1520/E0798-16.

[65] J. F. Ziegler. "Stopping of energetic light ions in elemental matter". *Journal of Applied Physics* 85.3 (1999), pp. 1249–1272. ISSN: 00218979. DOI: 10.1063/1.369844.

[66] W. H. Bragg and R. Kleeman. "XXXIX. On the α particles of radium, and their loss of range in passing through various atoms and molecules". *The London, Edinburgh, and Dublin Philosophical Magazine and Journal of Science* 10.57 (Sept. 1905), pp. 318–340. ISSN: 1941-5982. DOI: 10.1080/14786440509463378.

[67] D.R. Grimes, D.R. Warren, and M. Partridge. "An approximate analytical solution of the Bethe equation for charged particles in the radiotherapeutic energy range". *Scientific Reports* 7.1 (Dec. 2017), p. 9781. ISSN: 2045-2322. DOI: 10.1038/s41598-017-10554-0.

[68] Y.G. Li, Y. Yang, M.P. Short, Z-J Ding, Z. Zeng, and J. Li. "IM3D: A parallel Monte Carlo code for efficient simulations of primary radiation displacements and damage in 3D geometry". *Scientific Reports* 5.1 (Nov. 2016), p. 18130. ISSN: 2045-2322. DOI: 10.1038/srep18130.

[69] L. Huang. "Semiconductors under Ultrafast Laser Excitation: Optical Studies of the Dynamics". Thesis (PhD). Harvard University, 1997.

[70] J. Kolník, İ.H. Oğuzman, K.F. Brennan, R. Wang, P.P. Ruden, and Y. Wang. "Electronic transport studies of bulk zincblende and wurtzite phases of GaN based on an ensemble Monte Carlo calculation including a full zone band structure". *Journal of Applied Physics* 78.2 (July 1995), pp. 1033–1038. ISSN: 0021-8979. DOI: 10.1063/1.360405.

[71] Keithley Instruments Incorporated. *Model 4200-SCS Semiconductor Characterization System Reference Manual*. 4200-901-01 Revision P. Cleveland, Ohio, USA, 2013.

[72] M. Ťapajna, R.J.T. Simms, Y. Pei, U.K. Mishra, and M. Kuball. "Integrated optical and electrical analysis: Identifying location and properties of traps in AlGaN/GaN HEMTs during electrical stress". *IEEE Electron Device Letters* 31.7 (2010), pp. 662–664. ISSN: 07413106. DOI: 10.1109/LED.2010.2047092.

[73] J. Joh and J.A. del Alamo. "A Current-Transient Methodology for Trap Analysis for GaN High Electron Mobility Transistors". *IEEE Transactions on Electron Devices* 58.1 (2011), pp. 132–140.

[74] D. Bisi, M. Meneghini, C. De Santi, A. Chini, M. Dammann, P. Bruckner, M. Mikulla, G. Meneghesso, and E. Zanoni. "Deep-level characterization in GaN HEMTs-Part I: Advantages and limitations of drain current transient measurements". *IEEE Transactions on Electron Devices* 60.10 (2013), pp. 3166–3175. ISSN: 00189383. DOI: 10.1109/TED.2013.2279021.

[75] F.A. Marino, N. Faralli, D.K. Ferry, S.M. Goodnick, and M. Saraniti. "Figures of merit in high-frequency and high-power GaN HEMTs". *Journal of Physics: Conference Series* 193 (Nov. 2009), p. 012040. ISSN: 1742-6596. DOI: 10.1088/1742-6596/193/1/012040.

[76] A. Johnston. *Reliability and Radiation Effects in Compound Semiconductors*. WORLD SCIENTIFIC, 2010. DOI: 10.1142/7331.

[77] P.A. Butler, W.M. Waller, M.J. Uren, A. Allerman, A. Armstrong, R. Kaplar, and M. Kuball. "Ohmic Contact-Free Mobility Measurement in Ultra-Wide Bandgap AlGaN/AlGaN Devices". *IEEE Electron Device Letters* 39.1 (Jan. 2018), pp. 55–58. ISSN: 0741-3106. DOI: 10.1109/LED.2017.2771148.

[78] D.K. Schroder. *Semiconductor Material and Device Characterisation*. Third. Temple, Az.: Wiley-Interscience, 2006.

[79] M.J. Manfra, S.H. Simon, K.W. Baldwin, A.M. Sergent, K.W. West, R.J. Molnar, and J. Caissie. "Quantum and transport lifetimes in a tunable low-density AlGaN/GaN two-dimensional electron gas". *Applied Physics Letters* 85.22 (Nov. 2004), pp. 5278–5280. ISSN: 0003-6951. DOI: 10.1063/1.1827939.

[80] M.J. Manfra, K.W. Baldwin, A.M. Sergent, K.W. West, R.J. Molnar, and J. Caissie. "Electron mobility exceeding 160000 cm2/Vs in AlGaN/GaN heterostructures grown by molecular-beam epitaxy". *Applied Physics Letters* 85.22 (Nov. 2004), pp. 5394–5396. ISSN: 0003-6951. DOI: 10.1063/1.1824176.

[81] W.M. Waller, M.J. Uren, K.B. Lee, P.A. Houston, D.J. Wallis, I. Guiney, C.J. Humphreys, S. Pandey, J. Sonsky, and M. Kuball. "Subthreshold Mobility in AlGaN/GaN HEMTs". *IEEE Transactions on Electron Devices* 63.5 (May 2016), pp. 1861–1865. ISSN: 0018-9383. DOI: 10.1109/TED.2016.2542588.

[82] M. Silvestri, M.J. Uren, and M. Kuball. "Dynamic Transconductance Dispersion Characterization of Channel Hot-Carrier Stressed 0.25- μ m AlGaN/GaN HEMTs". *IEEE Electron Device Letters* 33.11 (Nov. 2012), pp. 1550–1552. ISSN: 0741-3106. DOI: 10.1109/LED.2012.2214200.

[83] S-I Takagi and A. Toriumi. "Quantitative understanding of inversion-layer capacitance in Si MOSFET's". *IEEE Transactions on Electron Devices* 42.12 (1995), pp. 2125–2130. ISSN: 00189383. DOI: 10.1109/16.477770.

[84] A. Hartstein and N. F. Albert. “Determination of the inversion-layer thickness from capacitance measurements of metal-oxide-semiconductor field-effect transistors with ultrathin oxide layers”. *Physical Review B* 38.2 (July 1988), pp. 1235–1240. ISSN: 0163-1829. DOI: 10.1103/PhysRevB.38.1235.

[85] J.R. Brews. “A charge-sheet model of the MOSFET”. *Solid-State Electronics* 21.2 (Feb. 1978), pp. 345–355. ISSN: 00381101. DOI: 10.1016/0038-1101(78)90264-2.

[86] V.W.L. Chin, T.L. Tansley, and T. Osotchan. “Electron mobilities in gallium, indium, and aluminum nitrides”. *Journal of Applied Physics* 75.11 (June 1994), pp. 7365–7372. ISSN: 0021-8979. DOI: 10.1063/1.356650.

[87] G. Bastard. *Wave mechanics applied to semiconductor heterostructures*. Les Ulis Cedex, France: Jouve, 1988.

[88] J. Antoszewski, M. Gracey, J.M. Dell, L. Faraone, T.A. Fisher, G. Parish, Y.-F. Wu, and U.K. Mishra. “Scattering mechanisms limiting two-dimensional electron gas mobility in $Al_{0.25}Ga_{0.75}N$/GaN modulation-doped field-effect transistors”. *Journal of Applied Physics* 87.8 (Apr. 2000), pp. 3900–3904. ISSN: 0021-8979. DOI: 10.1063/1.372432.

[89] J. S. Blakemore. *Solid State Physics*. Second Edition. Cambridge: Cambridge University Press, Oct. 1985. ISBN: 9781139167871. DOI: 10.1017/CBO9781139167871.

[90] M. E. Mora-Ramos, V. R. Velasco, and J. Tutor. “Scattering of electrons by polar optical phonons in AlGaN/GaN single heterostructures”. *Surface Science* 592.1-3 (2005), pp. 112–123. ISSN: 00396028. DOI: 10.1016/j.susc.2005.07.001.

[91] S. B. Lisesivdin, S. Acar, M. Kasap, S. Ozcelik, S. Gokden, and E. Ozbay. “Scattering analysis of 2DEG carrier extracted by QMSA in undoped Al 0.25Ga0.75N/GaN heterostructures”. *Semiconductor Science and Technology* 22.5 (2007), pp. 543–548. ISSN: 02681242. DOI: 10.1088/0268-1242/22/5/015.

[92] J. W. Harrison and J. R. Hauser. “Alloy scattering in ternary III-V compounds”. *Physical Review B* 13.12 (June 1976), pp. 5347–5350. ISSN: 0556-2805. DOI: 10.1103/PhysRevB.13.5347.

[93] N.F. Mott. “The electrical resistance of dilute solvent solutions”. *Proc. Roy. Soc. A.* 32.5 (1936), p. 19.

[94] M. Glicksman. “Mobility of Electrons in Germanium-Silicon Alloys”. *Physical Review* 111.1 (July 1958), pp. 125–128. ISSN: 0031-899X. DOI: 10.1103/PhysRev.111.125.

[95] W.M. Waller, S. Karboyan, M.J. Uren, K.B. Lee, P.A. Houston, D.J. Wallis, I. Guiney, C.J. Humphreys, and M. Kuball. “Interface State Artefact in Long Gate-Length AlGaN/GaN HEMTs”. *IEEE Transactions on Electron Devices* 62.8 (2015), pp. 2464–2469. ISSN: 00189383. DOI: 10.1109/TED.2015.2444911.

[96] D. Jena, A.C. Gossard, and U.K. Mishra. "Dislocation scattering in a two-dimensional electron gas". *Applied Physics Letters* 76.13 (Mar. 2000), pp. 1707–1709. ISSN: 0003-6951. DOI: 10.1063/1.126143. arXiv: cond-mat/0003199.

[97] C. Middleton. "Optimising heat flow in high performance wide and ultra-wide bandgap devices". Ph.D. University of Bristol, 2018.

[98] S.K. O'Leary, P. Siddiqua, W.A. Hadi, B.E. Foutz, M.S. Shur, and L.F. Eastman. "Electron Transport Within III-V Nitride Semiconductors". *Springer Handbook of Electronic and Photonic Materials*. Springer International Publishing, 2017, pp. 829–852. ISBN: 978-3-319-48931-5. DOI: 10.1007/978-3-319-48933-9.

[99] W. M. Waller. "Optimisation of AlGaN / GaN Power Devices". PhD thesis. University of Bristol, 2018.

[100] S. Schöche, P. Kühne, T. Hofmann, M. Schubert, D. Nilsson, A. Kakanakova-Georgieva, E. Janzén, and V. Darakchieva. "Electron effective mass in Al 0.72 Ga 0.28 N alloys determined by mid-infrared optical Hall effect". *Applied Physics Letters* 103.21 (Nov. 2013), p. 212107. ISSN: 0003-6951. DOI: 10.1063/1.4833195. arXiv: 1311.3684.

[101] T. Hofmann, P. Kühne, S. Schöche, Jr-Tai Chen, U. Forsberg, E. Janzén, N. Ben Sedrine, C. M. Herzinger, J. A. Woollam, M. Schubert, and V. Darakchieva. "Temperature dependent effective mass in AlGaN/GaN high electron mobility transistor structures". *Applied Physics Letters* 101.19 (2012), p. 192102. ISSN: 0003-6951. DOI: 10.1063/1.4765351.

[102] F. Stern. "Calculated Temperature Dependence of Mobility in Silicon Inversion Layers". *Physical Review Letters* 44.22 (June 1980), pp. 1469–1472. ISSN: 0031-9007. DOI: 10.1103/PhysRevLett.44.1469.

[103] B. Neuschl, K. Thonke, M. Feneberg, R. Goldhahn, T. Wunderer, Z. Yang, N. M. Johnson, J. Xie, S. Mita, A. Rice, R. Collazo, and Z. Sitar. "Direct determination of the silicon donor ionization energy in homoepitaxial AlN from photoluminescence two-electron transitions". *Applied Physics Letters* 103.12 (2013). ISSN: 00036951. DOI: 10.1063/1.4821183.

[104] R. J. Kaplar, A. A. Allerman, A. M. Armstrong, M. H. Crawford, J. R. Dickerson, A. J. Fischer, A. G. Baca, and E. A. Douglas. "Review—Ultra-Wide-Bandgap AlGaN Power Electronic Devices". *ECS Journal of Solid State Science and Technology* 6.2 (2017), Q3061–Q3066. ISSN: 2162-8769. DOI: 10.1149/2.0111702jss.

[105] J.R. Srour, C.J. Marshall, and P.W. Marshall. "Review of displacement damage effects in silicon devices". *IEEE Transactions on Nuclear Science* 50.3 (2003), pp. 653–670. ISSN: 0018-9499. DOI: 10.1109/TNS.2003.813197.

[106] B.-J. Kim, H.-Y. Kim, J. Kim, and S. Jang. "Neutron irradiation on AlGaN/GaN high electron mobility transistors on SiC substrates". *Journal of Crystal Growth* 326.1 (2011), pp. 205–207. ISSN: 00220248. DOI: 10.1016/j.jcrysgro.2011.01.098.

[107] J.C. Petrosky, J.W. McClory, T.E. Gray, and T.A. Uhlman. “Trap Assisted Tunneling Induced Currents in Neutron Irradiated AlGaN/GaN HFETs”. *IEEE Transactions on Nuclear Science* 56.5 (Oct. 2009), pp. 2905–2909. ISSN: 0018-9499. DOI: 10.1109/TNS.2008.2011807.

[108] L. Lü, J.-C. Zhang, J.-S. Xue, X.-H. Ma, W. Zhang, Z.-W. Bi, Y. Zhang, and Y. Hao. “Neutron irradiation effects on AlGaN/GaN high electron mobility transistors”. *Chinese Physics B* 21.3 (2012), p. 037104. ISSN: 1674-1056. DOI: 10.1088/1674-1056/21/3/037104.

[109] Fanny Berthet, S Petitdidier, Y Guhel, J L Trolet, P Mary, C Gaquière, and B Boudart. “Influence of Neutron Irradiation on Electron Traps Existing in GaN-Based Transistors”. *IEEE Transactions on Nuclear Science* 63.3 (June 2016), pp. 1918–1926. ISSN: 0018-9499. DOI: 10.1109/TNS.2016.2566683.

[110] P.A. Butler, M.J. Uren, B. Lambert, and M. Kuball. “Neutron Irradiation Impact on AlGaN/GaN HEMT Switching Transients”. *IEEE Transactions on Nuclear Science* 65.12 (Dec. 2018), pp. 2862–2869. ISSN: 0018-9499. DOI: 10.1109/TNS.2018.2880287.

[111] D. Floriot, V. Brunel, M. Camiade, C. Chang, B. Lambert, Z. Ouarch-Provost, H. Blanck, J. Grunenputt, M. Hosch, H. Jung, J. Splettstober, and U. Meiners. “GH25-10: New qualified power GaN HEMT process from technology to product overview”. *European Microwave Week 2014: "Connecting the Future", EuMW 2014 - Conference Proceedings; EuMIC 2014: 9th European Microwave Integrated Circuits Conference* (2014), pp. 225–228. DOI: 10.1109/EuMIC.2014.6997833.

[112] N Bainbridge. “ASP particle accelerator”. *AWE Discovery Journal* 9 (2004).

[113] L.W. Packer, M. Gilbert, S. Hughes, S. Lilley, R. Pampin, and J.-C. Sublet. “UK fusion technology experimental activities at the ASP 14MeV neutron irradiation facility”. *Fusion Engineering and Design* 87.5 (2012), pp. 662–666. ISSN: 0920-3796. DOI: 10.1016/j.fusengdes.2012.01.044.

[114] T. Guymer. Private communication. 2016.

[115] S. C. Binari, K. Ikossi, J.A. Roussos, W. Kruppa, D. Park, H.B. Dietrich, D. D. Koleske, A.E. Wickenden, and R.L. Henry. “Trapping effects and microwave power performance in AlGaN/GaN HEMTs”. *IEEE Transactions on Electron Devices* 48.3 (2001), pp. 465–471. ISSN: 00189383. DOI: 10.1109/16.906437.

[116] G. Koley, V. Tilak, L.F. Eastman, and M.G. Spencer. “Slow transients observed in AlGaN/GaN HFETs: Effects of SiNx passivation and UV illumination”. *IEEE Transactions on Electron Devices* 50.4 (2003), pp. 886–893. ISSN: 00189383. DOI: 10.1109/TED.2003.812489.

[117] A. M. Wells, M. J. Uren, R. S. Balmer, K. P. Hilton, T. Martin, and M. Missous. "Direct demonstration of the 'virtual gate' mechanism for current collapse in AlGaN/GaN HFETs". *Solid-State Electronics* 49.2 (2005), pp. 279–282. ISSN: 00381101. DOI: 10.1016/j.sse.2004.10.003.

[118] H. Chandrasekar. Private communication. 2018.

[119] O. Mitrofanov and M. Manfra. "Mechanisms of gate lag in GaN/AlGaN/GaN high electron mobility transistors". *Superlattices and Microstructures* 34.1 (2003), pp. 33–53. ISSN: 0749-6036. DOI: https://doi.org/10.1016/j.spmi.2003.12.002.

[120] R. H. Kingston and A. L. McWhorter. "Relaxation time of surface states on germanium". *Physical Review* 103.3 (1956), pp. 534–540. ISSN: 0031899X. DOI: 10.1103/PhysRev.103.534.

[121] A. Van Der Ziel. "On the noise spectra of semi-conductor noise and of flicker effect". *Physica* 16.4 (1950), pp. 359–372. ISSN: 0031-8914. DOI: 10.1016/0031-8914(50)90078-4.

[122] P. Dutta and P. M. Horn. "Low-frequency fluctuations in solids: 1/f noise". *Reviews of Modern Physics* 53.3 (July 1981), pp. 497–516. ISSN: 0034-6861. DOI: 10.1103/RevModPhys.53.497.

[123] D. M. Fleetwood. "1/f Noise and Defects in Microelectronic Materials and Devices". *IEEE Transactions on Nuclear Science* 62.4 (Aug. 2015), pp. 1462–1486. ISSN: 0018-9499. DOI: 10.1109/TNS.2015.2405852.

[124] R. Jiang, X. Shen, J. Fang, P. Wang, E.X. Zhang, J. Chen, D.M. Fleetwood, R.D. Schrimpf, S.W. Kaun, E.C.H. Kyle, J.S. Speck, and S.T. Pan-telides. "Multiple defects cause degradation after high field stress in AlGaN/GaN HEMTs". *IEEE Transactions on Device and Materials Reliability* 18.3 (2018), pp. 364–376. ISSN: 15582574. DOI: 10.1109/TDMR.2018.2847338.

[125] M. Meneghini, I. Rossetto, D. Bisi, A. Stocco, A. Chini, A. Pantellini, C. Lanzieri, A. Nanni, G. Meneghesso, and E. Zanoni. "Buffer traps in Fe-doped AlGaN/GaN HEMTs: Investigation of the physical properties based on pulsed and transient measurements". *IEEE Transactions on Electron Devices* 61.12 (2014), pp. 4070–4077. ISSN: 00189383. DOI: 10.1109/TED.2014.2364855.

[126] F. Alvarez, A. Alegra, and J. Colmenero. "Relationship between the time-domain Kohlrausch-Williams-Watts and frequency-domain Havriliak-Negami relaxation functions". *Physical Review B* 44.14 (Oct. 1991), pp. 7306–7312. ISSN: 0163-1829. DOI: 10.1103/PhysRevB.44.7306.

[127] J.T. Pottage. Private communication. 2018.

[128] T. Goorley, M. James, T. Booth, F. Brown, J. Bull, L. J. Cox, J. Durkee, J. Elson, M. Fensin, R. A. Forster, J. Hendricks, H. G. Hughes, R. Johns, B. Kiedrowski, R. Martz, S. Mashnik, G. McKinney, D. Pelowitz, R. Prael, J. Sweezy, L. Waters, T. Wilcox, and T. Zukaitis. "Initial MCNP6 Release Overview". *Nuclear Technology* 180.3 (2012), pp. 298–315. ISSN: 0029-5450. DOI: 10.13182/NT11-135.

[129] T. Figielski. "Theory of Carrier Recombination at Dislocations in Germanium". *Physica Status Solidi (b)* 6.2 (Jan. 1964), pp. 429–440. ISSN: 03701972. DOI: 10.1002/pssb.19640060214.

[130] P. Moens, A. Banerjee, M. J. Uren, M. Meneghini, S. Karboyan, I. Chatterjee, P. Vanmeerbeek, M. Casar, C. Liu, A. Salih, E. Zanoni, G. Meneghesso, M. Kuball, and M. Tack. "Impact of buffer leakage on intrinsic reliability of 650V AlGaN/GaN HEMTs". *Technical Digest - International Electron Devices Meeting, IEDM* 2016-February (2015), pp. 35.2.1–35.2.4. ISSN: 01631918. DOI: 10.1109/IEDM.2015.7409831.

[131] M.J. Uren, K.J. Nash, R.S. Balmer, T. Martin, E. Morvan, N. Caillas, S.L. Delage, D. Ducatteau, B. Grimbert, and J.C. De Jaeger. "Punch-through in short-channel AlGaN/GaN HFETs". *IEEE Transactions on Electron Devices* 53.2 (Feb. 2006), pp. 395–398. ISSN: 0018-9383. DOI: 10.1109/TED.2005.862702.

[132] M.J. Uren, J. Moreke, and M. Kuball. "Buffer design to minimize current collapse in GaN/AlGaN HFETs". *IEEE Transactions on Electron Devices* 59.12 (2012), pp. 3327–3333. ISSN: 00189383. DOI: 10.1109/TED.2012.2216535.

[133] H. J. von Bardeleben, J.L. Cantin, U. Gerstmann, A. Scholle, S. Greulich-Weber, E. Rauls, M. Landmann, W.G. Schmidt, A. Gentils, J. Botsoa, and M.F. Barthe. "Identification of the Nitrogen Split Interstitial $(N\text{-}N)_N$ in GaN". *Physical Review Letters* 109.20 (Nov. 2012), p. 206402. ISSN: 0031-9007. DOI: 10.1103/PhysRevLett.109.206402.

[134] D.C. Look, G.C. Farlow, P.J. Drevinsky, D.F. Bliss, and J.R. Sizelove. "On the nitrogen vacancy in GaN". *Applied Physics Letters* 83.17 (2003), pp. 3525–3527. DOI: 10.1063/1.1623009.

[135] J. Neugebauer and C.G. Van De Walle. "Atomic geometry and electronic structure of native defects in GaN". *Physical Review B* 50.11 (Sept. 1994), pp. 8067–8070. ISSN: 01631829. DOI: 10.1103/PhysRevB.50.8067.

[136] University of Rochester - Laboratory for Laser Energetics. *About OMEGA*. 2019. URL: http://www.lle.rochester.edu/omega_facility/omega/.

[137] H. W. Herrmann, C. S. Young, J M Mack, Y. H. Kim, A. McEvoy, S. Evans, T. Sedillo, S. Batha, M. Schmitt, D. C. Wilson, J. R. Langenbrunner, R. Malone, M. I. Kaufman, B. C. Cox, B. Frogget, E. K. Miller, Z. A. Ali, T. W. Tunnell, W. Stoeffl, C. J. Horsfield, and M. Rubery. "ICF gamma-ray reaction history diagnostics". *Journal of Physics: Conference*

Series 244.3 (Aug. 2010), p. 032047. ISSN: 1742-6596. DOI: 10.1088/1742-6596/244/3/032047.

[138] Y. Kim et al. “D-T gamma-to-neutron branching ratio determined from inertial confinement fusion plasmas”. *Physics of Plasmas* 19.5 (May 2012), p. 056313. ISSN: 1070-664X. DOI: 10.1063/1.4718291.

[139] M.J. Berger, J.H. Hubbell, S.M. Seltzer, J. Chang, J.S. Coursey, R. Sukumar, D.S. Zucker, and K. Olsen. *XCOM: Photon Cross Sections Database*. 2010. URL: https://www.nist.gov/pml/xcom-photon-cross-sections-database (visited on 2019).

[140] A. Javanainen, V. Ferlet-Cavrois, J. Jaatinen, H. Kettunen, M. Muschitiello, F. Pintacuda, M. Rossi, J.R. Schwank, M.R. Shaneyfelt, and A. Virtanen. “Semi-Empirical Model for SEGR Prediction”. *IEEE Transactions on Nuclear Science* 60.4 (Aug. 2013), pp. 2660–2665. ISSN: 0018-9499. DOI: 10.1109/TNS.2012.2236105.

[141] S. Stoffels, M. Melotte, M. Haussy, R. Venegas, D. Marcon, M. Van Hove, and S. Decoutere. “Stability Evaluation of Insulated Gate AlGaN/GaN Power Switching Devices Under Heavy-Ion Irradiation”. *IEEE Transactions on Nuclear Science* 60.4 (Aug. 2013), pp. 2712–2719. ISSN: 0018-9499. DOI: 10.1109/TNS.2013.2272331.

[142] J.-L. Leray, S. Bazzoli, N. Authier, J.-E. Sauvestre, J. Baggio, J. Raimbourg, J.-P. Seaux, J. Gazave, J.-C. Gomme, J.-L. Bourgade, V.Y. Glebov, G. Pien, T.C. Sangster, and C. Stoeckl. “Observation and modeling of currents induced by 14 MeV neutron recoils in dielectrics at high neutron fluxes”. *2007 9th European Conference on Radiation and Its Effects on Components and Systems*. IEEE, Sept. 2007, pp. 1–6. ISBN: 978-1-4244-1704-9. DOI: 10.1109/RADECS.2007.5205482.

[143] W. T. Anderson, R. C. Harrison, J. Gerdes, J. M. Beall, and J. A. Roussos. “Combined Pulsed Neutron and Flash X-ray Radiation Effects in GaAs MMICs”. *IEEE GaAs Symposium Digest* (1988), pp. 53–56.

[144] J.S. Melinger, S Buchner, D. McMorrow, W.J. Stapor, T.R. Weatherford, A.B. Campbell, and H. Eisen. “Critical evaluation of the pulsed laser method for single event effects testing and fundamental studies”. *IEEE Transactions on Nuclear Science* 41.6 (Dec. 1994), pp. 2574–2584. ISSN: 0018-9499. DOI: 10.1109/23.340618.

[145] S.P. Buchner, F. Miller, V. Pouget, and D.P. McMorrow. “Pulsed-Laser Testing for Single-Event Effects Investigations”. *IEEE Transactions on Nuclear Science* 60.3 (June 2013), pp. 1852–1875. ISSN: 0018-9499. DOI: 10.1109/TNS.2013.2255312.

[146] V. Pouget, H. Lapuyade, P. Fouillat, D. Lewis, and S. Buchner. “Theoretical Investigation of an Equivalent Laser LET”. *Microelectronics Reliability* 41.9-10 (Sept. 2001), pp. 1513–1518. ISSN: 00262714. DOI: 10.1016/S0026-2714(01)00156-1.

[147] J.M. Hales, A. Khachatrian, S. Buchner, N. J.-H. Roche, J. Warner, Z.E. Fleetwood, A. Ildefonso, J.D. Cressler, V. Ferlet-Cavrois, and D. Mcmorrow. “Experimental Validation of an Equivalent LET Approach for Correlating Heavy-Ion and Laser-Induced Charge Deposition”. *IEEE Transactions on Nuclear Science* 65.8 (Aug. 2018), pp. 1724–1733. ISSN: 0018-9499. DOI: 10.1109/TNS.2018.2828332.

[148] J.M. Hales, A. Khachatrian, S. Buchner, N. J.-H. Roche, J. Warner, and D. McMorrow. “A Simplified Approach for Predicting Pulsed-Laser-Induced Carrier Generation in Semiconductor”. *IEEE Transactions on Nuclear Science* 64.3 (Mar. 2017), pp. 1006–1013. ISSN: 0018-9499. DOI: 10.1109/TNS.2017.2665546.

[149] A. Ildefonso, Z.E. Fleetwood, G.N. Tzintzarov, J.M. Hales, D. Nergui, M. Frounchi, A. Khachatrian, S.P. Buchner, D. Mcmorrow, J.H. Warner, J. Harms, A. Erickson, K. Voss, V. Ferlet-Cavrois, and J.D. Cressler. “Optimizing Optical Parameters to Facilitate Correlation of Laser- and Heavy-Ion-Induced Single-Event Transients in SiGe HBTs”. *IEEE Transactions on Nuclear Science* 66.1 (Jan. 2019), pp. 359–367. ISSN: 0018-9499. DOI: 10.1109/TNS.2018.2882821.

[150] C.M. Hsieh, P.C. Murley, and R.R. O’Brien. “A field-funneling effect on the collection of alpha-particle-generated carriers in silicon devices”. *IEEE Electron Device Letters* 2.4 (Apr. 1981), pp. 103–105. ISSN: 0741-3106. DOI: 10.1109/EDL.1981.25357.

[151] A. R. Knudson, A. B. Campbell, J. R. Hauser, M. Jessee, W. J. Stapor, and P. Shapiro. “Charge Transport by the Ion Shunt Effect”. *IEEE Transactions on Nuclear Science* 33.6 (1986), pp. 1560–1564. ISSN: 0018-9499. DOI: 10.1109/TNS.1986.4334641. URL: http://ieeexplore.ieee.org/document/4334641/.

[152] M. Singh, M.J. Uren, T. Martin, S. Karboyan, H. Chandrasekar, and M. Kuball. “’Kink’ in AlGaN/GaN-HEMTs: Floating buffer model”. *IEEE Transactions on Electron Devices* 65.9 (2018), pp. 3746–3753. ISSN: 00189383. DOI: 10.1109/TED.2018.2860902.

[153] E.T.F. Rogers, J. Lindberg, T. Roy, S. Savo, J.E. Chad, M.R. Dennis, and N.I. Zheludev. “A super-oscillatory lens optical microscope for subwavelength imaging”. *Nature Materials* 11.5 (May 2012), pp. 432–435. ISSN: 1476-1122. DOI: 10.1038/nmat3280.

[154] J.P. Biersack and L.G. Haggmark. “A Monte Carlo computer program for the transport of energetic ions in amorphous targets”. *Nuclear Instruments and Methods* 174.1-2 (2002), pp. 257–269. ISSN: 0029554X. DOI: 10.1016/0029-554x(80)90440-1.

[155] J. P. Biersack and J. F. Ziegler. “The Stopping and Range of Ions in Solids”. *Ion Implantation Techniques*. Berlin, Heidelberg: Springer Berlin Heidelberg, 1982, pp. 122–156. DOI: 10.1007/978-3-642-68779-2_5.

[156] M.T. Robinson. "The temporal development of collision cascades in the binary-collision approximation". *Nuclear Instruments and Methods in Physics Research Section B: Beam Interactions with Materials and Atoms* 48.1-4 (Mar. 1990), pp. 408–413. ISSN: 0168583X. DOI: 10.1016/0168-583X(90)90150-S.

[157] M.T. Robinson. "The binary collision approximation: Background and introduction". *Radiation Effects and Defects in Solids* null.1 (July 1994), pp. 3–20. ISSN: 1042-0150. DOI: 10.1080/10420159408219767.

[158] C.A. Klein. "Bandgap Dependence and Related Features of Radiation Ionization Energies in Semiconductors". *Journal of Applied Physics* 39.4 (Mar. 1968), pp. 2029–2038. ISSN: 0021-8979. DOI: 10.1063/1.1656484.

[159] European Space Agency (ESA). *Semiconductor Electron-Hole Pair Creation Energies*. 2007. URL: http://sci.esa.int/future-missions-department/41035-semiconductor-electron-hole-pair-creation-energies/ (visited on 04/02/2019).

[160] P. J. Sellin and J. Vaitkus. "New materials for radiation hard semiconductor dectectors". *Nuclear Instruments and Methods in Physics Research, Section A: Accelerators, Spectrometers, Detectors and Associated Equipment* 557.2 (2006), pp. 479–489. ISSN: 01689002. DOI: 10.1016/j.nima.2005.10.128.

[161] M. Kuball, J.M. Hayes, M.J. Uren, I. Martin, J.C.H. Birbeck, R.S. Balmer, and B.T. Hughes. "Measurement of temperature in active high-power AlGaN/GaN HFETs using Raman spectroscopy". *IEEE Electron Device Letters* 23.1 (Jan. 2002), pp. 7–9. ISSN: 0741-3106. DOI: 10.1109/55.974795.

[162] T. Katsuno, T. Manaka, T. Ishikawa, H. Ueda, T. Uesugi, and M. Iwamoto. "Degradation analysis and current collapse imaging of AlGaN/GaN HEMTs by measurement of electric field-induced optical second-harmonic generation". *Microelectronics Reliability* 54.9-10 (2014), pp. 2227–2231. ISSN: 00262714. DOI: 10.1016/j.microrel.2014.07.025.

[163] T. Katsuno, T. Manaka, T. Ishikawa, H. Ueda, T. Uesugi, and M. Iwamoto. "Current collapse imaging of Schottky gate AIGaN/GaN high electron mobility transistors by electric field-induced optical second-harmonic generation measurement". *Applied Physics Letters* 104.25 (2014). ISSN: 00036951. DOI: 10.1063/1.4885838.

[164] J. H. Bechtel and W. L. Smith. "Two-photon absorption in semiconductors with picosecond laser pulses". *Physical Review B* 13.8 (Apr. 1976), pp. 3515–3522. ISSN: 0556-2805. DOI: 10.1103/PhysRevB.13.3515.

[165] E.W. Van Stryland, H. Vanherzeele, M. A. Woodall, M. J. Soileau, A.L. Smirl, S. Guha, and T.F. Boggess. "Two Photon Absorption, Nonlinear Refraction, And Optical Limiting In Semiconductors". *Optical Engineering* 24.4 (1985). ISSN: 0091-3286. DOI: 10.1117/12.7973538.

[166] J. Miragliotta and D.K. Wickenden. “Transient photocurrent induced in gallium nitride by two-photon absorption”. *Applied Physics Letters* 69.1996 (1996), pp. 2095–2097. ISSN: 00036951. DOI: 10.1063/1.116891.

[167] J.M. Hales. Private communication. 2018.

[168] N.J. Everall. “Modeling and Measuring the Effect of Refraction on the Depth Resolution of Confocal Raman Microscopy”. *Applied Spectroscopy* 54.6 (June 2000), pp. 773–782. ISSN: 0003-7028. DOI: 10.1366/0003702001950382.

[169] D. McMorrow, J.M. Hales, A. Khachatrian, S.P. Buchner, and J.H. Warner. “Radiation effects testing via semiconductor nonlinear optics: successes and challenges”. *Proc. of SPIE*. Ed. by Michael K. Rafailov. Vol. 1019307. May 2017. May 2017, p. 1019307. DOI: 10.1117/12.2262841.

[170] J.W. Pomeroy and M. Kuball. “Solid immersion lenses for enhancing the optical resolution of thermal and electroluminescence mapping of GaN-on-SiC transistors”. *Journal of Applied Physics* 118.14 (Oct. 2015), p. 144501. ISSN: 0021-8979. DOI: 10.1063/1.4932029.

[171] W. Stefan, B. Grobler, M. Gluch, and H. Heinz. “Confocal laser scanning microscopy”. URL: http://www.webcitation.org/6PuXY8bZH.

[172] D.I. Kovsh, S. Yang, D.J. Hagan, and E.W. Van Stryland. “Nonlinear optical beam propagation for optical limiting”. *Applied Optics* 38.24 (Aug. 1999), p. 5168. ISSN: 0003-6935. DOI: 10.1364/AO.38.005168.

[173] C. Klingshirn. *Semiconductor Optics*. Third. Berlin, Heidelberg: Springer Berlin Heidelberg, 2007. ISBN: 978-3-540-38345-1. DOI: 10.1007/978-3-540-38347-5.

[174] A. Matulionis. “Feature article: Hot phonons in GaN channels for HEMTs”. *Physica Status Solidi (A) Applications and Materials Science* 203.10 (2006), pp. 2313–2325. ISSN: 18626300. DOI: 10.1002/pssa.200622101.

[175] H. Mizuta, K. Yamaguchi, and S. Takahashi. “Surface Potential Effect on Gate-Drain Avalanche Breakdown in GaAs MESFET’s”. *IEEE Transactions on Electron Devices* 34.10 (1987), pp. 2027–2033. ISSN: 15579646. DOI: 10.1109/T-ED.1987.23194.

[176] W. Saito, T. Nitta, Y. Kakiuchi, Y. Saito, K. Tsuda, I. Omura, and M. Yamaguchi. “Suppression of Dynamic On-Resistance Increase and Gate Charge Measurements in High-Voltage GaN-HEMTs With Optimized Field-Plate Structure”. *IEEE Transactions on Electron Devices* 54.8 (Aug. 2007), pp. 1825–1830. ISSN: 0018-9383. DOI: 10.1109/TED.2007.901150.

Acronyms

2DEG Two-dimensional Electron Gas. 8, 10, 11, 13–19, 23, 24, 26, 35, 36, 42, 48, 56, 59, 60, 62, 63, 71, 79, 80, 84–87, 93–96, 98, 104, 107, 121, 156, 157, 165, 184, 189, 190

AC Alternating Current. 48

AFM Atomic Force Microscope. 180, 181, 183

AlGaN aluminium gallium nitride. 6–10, 12, 13, 15–18, 20, 26, 34, 36, 41, 42, 49, 57, 59, 60, 67, 74, 84–87, 90, 95, 96, 103–105, 107, 130, 154–156, 185, 189, 190

AlN aluminium nitride. 6, 15, 17, 65, 74, 190

BCA binary collision approximation. 33

BTE Boltzmann Transport Equation. 25, 26, 33

CCDs charge coupled devices. 2

CTS Current Transient Spectroscopy. 47, 48, 53, 89, 90, 93

DC Direct Current. 43, 45, 48, 52, 53, 107, 113, 114, 116–121, 123, 130, 131, 164, 190

DIL dual in-line. 44, 45

DiVA dynamic iV analysis. 113

DLTS Deep Level Transient Spectroscopy. 90

DoF Depth of Field. 140, 142

DRAMs dynamic random access memories. 2

DUT device under test. xi, 44, 46–48, 53, 109, 111, 113–116, 122, 125, 126, 191

EDX Energy-dispersive X-ray spectroscopy. 45

EFISHG Electric-Field Induced Second Harmonic Generation. 138

EHP electron-hole plasma. 145, 147

EMP electro-magnetic pulse. 114, 115

FET field effect transistor. 7, 42, 60

FWHM Full Width at Half Maximum. 52, 132, 140, 142, 143, 145, 147, 148, 162, 163, 174, 176, 178

GaAs gallium arsenide. 6, 190

GaN gallium nitride. 1, 6–12, 14–18, 20, 26, 27, 31, 33, 34, 36–38, 41, 42, 45, 59, 65, 67, 74, 84, 90, 95, 96, 103, 105, 107, 110, 111, 122, 124–126, 130, 135, 139, 141, 142, 145, 154–156, 185, 189, 190

GSG Ground-Signal-Ground. 50–52, 130

HEMT High Electron Mobility Transistor. 7–14, 18–20, 23, 24, 26, 28, 35, 36, 42, 45–47, 50, 52, 56, 60, 71, 84, 89–95, 97–99, 101, 103–107, 109–113, 115–127, 129–131, 133, 136, 138, 140, 147, 152, 154, 156–160, 162, 164, 165, 167, 168, 170, 171, 173, 176, 178–181, 183–187, 189–191

HFET heterojunction field effect transistor. 7, 12

ICF Inertial Confinement Fusion. 44, 109–114, 116, 117, 121–126, 190

LEDs light-emitting diodes. 1, 6

LET linear energy transfer. xi, 9, 36–38, 42, 110, 128, 129, 160

MBE Molecular beam epitaxy. 12

MCNP Monte Carlo N-particle. 32, 37, 101, 135

MIS metal-insulator-semiconductor. 111, 123, 126

MMICs monolithic microwave integrated circuits. 8, 20, 126

MOCVD Metal organic chemical vapour deposition. 12

NA Numerical Aperture. 142, 143

NED Nuclear Effects Diagnostic. 113, 115, 116, 122, 126

NIEL Non-Ionising Energy Loss. 5, 27, 90

OBIC Optical Beam Induced Current. 186

PCB Printed Circuit Board. 44, 91, 113–117, 124–126

PID Proportional Integral Differential. 50, 92

PKA Primary Knock-on Atom. 27, 31–33, 36, 37, 42, 103, 109, 111, 135, 136, 147, 160, 178, 184, 187

PRF Pulse Repetition Frequency. 52, 129, 144, 160, 162–167, 173, 174, 177, 178, 186, 191

PSU Power Supply Unit. 52, 117, 119, 130

RF radio frequency. 8, 20, 44, 52, 113, 114, 130

RPP Rectangular Parallelpiped. 128

SAA South Atlantic Anomaly. 3, 4, 8

SEE Single Event Effect. 8, 9, 27, 53, 109, 110, 121, 125, 127, 128, 159, 160, 167, 178, 184, 187, 190, 191

SEGR Single Event Gate Rupture. 110, 116, 122, 125

SES Single Event Switching. 110, 124, 125

SEUs single event upsets. 4, 5

SGEMP system-generated electromagnetic pulse. 115

Si silicon. 6, 12, 45, 111, 124–126, 190

SiC silicon carbide. 6, 8, 12, 20, 125, 130, 141

SIL Solid Immersion Lens. 142, 143

SMUs Source Measure Units. 43, 45–48, 53, 93

SNL Sandia National Laboratories. 57, 64, 70, 76

SOI silicon-on-insulator. 129

SPA Single Photon Absorption. 132, 141, 142, 144, 158

SRAM static random access memory. 129

SRIM Stopping and Range of Ions in Matter. 37

TCAD Technology computer-aided design. 70, 71, 93, 129, 155, 156, 187

TCC Target Chamber Centre. 110, 111, 113, 115, 116, 125, 126

TIM Target Insertion Module. 113, 125

TNT trinitrotoluene. 2

TPA Two Photon Absorption. 39, 44, 53, 128, 129, 132, 134, 138–145, 147, 150, 158–160, 186, 191

TRIM Transport of Ions in Matter. 33, 135, 136

UMS United Monolithic Semiconductor. 130, 141

UoB University of Bristol. 44, 45

UWBG Ultra-Wide Band-Gap. 9, 12, 17, 59, 84, 85, 87, 107

WBG Wide Band-Gap. 8, 9, 85, 89, 107, 189

“The Moving Finger writes; and, having writ,
Moves on: nor all thy Piety nor Wit
Shall lure it back to cancel half a line,
Nor all thy Tears wash out a Word of it.”

- Rubáiyát of Omar Khayyám